Imperial College London

Development of Versatile Imaging Tools for Mechanical and Chemical Interrogation of Biological Systems

PhD Thesis

Konstantinos Kalyviotis

A thesis submitted to the Department of Bioengineering, Imperial College London for the Award of the PhD in Bioengineering Research and the Diploma of Imperial College, PhD degree.

Imperial College London
Department of Bioengineering

January 2023

Statement of Originality

I declare that this thesis is my own work under the supervision of Dr Periklis (Laki) Pantazis. The work was performed in the Department of Bioengineering at Imperial College London. All published and unpublished materials used in the thesis have been given full acknowledgement. This work has not been previously submitted, in whole or in part, to any other academic institution for a degree, diploma, or any other qualification.

Konstantinos Kalyviotis
January 2023, London

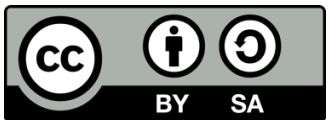
Copyright Notice

The copyright of this thesis rests with the author. Unless otherwise indicated, its contents are licensed under a Creative Commons Attribution-ShareAlike 4.0 International (CC BY-SA[1]).

Under this licence, you may copy and redistribute the material in any medium or format for both commercial and non-commercial purposes. You may also create and distribute modified versions of the work. This on the condition that: you credit the author and share any derivative works under the same licence.

When reusing or sharing this work, ensure you make the licence terms clear to others by naming the licence and linking to the licence text. Where a work has been adapted, you should indicate that the work has been changed and describe those changes.

Please seek permission from the copyright holder for uses of this work that are not included in this licence or permitted under UK Copyright Law.



[1] For the complete CC BY-SA 4.0 licence visit https://creativecommons.org/licenses/by-sa/4.0/.

Acknowledgments

«Εὐποιίας ἧς ἔτυχες μνημόνευε»

"Remember the good things you have received"

Cleobulus of Rhodes

"Remember the good things you have received." This phrase of Cleobulus of Rhodes always comes to my mind every time I am to write acknowledgements. It's been there in my mind since I started my undergraduate studies and still follows me all these years at the end of my PhD.

I stand amazed when it's already been more than four years since my father drove me to the airport in Thessaloniki for my flight to London. I remember the feeling as we left our family home in my beautiful Arnea, driving through the autumn-coloured mountain Cholomon on our way to Thessaloniki. It was a weird uneasy excitement that I shared with the dearests of my friends and loved ones. A feeling that transformed into gratitude and optimism for the future, our new future, as I was watching the "British" night sky from the window of my first room in London.

And this brings me to the first person I would like to thank, my supervisor and mentor, Dr Laki Pantazis. He was there for me from the first moment with his beautiful family (Nadine, Leopold and Phyllis). They opened their house for me and gave me a place to feel at home until I settled in London a month later. It was the same support they gave me when I went to Basel for my internship and I cannot put

into words how grateful I am. Laki, thank you very much for everything you taught me, everything you are teaching me and everything I am sure you will continue to teach me as a colleague, mentor and friend. Nadine, Leo and Phyllis, thank you for welcoming me so wholeheartedly in London. I will always be grateful.

The first months of my PhD were quite unusual as I was the only member of the lab for more than one year. However, I can tell you that I did not feel alone at all. And this is because I met in the Department of Bioengineering some of the kindest people who kept me company and knocked multiple times per day on the door of B104 in the Bessemer building to say hi, ask me how I am doing and offer a helping hand throughout the years. Ken, Joel, Jo, Darek, Julian, Miguel, Alan, Chris, Marc, Daze, Kosta, Nana, Ji, Brita, Estelle, Martina, Enrico, Julia, Angele, Neelima, Julie, Sofia, Catalina, Ugur, Guglielmo, Michalis, Maria, Jacques, Beth, Marta, Jennifer, Adele, Paloma, Marta, Greg, Sharad, thank you for everything.

Now, I want to wholeheartedly thank all the members of the Pantazis lab who were always there for me and supported me when experiments were not going well. First, the old lab members in Basel who welcomed me so warmly for my internship. Maaike, Hanyu, Sine, Ali, Dan and Manuel, I am so grateful for all the great discussions we had about research, music, life and so much more. And now, the new and past members of the team in London. Elijah, Edagül, Julian, Maëlle, Aysen, Alex, Yacout, Maria, Vishnu, Athina, Daniel, Andrew, Fabian, Pom, Zhao, Lorena, Fotini, Adele, Aurelien, Debby, thank you each one for making the gloom days bright and every day beautiful. I am really grateful. I am sure we will continue have so much fun in the future! Wish you all the best from the bottom of my heart!

I want also to take the opportunity and thank the members of the Vermot and Salem labs. Dr Julien Vermot, Dr Victoria Salem, Emmanuelle, Kinga and Ben, thank you

wholeheartedly for your kind and supportive presence in the lab and our everyday life! We have so much fun!

A special thank you is to my dearest Foivos, who was the person who supported me in a moment of my PhD when someone could easily give up. He stayed on my side, helped me and talked me through the basics. Since then, we have drunk a loooot of coffee (and tea) and spent many hours discussing everything that someone can imagine. The moment he finished his PhD was a moment of joy and I am so happy to call him a friend! I wish him all the best from my heart!

And now is the time to thank the other "Greeks" in the Department who were and are always there for me. My dearests Simo, Kosti and Giorgo, I am sooo grateful to have met you, my friends! I wish you all the best for the future!

I also want to thank Dr Chris Rowlands and Dr Sylvain Ladame, who provided their critical criticism when needed while offering their support effortlessly. I want to thank Cocoa from the Rowland's lab, who made my experience working with optics enjoyable and smiley!

In addition, I want to thank Dr Marc Morgan, Dr Sam Horrell (whom by the way I met on Twitter) and Dr Nicholas Glykos, who supported me and still support me with all the protein crystallisation and X-ray diffraction experiments. They were there to tell me that a lot of people have crystallised salts and they thought it was protein! I am so happy to have met you and I am sure we will do some amazing experiments in the future!

I would like also to thank Dr Jian Shi and Dr Nordine Helassa for their support and stimulative discussions on GenEPi. Also, I want to thank Dr Carlos Pardo-Pastor and

Dr Jody Rosenblatt for the exciting interactions we have had the past few months. It makes me excited for the future!

I want to also thank the other PhD Reps at the Departments of Bioengineering, Krysia, Leah, Andra, Maria, Leah, Alba, Anna, Pooja, with whom I shared so many interesting discussions (and pizzas) and tried to make our PhD life better! Thank you for all your support and for your patience! Also, I would like to thank the other members of the newly founded Young Researcher Committee of the European Zebrafish Society, Vania, Max, Annelies and Tim, who kept me motivated and put a smile on my face until the very last moment! Thank you all and let's rock that YoRC session in Krakow meeting!

Also, I would like to thank my friends in London and in Greece who kept me sane through the years with their great company. Thank you, Fr Paisie, Fr Dimitri, Vassili, Petro, Alexandre, Evi, Vaggeli, Maraki, Dimitri, Pano, Michali, Eleni, Panagiotaki, Jordan, Maria, Strato! I am really thankful you made this journey so amazing!

Here, I would like thank to my two examiners, Dr Naomi Nakayama and Dr Yanlan Mao. The journey through my viva was made insightful due to the absolutely wonderful discussions we had. Their invaluable feedback not only shaped the refinement of my thesis but also inspired me for the future and I hope some of the Figure 4/5s we discussed will become reality in the future! I am truly fortunate to have had the privilege of your guidance and support!

And now is the moment, I would like to thank my parents, who made me the person I am today by raising me so selflessly. However, as they do not understand the English language, I will write in Greek. Πατέρα, μάνα, σε αυτό το σημείο θα ήθελα να σας ευχαριστήσω από τα βάθη της καρδιάς μου γιατί ήσασταν πάντα εκεί να με

στηρίζεται σε κάθε βήμα μου προσπαθώντας ποτέ να “μην σκόψουμε το παιδί”. Είστε μεγάλη πηγή έμπνευσης για μένα! Σας ευχαριστώ για όλα και θα σας είμαι πάντοτε ευγνώμων! Χωρίς εσάς δεν θα ήμουν ο άνθρωπος που είμαι και οι λέξεις δεν είναι αρκετές να περιγράψουν αυτά που νιώθω. Πολλοί επαναλαμβάνοντας τον λόγο του Μ. Αλεξάνδρου λένε πως στους γονείς μας χρωστάμε το «ζῆν», αλλά μάλλον σε σας οφείλω το «εὖ ζῆν» μου!

Finally, I would like to thank the most prominent person in my life to whom I dedicate this thesis. The love of my life and beautiful wife, Christina! She is always there for me, although I do not understand it sometimes. She smiles when I smile and she is excited when I am excited! I admire her because she is the most assertive person I know. We have been together 10 years since we met in Alexandroupolis on a bus going for the first lecture of our undergraduate years. And last summer we celebrated 1 year of marriage! Christina, you are the best thing that happened in my life, and you continue making every day better than the other! ありがとう!

«δόσις δ’ ὀλίγη τε φίλη τε».

Στην γλυκιά σύζυγό μου Χριστίνα
Αγάπη και συνοδοιπόρο
που ομορφαίνει την ζωή μου
συνεχώς και περισσότερο

Και στους αγαπητούς γονείς μου
Ευάγγελο και Μονεμβασία
εσαεί ευγνώμων

Abstract

Living multicellular organisms exhibit both organisational structures and dynamic behaviours. Common to all is the necessity to preserve information for robust organism development and the need to sense and adapt to environmental changes. Hence, to understand holistically a biological system, interrogation of both its biochemical and biomechanical components is needed. Here, I detail my work on developing advanced optical precision imaging tools that enable the study of the biochemical and mechanical nature of biological systems.

First, I present my work on Piezo1, an ion channel directly gated by mechanical forces essential for cellular mechanosensation across biological kingdoms. I describe my efforts in testing, further developing, and validating both *in vitro* and *in vivo* the first genetically-encoded fluorescent biosensor for Piezo1-dependent activity, named GenEPi. Then, I describe my efforts on primed conversion, a novel method for axially confined and non-toxic photoconversion of green-to-red photoconvertible fluorescent proteins. I detail my work on improving primed conversion efficiency using a semi-rational protein engineering approach combined with X-ray crystallography and describe the evaluation of primed conversion implementation in a single-objective light-sheet microscope. Finally, I present my work on bioharmonophores, a new class of polymer-encapsulated biodegradable Second Harmonic Generation

nanoprobes, which overcome inherent limitations of fluorescent probes and can be used for specific cell targeting without expected adverse effects.

Altogether, this advanced imaging toolkit, which includes a biosensor (GenEPi), improved fluorescent proteins (primed conversion), a novel microscope (primed conversion) and SHG nanoprobes (bioharmonophores) is poised to change the way we capture the intricate interplay between biochemical and mechanical signals that influence the fundamental processes of life, providing a holistic view of systems biology.

Contribution Statement

As the presented work was highly collaborative, forming long-term projects in the Pantazis Lab and extended collaborative teams, the contributions of the several researchers who supported the work presented in this thesis are acknowledged below.

All Chapters

Dr Periklis (Laki) Pantazis supervised the projects. Dr Periklis (Laki) Pantazis and Konstantinos Kalyviotis were involved in the conceptualisation of experiments and discussions on the analysed data. Konstantinos Kalyviotis was involved in the design and planning of experiments and performed the data analysis of the acquired datasets, except mentioned otherwise below.

Chapter 2

- Sine Yaganoglu (ETH Zurich) designed and performed the systematic screening experiments presented in Fig. 26 and Table 5. She also performed the statistical analysis presented in appendix A.5.
- Dr Jian Shi (University of Leeds) carried out the electrophysiology experiments.
- Dr Maaike Welling generated the dox-inducible mESC line and performed the initial differentiation experiments.
- Tatiana Lopes, under the supervision of Dr Victoria Salem, assisted Konstantinos Kalyviotis with further differentiation experiments.
- Konstantinos Kalyviotis and See Swee (Elijah) Tang designed and generated the XLGenEPi plasmid.

- Dr Armando Del Rio Hernandez provided access to a TIRF microscope and Dr Dariusz (Darek) Lachowski assisted Konstantinos Kalyviotis with the TIRFM imaging.
- Dr Dörthe Julich and Dr Scott A. Holley generated the zebrafish transgenic line assisted by Konstantinos Kalyviotis.
- Christina Vagena-Pantoula, under the supervision of Dr Julien Vermot, and Konstantinos Kalyviotis carried out the in vivo characterisation experiments.
- Christina Vagena-Pantoula assisted with the zebrafish heart imaging experiments.
- Dr Bettina (Tina) Trauernicht (Acquifer), Dr Jochen Gehrig (Acquifer) and Dr Thomas Laurent (Acquifer) provided access to the ACQUIFER Imaging Machine and supported Konstantinos Kalyviotis and Christina Vagena-Pantoula with the *in vivo* longitudinal analysis of GenEPi expression upon heat-shock.
- Konstantinos Kalyviotis did all other experiments and data analysis.

Chapter 3

- Dr Marc Morgan (Imperial X-ray Facilities Manager) assisted with the designing of the crystallisation optimisation experiments, the handling of the produced crystals, and the data analysis.
- Dr Sam Horrell (Diamond Light Source) assisted with the handling of produced crystals during the X-ray diffraction experiments and performed the X-ray data acquisition.
- Konstantinos Kalyviotis conceptualised the semi-rational protein engineering approach, the X-ray diffraction experiments and established the collaboration with Dr Sam Horrell (Diamond Light Source) with the support of Dr Periklis (Laki) Pantazis.

- Dr Christopher Rowlands and Dr Ke Guo designed and constructed the single-objective primed conversion microscope.
- Dr Ke Guo assisted with the imaging experiments using the primed conversion single-objective light-sheet microscope and performed initial data analysis of the acquired datasets.
- Konstantinos Kalyviotis did all other experiments and data analysis.

Chapter 4

- Dr Ali Yasin Sonay and Dr Periklis (Laki) Pantazis conceptualised and developed bioharmonophores.
- Dr Ingo Lieberwirth (Max Planck Institute for Polymer Research) performed the TEM experiments of bioharmonophore samples prepared by Konstantinos Kalyviotis and Aysen Unsal.
- Konstantinos Kalyviotis performed the data analysis of the acquired TEM data and discussed the results with Dr Periklis (Laki) Pantazis, Dr Katharina Landfester (Max Planck Institute for Polymer Research) and Dr Ingo Lieberwith.
- Konstantinos Kalyviotis did all other experiments and data analysis.

Related Work

Peer-Reviewed Publications and Preprints

****Equal contribution** **†Correspondence**

In revision

- Gaudiano E, Eisert R, Bradshaw G**, Kalyviotis K**, Montero Llopis P, Clark M, Anekal P, LaFleur M, Markson S, Buck S, Sorger P, Freeman G, Pantazis P, Kalocsay M† and Sharpe A†. PD-1 inhibits PIEZO1 on CD8+ T cells to impair antitumor immunity. *Nature*.
- Ulucay E, Bollier P**, Spilioti M**, Yasin Sonay A, **Kalyviotis K†**, Pantazis P†. Synthesis and functionalisation of biodegradable Second Harmonic Generation nanoprobes for cell targeting. *Current Protocols*.

2023

- Yaganoglu S**, **Kalyviotis K****, Vagena-Pantoula C, Jülich D, Gaub B.M, Welling M, Lopes T, Lachowski D, Tang S.S, Del Rio Hernandez A, Salem V, Müller D.J, Holley S.A, Vermot J, Shi J, Helassa N, Török K, Pantazis P†. Highly specific and non-invasive imaging of Piezo1-dependent activity across scales using GenEPi. *Nat Commun* 14, 4352. https://doi.org/10.1038/s41467-023-40134-y
- **Kalyviotis K** & Pantazis P†. Primed conversion: The emerging player of precise and nontoxic photoconversion. *Journal of Microscopy*, 00, 1–8. https://doi.org/10.1111/jmi.13244
- Guo K, **Kalyviotis K**, Pantazis P, Rowlands CJ. Hyperspectral Oblique Plane Microscopy Enables Spontaneous, Label-Free Imaging of Biological Dynamic Processes in Live Animals. *bioRxiv*. https://doi.org/10.1101/2023.03.15.532804

2021

- Yasin Sonay A, **Kalyviotis K**, Yaganoglu S, Unsal A, Konantz M, Teulon C, Lieberwirth I, Sieber S, Jiang S, Behzadi S, Crespy D, Landfester K, Roke S, Lengerke C, Pantazis P†. Biodegradable harmonophores for targeted high resolution in vivo tumor imaging. *ACS Nano*. https://doi.org/10.1021/acsnano.0c10634

2020

- Welling M, **Kalyviotis K**, Pantazis P†. Primed Track: Reliable Volumetric Single-cell Tracking and Lineage Tracing of Living Specimen with Dual-labelling Approaches. *Bio-protocol* 10(11): e3645. https://doi.org/10.21769/BioProtoc.3645
- **Kalyviotis K**, Qin H, Pantazis P†. PhOTO zebrafish and primed conversion: advancing the mechanistic view of development and disease. In: Gerlai RT, editor. Behavioral and Neural Genetics of Zebrafish: Academic Press. p. 309-22. https://doi.org/10.1016/B978-0-12-817528-6.00019-X

Invited Manuscripts

- **Kalyviotis K**, Welling M, B Bénéfice M, Pantazis P†. Use of primed convertible fluorescent proteins for cell lineage tracing. (*Current Protocols*, in preparation)

Scientific Posts

2021

- **Kalyviotis K**. Primed conversion: the Basics. *Focal Plane*. https://doi.org/10.1242/focalplane.7373

Presentations and Posters

****Equal contribution** **†Correspondence**

- **Konstantinos Kalyviotis****, Sine Yaganoglu**, Periklis Pantazis†. Highly specific and non-invasive imaging of Piezo1-dependent activity across scales using GenEPi. Fluorescent Proteins and Biological Sensors VII, HHMI, 10-13 September 2023, (Conference, Oral poster blitz talk and poster presentation)

  Janelia/HHMI Travel Scholarship

- **Konstantinos Kalyviotis**. Highly specific and non-invasive imaging of Piezo1-dependent activity across scales using GenEPi. Seeing is believing, EMBL/EMBO, 4-7 October 2023, (Conference, Invited oral presentation)

  EMBO and EMBL Symposia Fellowship (1 out of 20 awarded)

- **Konstantinos Kalyviotis**. Highly specific and non-invasive imaging of Piezo1-dependent activity across scales using GenEPi. 12th European Zebrafish Meeting 2023, EZS, 9-13 July 2023, (Conference, Invited oral presentation)

  Christine Beattie Award 2023 (International Zebrafish Society) for "demonstrating excellence in the field of zebrafish research and exhibiting promise as a future leader in the zebrafish field"

- Lorena Garcia-Foncillas**, Fotini Kioutsouki**, **Konstantinos Kalyviotis†** & Periklis Pantazis†. Analysis of membrane Piezo1 kinetics using GenEPi-A new tool for non-invasive imaging of Piezo1 activity. Crick Bioimage Analysis Symposium 2022, Francis Crick Institute, 21-22 November 2022, (Poster presentation, https://doi.org/10.25418/crick.21552363)

- **Konstantinos Kalyviotis**,** Sine Yaganoglu**, Nordine Helassa, Benjamin M. Gaub, Maaike Welling, Tatiana Goncalves Lopes, Dariusz Lachowski, Jian Shi, See S. Tang, Armando Del Rio Hernandez, Victoria Salem, Daniel J. Müller, Katalin Török, **Periklis Pantazis†**. Direct functional imaging of Piezo1 dynamics with the designed fluorescent reporter GenEPi. 17th International Zebrafish Conference, IZFS, 22-26 June 2022 (flash talk by PP and poster presentation)

- **Konstantinos Kalyviotis**,** Sine Yaganoglu**, Nordine Helassa, Benjamin M. Gaub, Maaike Welling, Tatiana Goncalves Lopes, Dariusz Lachowski, Jian Shi, See S. Tang, Armando Del Rio Hernandez, Victoria Salem, Daniel J. Müller, Katalin Török, Periklis Pantazis†. Direct functional imaging of Piezo1 dynamics with the designed fluorescent reporter GenEPi. Mechanobiology in Development and Disease, EMBO/EMBL Symposium, 15-18 May 2022 (flash talk and poster presentation)

- **Konstantinos Kalyviotis**,** Sine Yaganoglu**, Nordine Helassa, Benjamin M. Gaub, Maaike Welling, Tatiana Goncalves Lopes, Dariusz Lachowski, Jian Shi, See S. Tang, Armando Del Rio Hernandez, Victoria Salem, Daniel J. Müller, Katalin Török, Periklis Pantazis†. Direct functional imaging of Piezo1 dynamics with the designed fluorescent reporter GenEPi. BSDB/BSCB Joint Spring Meeting 2022, BSDB/BSCB, 3-6 April 2022 (poster presentation)

- **Konstantinos Kalyviotis**,** Sine Yaganoglu**, Nordine Helassa, Benjamin M. Gaub, Maaike Welling, Tatiana Goncalves Lopes, Dariusz Lachowski, Jian Shi, See S. Tang, Armando Del Rio Hernandez, Victoria Salem, Daniel J. Müller, Katalin Török, Periklis Pantazis**†**. GenEPi: A fluorescent reporter for mechanical stimuli and Piezo1 activity. 4th London Stem Cell Network Symposium, LSCN, 19 October 2021 (Poster presentation)

- **Konstantinos Kalyviotis**, Hanyu Qin, Dan-Felix Scherrer, Maaike Welling, Periklis Pantazis**†**. PhOTO-Bow: Using primed conversion for single-cell tracking and clonal analysis. Virtual 80th Annual Meeting of Society of Developmental Biology, SDB, 12-16 July 2021 (Poster presentation)

  Society for Developmental Biology Student/Postdoc Annual Meeting Grant Award

- **Konstantinos Konstantinos**, Maaike Welling, Hanyu Qin, Periklis Pantazis**†**. Primed conversion for advanced in vivo precision imaging. Virtual 11th European Zebrafish Meeting 2020, EuFishBioMed, October 2020 (Poster presentation awarded with registration grant and best poster award)

  EuFishBioMed Society Meeting Registration Grant Award

  Best Poster Award accompanied by EuFishBioMed (currently EZS) sponsored annual membership to the society

- Maaike Welling, **Konstantinos Kalyviotis**, Periklis Pantazis**†**. Primed Track: reliable volumetric single-cell tracking and lineage tracing of living specimen with dual-labelling approaches. Virtual 12th Light Sheet Fluorescence Microscopy Conference 2020, Royal Microscopical Society, September 2020 (Poster presentation)

Contents

Statement of Originality ii

Copyright Notice iii

Acknowledgments iv

Abstract x

Contribution Statement xii

Related Work xv

Peer-Reviewed Publications and Preprints xv

Scientific Posts xvi

Presentations and Posters xvi

Contents xix

List of Figures xxii

List of Tables xxvi

Abbreviations xxvii

Chapter 1. Introduction 1

1.1 Cell labelling for chemical interrogation of biological systems 3

1.1.1 Direct observation 3

1.1.2 Interspecies transplantations and vital dyes 5

1.1.3 Fluorescence 5

1.1.3.1 The Green Fluorescent Protein and bioimaging 7

1.1.3.2 Genetic markers for lineage tracing 8

1.1.3.3 Genetic recombination approaches 11

1.1.3.4 Limitations of lineage tracing using genetically encoded markers and combinatorial events 11

1.1.4 Photomodifiable fluorescent proteins and photochromism 12

1.1.4.1 Photoconvertible fluorescent proteins and 405nm photoconversion 13

1.1.4.2 Photoconvertible fluorescent proteins for lineage tracing 15

1.1.4.3 Primed conversion 16

1.1.4.4 Benefits of primed conversion 19

1.1.4.5 Primed conversion for precise lineage tracing 21

1.1.5 Inherent limitations of fluorescent probes 23

1.1.5.1 Bleaching 23

1.1.5.2 Blinking 23

1.1.5.3 Saturation *23*
1.1.6 Second Harmonic Generation nanoprobes for specific cell labelling 24

1.2 Mechanical interrogation of biological systems **28**
1.2.1 Cellular mechanosensation and mechanotransduction 29
1.2.2 Methods to measure cell mechanics 31
1.2.3 Piezo1 mechanosensitive ion channels 33
1.2.3.1 Piezo protein family *33*
1.2.3.2 Piezo1 structure *37*
1.2.3.3 Piezo1 gating *37*
1.2.3.4 Chemical modulators of Piezo1 activity *40*

1.3 Aims of this thesis **41**
1.3.1 Mechanical interrogation of biological systems 42
1.3.1.1 Piezo1 research limitations *42*
Aim 1. Develop a non-invasive optical sensor to study Piezo1-dependent activity both in vitro and in vivo *42*
1.3.2 Biochemical interrogation of biological systems 43
1.3.2.1 Primed conversion limitations I *43*
1.3.2.2 Primed conversion limitations II *43*
Aim 2. Develop a primed conversion imaging toolkit for precision imaging in development and disease *44*
1.3.2.3 Bioharmonophores limitations *44*
Aim 3. Evaluate bioharmonophores degradation in vitro and upon cellular uptake *45*

Chapter 2. An optical reporter of Piezo1-dependent activity **46**
2.1 Reporter engineering 46
2.2 Reporter characterisation 50
2.2.1 Electrophysiology analysis *50*
2.2.2 Response to the Piezo1-specific agonist Yoda1 ..... *55*
2.2.3 Chelation of extracellular calcium with EGTA *56*
2.2.4 Loss-of-function mutagenesis of GenEPi *57*
2.3 Analysis of transient, local mechanical stimuli on the membrane of cells 58
2.3.1 Localisation of GenEPi on the cell membrane using TIRFM *58*
2.3.2 Membrane diffusivity analysis of GenEPi *59*
2.3.3 Activity of GenEPi clusters on the cell membrane *61*
2.4 Analysis of contraction-triggered mechanical stimulation in microtissues 63
2.4.1 GenEPi response during cardiac contraction in 3D microtissues *63*
2.4.2 Chemical modulation of cardiac contraction *63*
2.5 Monitoring pharmacological modulation of Piezo1-dependent activity in vivo 67
2.5.1 A zebrafish transgenic system to study Piezo1 in vivo using GenEPi *67*
2.5.2 Pharmacological modulation of Piezo1 activity in vivo *72*
2.5.3 GenEPi response during cardiac contraction in vivo *73*
2.6 Discussion on GenEPi 75

Chapter 3. Primed conversion advanced imaging toolkit **82**
3.1 Develop of an in-house high-throughput protein screening methodology 82
3.2 Optimisation of primed conversion conditions 86
3.3 Evaluation of primed conversion using 488nm and 633nm simultaneous illumination in a CLSM 90
3.4 Rational engineering of primed conversion using the mEos protein family 93
3.5 X-ray crystallography of pr-mEosFP 100

3.6 Evaluation of primed conversion implementation in a single-objective light-sheet microscope 108
3.7 Discussion on primed conversion 110

Chapter 4. Bioharmonophores characterisation of degradation 114
4.1 Bioharmonophores degradation characterisation in vitro using TEM 114
4.2 Bioharmonophores degradation upon cellular uptake 116
4.3 Discussion on bioharmonophores 117

Chapter 5. Conclusions and Outlook 121

GenEPi as a versatile tool to image mechanosensation 122

The next generation of primed conversion bioimaging toolkit 124

Bioharmonophores as the next generation of SHG nanoprobes 127

Future of Advanced Optical Precision Imaging in systems biology 130

Chapter 6. Materials and Methods 132
Molecular cloning 132
Cell culture and transfection 133
Generation of inducible GenEPi-mESC cell lines 135
Confocal and Total Internal Reflection Microscopy (TIRFM) imaging 136
X-ray crystallography 137
Patch-clamp electrophysiology 138
Live staining and immunostaining 139
Zebrafish transgenesis and in vivo experiments 139
Protein purification 140
Bioharmonophores synthesis and functionalisation 141
Transmission Electron Microscopy 142
Subcellular localisation of bioharmonophores upon cellular uptake 142
Image processing and analysis 142
Statistical analysis 144

References 146

Appendix 164
A.1 List of primers 164
A.2 List of plasmids 165
A.3 Different fluorescent proteins and their respective maximum excitation and emission wavelengths used to generate Fig. 6C 166
A.4 Piezo1 and Piezo2 protein sequences used for the similarity analyses 169
A.5 Statistical analysis results for Fig. 26 193
A.6 Sequence alignment of pr-FPs of the mEos family and amino acid ratios per position 194

List of Figures

Fig. 1. Cells are the building bricks of the human body. 1
Fig. 2. Drosophila genes identified in the 1980s are nowadays known to be important for human development and cancer progression. 3
Fig. 3. The embryonic cell lineage of C. elegans. 4
Fig. 4. Interspecies transplantations to study migration of neural crest cells in chicken embryos. 6
Fig. 5. Jablonski energy diagrams illustrating the electronic and vibrational states and the possible transitions during the absorption of an λ_{ex} photon by a π-electron. 7
Fig. 6. Chromophore of GFP and characteristics of other fluorescent proteins available for biological research. 10
Fig. 7. The three types of photochromism in fluorescent proteins. 13
Fig. 8. Mechanism of 405nm photoconversion. 14
Fig. 9. The PhOTO vector and lines. 16
Fig. 10. Primed conversion of Dendra2 in a polyacrylamide gel and the initial hypothesis for the primed conversion mechanism. 17
Fig. 11. Mechanism of primed conversion. 18
Fig. 12. Axially confined primed conversion to label individual cells and reveal single neuron morphology in living zebrafish embryos. 20
Fig. 13. Primed conversion for precise lineage tracing in mouse embryos. 22
Fig. 14. Phase matching for the generation of Second Harmonic signal and energy diagrams of two-photon excited fluorescence and Second Harmonic Generation. 25
Fig. 15. Bioharmonophores are biodegradable SHG nanoprobes that can be used for precision targeting of tumour cells in vivo. 27
Fig. 16. Biochemical and mechanical feedback loops are important to fully understand development, homeostasis and disease progression. 28
Fig. 17. Basic protein components of cellular mechanosensation and mechanotransduction apparatus for force sensing, force transmission and force generation. 30
Fig. 18. Mechanosensitive ion channels can be found in both prokaryotic and eukaryotic organisms. 31

Fig. 19. Piezo1 and Piezo2 sequence alignments show high sequence similarity among vertebrates. 33
Fig. 20. Piezo1 is expressed in a wide range of human tissues.....35
Fig. 21. Mouse Piezo1 forms a three-bladed propeller-shaped homotrimeric structure.....38
Fig. 22. Piezo1 responds to several types of mechanical stimuli.....39
Fig. 23. General gating models of mechanosensitive ion channels.....39
Fig. 24. The PhD project rationale to develop an advanced imaging toolkit for biochemical and mechanical interrogation of biological systems.....41
Fig. 25. The Piezo1 microdomain hypothesis and the suggested design to develop an optical reporter for Piezo1-dependent activity. 47
Fig. 26. Design and systematic screen to identify an optical reporter of Piezo1 activity. 49
Fig. 27. Pressure-dependent responses evoked by negative pressure. 51
Fig. 28. The mechanosensitive response to repetitive stimulation of Piezo1 within GenEPi is similar to wild-type Piezo1. 52
Fig. 29. The pharmacological property of Piezo1 within GenEPi does not differ from wild-type Piezo1. 53
Fig. 30. The GenEPi R2456H mutant displays a delayed inactivation phenotype.. 54
Fig. 31. GenEPi responds to the Piezo1-specific agonist Yoda1.....55
Fig. 32. GenEPi shows Piezo1-specific response that critically depends on extracellular calcium influx which can be abolished by extracellular calcium chelation. 56
Fig. 33. GenEPi-S217L variant shows altered subcellular localisation and does not respond to Yoda1. 57
Fig. 34. Doxycycline induction of GenEPi expression on the membrane of XLGenEPi transfected HEK293T cells used for TIRFM imaging.....59
Fig. 35. GenEPi is evenly distributed over the ventral surface of different cell types.....60
Fig. 36. GenEPi reflects the membrane diffusion of wt-Piezo1. 61
Fig. 37. GenEPi captures Piezo1-dependent activity to transient, local mechanical stimuli on the cell membrane.. 62
Fig. 38. GenEPi reports cardiomyocyte contraction-triggered mechanical stimulation with high spatiotemporal resolution.....64
Fig. 39. GenEPi responses are triggered by the contraction of the beating cardiomyocytes within the differentiated microtissues.....66
Fig. 40. A zebrafish transgenic model for temporal control of GenEPi expression *in vivo*. 68
Fig. 41. Longitudinal analysis of GenEPi expression post-heat-shock in *Tg(hsp70:GenEPi)* zebrafish.....69

Fig. 42. GenEPi is homogeneously expressed and mainly localises to the plasma membrane of individual cells after heat-shock of Tg(hsp70:GenEPi) zebrafish. 70
Fig. 43. Transient induction of systemic expression of GenEPi in transgenic embryos does not affect their development to adulthood. 71
Fig. 44. GenEPi resolves Piezo1-dependent activity changes *in vivo* upon pharmacological intervention. 73
Fig. 45. GenEPi reports shear stress dependent Piezo1 activation during cardiac contraction in vivo. 74
Fig. 46. GenEPi can be used for comparative Piezo1-dependent activity studies. 80
Fig. 47. Future engineering of GenEPi could produce other biosensors for Piezo1-dependent activity. 81
Fig. 48. A new screening methodology for faster and less laborious screening of protein engineered FP variants. 83
Fig. 49. Successful fluorescence imaging and 405nm photoconversion of pelleted bacterial cells expressing Dendra2 prepared following the new screening methodology. 85
Fig. 50. Primed conversion using a ET460LP filter. 86
Fig. 51. Primed conversion of Dendra2 using the 460LP excitation filter is not successful. 88
Fig. 52. Increasing illumination time using 460LP excitation filter does not lead to primed conversion of purified Dendra2. 89
Fig. 53. Primed conversion using 488nm and 633nm simultaneous illumination. 91
Fig. 54. Other pr-FPs can be also primed converted with 488nm and 633nm simultaneous illumination. 92
Fig. 55. mEos fluorescent protein family and mutations introduced to generate protein variants with different characteristics. 94
Fig. 56. Rational engineering of primed conversion using the mEos FP family. 95
Fig. 57. Positions that could affect positively primed conversion. 96
Fig. 58. Positions that could affect negatively primed conversion. 97
Fig. 59. Site directed mutagenesis plan to identify positions that affect primed conversion. 98
Fig. 60. Site-directed mutagenesis of pr-mEosFP and pr-mEos4b suggests that position 40 is important for improving primed conversion efficiency. 99
Fig. 61. Site-directed mutagenesis of mEos4b shows that T40S is not sufficient to engineer primed convertibility. 100
Fig. 62. Successful large-scale pr-mEosFP protein expression and characterisation. 103
Fig. 63. Setup of the in-house hanging drop crystallisation setup. 104

Fig. 64. Initial crystallisation screen resulted in salt crystals instead of protein crystals. 105
Fig. 65. pr-mEosFP protein crystals and representative diffraction pattern upon X-ray irradiation. 106
Fig. 66. pr-mEosFP protein crystals of the optimisation screening and representative diffraction pattern upon X-ray irradiation. 107
Fig 67. Schematic diagram of the single-objective primed conversion light-sheet microscope (pcOPM). 109
Fig. 68. Successful primed conversion of Dendra2 using the pcOPM. 109
Fig. 69. Successful in vivo primed conversion using the pcOPM system. 113
Fig. 70. Synthesised bioharmonophores have similar structures when characterised using Transmission Electron Microscopy. 115
Fig. 71. Proteinase K induced bioharmonophores degradation characterised by Transmission Electron Microscopy at different time points. 116
Fig. 72. Bioharmonophores accumulate in lysosomes after cellular uptake and produce a bright SHG signal prior to biodegradation. 118
Fig. 73. The concept of bioharmonophores mediated photodynamic therapy. 119

List of Tables

Table 1. Primed convertible variants of green-to-red photoconvertible FPs. . 19
Table 2. Comparison of basic properties of SHG nanoprobes and fluorescent proteins. 26
Table 3. Indicative list of biological processes Piezo1 is involved in. 36
Table 4. Available agonists and antagonists of Piezo1. 40
Table 5. Summary of systematic screening results. 50

Abbreviations

2D	two-dimensional
3D	three-dimensional
4D	four-dimensional
2P	two-photon
AFM	atomic force microscopy
ATP	adenosine-triphosphate
bp	base pair
cAMP	cyclic adenosine monophosphate, an intracellular signaling molecule
cDNA	complementary DNA
CMV	cytomegalovirus immediate early enhancer
DAPI	diamino-2-phenylindole
DMSO	dimethyl sulfoxide
DNA	deoxyribonucleic acid
Dox	doxycycline
dpf	days post fertilisation
dSTORM	direct stochastic optical reconstruction microscopy
EB	embryoid body
ECM	extracellular matrix
ER	endoplasmic reticulum
FACS	fluorescence-activated cell sorting
FLIM	fluorescence lifetime imaging microscopy
FP	fluorescent protein
FRET	Förster/fluorescence resonance energy transfer
GCaMP	genetically-encoded green calcium indicator, based on GFP, Calmodulin and myosin light chain kinase M13 peptide
(e)GFP	(enhanced) green fluorescent protein
paGFP	photoactivatable GFP
GSGG	Glycine-Serine-Glycine-Glycine peptide
H2B	Histone H2B
HEK293T	Human Embryonic Kidney 293T cells

HeLa	Cervical cancer cell line isolated from Henrietta Lacks
HFF	Human foreskin fibroblasts
hpf	Hours post fertilisation
hsp70-l	Heat shock protein 70-like zebrafish promoter
K2P	Two-pore-domain potassium channel
Lox	locus of X-ing over, Cre target sequences for recombination
mESCs	mouse embryonic stem cells
mRNA	messenger RNA
nIR	near-infraRed
ORF	open reading frame
OPM	oblique plane microscopy
PCR	polymerase chain reaction
PDT	photodynamic therapy
RFP	red fluorescent protein
RNA	ribonucleic acid
RR	ruthenium red
rtTA	reverse tetracycline transactivator
SHH	sonic hedgehog
SMO	smoothened
Taz	transcriptional co-activator with PDZ binding motif
TAM	tamoxifen
4-OHT	4-hydroxy-tamoxifen
TIRF	total internal reflection fluorescence microscopy
TRE	tetracycline-responsive element
TREK	TWIK-related potassium channel
TWIK	tandem of pore domains in a weakly inwardly rectifying potassium channel
WGA	wheat germ agglutinin, a plant lectin that binds to the glycoproteins or glycolipids present in the plasma membrane
WT	wild type, the phenotype found in nature, generated by the unmodified version of a gene
Yap	Yes-associated protein, transcriptional co-activator

Chapter 1. Introduction

"The gift of the great microscopist is the ability to think with the eyes and see with the brain"

Daniel Mazia

Living organisms, such as humans, are highly organised dynamic structures (**Fig. 1**). Cells are the basic building bricks of living beings and have the same properties of life: they can reproduce; they interact and communicate; they are evolutionary and although they are to some extend pre-programmed, they are also adaptive (Gómez-Márquez, 2021, Witzany, 2020).

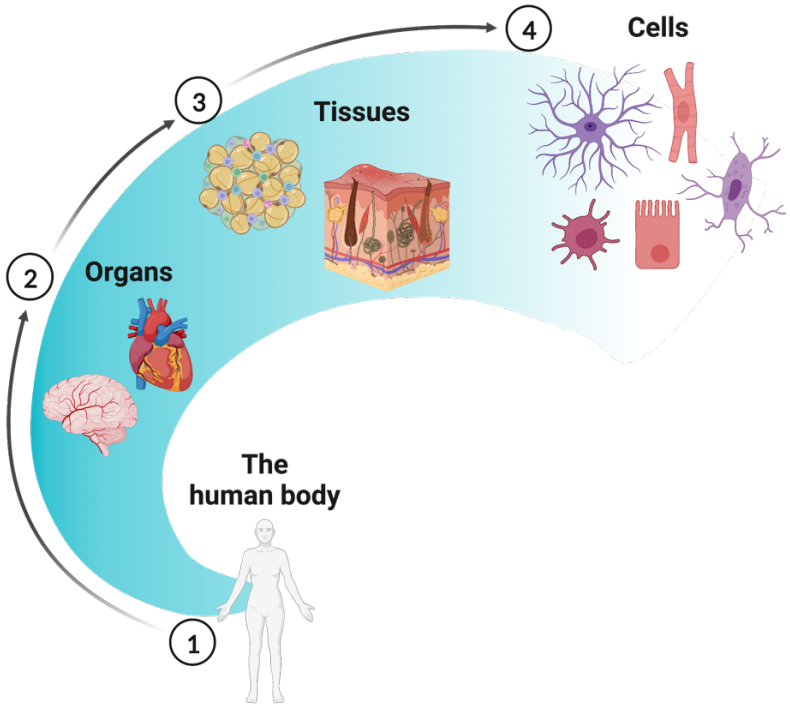


Fig. 1. Cells are the building bricks of the human body. The human body consists of multiple organs and tissues with separate and unique functions working together to maintain homeostasis. *(Created with BioRender.com).*

In the early ages of Embryology, Aristotle described the "genesis" of the chick embryo and egg (Aristotle and Peck, 1943) as an active process of researching the "Generation of Animals". Since then, the aim of blue skies research in developmental biology remains the same. It is a research continuum to understand the processes of life and how the zygote develops from a single cell to a complex multicellular organism. Although this kind of research is mainly driven by curiosity, its implications to human health are not to be ignored. Many genes, which have been previously discovered or characterised to control development in model organisms such as mice and zebrafish, we now know control development in all organisms, including humans. The developmental biologists Nüsslein-Vollhard and Wieschaus identified genes, such as Gooseberry and Patch (Nüsslein-Volhard and Wieschaus, 1980) (**Fig. 2**) and their regulatory pathways, that are nowadays well known for their crucial role in both human development and cancer progression (Ingham, 2018). For instance, mutations in the human ortholog of Hedgehog (*SHH*) cause holoprosencephaly, a congenital disease in which the two lobes of the forebrain are not separated, resulting in severe craniofacial defects and cyclopia in the most severe form (Roessler et al., 1996, Solomon et al., 2010). Gain-of-function mutations in the human ortholog of Smoothened (*SMO*) discovered in basal cell carcinomas, implicated *SMO* as a critical oncogene, thereby highlighting Hedgehog signalling as a possible anti-cancer target (Xie et al., 1998). Hence, understanding the chemical complexity of developmental processes and how regulatory systems in individual cells orchestrate embryo formation from the single-cell zygote to the fully formed organism is currently more than basic research as it is fundamental to the human experience (Wallingford, 2019) providing opportunities for translational science.

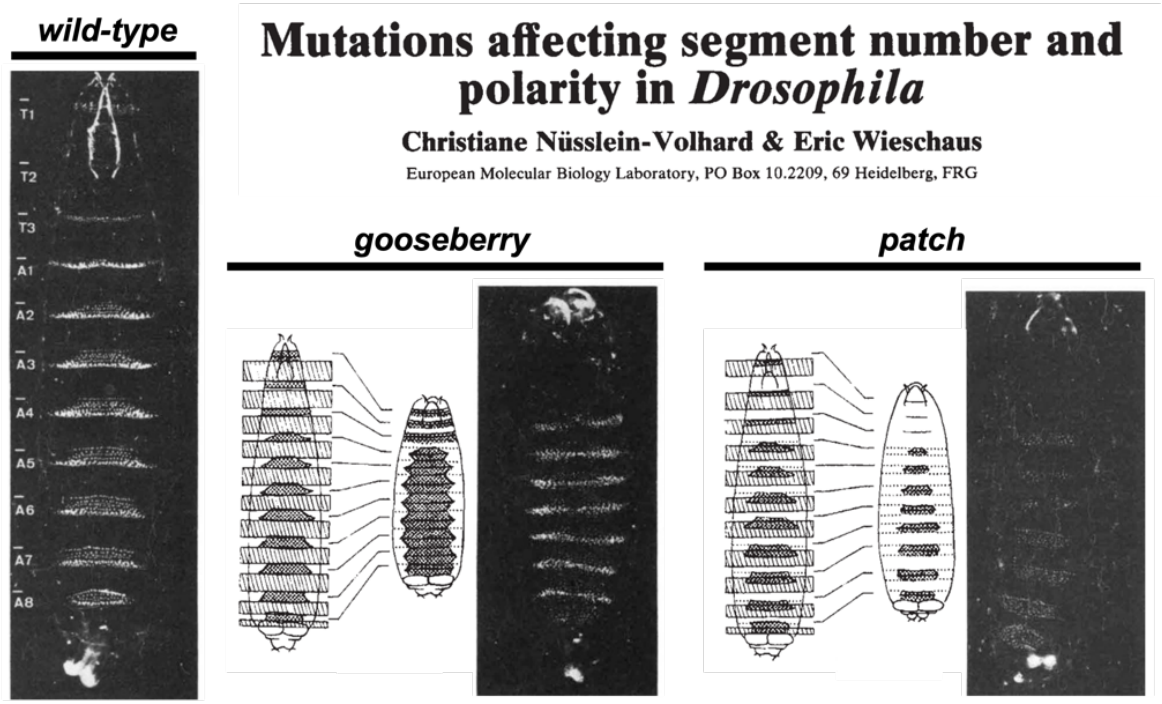


Fig. 2. *Drosophila* genes identified in the 1980s are nowadays known to be important for human development and cancer progression. The developmental biologists Nüsslein-Vollhard and Wieschaus identified genes with initially considered "funny" names (Hopkin, 2006), such as *gooseberry* and *patch*. Larvae homozygous for these genes show phenotypes with deleted regions in comparison to wild-type larvae. *(Adapted from (Nüsslein-Volhard and Wieschaus, 1980)).*

1.1 Cell labelling for chemical interrogation of biological systems

1.1.1 Direct observation

Lineage tracing is the identification of all progenies of a single-cell and the reconstruction of cell trajectories. From the late 18th century to the present, several cell tracking approaches have been used. The first embryology and developmental biology studies were based on direct observation of cell life spans using light microscopes. In contrast to the simplicity of the experiments, detailed fate maps of embryo development were produced advancing our understanding of mainly invertebrate development. In 1878, Charles O. Whitman and his colleagues observed directly single cells in leech embryos and showed that the fates of individual cells are determined early on in Clepsine development (Whitman, 1878). In 1952, Georges Nomarski introduced Differential Interference Contrast (DIC) to

enhance contrast in unstained and transparent samples (Nomarski, 1952). Sulston et al. took advantage of this optical technique and traced the embryonic cell lineage of *Caenorhabditis elegans* from zygote to hatched larva (Sulston et al., 1983) (**Fig. 3**). The relatively small number of cells in *C. elegans* enabled Sulston and his colleagues to determine a complete cell fate map of worm development (Sulston et al., 1983), an impressive achievement which was awarded the Nobel Prize in Physiology or Medicine 2002.

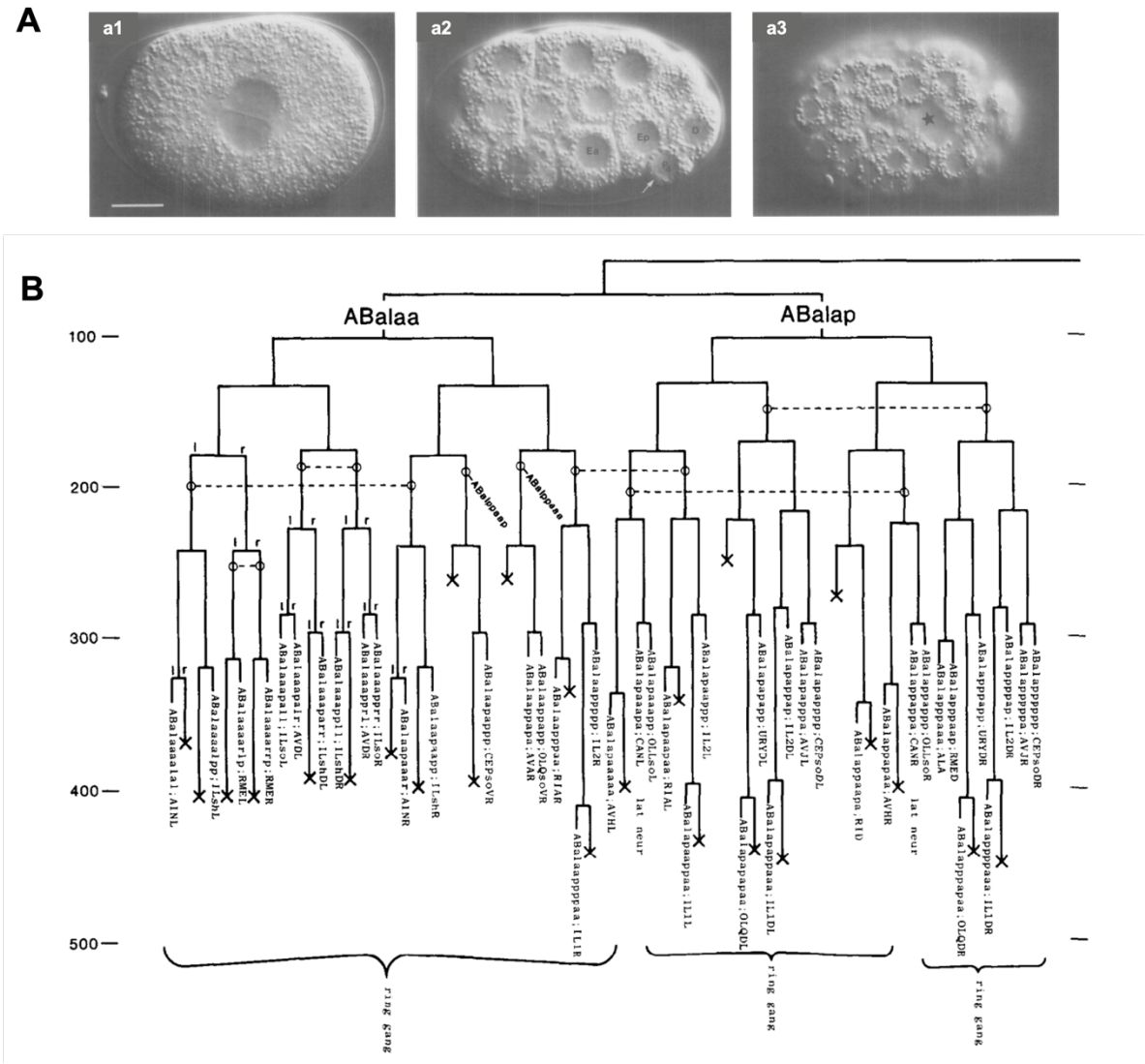


Fig. 3. The embryonic cell lineage of *C. elegans*. (A) DIC images of *C. elegans* embryo, (A1) just before cleavage, (A2) beginning of gastrulation and (A3) late gastrulation. (B) Complete cell lineage of C. elegans showing the progenies of cells from the first cleavage to hatching. *(Adapted from (Sulston et al., 1983)).*

1.1.2 Interspecies transplantations and vital dyes

Although the DIC-enhanced contrast of cells in unstained samples provided valuable insight into embryo development, it became clear that cell subpopulations of interest need to be labelled in a specific way in order to reveal more complex processes of development. Interspecies transplantations (Spemann and Mangold, 1924, Waddington, 1932, Le Douarin and Teillet, 1974) (**Fig. 4**) and vital dyes (Vogt, 1925, Honig and Hume, 1989, Honig and Hume, 1986, Baier et al., 1996) were introduced for the first time in the 1920s and revealed very important notions in development. For instance, in 1924, Spemann and Mangold made interspecies chimeras with embryos from three differentially pigmented newt species (Spemann and Mangold, 1924). Their experiments discovered the Spemann and Mangold organiser and introduced the concept of induction in vertebrate embryonic development (Spemann and Mangold, 1924) which until then was considered to be more deterministic. One year later, Walter Vogt implanted small pieces of agar impregnated with the vital dye Nile Blue into amphibian embryos and successfully followed the progeny of labelled cells during gastrulation in a more precise way (Vogt, 1925). Around 60 years later, lipophilic tracers, such as DiI, DiO, DiD, DiA and DiR, were introduced to label phospholipid bilayer membranes in live embryos (Honig and Hume, 1986, Honig and Hume, 1989). In 1996, Baier et al. used DiI and DiO to label the developing retinal axons and developed a systematic screening approach to identify key mutations affecting the retinotectal projection in zebrafish (Baier et al., 1996).

1.1.3 Fluorescence

Fluorescence is the result of one of the most interesting interactions between light and matter. In systems with optically excitable electrons, such as polyaromatic hydrocarbons, the aromatic π-orbitals line up in an overlapping way that creates an enlarged conjugation system. This enlarged conjugation system is characterised by

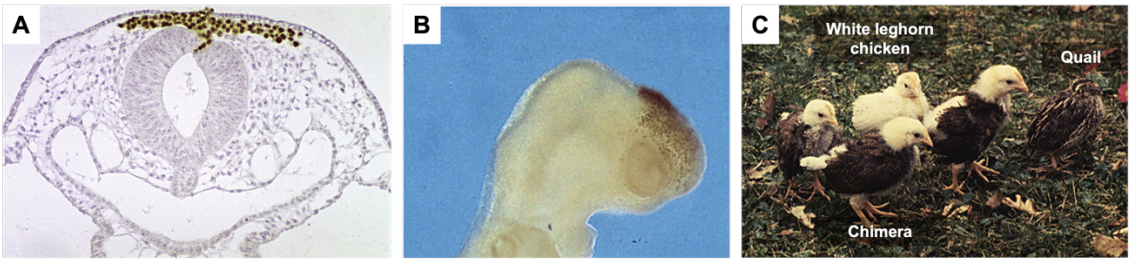


Fig. 4. Interspecies transplantations to study migration of neural crest cells in chicken embryos. Immunohistochemistry to identify quail cells in (A) a section and (B) a whole quail-chick embryo chimera. (C) Chimeric birds together with a chicken and a quail for comparison. *(Adapted from (Le Douarin, 2008), Nicole Marthe Le Douarin photograph on the bottom).*

an absorption λ_{ex} wavelength which depends on (i) the molecular niche around the chromophore and (ii) the extent of conjugation between the orbitals. When a photon of λ_{ex} is absorbed by a π-electron, the latter gets excited from the ground state S_0 into the excited state S_1. As higher vibrational states of S_1 are usually reached upon the λ_{ex} photon absorption, the excited electron undergoes a fast process called vibrational relaxation during which vibrational energy is dissipated and the electron "relaxes" to the lowest vibrational state of S_1. After that, the electron can return to the ground state while emitting a photon of λ_{em} wavelength in a process called fluorescence. Alternatively, the electron can undergo intersystem crossing (ISC) to reach a dark triplet state T_n. Electrons that reach the triplet state can remain there for long periods of time in the range of microseconds to several seconds without contributing to fluorescence (dark states) (Ha et al., 1997, Visser and Hink, 1999, Garcia-Parajo et al., 2000) (**Fig. 5**).

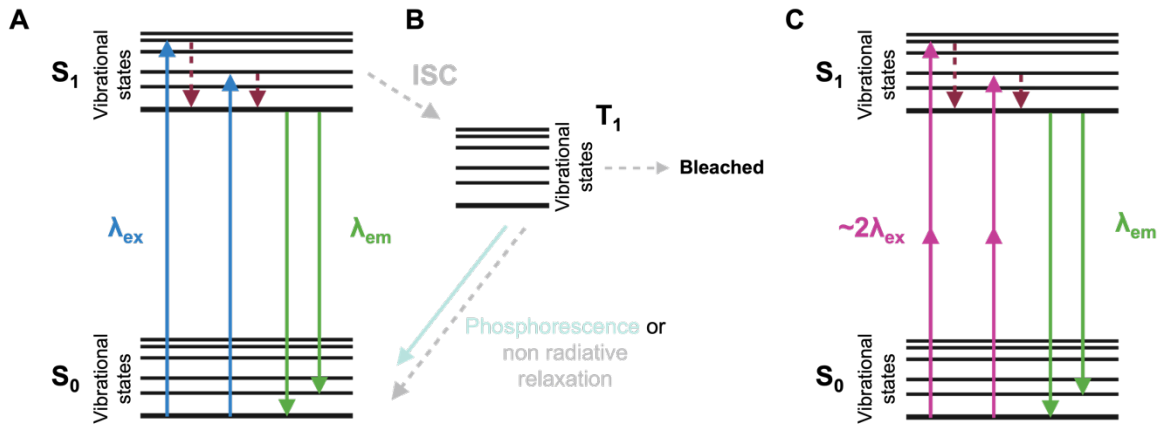


Fig. 5. Jablonski energy diagrams illustrating the electronic and vibrational states and the possible transitions during the absorption of an λ_{ex} photon by a π-electron. (A) 1-photon excited fluorescence. (B) Alternative non-radiative and radiative state processes via dark triplet states. (C) Two-photon excited fluorescence. *(Created with BioRender.com).*

1.1.3.1 The Green Fluorescent Protein and bioimaging

The discovery and characterisation of the green fluorescent protein (GFP) (Shimomura et al., 1962) in the early 1960s from *Aequorea victoria* changed biological imaging. The chromophore of GFP forms through cyclisation and oxidation of the internal tripeptide motif SYG (Ser65, Tyr66 and Gly67) which contains a highly conjugated imidazolidinone ring (Prasher et al., 1992, Cody et al., 1993). GFP has a characteristic absorption spectrum depending on its protonation state, which can be seen in its excitation spectrum as two peaks; one for the neutral form of the chromophore with a maximum at around 395nm and one for the anionic form of the chromophore with a maximum at around 475nm (**Fig. 6A-B**) The gene sequence that encodes GFP was cloned for the first time in 1992 but the significant potential to use it as a molecular probe was not realised until two years later. In 1994, Chalfie et al. showed that the gene of GFP can be easily expressed in both bacteria and eukaryotic cells and they used it to monitor gene expression and protein localisation in living organisms (Chalfie et al., 1994). The straightforward implementation of already established detection filters of organic dyes to image GFP and their ease of use made this FP one of the most important genetically-encoded imaging probes in biochemistry and molecular cell biology (Tsien, 1998).

Since these early studies, the GFP structure has been further refined/modified/engineered to produce a vast number of mutants, fusion proteins and biosensors which possess a multitude of characteristics, such as emitting different light, enhanced fluorescence and even sensing the presence of ions such as Ca^{2+} (Rodriguez et al., 2017, Tsien, 1998, Matz et al., 1999). All these variants are broadly referred to as fluorescent proteins (FPs). Most recent, fluorescent proteins from other species have been identified and isolated, resulting in expansion of the fluorescence colour palette (Matz et al., 1999, Shaner et al., 2004, Shaner et al., 2008). All these new features and coloured variants (**Fig. 6C-E**) allowed the monitoring of molecular processes (Rodriguez et al., 2017, Tsien, 1998), such as the detection of gene expression (Lewis and Errington, 1996, Chalfie et al., 1994), the subcellular localisation dynamics of molecules of interest (Lewis and Errington, 1996) and the visualisation of signalling and protein-protein interactions using molecular indicators, such as Förster/Fluorescence resonance energy transfer (FRET)-based sensors (Piston and Kremers, 2007).

1.1.3.2 Genetic markers for lineage tracing

As a natural consequence of their ease of use, genetically encoded markers have proven extremely useful tools for lineage tracing. Fluorescent proteins can be easily introduced in cells by e.g. direct injection of the mRNA or introduction of a plasmid DNA encoding for the FP under the control of a specific promoter. Compared to vital dyes, genetic markers do not spread to neighbour cells and, if they are stably expressed, they are inherited by all progenies. In zebrafish, the generation of transgenic lines with tissue- or cell-specific expression of FPs has been extensively used to study developmental processes. In 1997, Lin et al. reported for the first time the creation of zebrafish transgenic line which expressed GFP under the putative zebrafish promoter of gata-1, a transcription factor that is essential for erythroid cell

development (Long et al., 1997). Using this transgenic line which was generated by microinjections of plasmid DNA into single-cell zebrafish embryos (Stuart et al., 1988), they showed that the GFP expression patterns were consistent with the gata-1 mRNA expression and isolated early erythroid progenitor cells by fluorescence-activated cell sorting (FACS) for subsequent *in vitro* studies (Long et al., 1997). Similarly, around 10 years later, Carney et al. investigated the role of the sox10 gene in the generation of neural crest-derived sensory neurons (Carney et al., 2006) by generating a transgenic line carrying a construct driving GFP expression under the zebrafish sox10 promoter (Carney et al., 2006). This labelling approach allowed them to demonstrate that Sox10 function specifies sensory neuron precursors by regulating the proneural gene neurogenin1 (Carney et al., 2006).

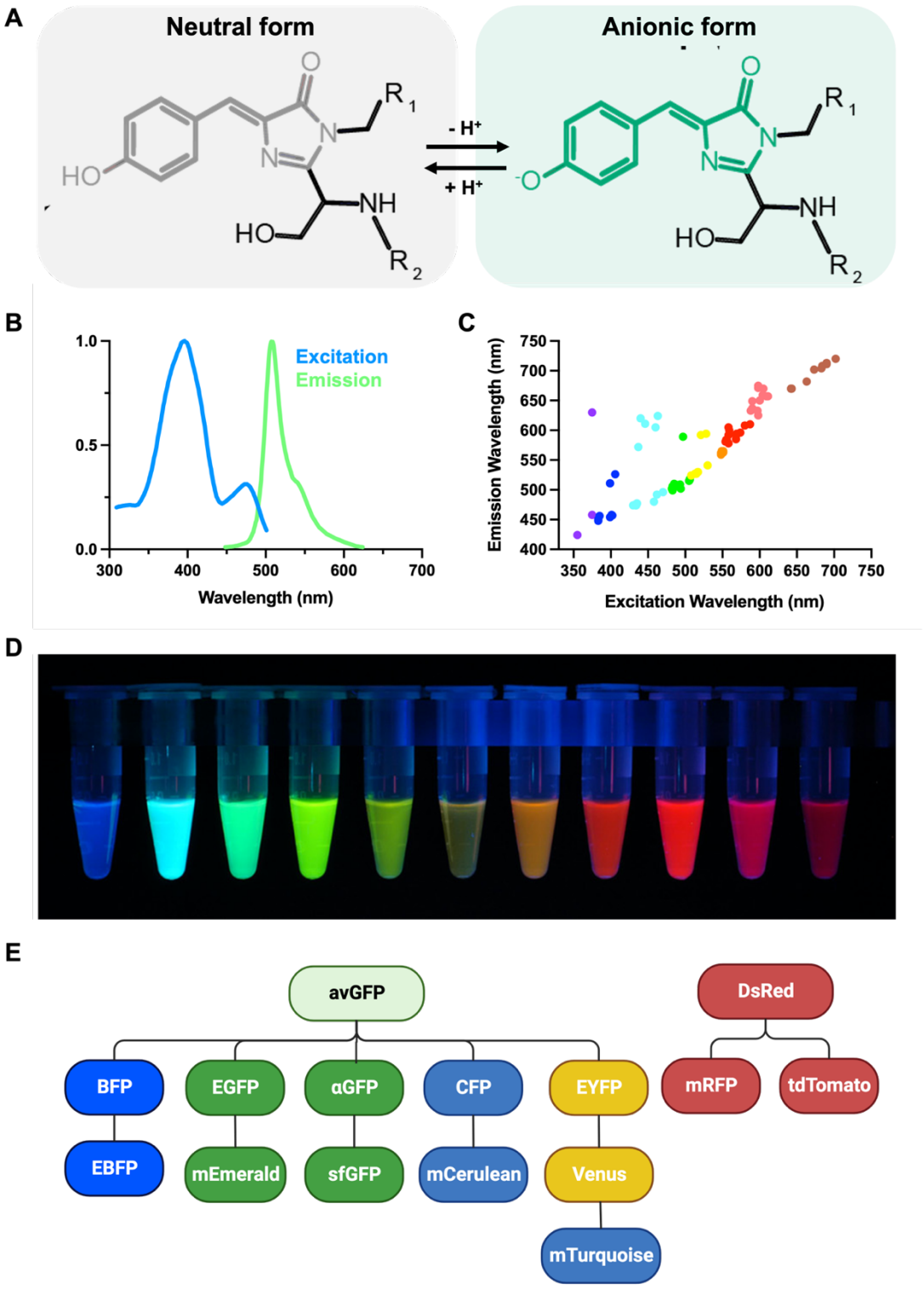


Fig. 6. Chromophore of GFP and characteristics of other fluorescent proteins available for biological research. (A) Chromophore of Aequorea victoria GFP (avGFP) in both the neutral (grey) and anionic (teal) form. (B) Excitation and emission spectra of avGFP (data obtained from FPBase.org). (C) Fluorescent protein variants according to their excitation and emission wavelength. Each dot represents a fluorescent protein coloured according to its excitation wavelength. (Data from Talley Lamber and Kurt Thorn, fpvis.org). (D) Different monomeric FPs with different spectral properties (Adapted from tsienlab.ucsd.edu/). (E) The lineages of the avGFP and DsRed fluorescent proteins which influenced biological imaging and are still commonly used for cell and protein labelling and tracking of dynamics (Adapted from FPBase.org).

1.1.3.3 Genetic recombination approaches

In addition to the constitutively expressed FP approaches, genetic recombination enabled researchers to temporally control labelling of cell populations. Nowadays, the most common method for genetic fate mapping is the use of site-specific recombinases, such as the Cre recombinase (Abremski et al., 1983, Abremski and Hoess, 1984, Santoro and Schultz, 2002), that are expressed in a tissue- or cell-specific manner. As the Cre recombinase promotes DNA strand exchanges, it can activate the expression of a genetic marker in a particular cell or subset of cells and eventually their progeny. Temporal control of recombination can be achieved by using ligand-inducible Cre variants and administration of a drug inducer (e.g. CreERT2 is activated by tamoxifen (TAM) or its active metabolite 4-hydroxy-tamoxifen (4-OHT)) (Pinzon-Olejua et al., 2017). In an extended combinatorial approach, multicolour single-cell labelling and parallelisation of lineage tracing have been achieved by random Cre recombination to differentially express combinations of spectrally distinct FPs (Livet et al., 2007). In this "rainbow" of coloured cells, single-cell progenies can be identified by a stochastic yet individually specific stoichiometric ratio of FPs and can be followed over extended time periods (Livet et al., 2007, Pan et al., 2013).

1.1.3.4 Limitations of lineage tracing using genetically encoded markers and combinatorial events

Although cell labelling methodologies using genetic markers and genetic recombination are powerful tools for lineage tracing, they present several limitations. The generation and the establishment of transgenic lines with a tissue- or cell-specific marker require previous knowledge of a particular gene promoter. Such a task can be laborious, as it requires a thorough characterisation of the labelling specificity (see for example the characterisation of ubi, a ubiquitous promoter in zebrafish by (Mosimann et al., 2011)). In random "rainbow"-like

labelling approaches, targeted marking of individual cells of interest is precluded because all the cells are labelled. Furthermore, the time needed to reach a stable steady-state fluorescence colour combination is often too long. This delay can render the identification of single-cell clones challenging, especially when highly dynamic biological systems, which are characterised by rapid cell divisions and migrations, are studied.

1.1.4 Photomodifiable fluorescent proteins and photochromism

To overcome these limitations, photomodifiable FPs can be used. Photomodifiable FPs can change their excitation and emission spectra upon high energy (violet or ultraviolet (UV)) light illumination either reversibly (i.e. photoswitchable FPs) or irreversibly (i.e. photoactivatable and photoconvertible FPs). For instance, the FP Dronpa switches from an on-to-off state reversibly (Ando et al., 2004), while photoactivatable GFP (paGFP) permanently changes from a non- or weak fluorescent state to a strongly fluorescent one (Patterson and Lippincott-Schwartz, 2002). This phenomenon, termed photochromism (**Fig. 7**), in which FPs switch between molecular states was first identified by Moerner, Tsien and colleagues in 1997 (Dickson et al., 1997). In this early study, it was demonstrated that single molecules of yellow FPs exhibit intermittent fluorescence emission (i.e. blinking) and that molecules trapped in a long-lived dark state (off-state) could be converted back to the emitting state (on-state) by illumination with 405nm light (Dickson et al., 1997). Subsequent studies have largely confirmed the model of dark state conversion proposed by Moerner et al. and several mechanisms have been revealed for the excited to dark state transitions, such as conformational dynamics of the chromophore (e.g. cis-trans isomerisation), excited state proton transfer, excited state solvation dynamics and triplet state conversion (Habuchi et al., 2005, Andresen et al., 2005, Shi et al., 2007, Haupts et al., 1998, Konold et al., 2014).

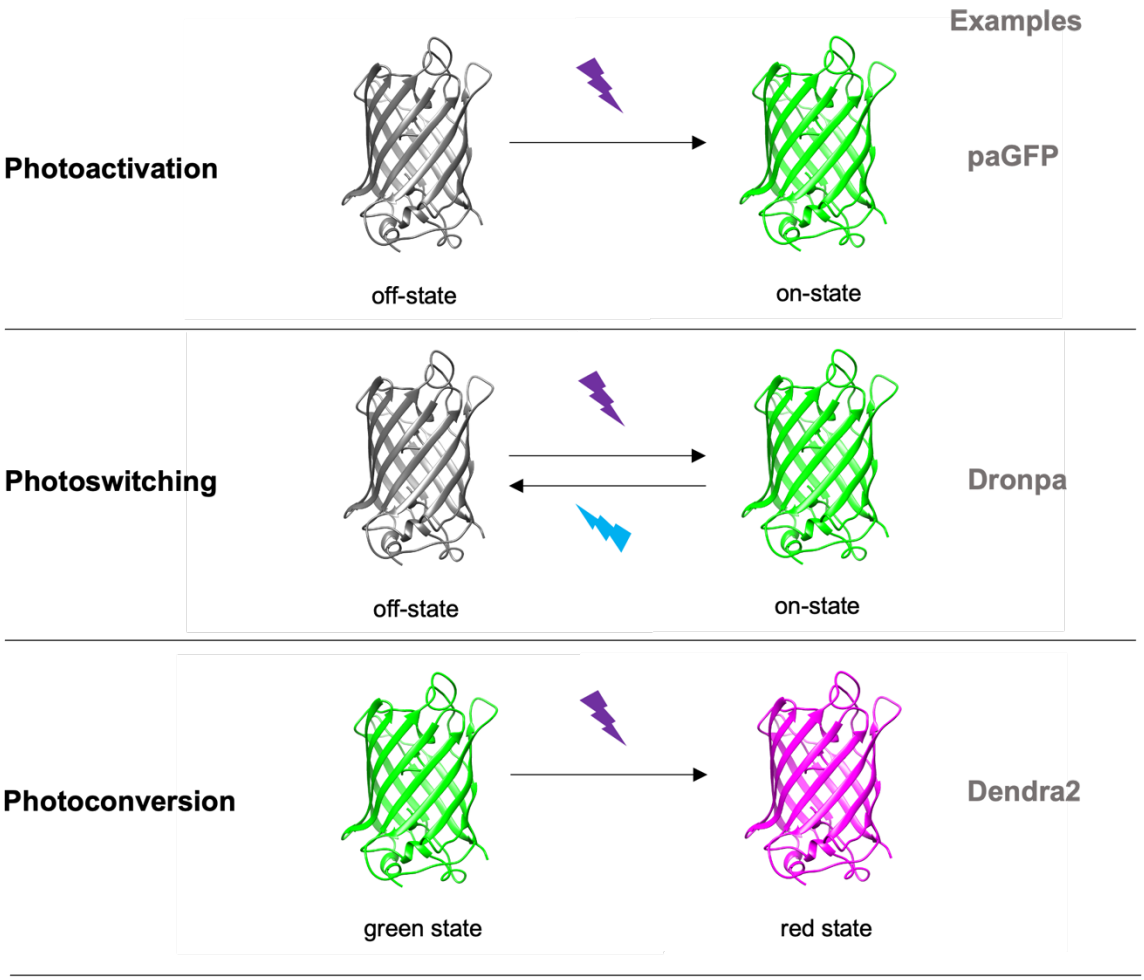


Fig. 7. The three types of photochromism in fluorescent proteins. Photoactivatable FPs, such as paGFP, can change from a non- or weak fluorescent state to a bright fluorescent state while photoswitchable FPs, such as Dronpa, can reversibly change between two fluorescent states upon light illumination. Photoconvertible FPs, such as Dendra2, can change their emission from green to red upon 405nm illumination.

1.1.4.1 Photoconvertible fluorescent proteins and 405nm photoconversion

Photoconvertible FPs, such as Dendra2, change their emission spectrum from green to red (Gurskaya et al., 2006). Traditionally, violet light of around 405nm is used for photoconversion. Upon violet-light illumination, all green-to-red photoconvertible FPs share a common photoconversion mechanism (**Fig. 8**). First, a bond cleavage occurs between the N_α and C_α atoms of chromophore's histidine. Then, a double bond is formed between the C_α and C_β atoms which eventually leads to the irreversible shift in emission and absorption (Nienhaus et al., 2005, Mizuno et al.,

2003). Although 405nm photoconversion can achieve very efficient photoconversion (Dempsey et al., 2014, Dempsey et al., 2012a), its use is limited to thin samples because of the non-axial confined nature of violet light photoconversion (i.e. in a 3D space it is not confined in the z axis). Additionally, the high energy of violet light can be phototoxic and cytotoxic after multiple or long exposure times as previously shown (Ramakrishnan et al., 2016, Waldchen et al., 2015).

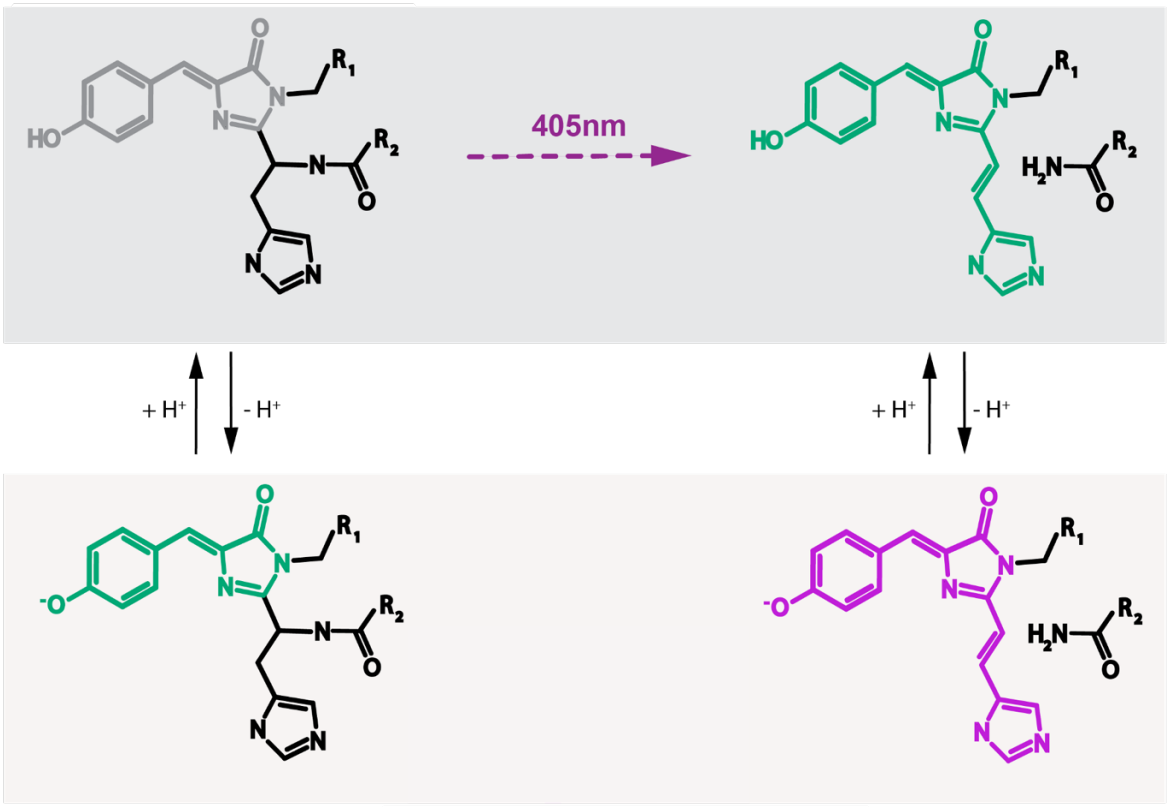


Fig. 8. Mechanism of 405nm photoconversion. A bond cleavage happens between the N_α and C_α atoms of chromophore's histidine. Then, a double bond is formed between the C_α and C_β atoms which leads to the irreversible shift in absorption and emission.

1.1.4.2 Photoconvertible fluorescent proteins for lineage tracing

As previously mentioned, photoconvertible FPs, in contrast to photoactivatable FPs, can be observed before and after photoconversion. Dempsey et al. took advantage of this feature and introduced transgenic zebrafish lines, named PhOTO (**Ph**otoconvertible **O**ptical **T**racking **O**f nuclear and membrane dynamics *in vivo*) zebrafish, which combine precise single-cell labelling and long-term lineage tracing (Dempsey et al., 2012a, Dempsey et al., 2014).

PhOTO zebrafish is a transgenic resource that ubiquitously expresses targeted fusions of the blue FP Cerulean (Rizzo et al., 2004) and the photoconvertible FP Dendra2 (Gurskaya et al., 2006). Specifically, the PhOTO vector (**Fig. 9A**) allows for the constitutive and 1:1 stoichiometric ratio expression of Cerulean and Dendra2 targeted either (i) to the cell membrane (memb) or (ii) the nucleus by means of an H2B fusion. By using the Tol2 transposase-mediated genome integration system, three transgenic zebrafish lines, named PhOTO-N, PhOTO-M and PhOTO-C were established. The PhOTO-N zebrafish line expresses H2B-Dendra2 and memb-Cerulean to selectively label nuclei and membranes, respectively. The complementary PhOTO-M zebrafish line expresses H2B-Cerulean and memb-Dendra2. PhOTO-C expresses cytosolic Dendra2 and nuclear Cerulean. In all PhOTO lines, the instantaneous photoconversion of Dendra2 allows for precise targeting, accurate segmentation and reconstruction of cell trajectories with high spatiotemporal resolution and signal-to-noise ratio. In parallel, the global view of the cell morphology and behaviour is retained by the compartment specific expression of Cerulean. Both PhOTO-N (**Fig. 9B**) and PhOTO-M have been used to reveal and highlight the complexity of developmental and post-developmental (e.g. fin regeneration) processes down to single-cell level (Dempsey et al., 2012a, Dempsey et al., 2014).

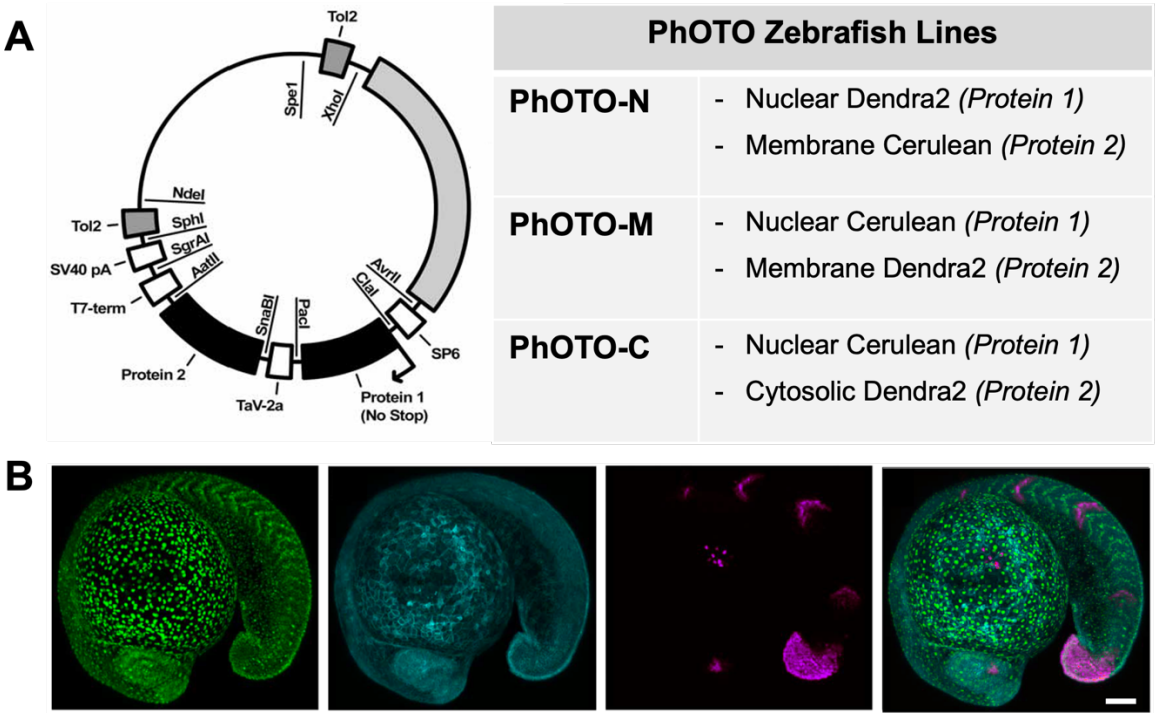


Fig. 9. The PhOTO vector and lines. (A) Schematic representation of the PhOTO vector and table with the main features of the three PhOTO zebrafish lines, PhOTO-N, PhOTO-M and PhOTO-C. (B) Representative heterozygous PhOTO-N expression in 18-19 hours post fertilization F1 transgenic zebrafish embryo. *(Adapted from (Kalyviotis et al., 2020)).*

1.1.4.3 Primed conversion

In 2015, Dempsey et al. reported a different photoconversion mechanism, termed primed conversion (Dempsey et al., 2015). The authors showed that Dendra2 can be successfully photoconverted from green to red by simultaneous illumination with 488nm and 730nm light, generating spectrally identical red species when photoconverted using 405nm light (Dempsey et al., 2015, Mohr et al., 2017) (**Fig. 10A**). They suggested that the green form of Dendra2 first absorbs the 488nm "priming" light to reach a long-lived intermediate state of a few milliseconds which differs from the fluorescent singlet state S_1 (Lichtman and Conchello, 2005). This intermediate state can then absorb the far-red "converting" photons, resulting in the green-to-red shift of the emission spectrum (Dempsey et al., 2015) (**Fig. 10B**). Very recently, to understand the mechanism of primed conversion Mohr et al. conducted a series of isotope experiments in which different O_2 concentrations were used to examine their effect on the "priming" state lifetime (Mohr et al., 2017). The findings

suggest that the "primed" state of primed conversion is a triplet T_1 "dark" intermediate state formed by intersystem crossing (ISC) from the S_1 state of the anionic chromophore (Mohr et al., 2017) (**Fig. 11**). They showed that this mechanism can be facilitated by substituting a single amino acid at position 69 (amino acid annotation is based on mEosFP sequence) to threonine or serine (Mohr et al., 2017). Using this knowledge, they rendered most known green-to-red photoconvertible proteins primed convertible (**Table 1**) and illustrated that the "pr-" variants (for prime convertible) are also more photostable (Mohr et al., 2017, Welling et al., 2019).

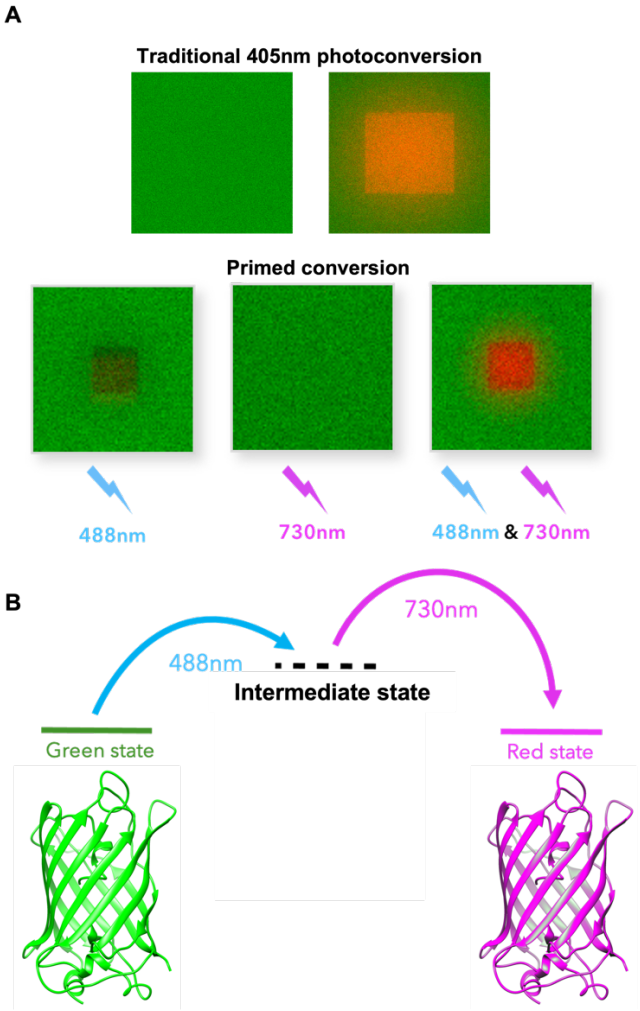


Fig. 10. Primed conversion of Dendra2 in a polyacrylamide gel and the initial hypothesis for the primed conversion mechanism. (A) Purified Dendra2 embedded in a polyacrylamide gel is photoconverted through traditional 405nm photoconversion or primed conversion via simultaneous illumination with 488nm and 730nm light. (B) The initial hypothesis proposed a primed conversion mechanism involving a long-lived 'intermediate state' (*Adapted from Dempsey et al., 2015*).

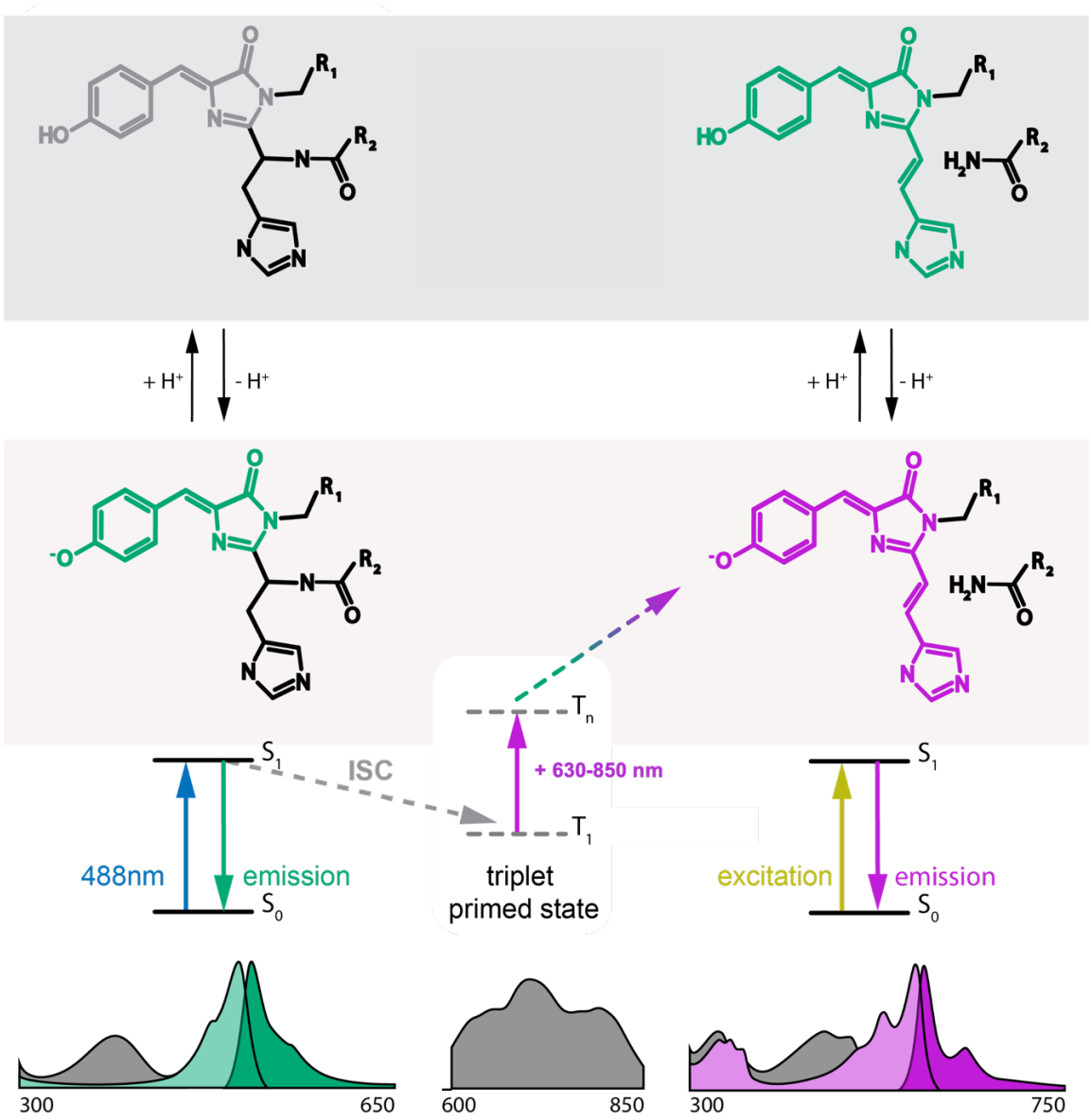


Fig. 11. Mechanism of primed conversion. The chromophore initially absorbs the 488nm "priming" light to reach a long-lived dark triplet state which can absorb a wide range of light ranging from the 630 to 850nm. Then, this triplet state can absorb the far-red "converting" photons resulting in the change of the spectral properties.

Table 1. Primed convertible variants of green-to-red photoconvertible FPs. The substitution of a single amino acid at position 69 (mEosFP annotation) renders most photoconvertible fluorescent proteins primed convertible. Currently, there are various available pr- variants of monomeric and oligomeric FPs and calcium sensors available. In addition, optogenetic tools, such as PhOCl, can be used with primed conversion. (*Adapted from (Kalyviotis et al., 2020) and (Mohr et al., 2017)*).

Category	Protein
Monomeric primed convertible FPs	Dendra2
	pr-mEosFP
	pr-mEos2
	pr-mEos3.1
	pr-mEos3.2
	pr-mEos4a
	pr-mEos4b
	pr-mKikGR
	mMaple
	mClavGR
Oligomeric primed convertible FPs	pr-Kaede
Optogenetic primed convertible tool	PhOCl
Primed convertible Ca^{2+} integrator	pr-CaMPARI
Primed convertible Ca^{2+} indicator	GR-GECO1.1
	GR-GECO1.2

1.1.4.4 Benefits of primed conversion

In contrast to violet light illumination, primed conversion can be confined in the axial dimension when the two (priming and converting) beams cross in a small volume. By simply adding a commercially available primed conversion filter and simultaneous dual laser illumination, confined primed conversion can be implemented in a confocal laser-scanning microscope (CLSM) (Mohr et al., 2016, Mohr and Pantazis, 2016) (**Fig. 12A**). Through this selective intersection of the two beams in a common focal spot, labelling of single-cells and/or subcellular compartments was achieved in very dense 3D environments, such as the brain (Mohr et al., 2016, Mohr et al., 2017, Klementieva et al., 2016, Dempsey et al., 2015, Turkowyd et al., 2017) (**Fig. 12B**). Recently, Klementieva et al. and Mohr et al. have

demonstrated that primed conversion can be also achieved using conventional red lasers found in every commercial fluorescence microscope (630-690nm) (Klementieva et al., 2016, Mohr et al., 2017). Hence, confined primed conversion can be performed in almost any confocal fluorescence microscope without extensive technical adjustments and optimisation.

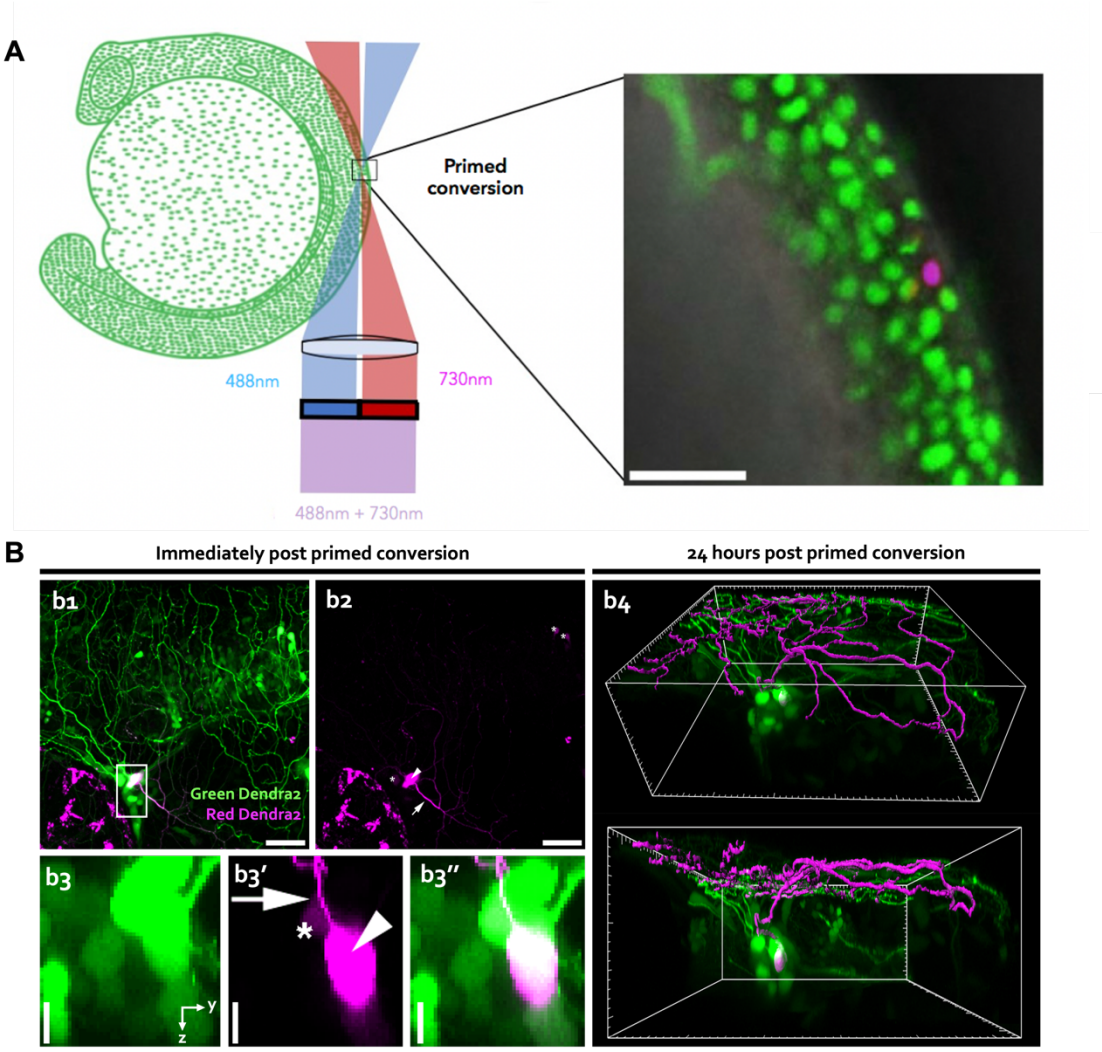


Fig. 12. Axially confined primed conversion to label individual cells and reveal single neuron morphology in living zebrafish embryos. (A) Photoconversion only occurs at the focus where the laser beams overlap. Axially confined primed conversion of H2B-Dendra2 in a single-cell nucleus of a PhOTO-N transgenic zebrafish embryo. Scale bar is 50μm. (B) (b1, b2) Primed conversion of Dendra2 in a single neuron in the trigeminal ganglion at 3 days post fertilisation (maximum intensity projection, ~82μm in depth), scale bar 50μm. The images were acquired immediately after photoconversion. (b3, b3′ and b3″) Higher magnification and axial orientation images of the boxed region in b1, axial scale bar 10μm. The arrow indicates a neurite extending from the cell soma and the arrowhead indicates the photoconverted cell. The asterisks in b2 and b3′ point cells which had noticeable red signal even before primed conversion. (b4) Different perspectives of neurite tracing 24 hours post primed conversion of Dendra2 in the cell soma. (*Adapted from (Kalyviotis et al., 2020)*).

1.1.4.5 Primed conversion for precise lineage tracing

Developing embryos are delicate biological structures in which intense or extensive imaging exposure periods can potentially lead to phototoxicity (Ichikawa et al., 2013, Jemielita et al., 2013). Primed conversion is less phototoxic than 405nm photoconversion and can be used in sensitive live biological samples, such as embryos. Although two-photon excitation has been previously used in developing mouse embryos for precise labelling with photoactivatable GFP (Plachta et al., 2011), the peak and average illumination intensities embryos experience are high resulting in affected development after repetitive two-photon imaging. In contrast to two-photon excitation, confined primed conversion enables spatially selective photoconversion with significantly less peak and average illumination intensities allowing for repetitive labelling. This low illumination energy meets the demand for gentle imaging conditions of light-sensitive biological samples. Very recently, Welling et al. developed a high-fidelity lineage tracing algorithm by combining primed conversion with light-sheet microscopy (Welling et al., 2019, Welling et al., 2020) (**Fig. 13**). In this setup, the use of primed conversion combined with volumetric imaging (Welling et al., 2019, Huisken et al., 2004, Keller et al., 2008) reduced phototoxicity, highlighting the potential of primed conversion in lineage tracing.

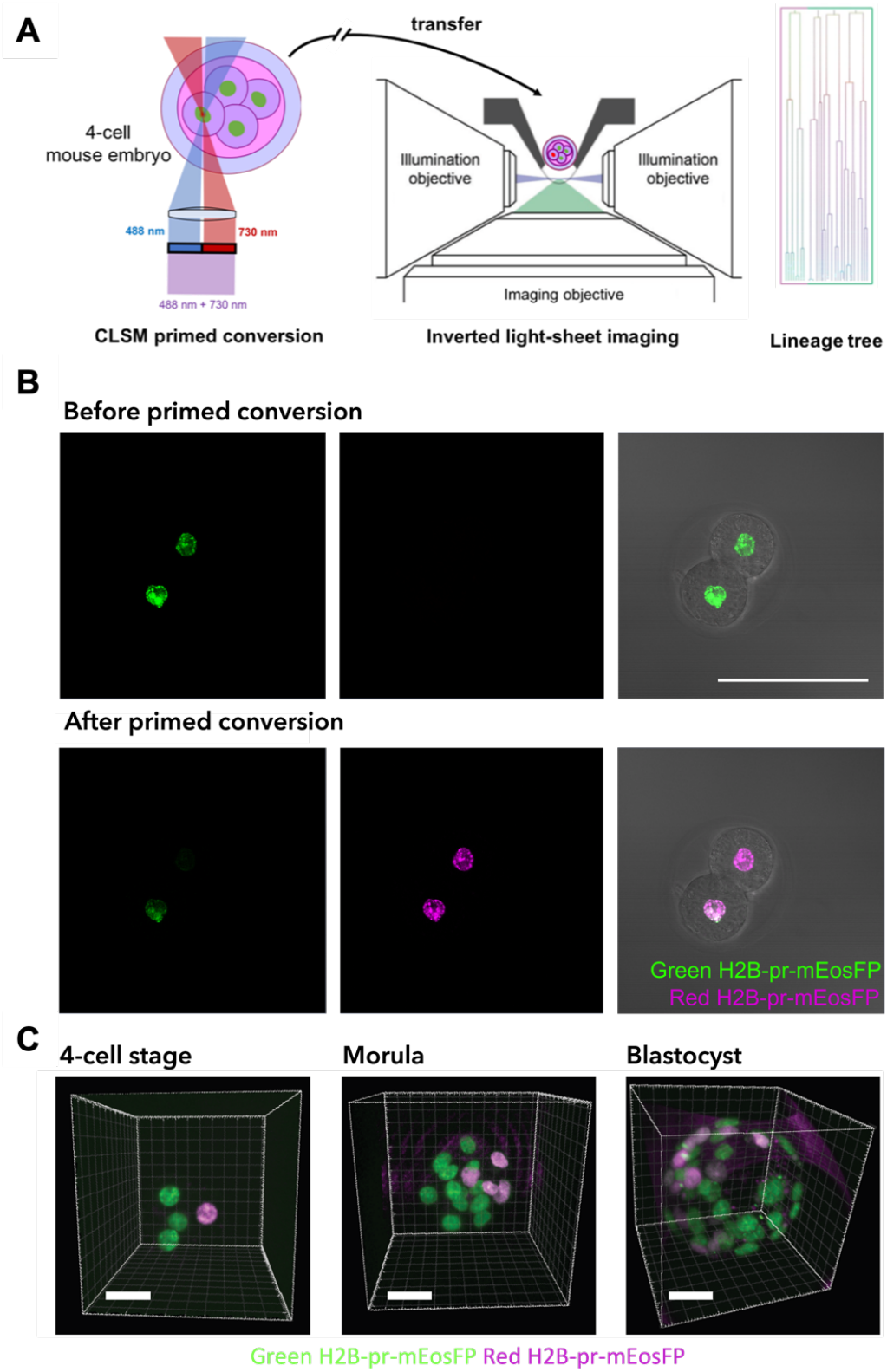


Fig. 13. Primed conversion for precise lineage tracing in mouse embryos. (A) Experimental protocol used by Welling et al. for precise single-cell primed conversion and volumetric imaging lineage tracing in mouse embryos. (B) 2-cell stage mouse embryo before and after primed conversion using different powers for the 730nm laser: 5mW for lower nucleus, 10mW for upper nucleus. Scale bar is 100µm. (C) Mouse embryos injected with mRNA encoding H2B-pr-mEosFP and converted at the 4-cell-stage develop normally and maintain visibility of the red label up to the early blastocyst stage. *(Adapted from (Welling et al., 2020)).*

1.1.5 Inherent limitations of fluorescent probes

1.1.5.1 Bleaching

As mentioned before, excited electrons in π-conjugated systems can return to the ground state by emitting a photon (fluorescence) or they can undergo ISC to reach a dark triplet state. Although triplet states can be beneficial for processes such as primed conversion, they are also chemically reactive. Triplet states can be either exited by non-radiative relaxation, phosphorescence or by reacting with nearby molecules. In the latter case, reactions with molecular oxygen in the surrounding environment results in the creation of singlet oxygen species that can irreversibly damage the chromophore structure which eventually ceases to fluoresce (bleaching).

1.1.5.2 Blinking

In some cases, a fluorescent molecule can repeatedly transfer between fluorescence emitting "on" states and dark "off" states, as it was initially described by Moerner, Tsien and colleagues in 1997 for the photochromism of yellow FPs, which results in large intensity fluctuations even under continuous illumination (blinking). Although these "off" periods are the basis for super-resolved direct stochastic optical reconstruction microscopy (dSTORM) (Fölling et al., 2008, Steinhauer et al., 2008), they create blocks of time when targeted molecules cannot be imaged and, subsequently, followed.

1.1.5.3 Saturation

Chromophores are limited in the maximum number of photons that can emit in a specific amount of time. And this is because re-emission of light from a fluorescent molecule occurs only when an excited electron is relaxed to the ground state S_0 and is available for a "new" absorption event. Thus, increasing the amount of exciting

light will increase the amount of emitted light until a "saturation" point at which the finite number of excited states per chromophore is reached.

Blinking, saturation and bleaching are inherent limitations of conventional fluorescent probes that can affect bioimaging experiments. Particularly, saturation and blinking can have a great impact on the number of photons that can be detected in a specific amount of time resulting in decreased signal-to-noise ratio (SNR). Although increasing the excitation light power or using longer exposure times can increase light during image acquisition, the temporal resolution and the stability of the fluorescent probe is decreased. Additionally, bleaching limits the maximum acquisition time that labelled cells or molecules can be tracked due to the irreversible loss of the marker fluorescence itself.

1.1.6 Second Harmonic Generation nanoprobes for specific cell labelling

To overcome these limitations, Second Harmonic Generation (SHG) nanoprobes have been used for both *in vitro* (Kachynski et al., 2008, Hsieh et al., 2009, Extermann et al., 2009, Sugiyama et al., 2018) and *in vivo* cell imaging (Pantazis et al., 2010, Malkinson et al., 2020, Sonay et al., 2021). SHG nanoprobes generate light through a second-order nonlinear optical process in which two photons of ω frequency interact with the nanoprobe non-symmetric material (usually crystalline structure without central symmetry point), combine and produce a single photon with 2ω frequency and half the wavelength (**Fig. 14A**). Unlike fluorescent probes, SHG nanoprobes do not blink or bleach and their signal does not saturate with increasing illumination intensity (Dempsey et al., 2012b). In addition, as SHG imaging in conventional microscopy setups requires the use of near-InfraRed (nIR) light, SHG nanoprobes can be easily used for deep tissue imaging where fluorescence imaging becomes challenging. Although SHG is very similar to two-photon (2P) fluorescence imaging (**Fig. 14B**), as both processes depend on two

photons hitting a site at once, the energy of the incident light is conserved in SHG and the process is at least six orders of magnitude faster compared to 2P fluorescence (femtoseconds [10^{-15}] for SHG, nanoseconds [10^{-9}] for fluorescence).

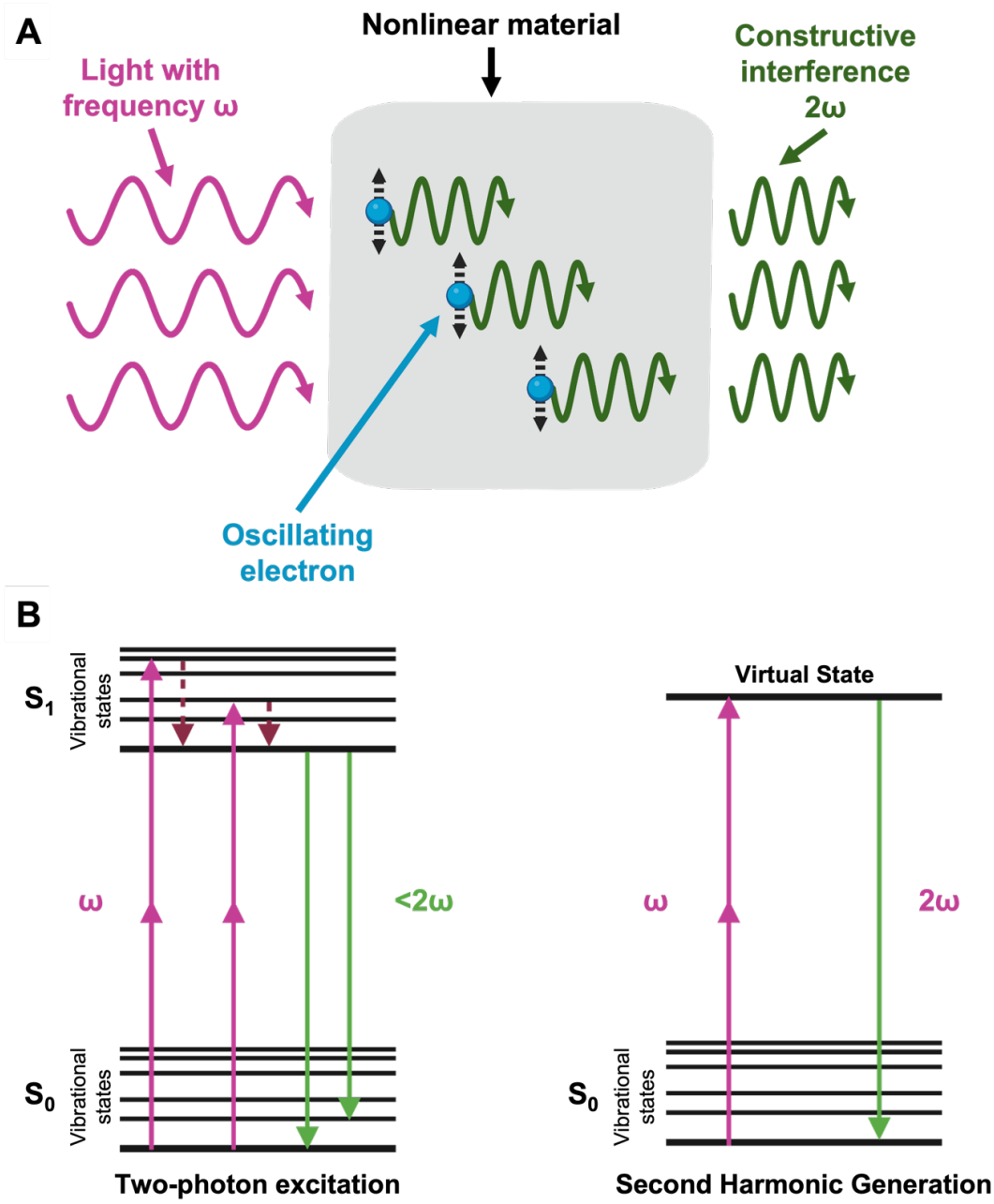


Fig. 14. Phase matching for the generation of Second Harmonic signal and energy diagrams of two-photon excited fluorescence and Second Harmonic Generation. (A) A nonlinear material interacts with the incident light and induces polarization in atomic level. For successful SHG production, the generated waves should constructively interfere. The latter occurs when the material satisfies phase-matching conditions, i.e. it is ordered like a non-centrosymmetric material. The signal coming from individual oscillating electrons shown in green is combined to generate an overall SHG signal. (B) Two-photon excited fluorescence in comparison with Second Harmonic Generation. Please not that SHG does not rely on electron excitation or emission, but effectively combines two photons into a single photon. The SHG signal wavelength is exactly half of the incident wavelength and energy is preserved. In addition, the SHG signal response time depends on the incident laser pulse. *(Created with Biorender.com).*

These two qualities of SHG imaging combined with the narrow signal profile of the SHG nanoprobes, increases SNR by excluding the broad typical emission of autofluorescence background in cells and tissue (Magouroux et al., 2012, Pantazis et al., 2010, Sugiyama et al., 2018). As SHG nanoprobes surface can be robustly functionalised in an efficient and relatively effortless way (see for example for $BaTiO_3$ SHG nanoprobes in (Culic-Viskota et al., 2012)), targeting of cells or proteins of interest allows for precise tracking even in deep tissue without the limitations of traditional fluorescence imaging. A summary of the basic properties of SHG nanoprobes in comparison with fluorescent proteins can be found in **Table 2**.

Table 2. Comparison of basic properties of SHG nanoprobes and fluorescent proteins.

	Genetically encoded	Narrow signal spectra (<10nm)	Multi-labelling imaging	No blinking	No bleaching	No saturation
SHG Nanoprobes	-	+	+	+	+	+
Fluorescent Proteins	+	-	+	-	-	-

Despite these advantages over fluorescent proteins, inorganic SHG nanoprobes, such as $BaTiO_3$ ones, can remain stable in cells and *in vivo* for long time periods which causes concerns for long-term health effects (Staedler et al., 2012). Potential health effects are considerable when such nanoprobes are to be used for diagnostic or therapeutic purposes, like in treating cancer. Although biocompatibility of nanoprobes can be increased by eliminating cellular uptake (Luo et al., 2018), diagnosis and therapy require specific uptake in order to increase the diagnostic value and eliminate "sick" cells without affecting the surrounding healthy tissue.

Recently, we introduced bioharmonophores, a new class of SHG nanoprobes (Sonay et al., 2021). Bioharmonophores consist of a self-assembling peptide core which is encapsulated in a polymer shell. They can be easily synthesised using the

emulsion-solvent evaporation method (Staff et al., 2013) (**Fig. 15A**) and three peptides with different assembling properties (triphenylalanine (Handelman et al., 2013), trileucine (Handelman et al., 2016) and pentalanine (Rabotyagova et al., 2010)) have been found to produce detectable SHG signal upon encapsulation. As bioharmonophores are made from peptides, they are biodegradable and hold great potential for diagnostic and therapeutic purposes. Like their inorganic predecessors, bioharmonophores do not blink nor bleach and their signal does not saturate, while their surface can be easily functionalised for cellular targeting. For instance, we have previously functionalised bioharmonophores with a p32-targetting peptide and successfully used them to target melanoma cancer cells in a zebrafish xenograft model (**Fig. 15B-C**).

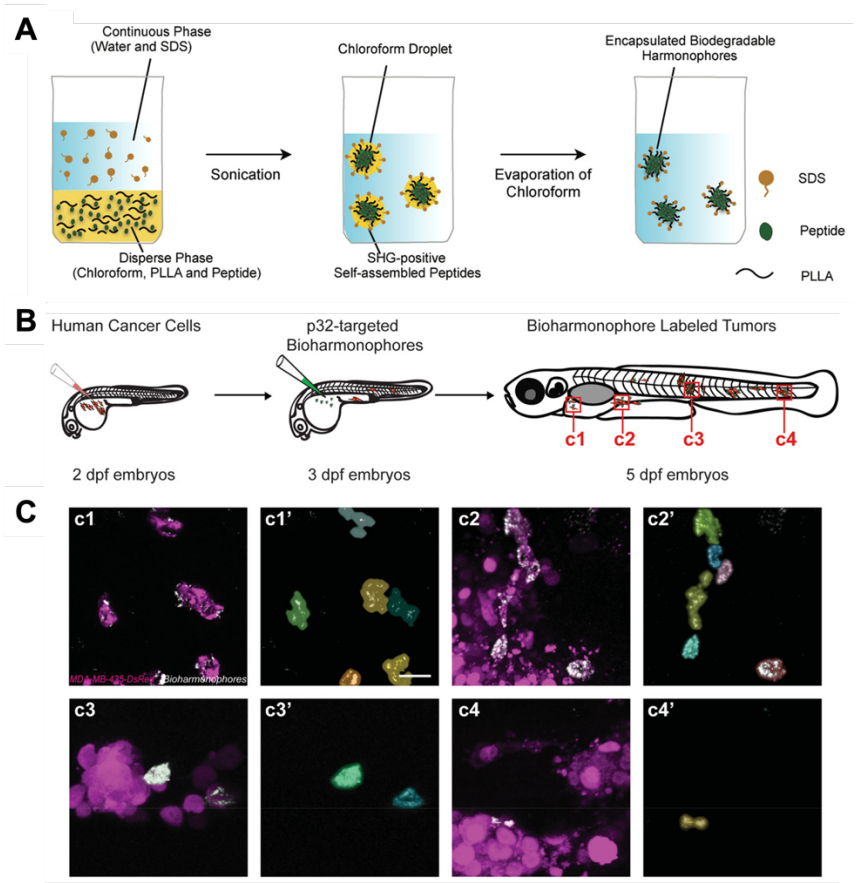


Fig. 15. Bioharmonophores are biodegradable SHG nanoprobes that can be used for precision targeting of tumour cells *in vivo*. (A) Schematic of the emulsion–solvent evaporation method for the synthesis of bioharmonophores. (B, C) Schematic showing the bioharmonophores zebrafish xenograft used for specific targeting of the tumour cells and insets of cancer cells labelled with bioharmonophores in regions depicted in (B). Scale bar, 15μm. *(Adapted from (Sonay et al., 2021)).*

1.2 Mechanical interrogation of biological systems

The rapid development of Molecular Biology in the middle of the 20th century revolutionised the way we approach biological research. Through the years, as explained in the previous section, several tools and approaches have been used to interrogate the biochemical nature of biological systems by labelling and tracking cells and proteins of interest. Clever and sophisticated experiments revealed complex phenomena, such as induction in vertebrate development and increased our understanding of cellular biology. However, solely biochemical signals cannot fully explain how cells interact with other cells and their surroundings to respond to the constant changes of their niche. Nowadays, it is evident that if we want to fully understand development, homeostasis and disease progression we need to uncover the feedback loops of the interplay between mechanical and biochemical signals behind these complex processes (Hannezo and Heisenberg, 2019, Heisenberg and Bellaiche, 2013, Paci and Mao, 2021) (**Fig. 16**).

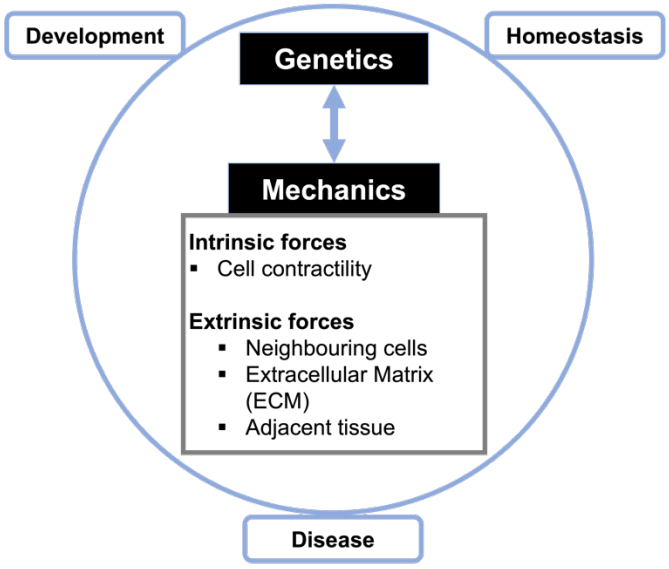


Fig. 16. Biochemical and mechanical feedback loops are important to fully understand development, homeostasis and disease progression. Cells respond to extrinsic and intrinsic forces by modulating their gene expression profiles and adapting to the constant changes of their surrounding cellular and extracellular environment. *(Adapted from (Vignes et al., 2022)).*

1.2.1 Cellular mechanosensation and mechanotransduction

Cellular mechanosensation and mechanotransduction is the ability of cells to perceive and respond to extrinsic and intrinsic mechanical stimuli. Cells have a range of molecular processes to mediate force sensation, force transmission and force generation from the cellular to the tissue level (Lecuit et al., 2011). Cells apply forces at the cellular level by using motor proteins, filamentous structures and polymerisation/depolymerisation of cytoskeletal proteins, such as microtubules (Kent and Lele, 2017). For example, myosin can interact with F-actin which subsequently changes the cytoskeletal architecture and its mechanical stress properties leading to force generation. At the cell level within a tissue, forces are transmitted between cells and their surrounding environment, typically the extracellular matrix (ECM), by adhesion proteins, such as cadherins (cell-cell forces) and integrins (cell-ECM forces) (Heisenberg and Bellaiche, 2013). Interestingly, integrins, which are part of cell adhesions, can also act as mechanosensors adopting closed, intermediate or open conformations in response to applied forces (Zhu et al., 2008). Such conformational changes are then transformed by mechanotransducers which interact with both mechanosensors and the cytoskeleton. For instance, talins which are cytoskeletal linker proteins bind both integrin cytoplasmic tails and actin filaments inside the cell to transmit mechanical signals (Goult et al., 2021). These mechanical signals trigger biochemical changes via secondary messengers, such as calcium and cAMP, or by activating cellular pathways, such as the Src kinase and the hippo pathway (Vining and Mooney, 2017, Mammoto et al., 2013). Eventually, transcriptional coactivators, such as Yap and Taz, translocate to the nucleus and regulate gene expression (Panciera et al., 2017). The transcriptional regulation closes the biomechanical feedback loop and leads to cellular changes in response to the mechanical stimuli, such as the growing of focal adhesions (FA) which affects the distribution of forces in the cell and increases the likelihood of FA to undergo further conformational changes (Riveline et al., 2001).

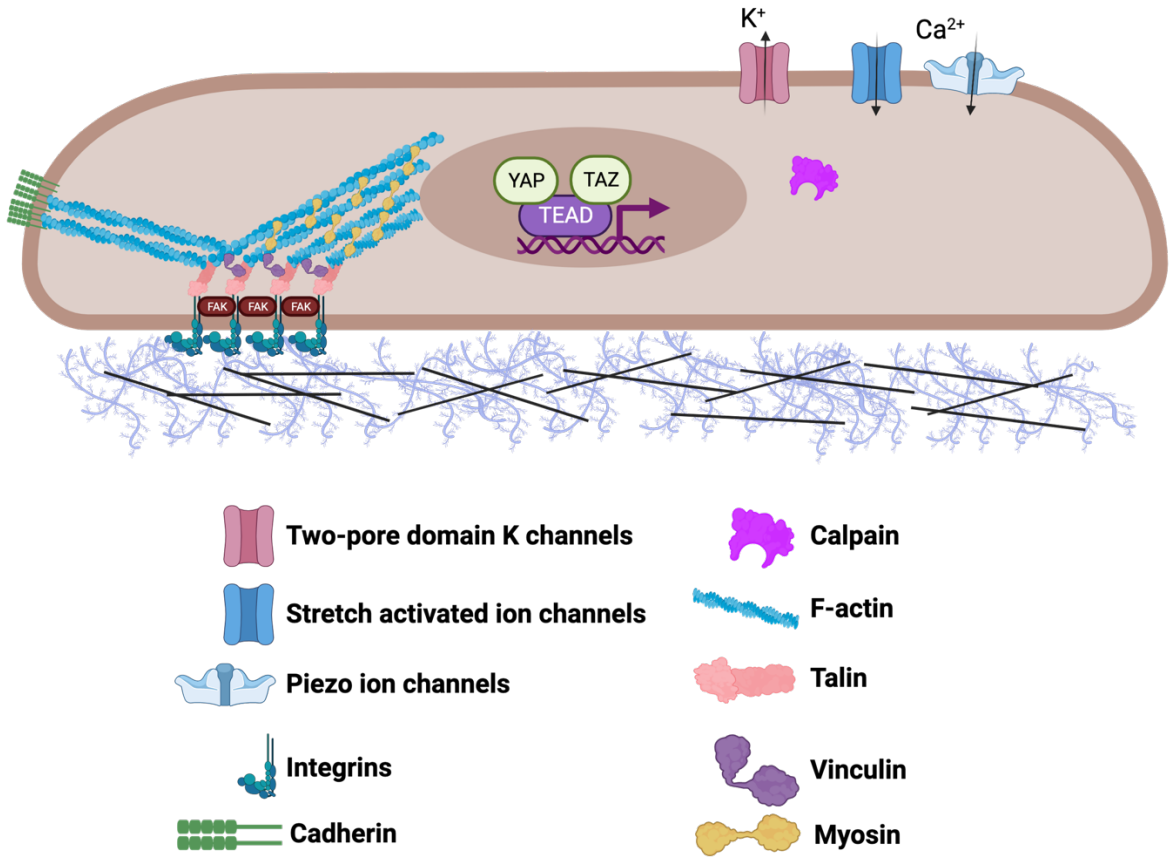


Fig. 17. Basic protein components of cellular mechanosensation and mechanotransduction apparatus for force sensing, force transmission and force generation. Cells interact with their extracellular environment, typically the ECM, via integrins which transmit forces by anchoring to the ECM and forming FA through recruitment of several proteins, such as vinculin and talin. FA are connected to actomyosin which is the contractile machinery of the cell. For cell force transmission within a tissue, actomyosin complex is also connected to cell-cell adhesion molecules, such as cadherins. Extrinsic forces are transformed into biochemical responses through the interaction of signalling molecules, such as the Focal Adhesion Kinase (FAK) and Src tyrosine kinase, with the FA proteins upon force-dependent conformational changes. Eventually, signalling cascades, such as the Src pathway, are activated and lead to transcriptional changes through nuclear translocation of transcriptional coactivators, such as Yap and Taz and transcriptional factors, such as TEAD. Furthermore, extrinsic mechanical stimuli can be sensed by several mechanosensors on the membrane of the cell, such as stretch-activated ion channels or two-pore domain potassium channels. As ions permeate the pores of these channels, secondary signalling processes are activated, such as the calpain cleave cytoskeletal proteins. *(Created with Biorender.com).*

Mechanosensitive ion channels are membrane proteins that play an essential role in fast signalling events during cellular mechanotransduction (Ridone et al., 2019, Jin et al., 2020, Gu and Gu, 2014). Such type of channels can be found in all kingdoms of life on our planet, including archaea, bacteria and eukaryotes (**Fig. 18**). Mechanosensitive ion channels are activated by mechanical forces exerted on the

cell membrane upon which the channels open and convert the stimuli into osmotic, electrical and/or chemical intracellular signals via secondary signalling molecules, such as calcium.

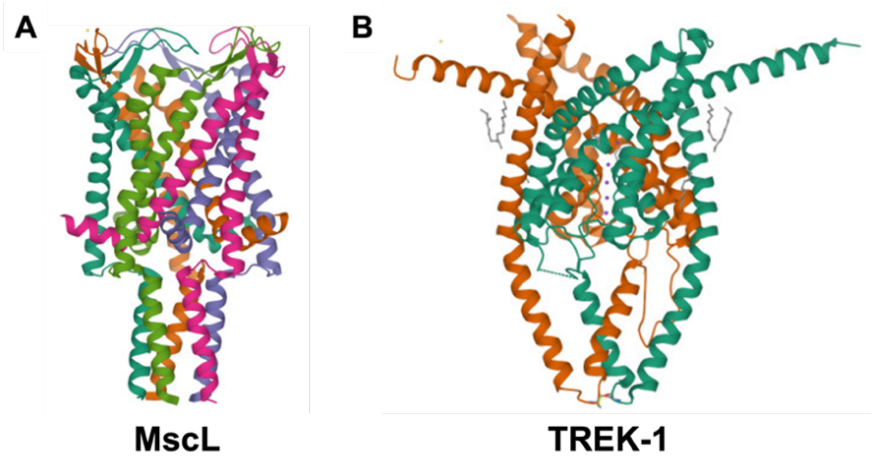


Fig. 18. Mechanosensitive ion channels can be found in both prokaryotic and eukaryotic organisms. (A) Structure of the mechanosensitive channel of large conductance (Mscl) of *M. tuberculosis* as determined by X-ray crystallography in cartoon mode (*PDB: 2OAR*). (B) Structure of the mechanosensitive two-pore domain potassium channel TREK-1 of *M. musculus* as determined by X-ray crystallography in cartoon mode (*PDB: 6CQ6*).

1.2.2 Methods to measure cell mechanics

Cellular mechanosensation and mechanotransduction are essential in myriad of physiological and pathophysiological processes in all stages of life of an organism, such as wound healing (Rosińczuk et al., 2016) and metastasis (Kai et al., 2016, Panciera et al., 2017). However, how these crucial cellular processes incorporate feedback at the cellular level is still an area of active research and a wide range of tools have been developed to interrogate cellular mechanics.

Atomic Force Microscopy (AFM), micropipette aspiration and microidentation have been used to measure stiffness, tension and general mechanical properties of individual cells, tissue and embryos (Gaub and Muller, 2017, Shellard and Mayor, 2021, Maître et al., 2012, Gautier et al., 2015). In addition, methods, such as magnetic (Savin et al., 2011, Fukui et al., 2021, Guilluy et al., 2014) and optical

tweezers (Bambardekar et al., 2015) and laser ablation (Sugimura et al., 2016, Marshall et al., 2022, Ma et al., 2009, Duda et al., 2019) can be used to either apply forces in a precise way by modulating probes from a distance using light or electromagnets, or infer mechanical tension in cells and tissues. Although these techniques allow for robust measurements of cellular mechanics, their use is limited by either their invasive nature or light depth penetration. Typically, direct contact with the sample or dissociation of the tissue is required for the use of tweezer techniques, which limits their potential to study mechanics in organismal level. More recent less invasive methods which take advantage of high resolution imaging of fluorescent lipid droplets to measure cellular forces (Campas et al., 2014, Campas, 2016) and osmotic pressure (Vian et al., 2022) *in vivo* require extensive training and expertise for their use (i.e. microinjection of the lipid droplets), fact that can restrict their adaptation to already established experimental pipelines.

As mentioned previously, protein engineering of FPs has resulted in a multitude of genetically-encoded indicators that can be used to study several cellular processes, such as calcium signalling. FRET sensors, which are widely used to study protein-protein interactions, have been developed to study cellular mechanics in a non-invasive way. The sensor design consists of a FP FRET pair with overlapping emission and excitation spectra separated by a spring-like peptide with known mechanical properties (Freikamp et al., 2016). Using this design, FRET-based sensors have been developed to study tension of several mechanotransducing molecules, such as collagen (Meng et al., 2011), vinculin (Grashoff et al., 2010), talin (Austen et al., 2015) and E-cadherin (Borghi et al., 2012, Cai et al., 2014). Notably, β-spectrin (Meng et al., 2011) and E-cadherin (Cai et al., 2014) FRET-based sensors have been also used *in vivo* to study touch sensing in *C. elegans* and collective cell migration in *D. melanogaster*. Although FRET tension sensors allow for precise calculation of tensile forces via imaging, their use is restricted to a small regime of

tensile forces, ranging from 1 to 10pN and they require extensive *in vitro* single molecule calibrations.

1.2.3 Piezo1 mechanosensitive ion channels

1.2.3.1 Piezo protein family

A class of mechanosensitive ion channels with no homology to other proteins are Piezo proteins which are named from the greek word *"πίεσις"* which means "pressure". Although Piezo1 gene (also known as FAM38a, or KIAA0233) was implicated in beta-amyloid deposition in the mid-2000s (Satoh et al., 2006), the ground-breaking discovery that it is an ion channel that can be directly gated by mechanical forces (Coste et al., 2010) revolutionised the field of biomechanics. The first Piezo1 mechanics article of the Patapoutian group in 2010 became the foundation stone of a rapidly evolving field which set the molecular basis of mechanosensation and jointly awarded Ardem Patapoutian the 2021 Nobel Prize in Physiology or Medicine.

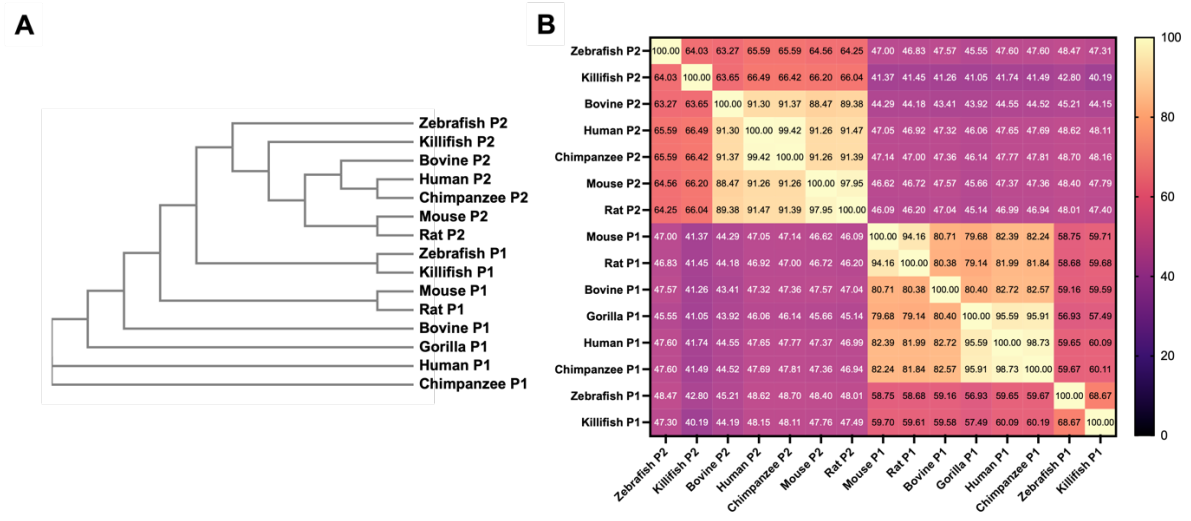


Fig. 19. Piezo1 and Piezo2 sequence alignments show high sequence similarity among vertebrates. (A) Cladogram of several vertebrate Piezo1 (P1) and Piezo2 (P2) protein sequences after sequence alignment. (B) Sequence identity matrix of the Piezo1 and Piezo2 protein sequences used for the alignment. Sequence alignment was done on the online server of Clustal Omega, ebi.ac.uk/Tools/msa/clustalo/.

The Piezo protein family has two members in most vertebrates, Piezo1 and Piezo2 (Coste et al., 2010)) which show high protein sequence similarity (**Fig. 19**). Functional homologs have been also identified both in plants (Mousavi et al., 2021, Radin et al., 2021) and invertebrates, such as *C. elegans* (Bai et al., 2020). While Piezo2 function is mainly restricted to the peripheral nervous system and is less studied (**Fig. 20A**), Piezo1 is expressed in a wide range of tissues and cells (**Fig. 20B-C**) (Uhlén et al., 2015) and has been shown to contribute to mechanotransduction in various organs and tissues (Zhang et al., 2021, Wang et al., 2016, Retailleau et al., 2015, Ploeg et al., 2021, Liang et al., 2017, Huang et al., 2016, Nguetse et al., 2020, Faucherre et al., 2014, Bae et al., 2013, Velasco-Estevez et al., 2020, Blumenthal et al., 2014, Peyronnet et al., 2013, Kulkarni et al., 2021, Gudipaty et al., 2017, Eisenhoffer et al., 2012, Miyamoto et al., 2014, Dalghi et al., 2021, Martins et al., 2016, Lee et al., 2021, Lee et al., 2014, McHugh et al., 2012, McHugh et al., 2010, Aglialoro et al., 2020, Yang et al., 2014, Li et al., 2015, Hung et al., 2016, Canales Coutiño and Mayor, 2021, Radin et al., 2021) (**Table 3**).

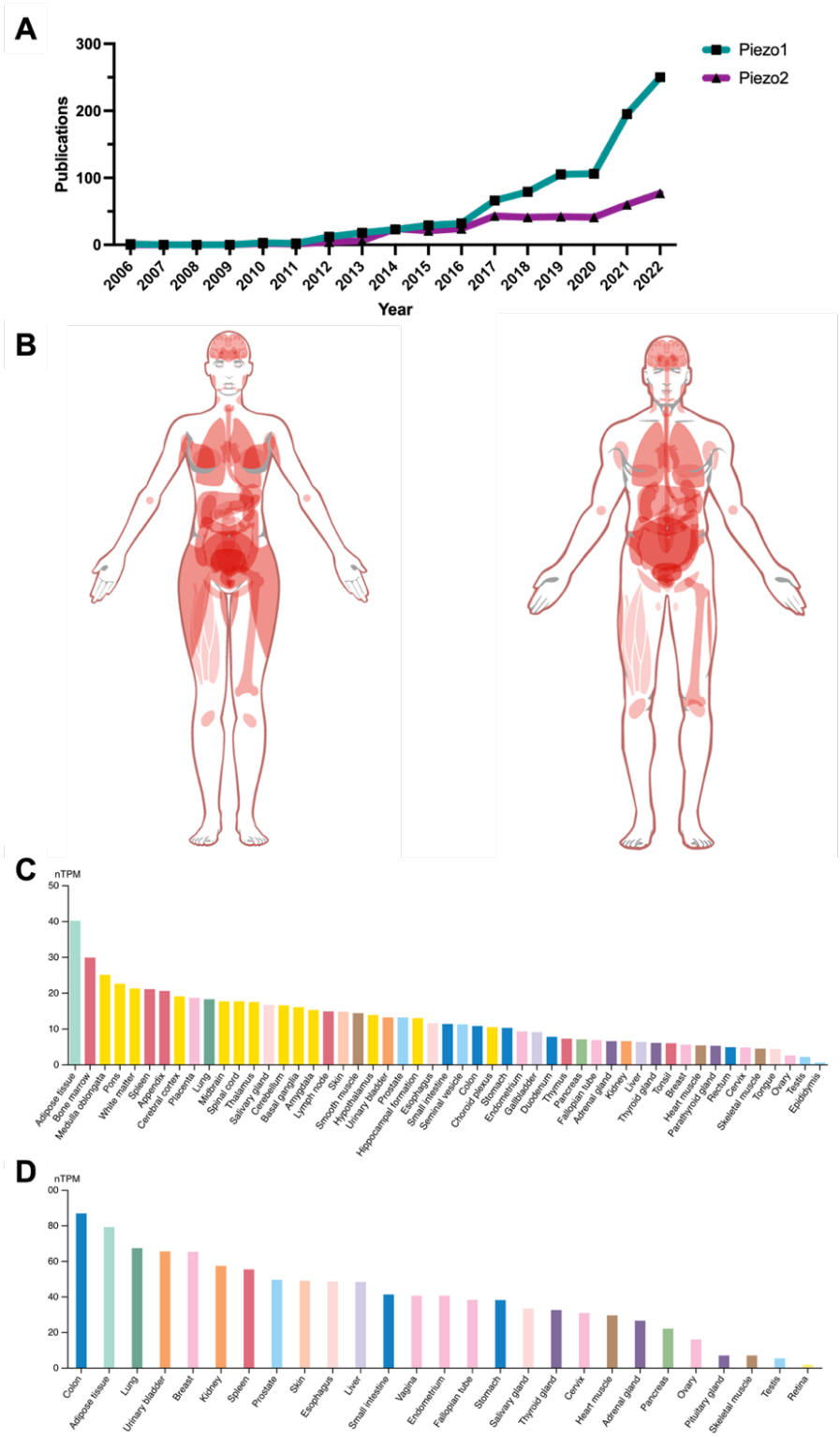


Fig. 20. Piezo1 is expressed in a wide range of human tissues. (A) Number of publications per year referring to Piezo1 and Piezo2. (B) Two human bodies showing an anatomical display of the expression levels of Piezo1. (C) Human Protein Atlas (HPA) RNA-seq tissue data of Piezo1 expression reported as nTPM (normalised protein-coding transcripts per million). (D) Genotype-Tissue Expression (GTEx) RNA-seq tissue data of Piezo1 expression reported as nTPM (normalised protein-coding transcripts per million). For (C) and (D), color-coding is based on tissue groups. *(Data on (A) retrieved from Pubmed searching for Piezo1 or FAM38a and Piezo2, respectively, accessed 19 December 2022, (B-D) adapted from proteinatlas.org, accessed 18 December 2022).*

Table 3. Indicative list of biological processes Piezo1 is involved in. *(Adapted from Yaganoglu and Kalyviotis et al.)*

Biological processes in which Piezo1 is important	References
Cardiovascular mechanosensation	(Fotiou et al., 2015, Huang et al., 2016, Liang et al., 2017, Lukacs et al., 2015, Ploeg et al., 2021, Retailleau et al., 2015, Wang et al., 2016, Zhang et al., 2021)
Erythrocyte mechanosensation and volume regulation	(Albuisson et al., 2013, Andolfo et al., 2013, Bae et al., 2013, Nguetse et al., 2020, Zarychanski et al., 2012)
Neural mechanosensation and differentiation	(Blumenthal et al., 2014, Pathak et al., 2014, Velasco-Estevez et al., 2020)
Epithelial cell mechanosensation	(Eisenhoffer et al., 2012, Gudipaty et al., 2017, Kulkarni et al., 2021, Peyronnet et al., 2013)
Bladder mechanosensation	(Dalghi et al., 2021, Miyamoto et al., 2014)
Kidney mechanosensation	(Martins et al., 2016)
Cartilage mechanosensation	(Lee et al., 2014, Lee et al., 2021)
Cell adhesion	(Aglialoro et al., 2020, McHugh et al., 2010, McHugh et al., 2012)
Cell migration	(Canales Coutiño and Mayor, 2021, Holt et al., 2021, Hung et al., 2016, Li et al., 2015, Yang et al., 2014)
Plant mechanosensation	(Radin et al., 2021, Mousavi et al., 2021)

Mutations in human Piezo1 have been implicated in diseases, such as dehydrated hereditary stomatocytosis (Andolfo et al., 2013, Albuisson et al., 2013) and general lymphatic dysplasia (Fotiou et al., 2015, Lukacs et al., 2015) and global knockout of Piezo1 in mice causes embryonic lethality (Li et al., 2014, Ranade et al., 2014), highlighting the importance of this channel for development, pathophysiology and homeostasis (Wu et al., 2017).

1.2.3.2 Piezo1 structure

Piezo1 is a large protein of around ~287kDa[2] which consists of ~2520 amino acids and was predicted to have several transmembrane regions (Coste et al., 2010). Several cryo-Electron Microscopy (cryo-EM) studies of the mouse Piezo1 protein (Geng et al., 2020, Zhao et al., 2018, Yang et al., 2022b) showed that it forms a homotrimer (**Fig. 21A-B**) and that its ion permeating pore resides in the C-terminus of the protein (Coste et al., 2015, Zhao et al., 2016) while showing a preference for divalent cations, such as calcium (Coste et al., 2012, Gottlieb et al., 2012). It exhibits a three-bladed propeller-shaped homotrimeric structure which has the three peripheral blade structures on the extracellular side, a central cap, three long beams on the intracellular side bridging the blade-like structures to the central cap and a transmembrane region (**Fig 21C**) between the other structural features (Zhao et al., 2018).

1.2.3.3 Piezo1 gating

There are several previous studies showing that Piezo1 responds to different types of mechanical stimuli (**Fig. 22**), such as stretching and pushing of the cell membrane (Coste et al., 2010), fluid shear stress (Ranade et al., 2014, Li et al., 2014), stiffness (Pathak et al., 2014), osmotic stress (Syeda et al., 2016) and cell confinement (Hung et al., 2016).

Although the exact mechanisms of the mechanosensitive ion channel gating are largely unknown due to the relatively young age of this research area in cellular mechanobiology, there are two main gating models accepted by the scientific community: (i) the force-from-lipids and (ii) the force-from-filament paradigms. The force-from-lipids model implies that the mechanical force exerted through the lipid

[2] The molecular weight was calculated based on the human Piezo1 protein sequence (UniProt Q92508) using the bioinformatics tool Compute pI/MW in the online bioinformatics platform Expasy, web.expasy.org/compute_pi/, accessed 18 December 2022.

bilayer alone without involvement of other cellular components activates the mechanosensitive ion channel, whereas in the force-from-filament model extrinsic or intrinsic forces from tethering to the cytoskeleton or ECM activate the ion channel (**Fig. 23**). Several studies have shown the importance of lipids for Piezo1 activation (Cox et al., 2016, Cox et al., 2017, Syeda et al., 2016, Ridone et al., 2020), while other studies show the importance of ECM and cytoskeletal components for regulating Piezo1-dependent activity (Pathak et al., 2014, Holt et al., 2021, Ellefsen et al., 2019). Recently, a crowding-induced mechanism has been also suggested for Piezo1 activation on the cell membrane (Jiang et al., 2021b).

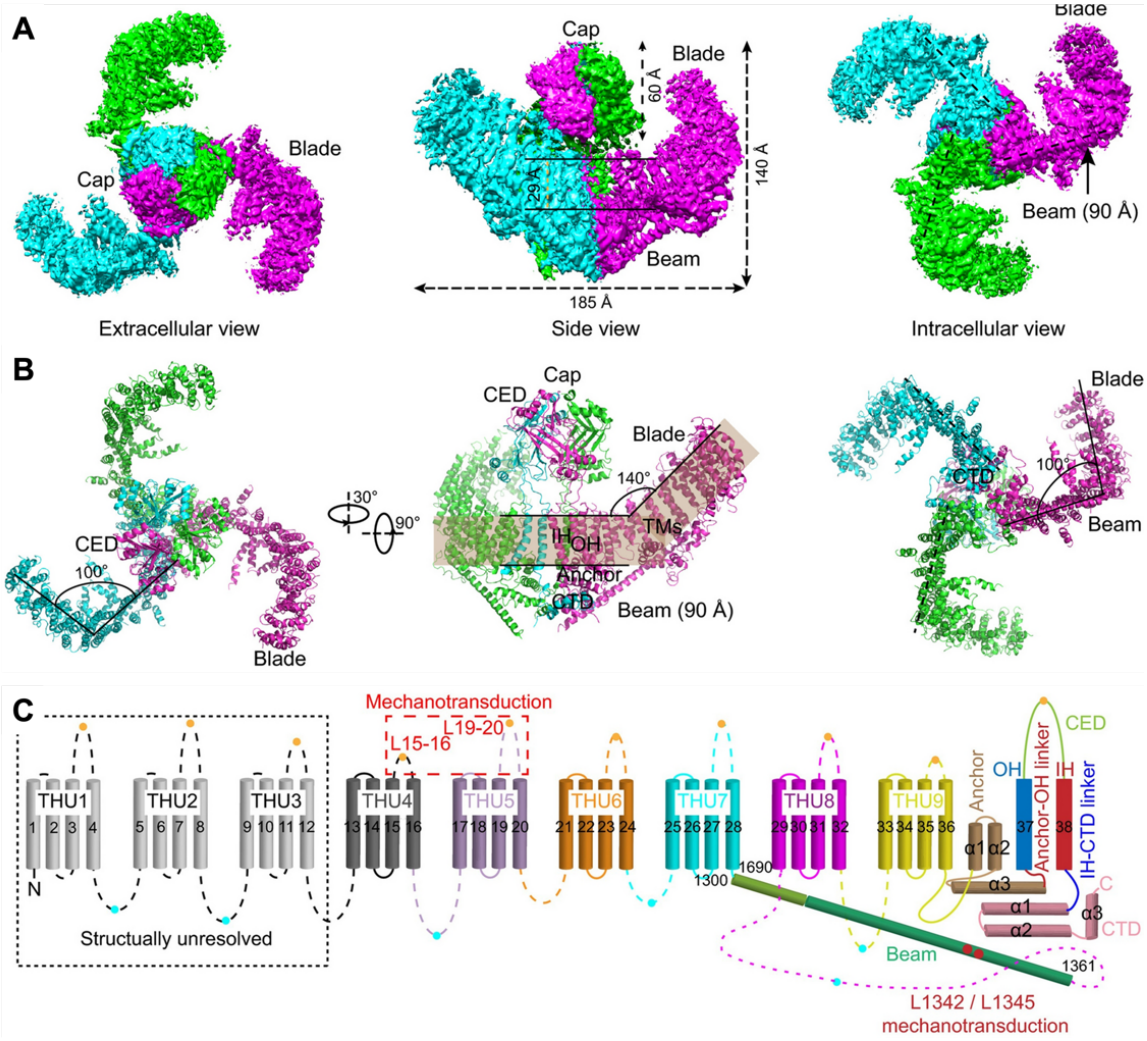


Fig. 21. Mouse Piezo1 forms a three-bladed propeller-shaped homotrimeric structure. Multiple views of the mouse Piezo1 structure in (A) surface and (B) cartoon mode showing the secondary structures of the protein. (C) The 38 transmembrane region topology of mouse Piezo1 showing the individual Transmembrane Helical Units (THU) and the other structural features *(Adapted from (Zhao et al., 2018))*.

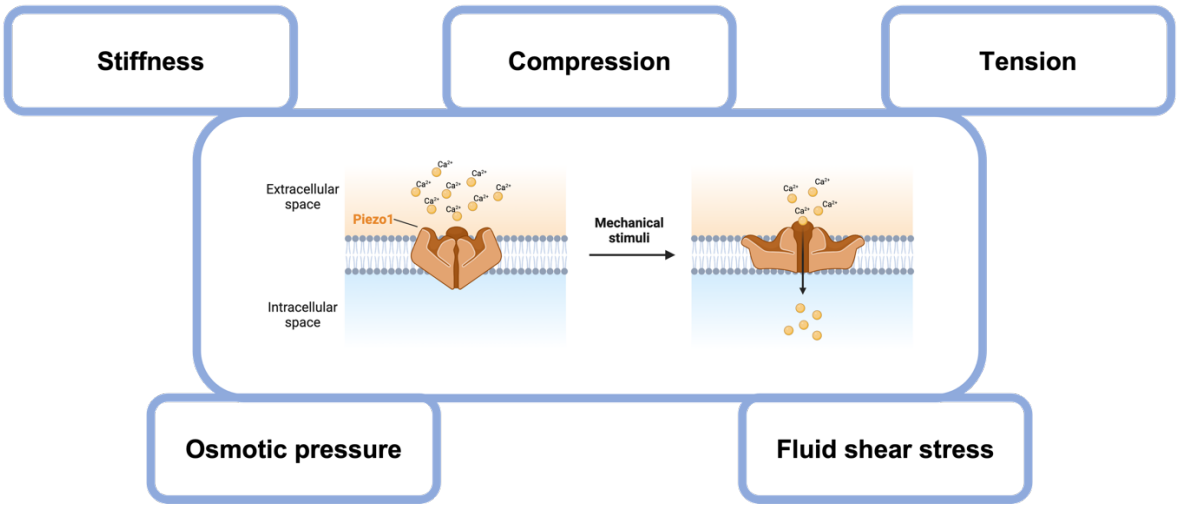


Fig. 22. Piezo1 responds to several types of mechanical stimuli. Piezo1 can respond to a range of different kinds of mechanical stimuli, such as compression and fluid shear stress, while it can sense differences in membrane tension, substrate stiffness and osmotic pressure. *(Created with Biorender.com).*

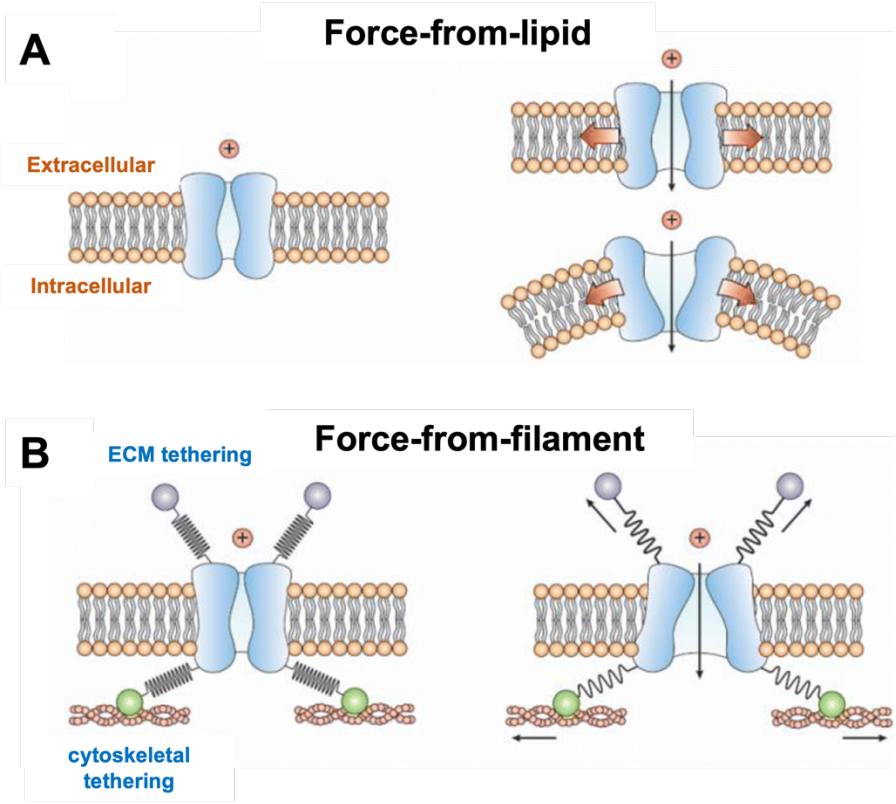


Fig. 23. General gating models of mechanosensitive ion channels. (A) The force-from-lipids and (B) the force-from-filaments models for gating of mechanosensitive ion channels. In the force-from-lipids model, forces directly applied to the channel through membrane lipids without the implication of other cytoskeletal components can activate the channel, whereas in the force-from-filament model the tethering of the channel with cytoskeletal or ECM components leads to activation. *(Adapted from (Ridone et al., 2019)).*

Table 4. Available agonists and antagonists of Piezo1. *(Adapted from (Della Pietra et al., 2020)).*

Agonists		Antagonists			
Yoda1	**Jedi1/2**	**Dooku1**	**Gadolinium Gd^{3+}**	**Ruthenium Red**	**GsMTx-4**
Selective		Selective	Non-selective		

1.2.3.4 Chemical modulators of Piezo1 activity

Currently, there is a small number of chemical and peptide compounds that can be used to modulate ion channel activity. The lanthanide Gd^{3+}, ruthenium red, the GsMTx-4 peptide isolated from the toxin of the spider *G. spatulate* and the antibiotics streptomycin and gentamycin are known to block most of the known mechanosensitive ion channels, including Piezo1 (Hamill and Mcbride, 1996, Coste et al., 2010, Bae et al., 2011) (**Table 4**). A screen of more than 3 million compounds to find Piezo1-specific chemical modulators identified one small molecule (2-[5-[[(2,6-dichlorophenyl) methyl]thio]-1,3,4-thiadiazol-2-yl]pyrazine), named Yoda1, which was the first chemical agonist of Piezo1 to be discovered acting probably as a gating modifier reducing the channel's mechanical activation threshold (Syeda et al., 2015). Recent chemical screens of designed Yoda1 analogues, identified Dooku1 (2-[(2,6-Dichlorobenzyl)thio)-5-(1*H*-pyrrol-2-yl)-1,3,4-oxadiazole), which antagonises Yoda1-dependent Piezo1 activation without affecting constitutive Piezo1 activity (Evans et al., 2018). Although for many years Yoda1 was the only available agonist for Piezo1 and screening for specific chemical modulators has been challenging, another pair of agonists was recently identified, Jedi1/2, which activate the channel through the extracellular side of the blade, indicating a long-range allosteric modulation mechanism of the channel's activity (Wang et al., 2018).

1.3 Aims of this thesis

During my PhD, I aimed to develop and validate an imaging toolkit for advanced optical precision imaging for both mechanical and biochemical interrogation of biological systems (**Fig. 24**).

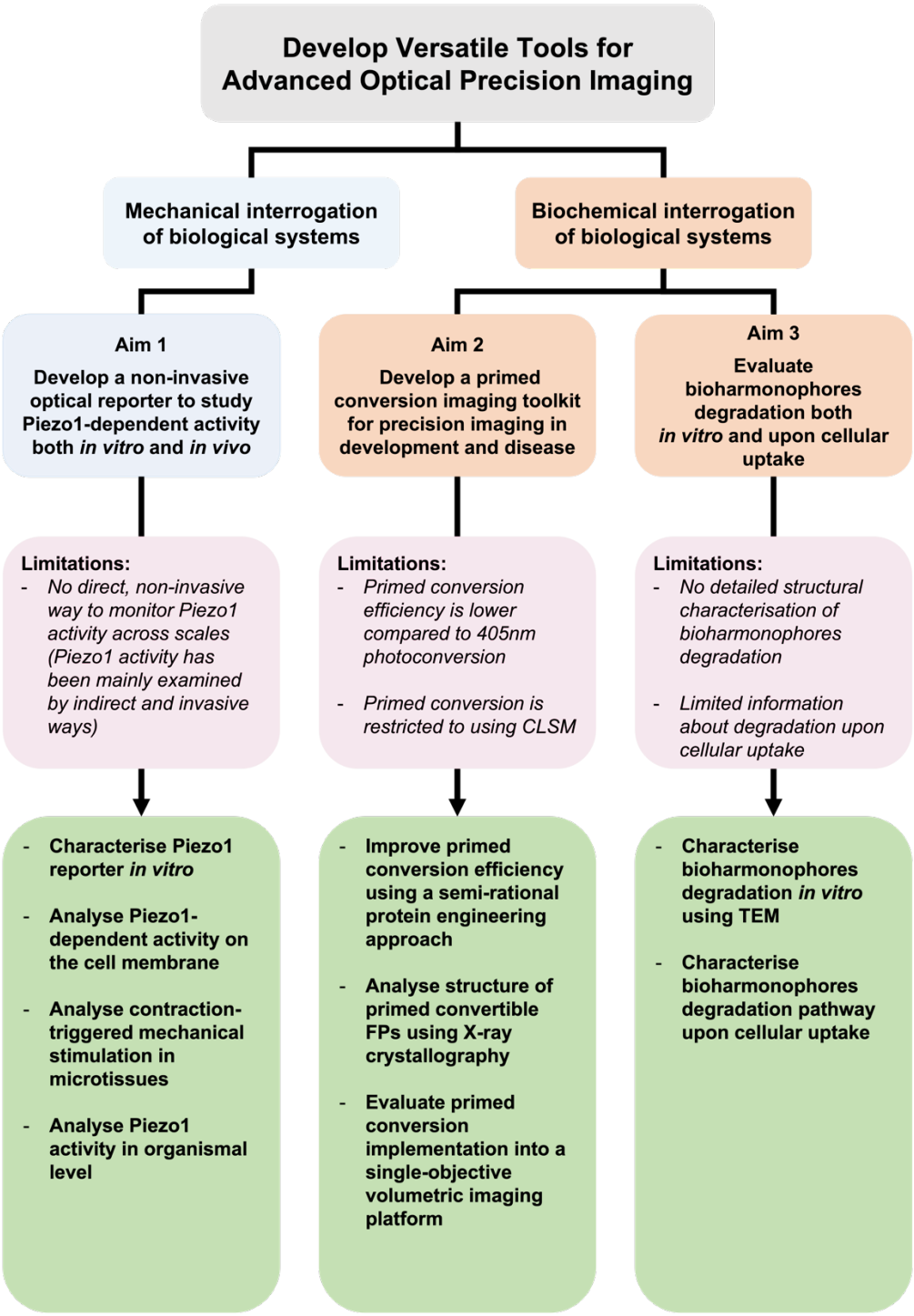


Fig. 24. The PhD project rationale to develop an advanced imaging toolkit for biochemical and mechanical interrogation of biological systems.

1.3.1 Mechanical interrogation of biological systems

For mechanical interrogation, I focused on continuing previous efforts in the Pantazis lab to develop and characterise a non-invasive optical biosensor for Piezo1-dependent activity.

1.3.1.1 Piezo1 research limitations

Since the discovery of the mechanical nature of Piezo1 channels, a longstanding yet largely unmet goal is to measure Piezo1 activity changes reliably and specifically with high spatiotemporal precision in a non-invasive way. Many studies have relied on optical monitoring of cytosolic calcium in response to stimulation of Piezo1 by controlled application of either mechanical forces or delivery of a chemical agonist or by monitoring morphological changes, protein expression, transcriptional changes and electrophysiology readouts. However, such approaches are not suitable for measuring Piezo1 activity in a non-invasive way at an organismal level, where various conditions, such as timing, frequency, intensity and localisation of mechanical stimuli, cannot be precisely controlled. In addition, given that cytoplasmic calcium increases occur in response to many signalling events besides Piezo1 activity, the source of a cytosolic calcium readout cannot be exclusively attributed to mechanical stimulation.

Aim 1. Develop a non-invasive optical sensor to study Piezo1-dependent activity both in vitro and in vivo

In Chapter 2, I describe my efforts to characterise *in vitro* and *in vivo* a Piezo1-specific optical sensor which we name GenEPi. After extensive *in vitro* characterisation to show that the Piezo1 channel within the sensor is functional like the wild-type (wt-)-Piezo1, I describe how I used the sensor to monitor Piezo1-dependent activity across scales: from the single cell level to that of the entire organism.

1.3.2 Biochemical interrogation of biological systems

For biochemical interrogation, I focused on photoconvertible FPs and primed conversion and the recently developed biodegradable SHG nanoprobes, bioharmonophores.

1.3.2.1 Primed conversion limitations I

Although primed conversion is a promising developing photoconversion technology, its conversion efficiency is relatively low when compared to 405nm photoconversion (standard photoconversion conditions described in (Mohr et al., 2016)). To overcome this limitation, longer exposure times or higher laser powers are required. These alterations to increase the photoconversion efficiency could lead to phototoxic effects after multiple rounds of imaging. Although the difference of the conversion efficiency could be partially explained by the nature of the process itself (i.e. primed conversion relies on the absorption of two photons instead of one photon in the case of traditional violet-light photoconversion), the fact that different variants of pr-FPs exhibit differences in their primed convertibility, suggests that primed conversion efficiency can be further improved. This improvement will render primed conversion faster, which will allow real-time monitoring of highly dynamic biological processes and will ensure effective photoconversion in deep tissue.

1.3.2.2 Primed conversion limitations II

Currently, *in vivo* examples of primed conversion are restricted to using a confocal laser scanning microscope. In confocal microscopy, point-by-point scanning along the entire specimen increases acquisition time which limits its applicability for large specimens, such as embryos and organoids. In a light-sheet microscope and especially in a single-objective one (Dunsby, 2008), optical sectioning throughout large samples can be achieved with minimal photodamage at speeds capable of

capturing transient biological phenomena (Sikkel et al., 2016). Thus, the implementation of primed conversion into a volumetric imaging system will allow capturing even more complex developmental dynamics with the sufficient spatiotemporal resolution.

Aim 2. Develop a primed conversion imaging toolkit for precision imaging in development and disease

To address both limitations discussed above and to develop the next generation of a primed conversion advanced imaging toolkit, I focused on two interrelated and interconnected tasks which are described in Chapter 3. First, I used a semi-rational approach to engineer primed convertible fluorescent proteins and increase their primed conversion efficiency. To understand the primed conversion mechanism at the atomic level and further guide my protein engineering, I conducted a series of protein crystallisation experiments followed by X-ray crystallography. Finally, in collaboration with the Rowland's Lab (Department of Bioengineering/Imperial College London), I evaluated the implementation of primed conversion into a single-objective volumetric imaging platform.

1.3.2.3 Bioharmonophores limitations

As mentioned above, bioharmonophores are a new class of polymer encapsulated biodegradable SHG nanoprobes which overcomes the inherent limitations of fluorescent probes. Triphenylalanine, pentalanine and trileucine peptides have been shown to produce strong SHG signal upon miniaturisation and encapsulation. Previous efforts in the Pantazis lab showed that bioharmonophores can be degraded both in cells and *in vivo*. However, the detailed degradation pathway upon cellular uptake and an *in vitro* structural analysis of the process, such as with Transmission Electron Microscopy (TEM), was missing.

Aim 3. Evaluate bioharmonophores degradation in vitro and upon cellular uptake

I address these limitations in Chapter 4 where I used TEM to monitor the degradation of freshly synthesised triphenylalanine bioharmonophores by proteinase K. In addition, I monitored the subcellular localisation of bioharmonophores upon cellular uptake to reveal the degradation pathway they follow.

Chapter 2. An optical reporter of Piezo1-dependent activity

"Measure what can be measured
and make measurable what cannot be"

Galileo Galilei

2.1 Reporter engineering

Previous efforts in the Pantazis lab resulted in the development of a genetically-encoded, non-invasive optical reporter of Piezo1-dependent activity. These efforts were based on the calcium microdomain hypothesis (Clapham, 2007). This hypothesis states that upon channel opening the concentration of calcium in the vicinity of the ion permeating pore would significantly increase in comparison with the closed channel (**Fig. 25A**). Therefore, it was hypothesised that targeting the ion permeating channel of Piezo1 with a genetically-encoded calcium indicator (GECI) will provide a specific readout (**Fig. 25B**).

In a systematic screening, five different GECIs (**Fig. 26A**) were tested and were selected to fulfil two key requirements: (i) low affinity to calcium (K_d ranging from 610-6122 nM) to avoid "reporting" non-specific cytosolic calcium increases and (ii) high dynamic range (F_{max}/F_{min} ranging from 13.8-31) to easily distinguish their ON/OFF states and the channel activation. In addition, two different types of flexible linkers (1X or 2X of GSGG) were tested in order to secure the proper folding of the

Piezo1 protein and to not alter the functionality of the channel while providing

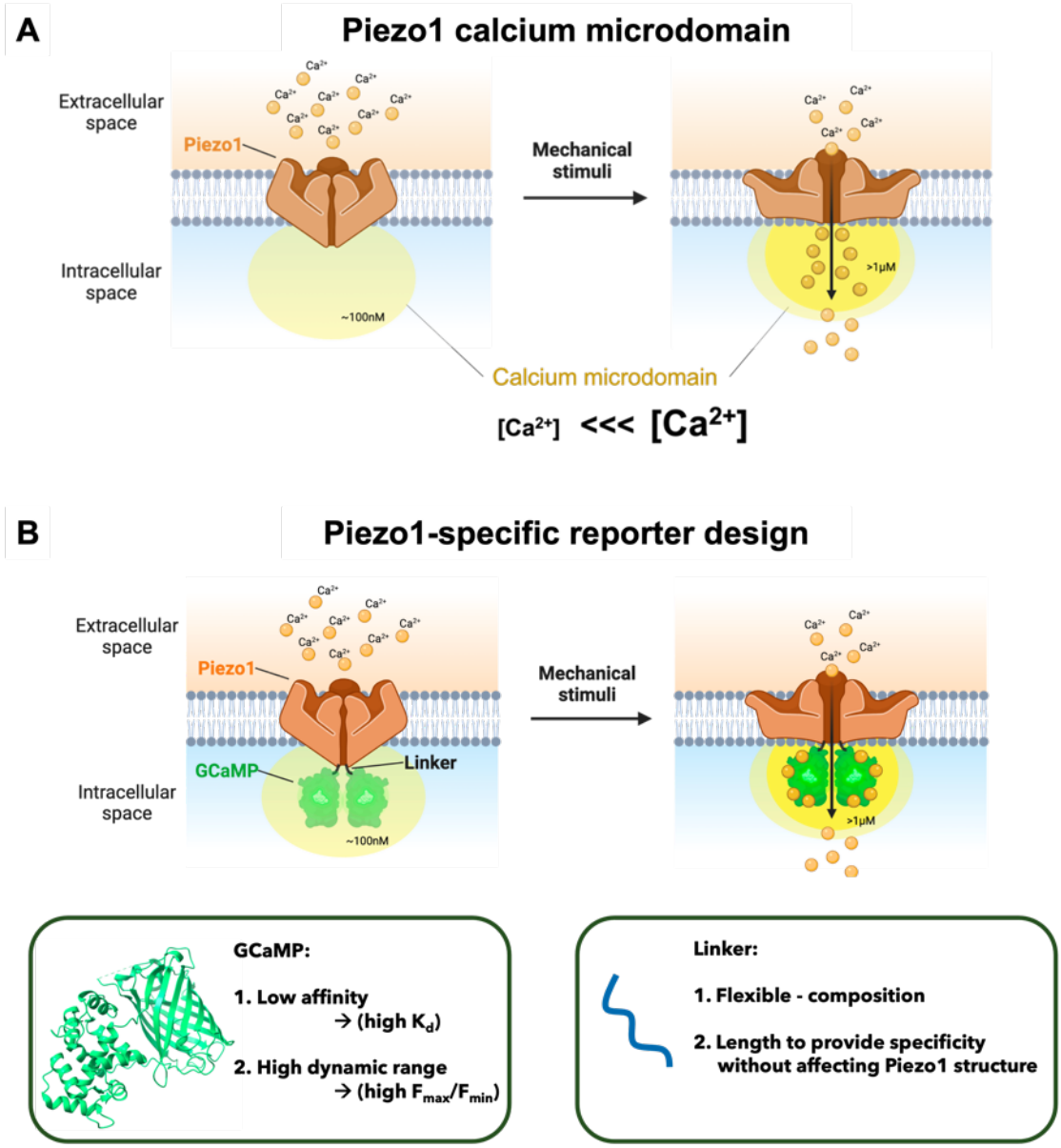


Fig. 25. The Piezo1 microdomain hypothesis and the suggested design to develop an optical reporter for Piezo1-dependent activity. (A) The microdomain hypothesis implies that when the channel is active due to mechanical stimulation or chemical agonism the calcium concentration near the vicinity of the pore increases dramatically. (B) To develop a Piezo1-specific optical reporter a low affinity GECI is targeted to the C-terminus of Piezo1 which resides in the cytosol via a flexible linker of defined length. *(Created with Biorender.com).* Briefly, upon channel opening, incoming calcium (depicted in yellow) binds to the GCaMP, triggering a conformational change that subsequently results in an increase in green fluorescence.

specificity of sensing (Chen et al., 2013). The generated variants were evaluated based on their response to both mechanical stimuli and cytosolic Ca^{2+} fluctuations that were independent of Piezo1 activity. To test their responses to mechanical

stimuli, variants were exposed to physiological levels of fluid shear stress (Malek et al., 1999) (**Fig. 26B**), which causes a Piezo1-dependent Ca^{2+} increase in HEK293T cells (Li et al., 2014). To determine the sensitivity of the variants to intracellular Ca^{2+} levels independent of Piezo1 function, the variants response to the Ca^{2+} ionophore ionomycin was tested (Zhivotovsky and Orrenius, 2011) (**Fig. 26B**). The screening results (**Fig. 26B**) showed that the fusion Piezo1-1XGSGG-GCaMP-G4 (GenEPi) fulfilled the initial requirements for a Piezo1 specific indicator and showed a robust response to the Piezo1-dependent stimuli (shear stress) (**Table. 5**). Notably, fusions of Piezo1 with GECIs of higher calcium affinity (e.g. GCaMP-G1 and GCaMP-G3) compared to the others used in the screening did not yield a specific response, confirming the initial reasoning to use low affinity GECIs. Furthermore, the duplication of the flexible linker unit (GSGG) was sufficient to abolish the specificity to Piezo1-dependend stimuli (see **Fig. 26B**, GCaMP-G4). This loss of specificity confirms the microdomain hypothesis for Piezo1 and demonstrates that the specificity of GenEPi to report Piezo1-dependent signals is the result of this design using both a flexible linker of defined length and a low calcium affinity GECI.

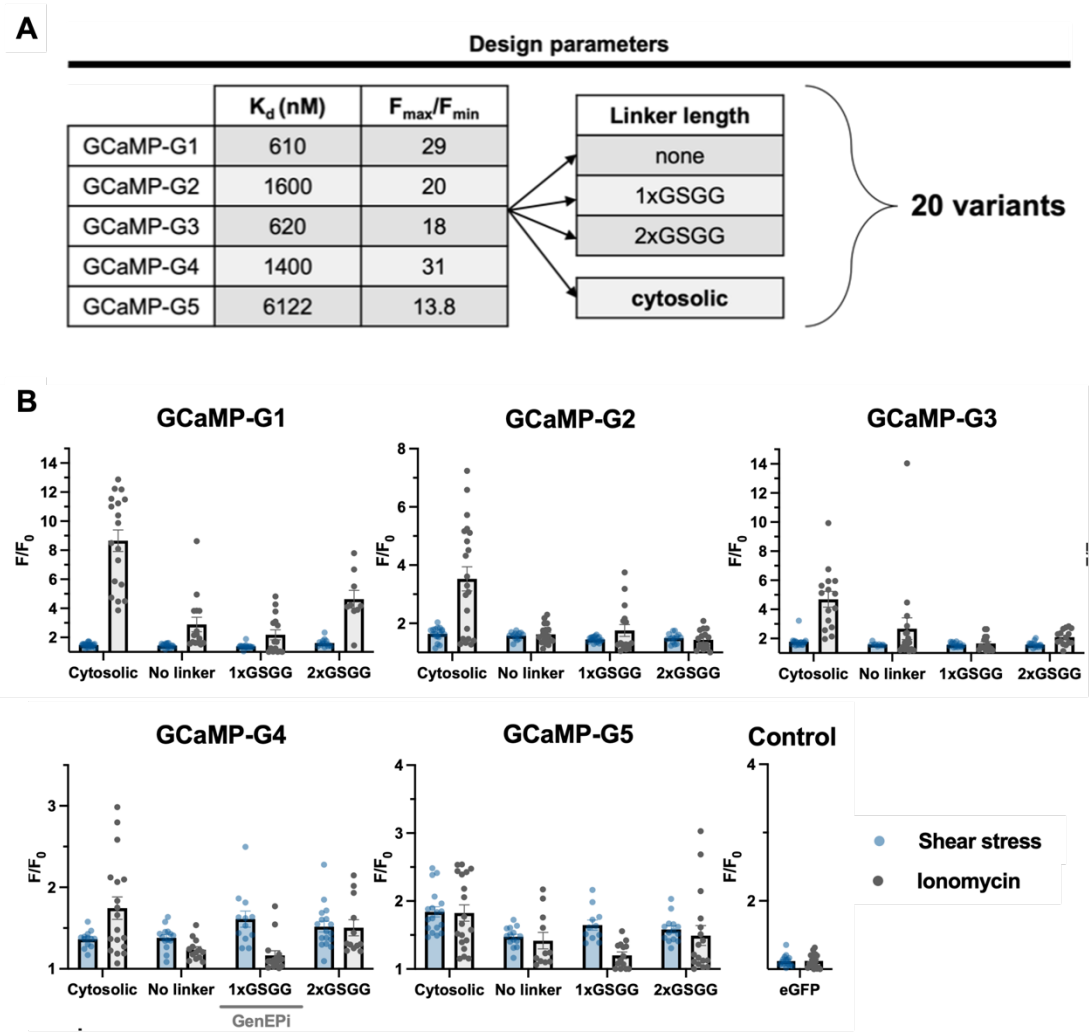


Fig. 26. Design and systematic screen to identify an optical reporter of Piezo1 activity. (A) Design of the reporter screen. Five different GCaMPs with low affinity for Ca^{2+} (GCaMP-G1 to -G5) were fused to the C-terminus of human Piezo1 without any linker, with the addition of a short linker (i.e. 1xGly-Ser-Gly-Gly (1XGSGG) linker sequence) and long linker (i.e. 2XGSGG linker sequence). (B) Results of the reporter screen. The response of the resulting 20 variants (including the co-transfected cytosolic GCaMPs and human Piezo1) to shear stress (10 dyne/cm^2, blue) and ionomycin (1 μM, black) and identified Piezo1-1XGSGG-GCaMP-G4 (GenEPi) as a specific reporter for mechanical stimuli. eGFP fused to human Piezo1 serves as a control for the noise acquired during imaging under either stimulus. Gray bars are means ± Standard error of the mean (SEM). Data from three independent experiments. *(Adapted from Yaganoglu and Kalyviotis et al.).*

Table 5. Summary of systematic screening results. The table illustrates which tested variants fulfilled the initial requirements (here: higher response to shear stress and lower response to ionomycin administration compared to the cytosolic response). The only variant which fulfilled both initial requirements was the fusion Piezo1-1XGSGG-GCaMP-G4 which is labelled with green shading. *(Adapted from Yaganoglu and Kalyviotis et al.).*

	GCaMP-G1		GCaMP-G2		GCaMP-G3	
	Shear Stress (reporter>cytosolic)	Ionomycin (reporter<cytosolic)	Shear Stress (reporter>cytosolic)	Ionomycin (reporter<cytosolic)	Shear Stress (reporter>cytosolic)	Ionomycin (reporter<cytosolic)
No linker	-	+	-	+	-	+
1XGSGG	-	+	-	+	-	+
2XGSGG	-	+	-	+	-	+

	GCaMP-G4		GCaMP-G5	
	Shear Stress (reporter>cytosolic)	Ionomycin (reporter<cytosolic)	Shear Stress (reporter>cytosolic)	Ionomycin (reporter<cytosolic)
No linker	-	+	-	-
1XGSGG	+	+	-	-
2XGSGG	+	-	-	-

2.2 Reporter characterisation

2.2.1 Electrophysiology analysis

To confirm that Piezo1 within GenEPi remains functional and that it is not affected by the C-terminal fusion, we conducted a series of patch-clamp electrophysiology experiments. The pressure-dependent responses evoked by negative pressure applied in a cell-attached recording configuration were similar for both GenEPi and wt-Piezo1 (**Fig. 27A-B**). Single channel measurements in cell-attached patches (**Fig. 27C-D**) showed that GenEPi has similar conductance values as wild-type Piezo1 (GenEPi, 25.5±0.6 pS and Piezo1, 24.9±0.8 pS), confirming that the conductivity of Piezo1 is not affected. Likewise, the channel kinetics of Piezo1 within GenEPi were preserved in response to repetitive mechanical stimulation (**Fig. 28**), the agonist Yoda1 and the generic ion channel inhibitor Ruthenium Red (RR) (**Fig. 29**). Furthermore, the electrochemical inactivation kinetic of GenEPi in response to mechanical stimuli was comparable to wild-type Piezo1 and shorter

than that of the Piezo1 delayed inactivation mutant R2456H (Zarychanski et al., 2012) (**Fig. 30**).

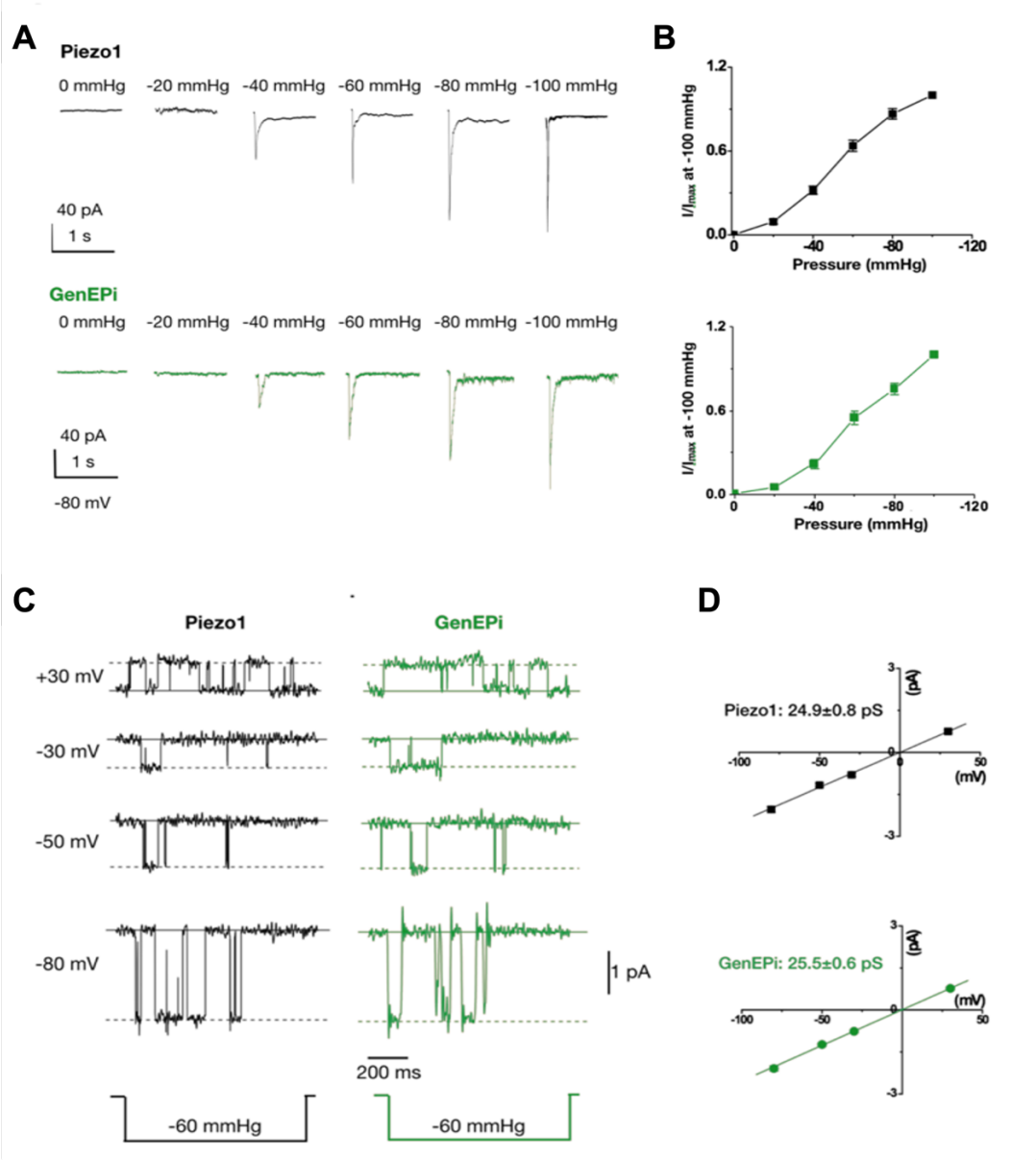


Fig. 27. Pressure-dependent responses evoked by negative pressure. (A) Representative traces of the currents from wild-type Piezo1 (black) and GenEPi (green) evoked by negative pressure of 0, -20, -40, -60, -80 and -100 mmHg at -80 mV with the cell-attached recording configuration. The current evoked by individual negative pressure was normalised to the maximum evoked by negative pressure of -100 mmHg. (B) Both wild-type Piezo1 (n=8 cells; 8 experiments) (black) and GenEPi (n=6 cells; 6 experiments) (green) show a similar pressure-dependent response. Unpaired t-test, p=0.11˃0.05, p=0.06˃0.05, p=0.20˃0.05 and p=0.07˃0.05 for pressure sensitivities to -20, -40, -60, and -80 mmHg between Piezo1 and GenEPi. (C) Representative traces of wild-type Piezo1 (black) or GenEPi (green) currents evoked by -60 mmHg pressure at different voltages of +30 mV, -30 mV, -50 mV and -80 mV. (D) The conductance value for wild-type Piezo1 (black) is 24.9±0.8 pS (n=6 cells from 6 experiments, mean ± SEM) and the conductance value for GenEPi (magenta) is 25.5±0.6 pS (n=6 cells from 6 experiments, mean ± SEM). Both channels show the typical 25 pS conductance of Piezo1 channel, indicating that ion selectivity of Piezo1 is preserved within GenEPi. *(Adapted from Yaganoglu and Kalyviotis et al.).*

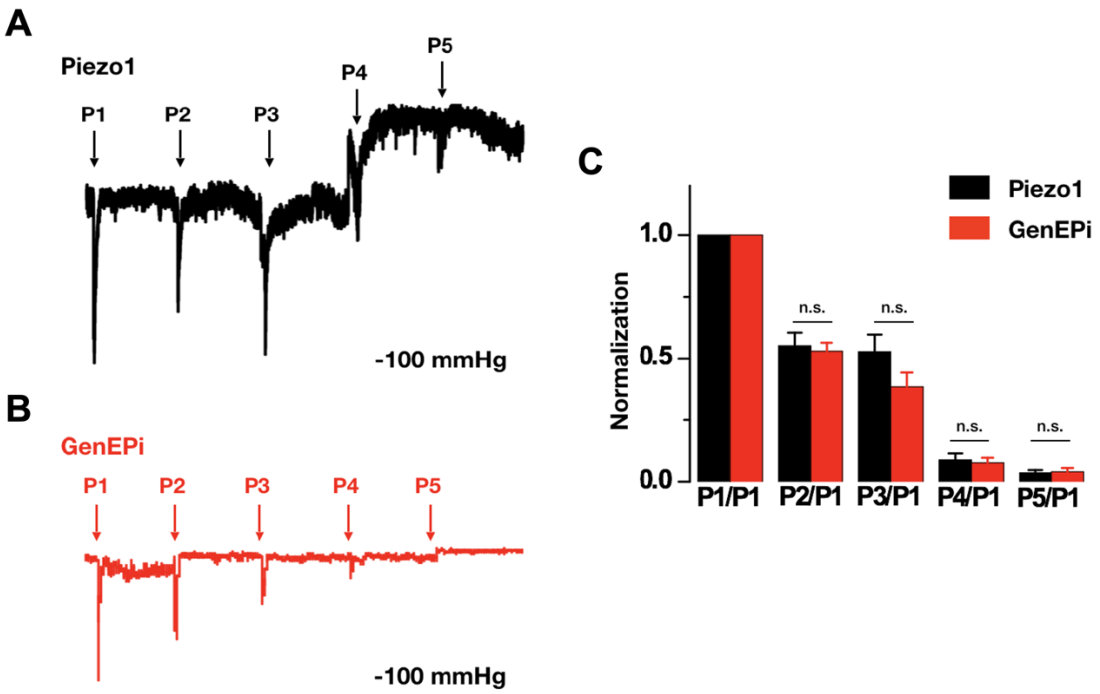


Fig. 28. The mechanosensitive response to repetitive stimulation of Piezo1 within GenEPi is similar to wild-type Piezo1. Representative traces of (A) wild-type Piezo1 and (B) GenEPi stimulated by repetitive negative pressure of -100 mmHg every 5 seconds at -80 mV with cell-attached recording configuration. (C) The peak current evoked by each negative pressure was normalised to the first one induced by the same pressure. Both wild-type Piezo1 and GenEPi show a similar response to repetitive negative pressure. Note that 5 out of 9 recordings in wild-type Piezo1 and 3 out of 9 recordings in GenEPi showed responses like the representative traces. Other recordings showed that no response was evoked by the repetitive stimuli of negative pressure after the first one. Unpaired t-test, $p=0.78>0.05$ for P2/P1, $p=0.21>0.05$ for P3/P1, $p=0.78>0.05$ for P4/P1 and $p=0.83>0.05$ for P5/P1. *(Adapted from Yaganoglu and Kalyviotis et al.).*

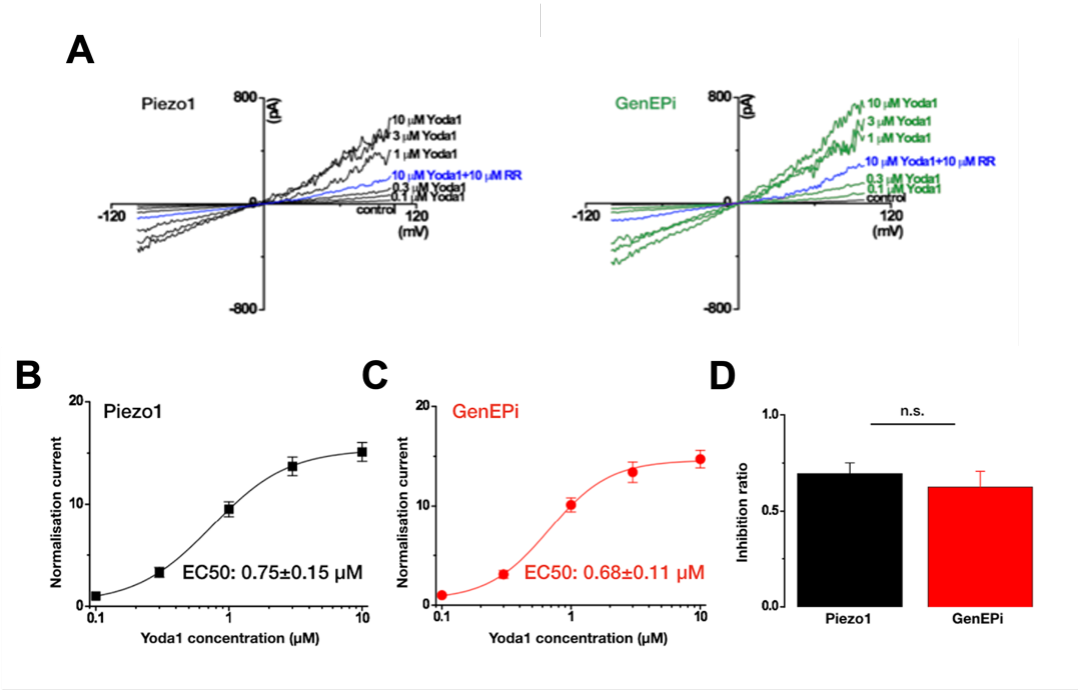


Fig. 29. The pharmacological property of Piezo1 within GenEPi does not differ from wild-type Piezo1. (A) Example traces of wild-type Piezo1 channels (black) or GenEPi (green) activated by 0.1, 0.3, 1, 3, 10 μM Yoda1 in the absence of mechanical stimulation. After the channel activities were evoked by 10 μM Yoda1, 10 μM ruthenium red (RR) was used to inhibit the currents (blue). (B) Yoda1 dose-dependent curve of wild-type Piezo1 currents shows that the EC_{50} value stays at 0.75±0.15 μM (n=6 cells from 6 experiments). (C) Dose-response curve also gives a similar EC_{50} value for GenEPi. The value is 0.68±0.11 μM (n=6 cells from 6 experiments). (D) Ratio inhibition of 10 μM ruthenium red to both wild-type Piezo and GenEPi currents induced by 10 μM Yoda1 is similar. Inhibition ratios of 10 μM ruthenium red to wild-type Piezo1 (0.70±0.06; n=4), and GenEPi (0.63±0.08; n=4) currents induced by 10 μM Yoda1 are similar without significant difference. Unpaired t-test, n.s.=p>0.05. The whole-cell currents were recorded in the absence of mechanical stimulation. *(Adapted from Yaganoglu and Kalyviotis et al.).*

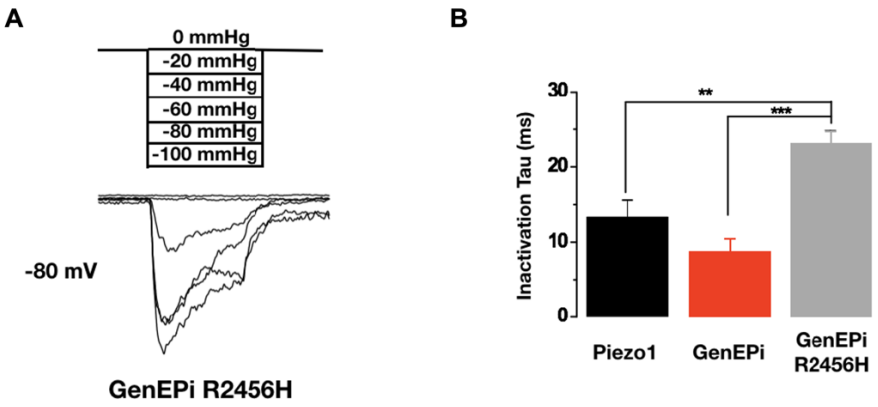


Fig. 30. The GenEPi R2456H mutant displays a delayed inactivation phenotype. (A) Representative traces of GenEPi R2456H mutant currents induced by the same negative pressures as the ones used in Fig. 27A for wild-type Piezo1 and GenEPi (-0, -20, -40, -60, -80, -100 mmHg) at -80 mV with cell-attached recording configuration. The currents have a delayed inactivation kinetics. (B) The inactivation time (Tau) of GenEPi-R2456H mutant is significantly longer than the inactivation time of either wild-type Piezo1 or GenEPi (n= 6 cells for 6 experiments each) at -60 mmHg. Unpaired t-test, **p=0.009<0.01 between Piezo1 and GenEPi R2456H, ***p=0.0002<0.001 between Piezo1 and GenEPi. *(Adapted from Yaganoglu and Kalyviotis et al.).*

2.2.2 Response to the Piezo1-specific agonist Yoda1

To confirm the functional specificity of GenEPi to optically report Piezo1-dependent activation, we tested its response to a range of concentrations of the Piezo1-specific small molecule agonist Yoda1 (Syeda et al., 2015). Briefly, to achieve high SNR and minimise overexpression effects, we transiently expressed GenEPi in HeLa cells using the dox-inducible XLGenEPi plasmid (see **Materials and Methods**) and subsequently exposed them to 5μM, 10μM, 25μM and 50μM of Yoda1. As shown in **Fig. 31**, GenEPi fluorescence significantly increased in response to all different Yoda1 concentrations tested, while fitting of the data with a simple linear regression model showed corelation of the GenEPi response to the Yoda1 regime used. Hence, we confirm that GenEPi responds to the Piezo1-specific agonist Yoda1 in a dose-dependent manner, which we attribute to progressive activation of more ion channels in individual cells.

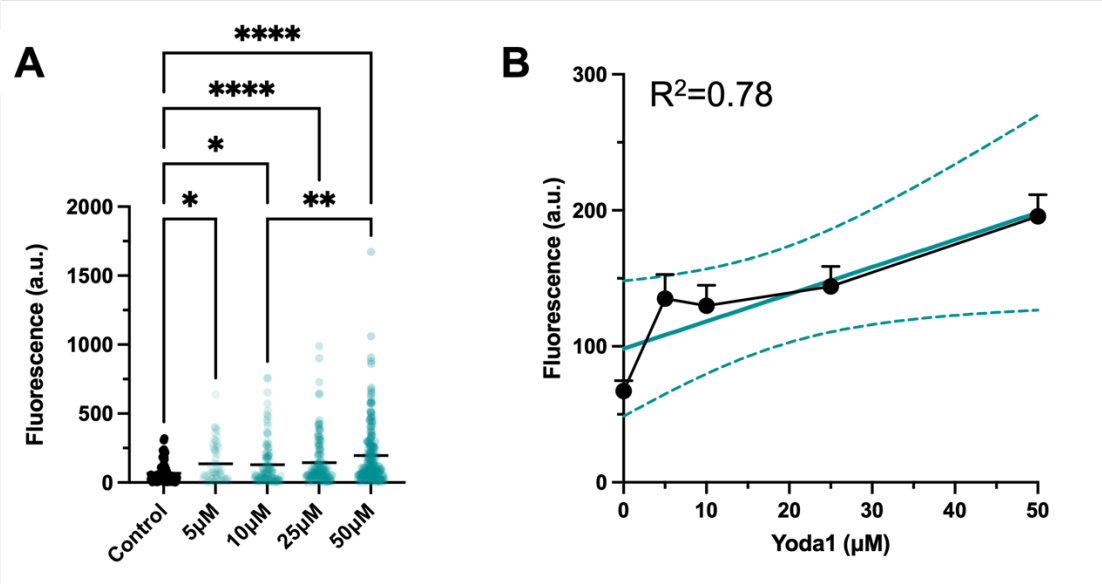


Fig. 31. GenEPi responds to the Piezo1-specific agonist Yoda1. (A) Response of GenEPi expressing HeLa cells to a range of Yoda1 concentrations: 5μM (n=62), 10μM (n=115), 25μM (n=137) and 50μM (n=197) or DMSO (control) (n=100). Kruskal-Wallis test. (B) GenEPi optical response to Yoda1 strongly correlates with the concentration of Yoda1. Simple linear regression model (solid green line) fitted on the means of each condition. 95% confidence interval (CI) shown as dashed lines, error bars: SEM. R^2=0.7798. *(Adapted from Yaganoglu and Kalyviotis et al.).*

2.2.3 Chelation of extracellular calcium with EGTA

To further confirm the specificity of GenEPi response, we chelated extracellular calcium with EGTA as previously described by Syeda et al. (Syeda et al., 2015). We reasoned that chelation of extracellular calcium will not elicit any GenEPi response as no calcium would flow through the channel. HeLa cells transiently expressing GenEPi using the dox-inducible XLGenEPi plasmid were exposed to 10μM Yoda1 (positive control), 2mM of EGTA and a combination of 2mM EGTA and 10μM Yoda1. As expected and shown in **Fig. 32**, GenEPi fluorescence significantly increased in response to the Yoda1 treatment (Yoda1), whereas chelation of extracellular calcium did not increase GenEPi fluorescence both in absence (EGTA) and presence of Yoda1 (Yoda1+EGTA). Notably, the chelation of the extracellular calcium did not affect the baseline fluorescence of GenEPi which is shown by the non-significant change of the fluorescence between the control and the EGTA containing treatment groups (**Fig. 32**). Altogether, we demonstrate that GenEPi shows a Piezo1 specific response which is affected by extracellular calcium chelation, confirming that its fluorescence increase is due to the calcium flow upon Piezo1 channel opening.

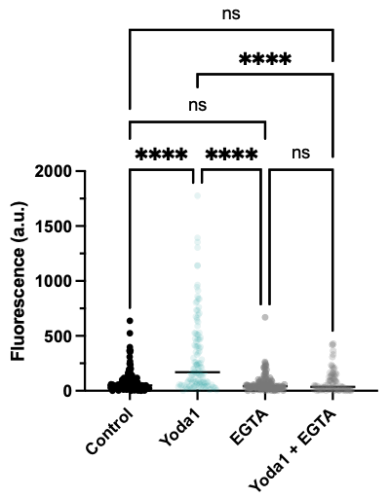


Fig. 32. GenEPi shows Piezo1-specific response that critically depends on extracellular calcium influx which can be abolished by extracellular calcium chelation. Response of GenEPi expressing HeLa cells to 10μM Yoda1 (n=124), 2mM EGTA (n=129) and 2mM EGTA and 10μM Yoda1 (n=82) or DMSO (control) (n=134). Kruskal-Wallis test. *(Adapted from Yaganoglu and Kalyviotis et al.).*

2.2.4 Loss-of-function mutagenesis of GenEPi

As mentioned before, loss-of-function missense mutations of Piezo1 have been linked to several diseases, such as generalised lymphatic dysplasia (Lukacs et al., 2015, Fotiou et al., 2015) and bicuspid aortic valve (Faucherre et al., 2020). Recently, the loss-of-function S217L (Serine 217 to Leucine) missense mutation of Piezo1 has been shown to exhibit reduced plasma membrane trafficking, reduced stability and higher ubiquitination compared to wt-Piezo1, which cannot be rescued by proteasome inhibition (Zhou et al., 2021).

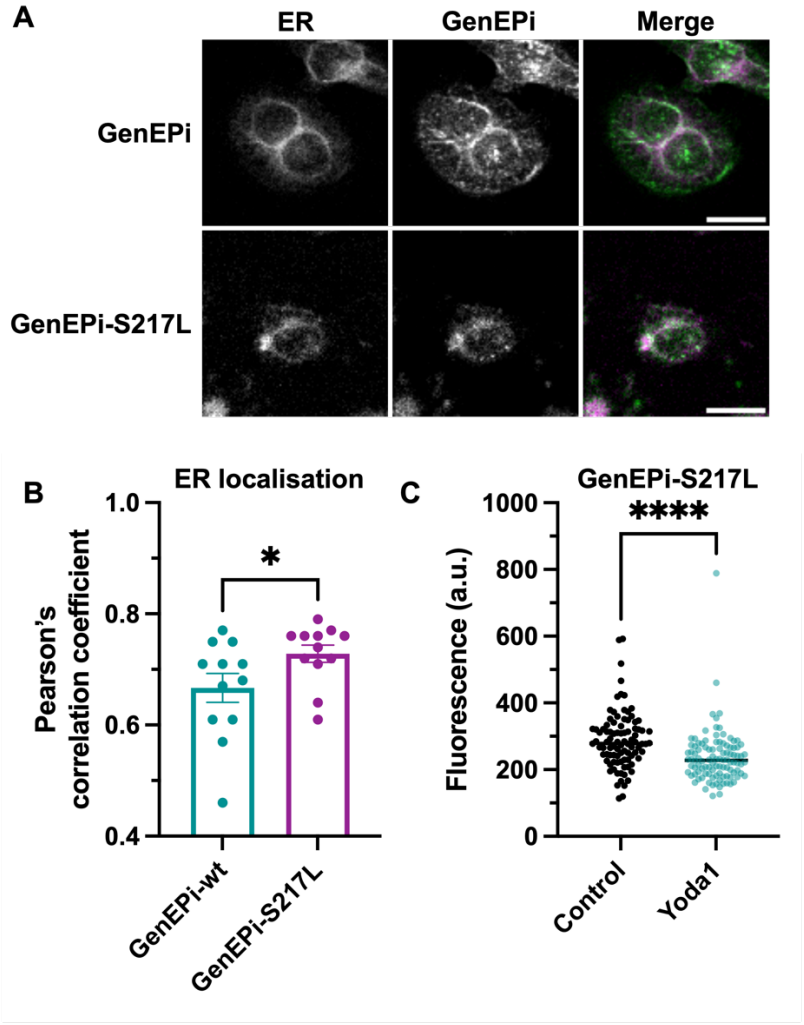


Fig. 33. GenEPi-S217L variant shows altered subcellular localisation and does not respond to Yoda1. (A) Representative images of HeLa cells expressing GenEPi or GenEPi-S217L stained with ER-tracker to visualise ER and anti-GFP to visualise GenEPi. Scale bar, 20μM. (B) Summary data showing the overlap of GenEPi (wt- or S217L) and the ER signal indicated by Pearson's correlation coefficient. (n=12 for each). Mann-Whitney test. (C) Response of GenEPi-S217L expressing HeLa cells to 10μM Yoda1 (n=104) or DMSO (control) (n=92). Mann-Whitney test. *(Adapted from Yaganoglu and Kalyviotis et al.).*

To further test the functionality of GenEPi and confirm that it can recapitulate Piezo1 disease conditions, we used site-directed mutagenesis to generate a GenEPi-S217L variant. As it has been previously shown that S217L mutants exhibit reduced membrane localisation and are mainly localised to the endoplasmic reticulum (ER), we tested whether the GenEPi-S217L mutant exhibits similar subcellular localisation. As shown in **Fig. 33**, non-mutated GenEPi localises both in the plasma membrane and the ER reflecting the subcellular localisation of wt-Piezo1, whereas GenEPi-S217L co-localises almost exclusively with the ER tracker. In addition, GenEPi-S217L does not respond to treatment with 10μM of Yoda1, yet surprisingly shows a significant decrease in its fluorescence. Overall, we demonstrate that GenEPi reflects the subcellular localisation of wt-Piezo1 and can recapitulate Piezo1 disease conditions which are linked to loss-of-function mutations.

In conclusion, our *in vitro* characterisation demonstrates that GenEPi provides high spatiotemporal resolution and functional specificity of Piezo1-dependent activity without compromising the nature and functionality of the channel.

2.3 Analysis of transient, local mechanical stimuli on the membrane of cells

After the characterisation under controlled experimental conditions (**Fig. 27-33)**, we tested whether GenEPi can visualise Piezo1-dependent activity during autonomous cellular processes, such as local cellular traction forces, using Total Internal Reflection Fluorescence Microscopy (TIRFM) (Ellefsen et al., 2019, Holt et al., 2021, Ridone et al., 2020).

2.3.1 Localisation of GenEPi on the cell membrane using TIRFM

First, we tested the ability of GenEPi to resolve the localisation dynamics of Piezo1 on the cell membrane of different cell types that transiently expressed GenEPi using the dox-inducible XLGenEPi plasmid (**Fig. 34**). After doxycycline induction to

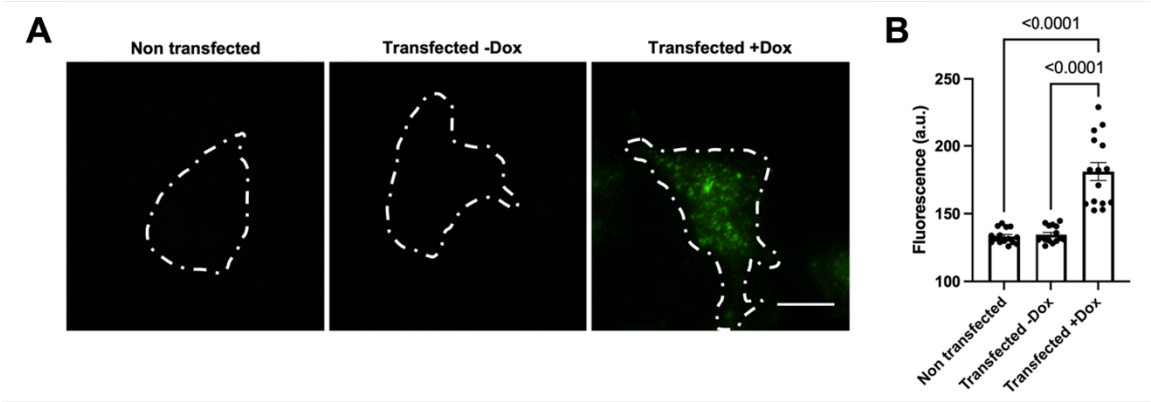


Fig. 34. Doxycycline induction of GenEPi expression on the membrane of XLGenEPi transfected HEK293T cells used for TIRFM imaging. (A) Representative TIRFM images of non-transfected, XLGenEPi transfected without doxycycline induction and XLGenEPi transfected with doxycycline induction HEK293T cells. Scale bar, 10μm. (B) Doxycycline induction leads to increased GenEPi expression and SNR. Whole cell fluorescence of n=15 cells, error bar: SEM. Ordinary one-way ANOVA test. *(Adapted from Yaganoglu and Kalyviotis et al.).*

temporally control the expression of the sensor, GenEPi was evenly distributed over the ventral surface of HEK293T, HFF and HeLa cells (**Fig. 35A**) reflecting the previously reported wt-Piezo1 membrane localisation in cells (Ellefsen et al., 2019, Holt et al., 2021, Ridone et al., 2020) (**Fig. 33A**). The number of GenEPi clusters per cell (**Fig. 35B**) was similar among the different cell types. Likewise, the area (**Fig. 35C**) and perimeter (**Fig. 35E**) of individual GenEPi clusters and their size distributions (**Fig. 35D, 35F**) did not differ between the cell lines, demonstrating that transient expression of GenEPi provides consistent localisation dynamics in different cellular contexts.

2.3.2 Membrane diffusivity analysis of GenEPi

As wild-type Piezo1 has been previously shown to readily diffuse in the cell membrane (Ellefsen et al., 2019, Holt et al., 2021, Ridone et al., 2020), we tested whether GenEPi shows similar dynamics. Time-lapse TIRFM imaging revealed that individual GenEPi clusters were mobile in the plasma membrane (**Fig. 36A**). To obtain apparent diffusion coefficients, we tracked GenEPi in the plasma membrane to build trajectories of individual clusters (**Fig. 36A**)

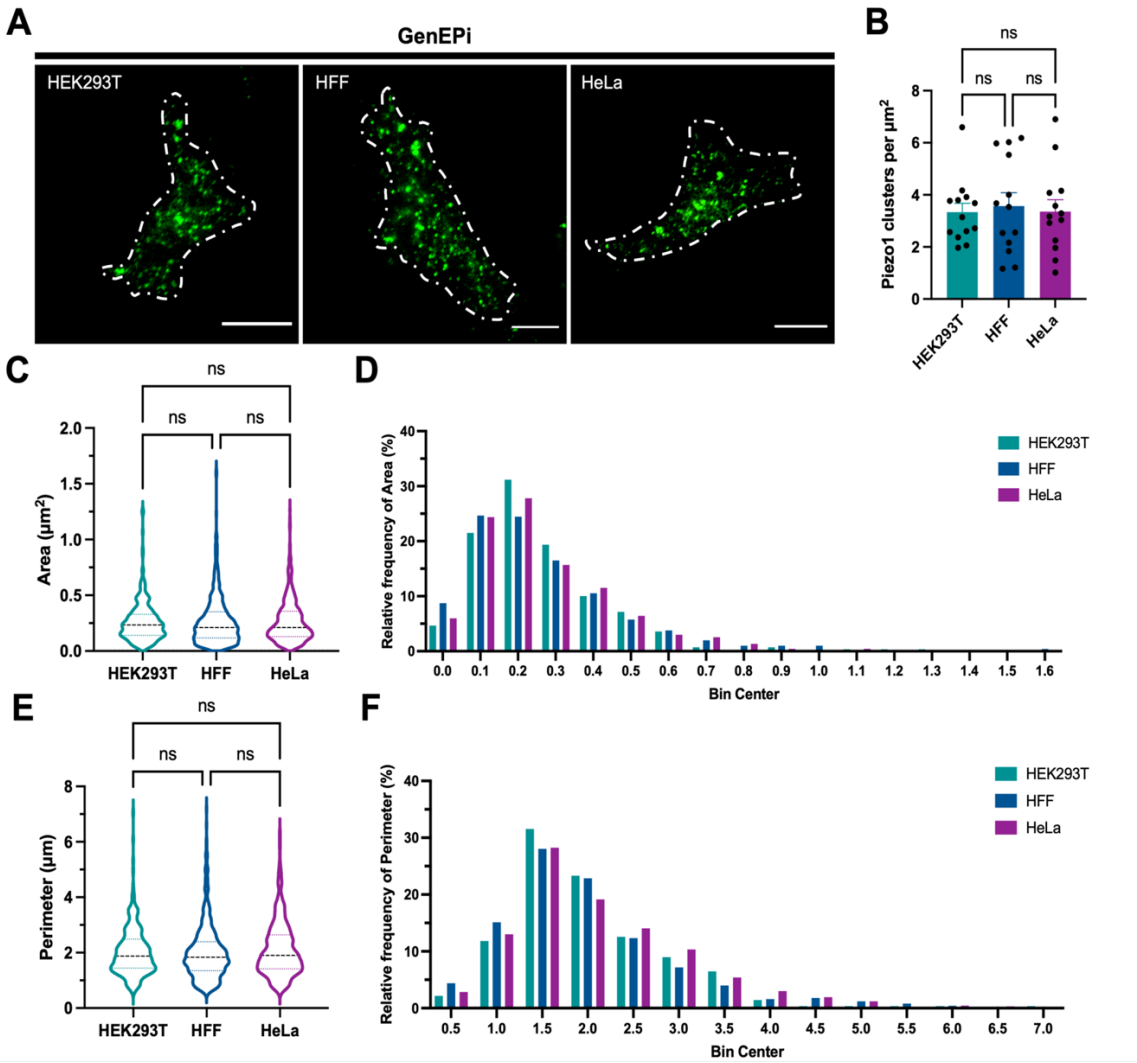


Fig. 35. GenEPi is evenly distributed over the ventral surface of different cell types. (A) Representative TIRFM images from the cell-substrate interface of live HEK293T, HFF and HeLa cells expressing GenEPi. Scale bar, 10µm. (B) Number of GenEPi clusters per cell in HEK293T, HFF and HeLa cells expressing GenEPi. n=13 cells, error bar: SEM. Ordinary one-way ANOVA test. (C-F) Quantification of GenEPi cluster area and perimeter as violin plots and their distributions in HEK293T, HFF and HeLa cells expressing GenEPi. HEK293T cells (n=279), HFF cells (n=503), HeLa cells (n=669); n=1 represents a single GenEPi (Piezo1) cluster. Kruskal-Wallis test. *(Adapted from Yaganoglu and Kalyviotis et al.).*

and plotted the Mean-Squared Displacement (MSD) of 5332 GenEPi tracks (**Fig. 36B**). The slope of the MSD yielded an apparent two-dimensional (2D) diffusion coefficient of ~0.005 µm^2/s, which is in the range of previously reported values for wild-type Piezo1 (Ellefsen et al., 2019, Holt et al., 2021, Ridone et al., 2020).

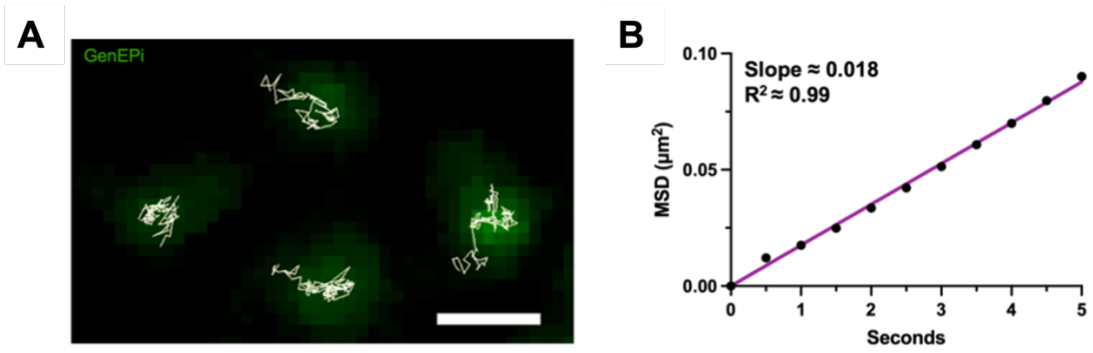


Fig. 36. GenEPi reflects the membrane diffusion of wt-Piezo1. (A) Tracking of GenEPi clusters imaged at 10 frames per second in live HEK293T cells reveals motility of the channel clusters. The background image shows fluorescence of GenEPi clusters captured during a single imaging frame (rectangular region with dashed line in image 37, 2-pixel median filter applied in FiJi/ImageJ (see Materials and Methods, Image processing and analysis). White lines depict the tracks of these clusters over several successive frames. Scale bar, 1μm. (B) Mean-squared displacement calculated from 5332 GenEPi tracks plotted as a function of time. Data fit to a straight line with a slope corresponding to a two-dimensional (2D) diffusion coefficient of 0.0044 $\mu m^2/s$. R^2 for linear fit to data is 0.9969. *(Adapted from Yaganoglu and Kalyviotis et al.).*

2.3.3 Activity of GenEPi clusters on the cell membrane

Piezo1 function has been reported to be related to autonomous cell processes in the absence of externally applied mechanical forces, such as local cellular traction forces (Ellefsen et al., 2019). Indeed, we observed distinguishable GenEPi responses over the ventral surface of the cells (**Fig. 37A**), with almost 50% of the clusters demonstrating a dynamic behaviour and activation. Notably, some of the GenEPi responses lasted for several seconds (**Fig. 37B-D)** and we reasoned that they could be the source of previously reported Piezo1-dependent calcium flickers (Ellefsen et al., 2019, Pathak et al., 2014). Taken together, GenEPi robustly reports diffusion dynamics comparable to wild-type Piezo1 channels and captures Piezo1-dependent activity to transient, local mechanical stimuli on the membrane of the cells.

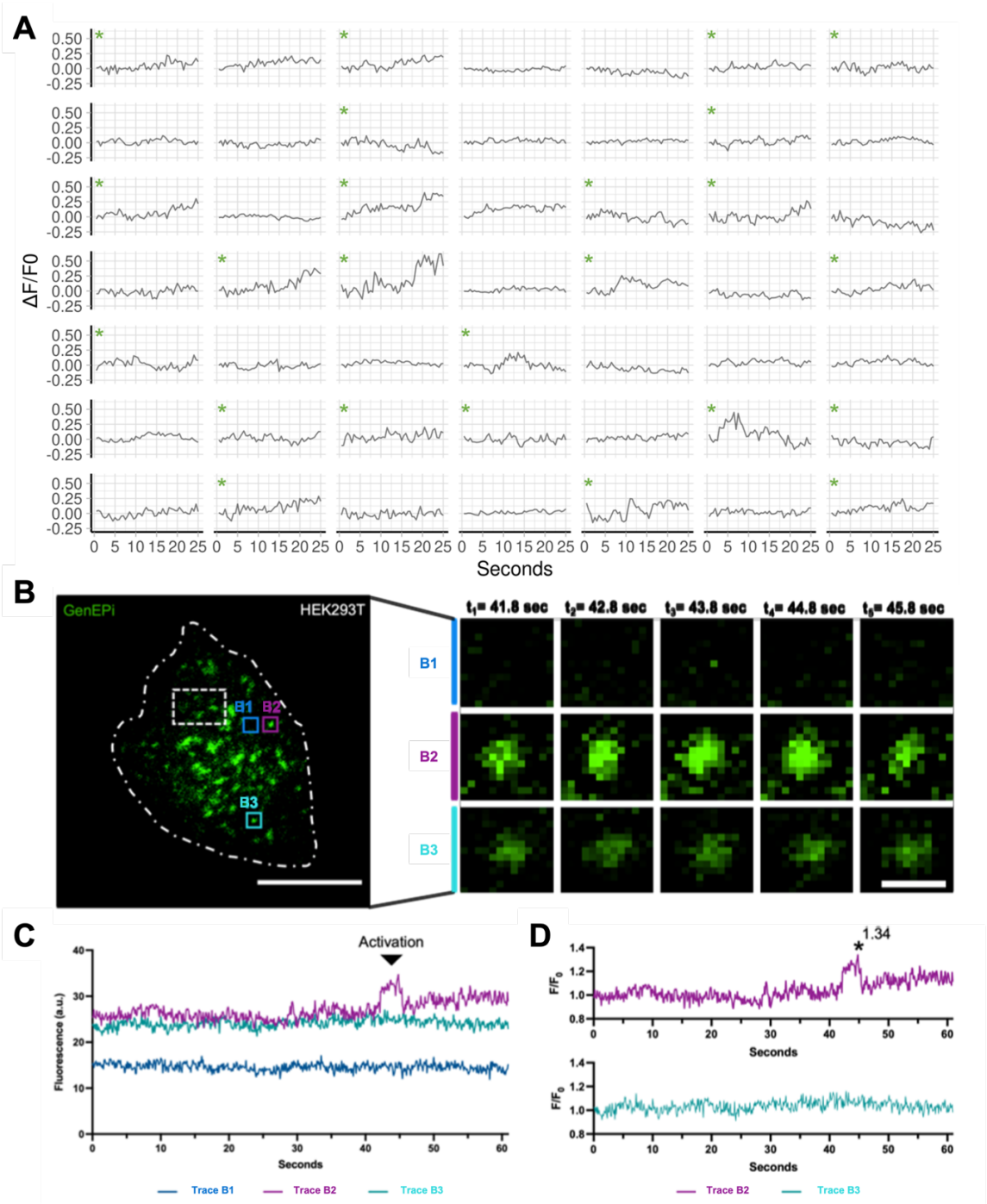


Fig. 37. GenEPi captures Piezo1-dependent activity to transient, local mechanical stimuli on the cell membrane. (A) GenEPi responses ($\Delta F/F_0$) of 49 individual clusters over the ventral surface of the HEK293T cell presented in Fig. 37B captured using TIRFM imaging. Clusters which showed distinguishable responses are labelled with green stars. Data were plotted in PlotTwist (Shiny apps). (B) Representative time-lapse images of GenEPi cluster dynamics in a single HEK293T cell expressing GenEPi. (B1-B3) (B1) Region without GenEPi cluster adjacent to a GenEPi cluster. (B2) Region with a GenEPi cluster which shows dynamic behaviour and changes in fluorescence. (B3) Region with a GenEPi cluster which does not show dynamic behaviour. Scale bars, 10μm and 1μm, respectively. (C) Raw values of fluorescence intensity profiles of the ROIs B1-B3 (Trace B1, Trace B2 and Trace B3) which show different GenEPi activity dynamics. (D) Fluorescence intensity profiles (F/F_0) of the ROIs B1-B3 which illustrate the different GenEPi activity dynamics. *(Adapted from Yaganoglu and Kalyviotis et al.).*

2.4 Analysis of contraction-triggered mechanical stimulation in microtissues

2.4.1 GenEPi response during cardiac contraction in 3D microtissues

To test the functional specificity and performance of GenEPi in an *in vitro* three-dimensional (3D), multicellular environment, we tested its response to homeostatic cell motions, such as cardiomyocyte contraction where Piezo1 has been shown to act as a key mechanotransducer (Jiang et al., 2021a). To this end, we generated dox-inducible GenEPi mouse embryonic stem cells (mESCs) (Iacovino et al., 2011) and differentiated these cells to cardiomyocytes (Wang et al., 2011). After 10 days of differentiation, regular beating patches of cells could be identified in microtissues. After transient induction of GenEPi expression, we observed cells that displayed noticeable GenEPi responses due to contraction-triggered mechanical stimulation within beating patches. Differentiated microtissues with multiple beating patches caused a robust systemic activation of GenEPi in response to the autonomous regular contraction of cardiomyocytes (**Fig. 38A**). Notably, in dissected microtissue, where single cells were attached to autonomously beating cardiomyocytes, GenEPi responses were restricted to places of local membrane displacement (**Fig. 38B-C**). In both conditions, the sub-second responses were qualitatively coupled to the autonomous regular beating of the cardiomyocytes (**Fig. 38B, 38D)**.

2.4.2 Chemical modulation of cardiac contraction

In order to confirm that the source of GenEPi responses were indeed cardiomyocyte contractions, we applied blebbistatin, a myosin inhibitor, which blocks the contractions and uncouples mechanical stimuli-induced Ca^{2+} influx from Ca^{2+} processes accompanying spontaneous cell contractions (Farman et al., 2008). Fast GenEPi responses decreased when contractions stopped in response to blebbistatin (**Fig. 39A**), confirming cardiomyocyte contractions as the source of GenEPi signals.

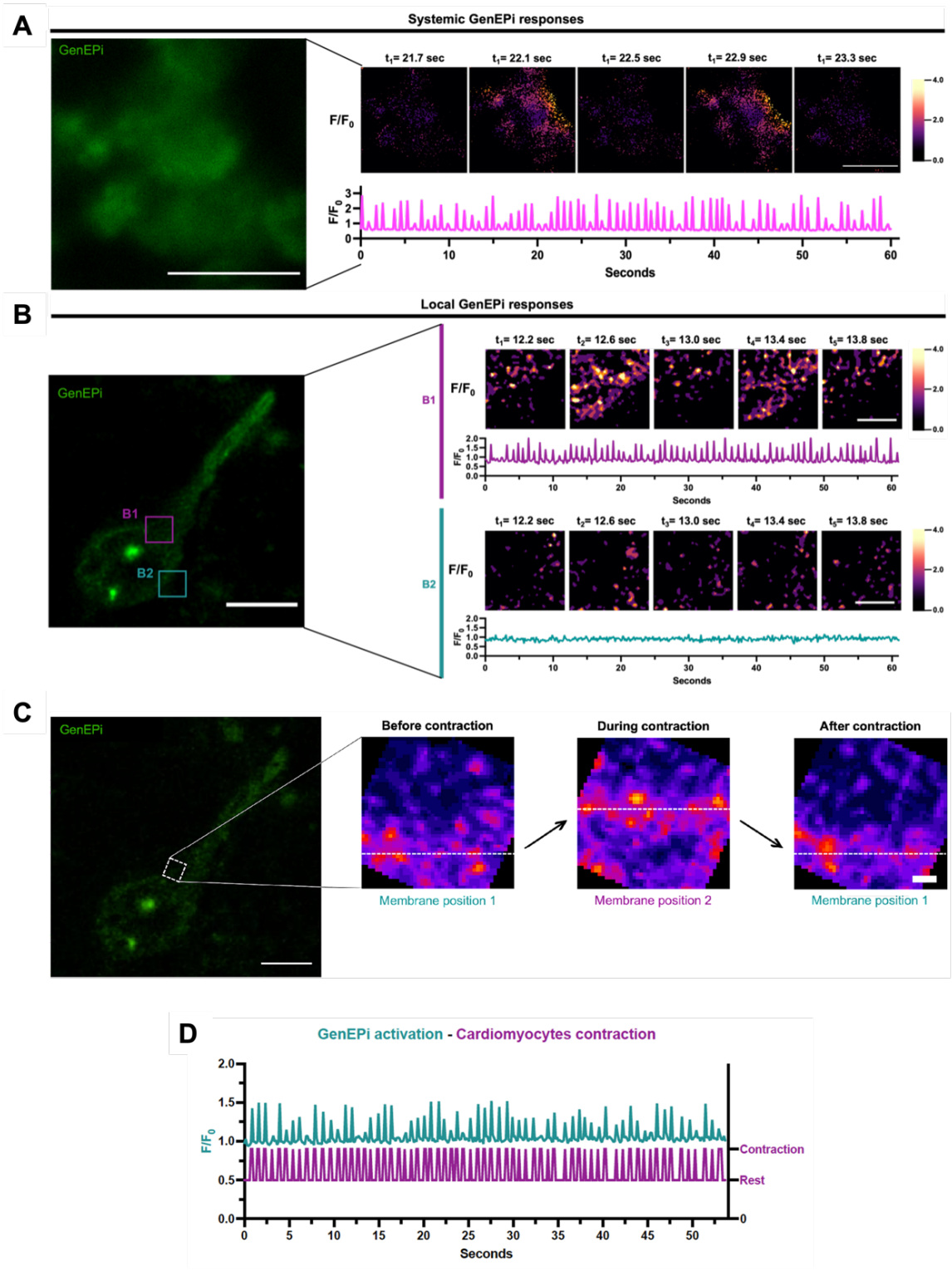


Fig. 38. GenEPi reports cardiomyocyte contraction-triggered mechanical stimulation with high spatiotemporal resolution. (A) Multicellular and systemic activation of GenEPi in response to autonomous contraction of cardiomyocytes in differentiated tissue within multiple beating patches. Representative time-lapse fluorescence intensity (F/F_0) images and profile of multiple responding cells embedded in the differentiated tissue of beating cardiomyocyte patches. Scale bar, 10 µm. (B) Single cell local responses of GenEPi in a dissected beating patch in response to the autonomous beating of cardiomyocytes. (B1, B2) Representative time-lapse fluorescence intensity (F/F_0) images and profiles of a responding (B1) and a non-responding (B2) ROI in a single cell attached to the beating cardiomyocyte patch. Scale bar, 5 µm. (C) GenEPi is activated in response to the contraction of autonomously beating cardiomyocytes which cause local

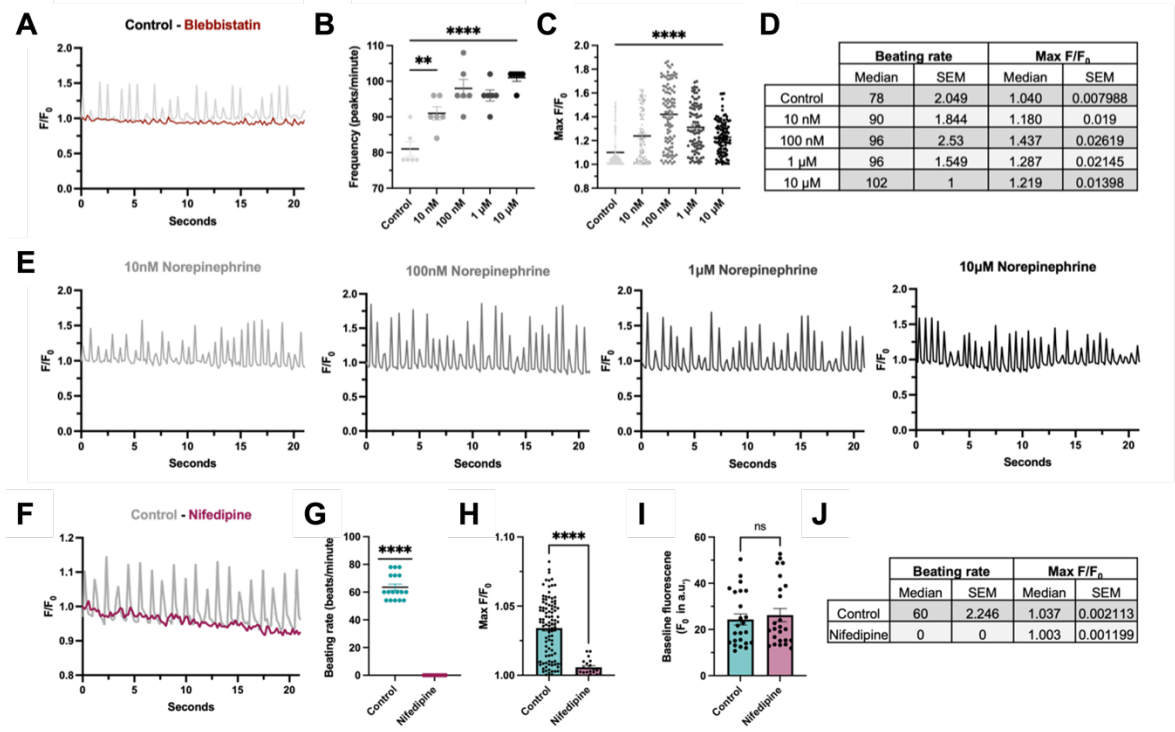
membrane displacement. In the "Before contraction" and "After contraction" frames the membrane is in "Membrane position 1", while during the contraction the membrane of the GenEPi expressing cell is displaced upwards by 1 µm to "Membrane position 2". Scale bars, 5 µm (left image) and µm (right panel). (D) Representative fluorescence intensity (F/F_0) profile (teal line) of GenEPi activation in response to cardiomyocyte contraction (purple line). Cardiomyocyte contraction was captured by changes in the intensity profile of the brightfield image due to cell movement. Data were transformed to a binary response with a minimum of 0.5 (rest) and maximum of 0.9 (contraction) for illustration purposes. GenEPi is activated in response to mechanical stimuli and membrane deformations due to the contraction of autonomously beating cardiomyocytes. *(Adapted from Yaganoglu and Kalyviotis et al.)*.

To complement our analysis, we tested the ability of GenEPi to respond and resolve higher frequency cardiomyocytes contractions. To this end, we employed norepinephrine, a ligand which activates adrenoreceptor signals and increases the contraction rate in cardiomyocytes (Wang et al., 2008). We indeed observed a significant increase in the frequency and the amplitude of GenEPi responses in proportion to the norepinephrine regime (10 nM to 10 µM) (**Fig. 39B-E**), validating the ability of GenEPi to temporally resolve cardiomyocyte contractions.

Additionally, to further demonstrate that other channels, such as L-type channels, do not contribute to the response of GenEPi, we treated differentiated beating cardiac microtissues with nifedipine which is known to block most L-type channels and has a strong negative ionotropic effect (Brixius et al., 2005, Mannhardt et al., 2017, Xi et al., 2010). Indeed, nifedipine treatment abolished the beating of cardiomyocytes within the differentiated cardiac microtissues, suggesting that L-type channels were effectively blocked (**Fig. 39F-H**). Yet, the baseline fluorescence of the GenEPi-expressing cells (**Fig. 39I-J**) was not affected by this blockade, indicating that other calcium channels, such as L-types channels, do not affect the Piezo1-dependent functional readout of GenEPi.

Overall, GenEPi shows high spatiotemporal resolution of Piezo1-dependent activity in both dissected and non-dissected microtissues, capable of specifically sensing

spontaneous as well as drug stimulated repetitive mechanical stimuli of beating cardiomyocytes.



	Beating rate		Max F/F_0	
	Median	SEM	Median	SEM
Control	78	2.049	1.040	0.007988
10 nM	90	1.844	1.180	0.019
100 nM	96	2.53	1.437	0.02619
1 µM	96	1.549	1.287	0.02145
10 µM	102	1	1.219	0.01398

	Beating rate		Max F/F_0	
	Median	SEM	Median	SEM
Control	60	2.246	1.037	0.002113
Nifedipine	0	0	1.003	0.001199

Fig. 39. GenEPi responses are triggered by the contraction of the beating cardiomyocytes within the differentiated microtissues. (A) Representative fluorescence intensity (F/F_0) profile from a ROI with systemic activation of GenEPi in response to cardiomyocyte contraction before (control) and after the addition of 100 µM blebbistatin, which shows that GenEPi responses are abolished. (B) Frequency of peaks, (C) amplitude of fluorescence intensity (F/F_0) changes and (D) median ± SEM values of B and C before (control) and after the addition of norepinephrine (range of concentrations, 10 nM-10 µM). n=6 ROIs, error bar: SEM. Ordinary one-way ANOVA and Kruskal-Wallis test, respectively. Data from three independent experiments. (E) Representative fluorescence intensity (F/F_0) profiles from a ROI with GenEPi activation in response to cardiomyocyte contraction after the addition of norepinephrine (range of concentrations, 10 nm-10 µM). (F) Representative fluorescence intensity (F/F_0) profile from a ROI with systemic activation of GenEPi in response to cardiomyocyte contraction before (control) and after the addition of 100 nM nifedipine. (G) Beating rate of cardiac microtissues before and after the addition of 100 nM nifedipine which abolishes the contraction of the beating cardiomyocytes. n=17 measurements from 3 independent biological replicates, error bar: SEM. Wilcoxon rank-sum test. (H) Amplitude of fluorescence intensity (F/F_0) changes before (control) and after the addition of 100 nM nifedipine. n=101 and n=20 measurements for control and nifedipine treatments, respectively, from 3 individual biological replicates, error bar: SEM. Two-tailed Mann-Whitney test. (I) Baseline fluorescence (F_0) before and after the addition of 100 nM nifedipine. n=24 ROIs containing multiple cells for each condition from 3 individual biological replicates, error bars: SEM. Two-tailed Mann-Whitney test. (J) Median ± SEM values of G and H before (control) and after the addition of 100 nM nifedipine. *(Adapted from Yaganoglu and Kalyviotis et al.).*

2.5 Monitoring pharmacological modulation of Piezo1-dependent activity in vivo

2.5.1 A zebrafish transgenic system to study Piezo1 in vivo using GenEPi

There is an increasing body of work that has revealed Piezo1's central role in mediating mechanosensation in a plethora of physiological and pathological conditions **(Table 3)**. Thus, visualising its activity *in vivo* will allow for understanding Piezo1's role in the interplay of mechanical and biochemical signals in development and disease (Hannezo and Heisenberg, 2019).

To investigate the ability of GenEPi to report Piezo1-dependent activity in the context of a whole organism, we generated a zebrafish transgenic line that allows for conditional manipulation of GenEPi expression using the zebrafish heat-shock promoter hsp70-l (Halloran et al., 2000) (**Fig. 40A,** see **Materials and Methods, Molecular cloning**). We reasoned that the transparency of zebrafish embryos combined with the direct optical readout of GenEPi would enable monitoring Piezo1-dependent activity of single-cells in the tissues, organs and organ systems within the organism. GenEPi expression was induced following heat-shock of *Tg(hsp70:GenEPi)* zebrafish for one hour at 37.5°C (**Fig. 40B**). Compared to non-heat-shocked embryos, GenEPi expression was systemic and reached a steady fluorescence state at ~4-5 hours post-heat-shock (**Fig. 40C-E and Fig. 41**). Like previous *in vitro* results (**Fig. 33**), GenEPi signal was mainly localized on the plasma membrane of different cell types, such as endocardium cells, neural retina cells and keratinocytes (**Fig. 40F and Fig. 42**). The temporal induction of systemic expression of GenEPi did not affect the development of embryos to adulthood and the heart rate of individual embryos did not differ in comparison to control non-heat-shocked embryos when the latter recovered from the heat-shock process (**Fig. 43**).

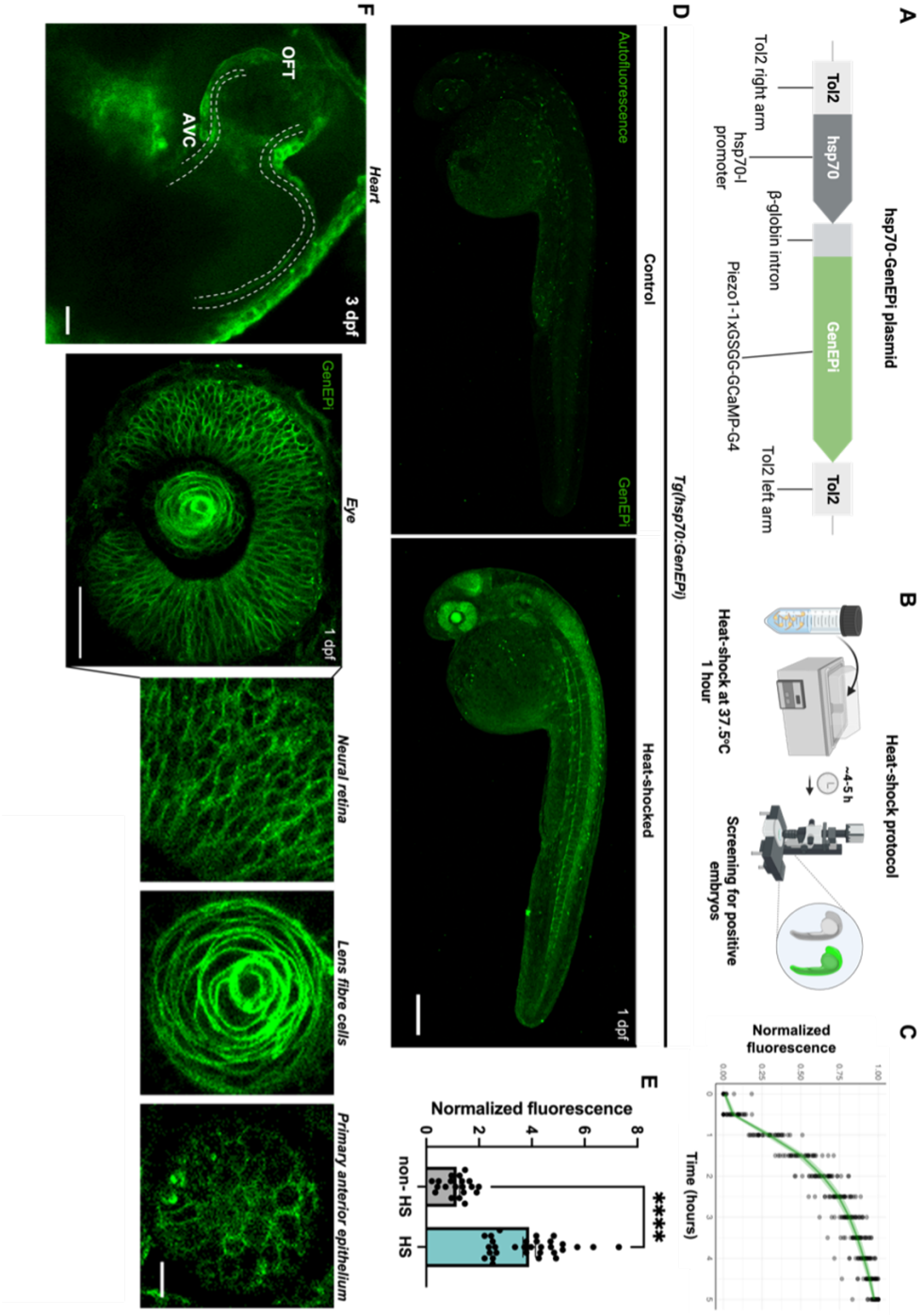


Fig. 40. A zebrafish transgenic model for temporal control of GenEPi expression *in vivo*. (A) Schematic of the pTol2-hsp70:GenEPi plasmid used for the zebrafish transgenesis. GenEPi is downstream of the zebrafish hsp70-l promoter after the β-globin rabbit intron. (B) Schematic of the heat-shock protocol used to induce the expression of GenEPi in *Tg(hsp70:GenEPi)* zebrafish. (C) Longitudinal analysis of GenEPi expression upon heat-shock of *Tg(hsp70:GenEPi)* zebrafish at 1 day post fertilization (dpf), fluorescence steady state is reached after ~4-5 hours. n=35 fish. (D) Representative fluorescence of a non- (non-HS) and heat-shocked (HS) *Tg(hsp70:GenEPi)* zebrafish at 1 dpf. Scale bar, 200 µm. (E) Increase in fluorescence intensity following the heat-shock protocol in B. (n=20 and n=31 non-heat-shocked (non-HS) and heat-shocked (HS) fish, respectively). (F) GenEPi expression in the developing heart, eye, neural retina, lens fibre cells and primary anterior epithelium in a 3 and 1dpf *Tg(hsp70:GenEPi)* zebrafish. Scale bar, 20 µm, 200 µm and 20 µm respectively. *(Adapted from Yaganoglu and Kalyviotis et al.).*

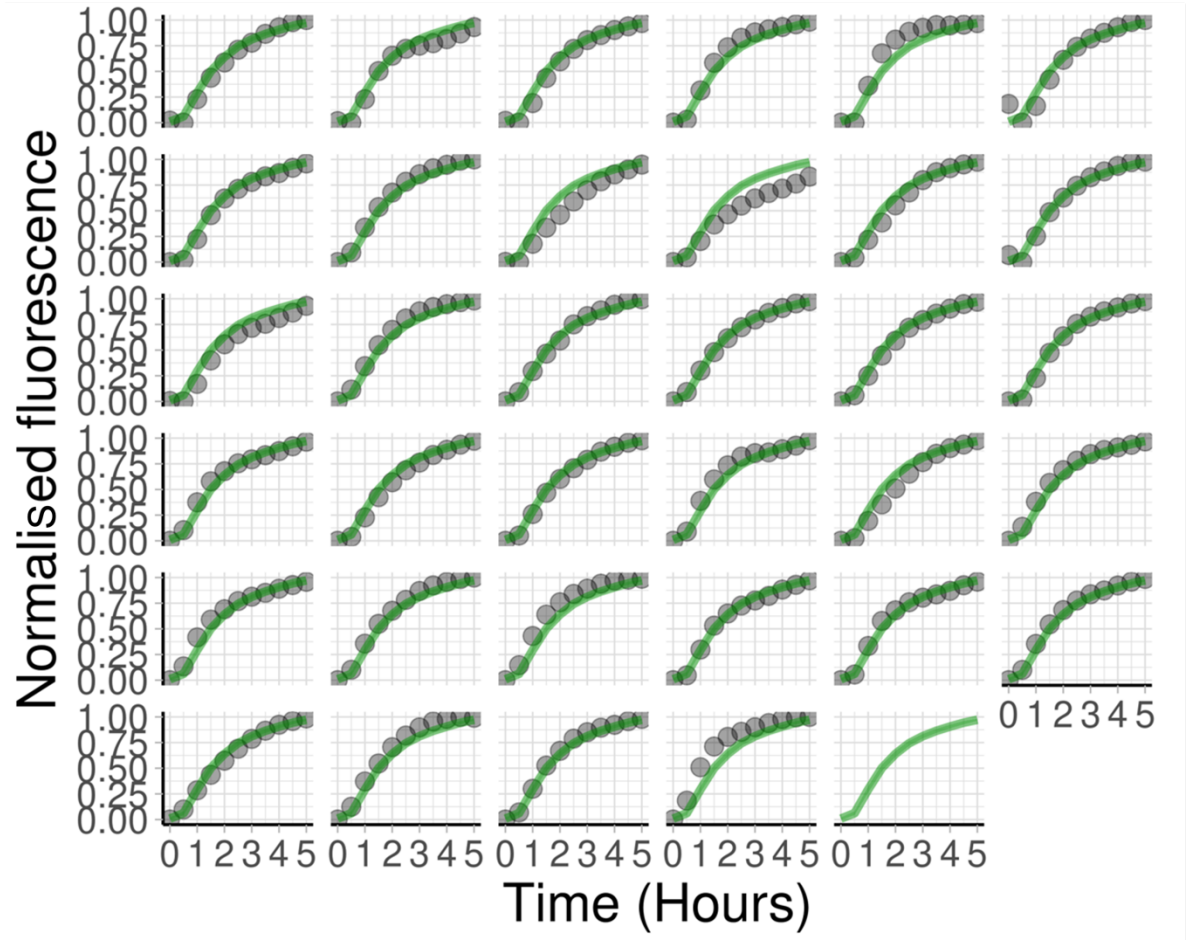


Fig. 41. Longitudinal analysis of GenEPi expression post-heat-shock in *Tg(hsp70:GenEPi)* zebrafish. Each graph displays the normalised fluorescence intensity of 35 individual *Tg(hsp70:GenEPi)* zebrafish post-heat-shock presented in **Fig. 40C**. Data were plotted in PlotTwist (Shiny apps). *(Adapted from Yaganoglu and Kalyviotis et al.).*

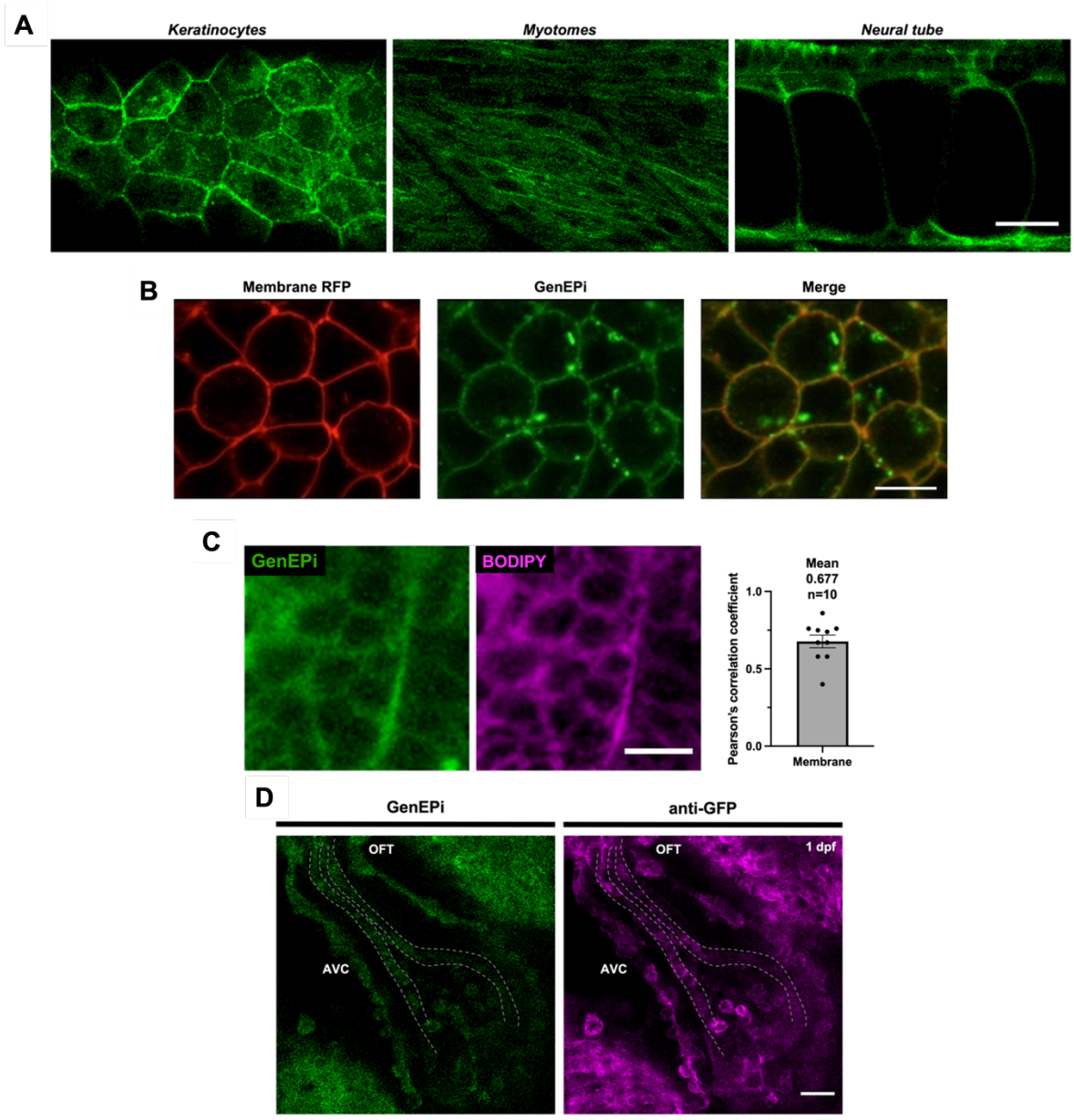


Fig. 42. GenEPi is homogeneously expressed and mainly localises to the plasma membrane of individual cells after heat-shock of *Tg(hsp70:GenEPi)* zebrafish. (A) Representative GenEPi expression in keratinocytes, myotomes and part of the neural tube in *Tg(hsp70:GenEPi)* zebrafish at 30 hpf. Scale bar, 20 μm. (B) GenEPi colocalises with membrane-RFP in *Tg(hsp70:GenEPi)* zebrafish injected with membrane-RFP mRNA at 12 somites stage (14 hpf). Scale bar, 10 μm. (C) Colocalisation analysis of GenEPi and BODIPY in *Tg(hsp70:GenEPi)* zebrafish at 30 hpf and Pearson's correlation coefficient. n=10 ROIs with at least 2 individual cells. Scale bar, 10 μm. (D) Anti-GFP immunostaining of heat-shocked *Tg(hsp70:GenEPi)* zebrafish, which confirms the expression of GenEPi in endocardium and myocardium cells at 1 dpf. Scale bar, 20 μm. *(Adapted from Yaganoglu and Kalyviotis et al.).*

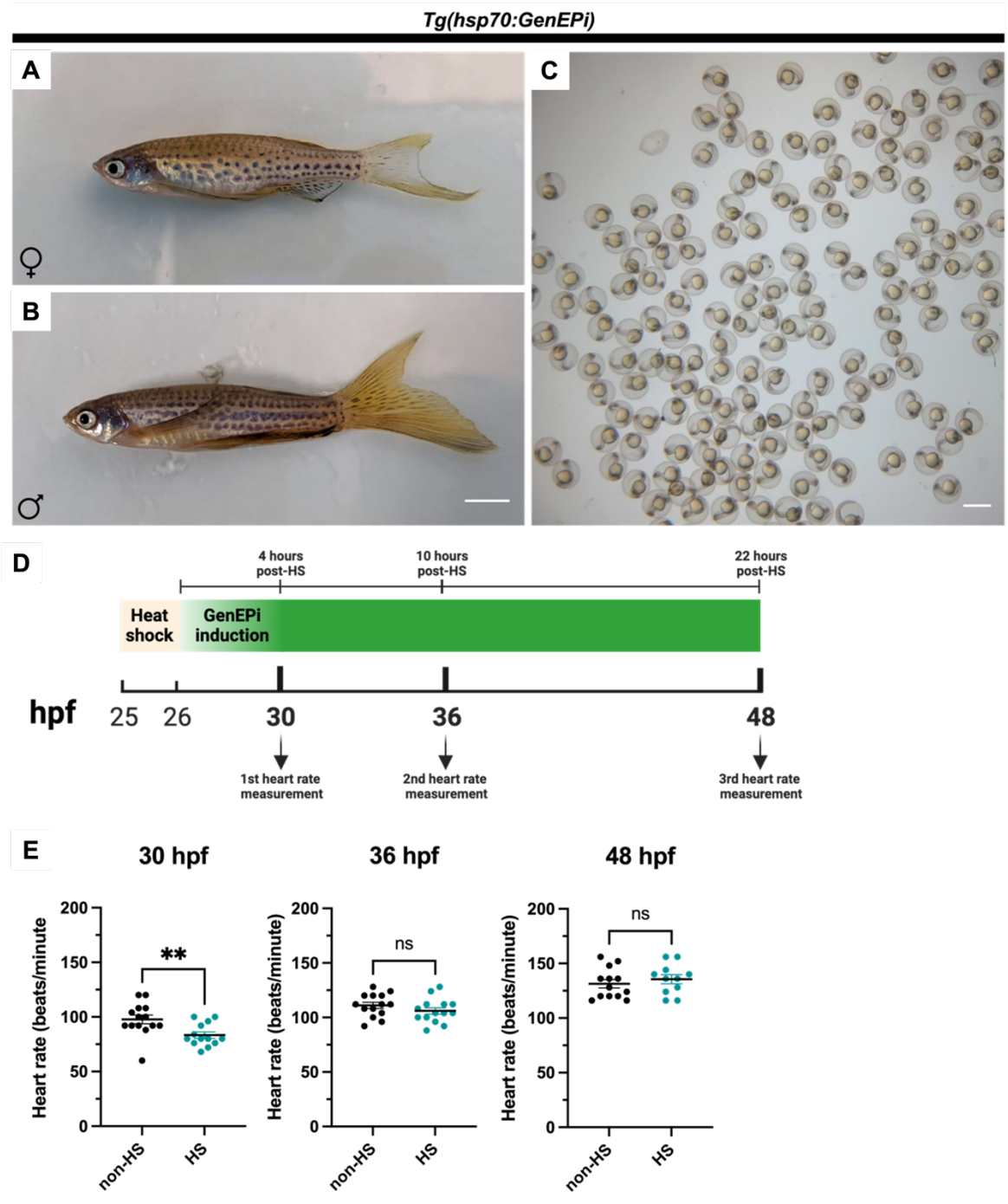


Fig. 43. Transient induction of systemic expression of GenEPi in transgenic embryos does not affect their development to adulthood. (A) Brightfield image of a female and (B) male *Tg(hsp70:GenEPi)* adult zebrafish (WT/TL background) that were heat-shocked to induce GenEPi expression at 1 dpf. Scale bar, 5 mm. (C) *Tg(hsp70:GenEPi)* zebrafish produce healthy embryos when crossed. Scale bar, 1 mm. (D) Time course of the heart beating measurement experiments presented in (E). (E) Heart rate of individual *Tg(hsp70:GenEPi)* zebrafish heat-shocked (HS) to induce GenEPi expression at 1 dpf. Notably, the heart rate of the heat-shocked embryos does not differ to control non-heat-shocked (non-HS) zebrafish when the latter have recovered from the heat-shock process. Please note that GenEPi can be still observed at 48hpf. *(Adapted from Yaganoglu and Kalyviotis et al.).*

2.5.2 Pharmacological modulation of Piezo1 activity in vivo

As zebrafish are potent models for drug and toxicity screening (MacRae and Peterson, 2015, Cassar et al., 2020) and only a few modulators of Piezo1 activity are known (Evans et al., 2018, Syeda et al., 2015), we assessed the activity of GenEPi upon pharmacological intervention *in vivo*. As a proof-of-principle, we used the agonist Yoda1 and the generic ion channel inhibitor RR to probe Piezo1 function following a similar approach to our *in vitro* analyses and electrophysiology experiments (**Fig. 29A**). Heat-shocked *Tg(hsp70:GenEPi)* zebrafish embryos in egg medium (E3 medium) were sequentially incubated in 10 μM Yoda1, 10 μM Yoda1 and 10 μM RR and 10 μM RR followed by washing out in E3 medium (see **Online Methods**, **Zebrafish transgenesis and *in vivo* pharmacological intervention experiments**). To enable rapid interpretation of GenEPi response over a large field of view, we used a widefield fluorescence microscope. We focused on the developing eye, a large organ in direct contact with the egg medium easily accessible for imaging and pharmacological interventions. Heat-shocked *Tg(hsp70:GenEPi)* fish showed instantaneous and significant fluorescence increase in response to 10 μM Yoda1 (**Fig. 44A-B**), whereas transfer to a solution containing 10 μM Yoda1 and 10 μM of RR (**Fig. 44A-B**) inhibited GenEPi activation, consistent with our electrophysiology results (**Fig. 29A**). Zebrafish transferred to 10 μM RR demonstrated further decrease in fluorescence intensity (**Fig. 44A-B**). Notably, washing out of the zebrafish in the original E3 medium restored the fluorescence of GenEPi to pre-treatment activity levels (**Fig. 44A-B**) demonstrating that GenEPi retains the pharmacological properties of Piezo1.

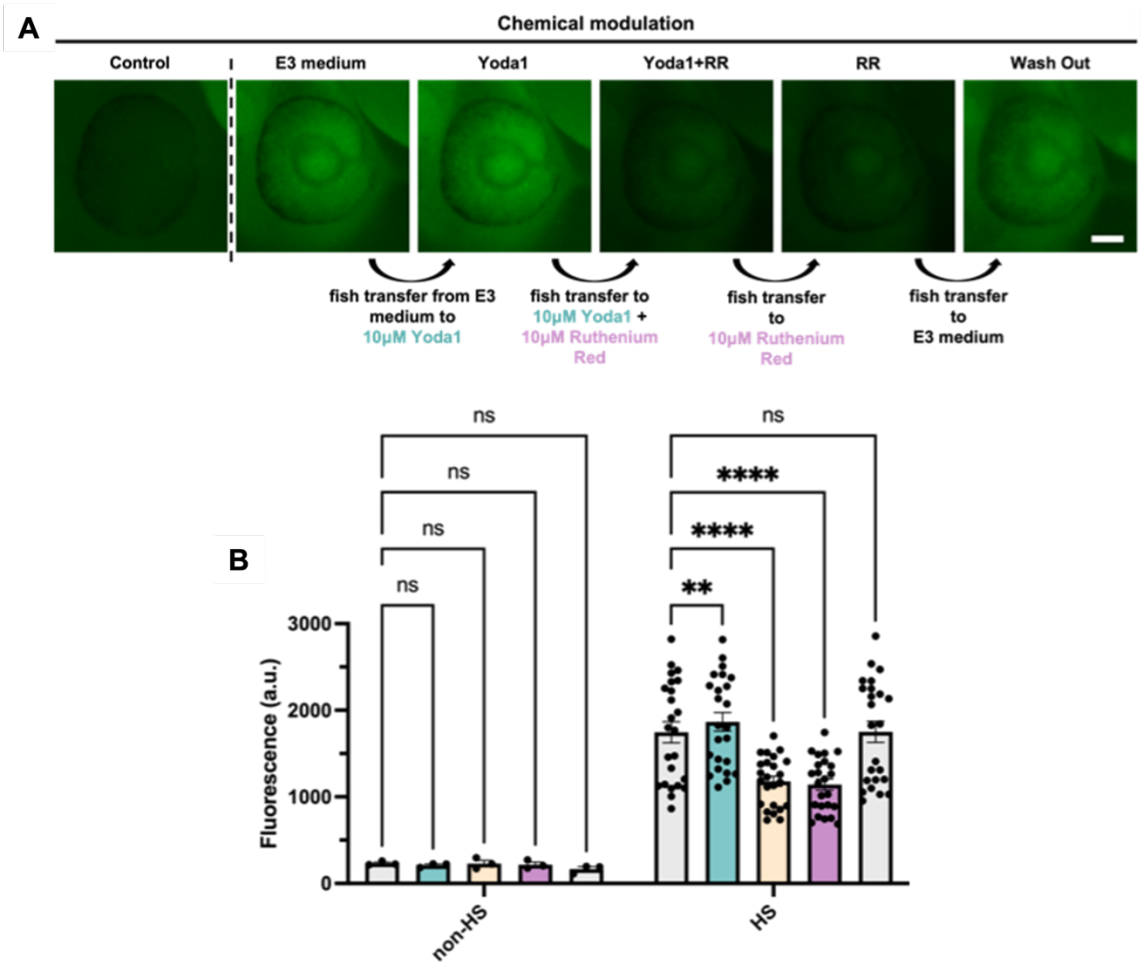


Fig. 44. GenEPi resolves Piezo1-dependent activity changes *in vivo* upon pharmacological intervention. (A) Representative images of GenEPi expression in the eye of a 1dpf *Tg(hsp70:GenEPi)* zebrafish during the chemical modulation of channel's activity by Yoda1 and RR. Scale bar, 50 μm. (B) Raw fluorescence intensity of control and *Tg(hsp70:GenEPi)* zebrafish during the chemical modulation of GenEPi activity in 10 μM Yoda1, 10 μM Yoda1 and 10 μM RR, 10 μM RR and wash out to E3 medium. Non-heat-shocked embryos which do not express GenEPi showed non-significant response both in presence or absence of Yoda1 or RR (paired data of n=3 and n=24 non-HS and HS transgenic zebrafish, respectively). Two-way ANOVA test. *(Adapted from Yaganoglu and Kalyviotis et al.).*

2.5.3 GenEPi response during cardiac contraction in vivo

As we showed in **Fig. 38-39**, GenEPi can report cardiomyocyte contraction-triggered mechanical stimulation with high spatiotemporal resolution within 3D cardiac microtissues. To test whether GenEPi can also monitor Piezo1-dependent activity during heart contraction *in vivo*, we imaged heat-shocked *Tg(hsp70:GenEPi)* zebrafish embryo hearts at 2dpf. Interestingly, GenEPi fluorescence at the atrioventricular canal (AVC) of *Tg(hsp70:GenEPi)* zebrafish hearts showed a two-phase increase for each beating cycle, which is highly stereotypical (**Fig. 45A**).

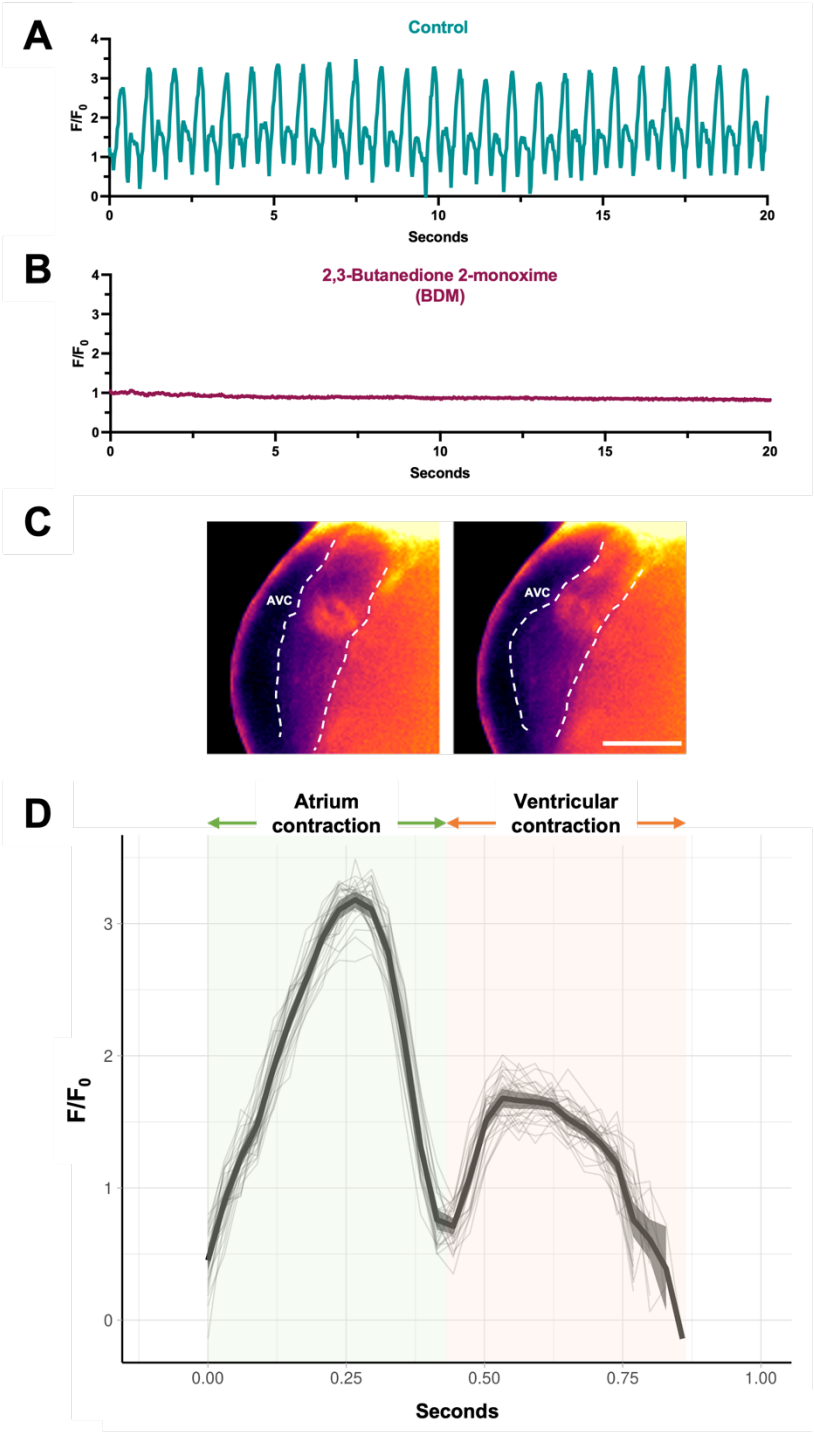


Fig. 45. GenEPi reports shear stress dependent Piezo1 activation during cardiac contraction *in vivo*. (A) Representative fluorescence intensity (F/F_0) profile from the AVC of a *Tg(hsp70:GenEPi)* zebrafish heart which shows the two-phase GenEPi activation. (B) Representative fluorescence intensity (F/F_0) profile from the same ROI in A at the AVC of the same *Tg(hsp70:GenEPi)* zebrafish heart after treatment with BDM which abolishes heart beating, showing absence of GenEPi responses (C) Representative images of a *Tg(hsp70:GenEPi)* zebrafish heart which shows the GenEPi activation during atrium and ventricular contraction, respectively. Scale bar, 100µm. (D) Mean of 27 GenEPi responses of individual heart beating cycles with 95% CI presented as grey shading. Note that GenEPi activation is highly stereotypical during zebrafish heart beating cycle, probably triggered by shear stress forces. Data were plotted in PlotTwist (Shiny apps). *(Adapted from Yaganoglu and Kalyviotis et al.).*

This two-phase GenEPi response was abolished by the non-selective myosin ATPase inhibitor 2,3-butanedione 2-monoxime (BDM) (Herrmann et al., 1992), confirming that the beating of the zebrafish heart triggered GenEPi activation (**Fig. 45B**). However, solely the contraction of the heart at the AVC cannot explain the two-phase response which seems to coincide with the contraction of the atrium and the ventricle, respectively. Previously, it has been demonstrated that shear stress forces change dramatically during the zebrafish heart contraction (Lee et al., 2013, Foo et al., 2020). More specifically, it has been shown that the wall shear stress forces at the AVC show a two-phase increase with one peak during atrium contraction and one during ventricle contraction at 40-50hpf. Considering the high similarity of the GenEPi response to how shear stress forces change during zebrafish heart contraction at the AVC and that Piezo1 is known to respond to shear stress, we reasoned that the activation observed is probably triggered by shear stress and not by the contraction itself. In the future, specific expression of GenEPi to the endocardium or the myocardium will provide a definite answer whether the GenEPi activation we observed is caused by the contraction and/or the shear stress forces present during the zebrafish heart beating.

Overall, we confirm that the ability of GenEPi to resolve Piezo1-dependent activity is preserved *in vivo* and we demonstrate a robust and reliable *in vivo* GenEPi system that is able to generate information rich and physiologically relevant readouts.

2.6 Discussion on GenEPi

As the pivotal role of mechanics in cellular processes gains increasing recognition, there is a need to study mechanical forces across different biological scales, and ideally in a non-invasive way. Building upon prior efforts within the Pantazis lab to develop an optical Piezo1-specific activity reporter, we introduced GenEPi which is

designed to provide a highly specific and non-invasive functional readout of Piezo1-dependent activity from the single cell level to that of the entire organism.

The engineering of GenEPi was achieved by successfully targeting a low-affinity and high dynamic range GCaMP to the Ca^{2+} microdomain of the Piezo1 channel using a flexible linker of defined length (**Fig. 25**). Notably, our systematic screening underscored the critical role of (i) *amino acid composition* and (ii) *linker length* in securing the specificity of Ca^{2+} imaging solely to Piezo1-dependent stimuli. The importance of this design is exemplified by the sensitivity loss observed upon duplicating the flexible linker unit (GSGG), emphasising its role in preserving the specificity to Piezo1-dependent signals (**Fig. 26B** and **Table 5**, GCaMP-G4). Contrary to potential concerns raised by previous work indicating alterations in channel response with a C-terminal GFP fusion to mouse Piezo1 without a flexible linker (Cox et al., 2016), our use of a flexible linker demonstrated that the functionality of the channel remains unaffected, faithfully reflecting the responses of wt-Piezo1 (**Fig. 27-30**). These results substantiate our assertion that the design principle of GenEPi (**Fig. 25B**) can indeed serve as a blueprint for the development and engineering of optical reporters for other ion channels, such as Piezo2 (Coste et al., 2010), without compromising their functionality.

GenEPi's ability to robustly report Ca^{2+} influx upon channel opening (**Fig. 32**) with high spatiotemporal resolution underscores its effectiveness. However, challenges arise when correlating different forces and activation states to the on-off type GenEPi's fluorescence response (**Fig. 46**). Addressing these complexities which surround the interpretation of mechanical forces in correlation with GenEPi's fluorescence response, necessitates a nuanced analysis and meticulous *in vitro* calibration measurements. In addition, future engineering could explore the integration of improved fluorescent probes and GECIs (**Fig. 47**) that in combination with experiment-specific calibration measurements could secure a quantitative

readout of applied forces. The use of fluorescence lifetime (FLIM) calcium biosensors (van der Linden et al., 2021a), which have been recently introduced, stands as a potential enhancement. The integration of FLIM imaging can offer not only optical measurements but also quantitative insights into calcium concentration dynamics upon channel opening. Such advancements will be pivotal in facilitating a more precise understanding of the mechanical landscape sensed by Piezo1 while deciphering the intricacies of Piezo1-dependent mechanotransduction across different biological scales and contexts. However, given the inherent limitation of the biosensor design to exclusively report Piezo1-specific activity, it will remain challenging to differentiate between various types of forces (such as shear stress, tension, or a combination thereof). The nature of the biosensor design makes it difficult to discern the specific type of force that activates Piezo1.

GenEPi's seamless non-invasive intensiometric visualization of Piezo1-dependent activity unifies previously separated readouts of channel function and localisation dynamics (**Fig. 35-37**). Its applicability across diverse cellular systems, without noticeable adverse physiological effects under temporally controlled overexpression, positions it as a versatile tool for various experimental setups. In the future, use of our already developed targeted CRISPR/Cas approaches to tag endogenous Piezo1 will promote our understanding of how Piezo1 senses and interprets a variety of intrinsic and extrinsic mechanical and, recently discovered, non-mechanical stimuli (Moroni et al., 2018). Currently, we have successfully generated and are testing a mouse transgenic line in which the endogenous Piezo1 is tagged with GCaMP-G4 via the GSGG flexible linker. This approach will ensure the monitoring of endogenous Piezo1 activity in all tissues where Piezo1 is normally expressed without the need for exogenously overexpressing GenEPi.

The universality of GenEPi is further exemplified by our zebrafish model (**Fig. 40-45**), showcasing its efficacy in resolving Piezo1-dependent stimulation in both *in*

vitro and *in vivo* settings. The GenEPi transgenic line emerges as a pivotal tool for surveying hypotheses derived from previous *in vitro* results and exploring Piezo1-dependent activity across varied pathophysiological conditions. In the future, we aim to use GenEPi and similar biosensors to extract "force maps" during early embryo development in combination with already established lineage tracing tools. These "force maps" will be used to produce models on how mechanical forces influence cell behaviours, such as cell migration, and cell fate specification in early embryos before asymmetry breaking, elucidating the complex interplay of mechanics in cell fate determination.

Anticipating the use of GenEPi in investigating Piezo1-dependent mechanical signals in cardiac development and morphogenesis, we highlight its potential to elucidate how mechanical forces change during zebrafish heart beating throughout development. We have demonstrated that GenEPi exhibits a biphasic response during the zebrafish heart beating cycle (**Fig. 45**), aligning with previously characterised shear stress forces in the zebrafish heart (Lee et al., 2013, Foo et al., 2020). This observation offers a promising avenue for future research. However, as mentioned previously, further experiments involving the grafting of magnetic beads or the injection of ferromagnetic materials into the bloodstream are needed to determine the specific types of forces that GenEPi can resolve during heart beating.

The scarcity of identified modulators of Piezo1 activity accentuates the need for targeted drug discovery pipelines. GenEPi, with its capacity to provide a specific functional readout of Piezo1 activity, addresses a critical gap. Our zebrafish model emerges as a cost-effective and scalable *in vivo* pharmacological intervention system, facilitating direct imaging of compound effects on Piezo1 activity in different organs. This refined approach could distinguish between systemic and tissue-specific modulation of channel function, offering the prospect of selecting lead

compounds with minimal side effects, given the multifaceted functions Piezo1 channels exert (Ehmke, 2018).

Overall, GenEPi emerges not only as the first optical Piezo1-specific activity reporter but also as a catalyst for further engineering and refinement of a new-class of biomechanics biosensors. The envisioned improvements and additional experiments, position GenEPi as a dynamic platform with the potential to unravel intricate biological processes governed by cellular mechanics. GenEPi stands at the forefront, offering unprecedented insights into Piezo1-dependent activity and laying the groundwork for future breakthroughs advancing the field of systems mechanobiology.

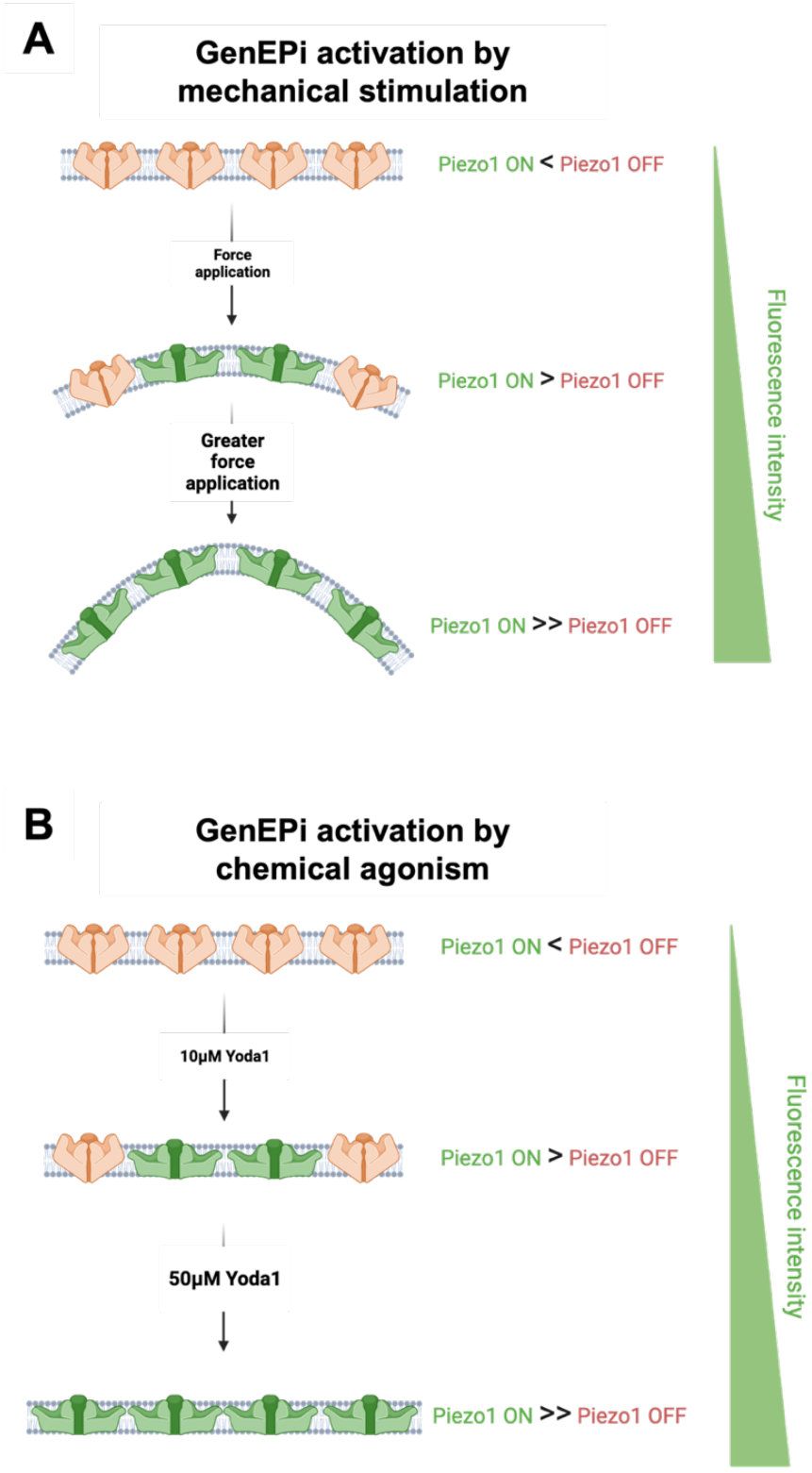


Fig. 46. GenEPi can be used for comparative Piezo1-dependent activity studies. (A) Our 3D cardiac microtissue experiments suggest that GenEPi activation depends on the amplitude of the applied force. (B) Similarly, our Yoda1 experiments show a dose-dependent response of GenEPi. Altogether, although GenEPi cannot be used currently for quantitative force measurements, it can be used for inter- or intra- cellular comparative studies in which different activation states can be correlated to GenEPi florescence. *(Created with Biorender.com).*

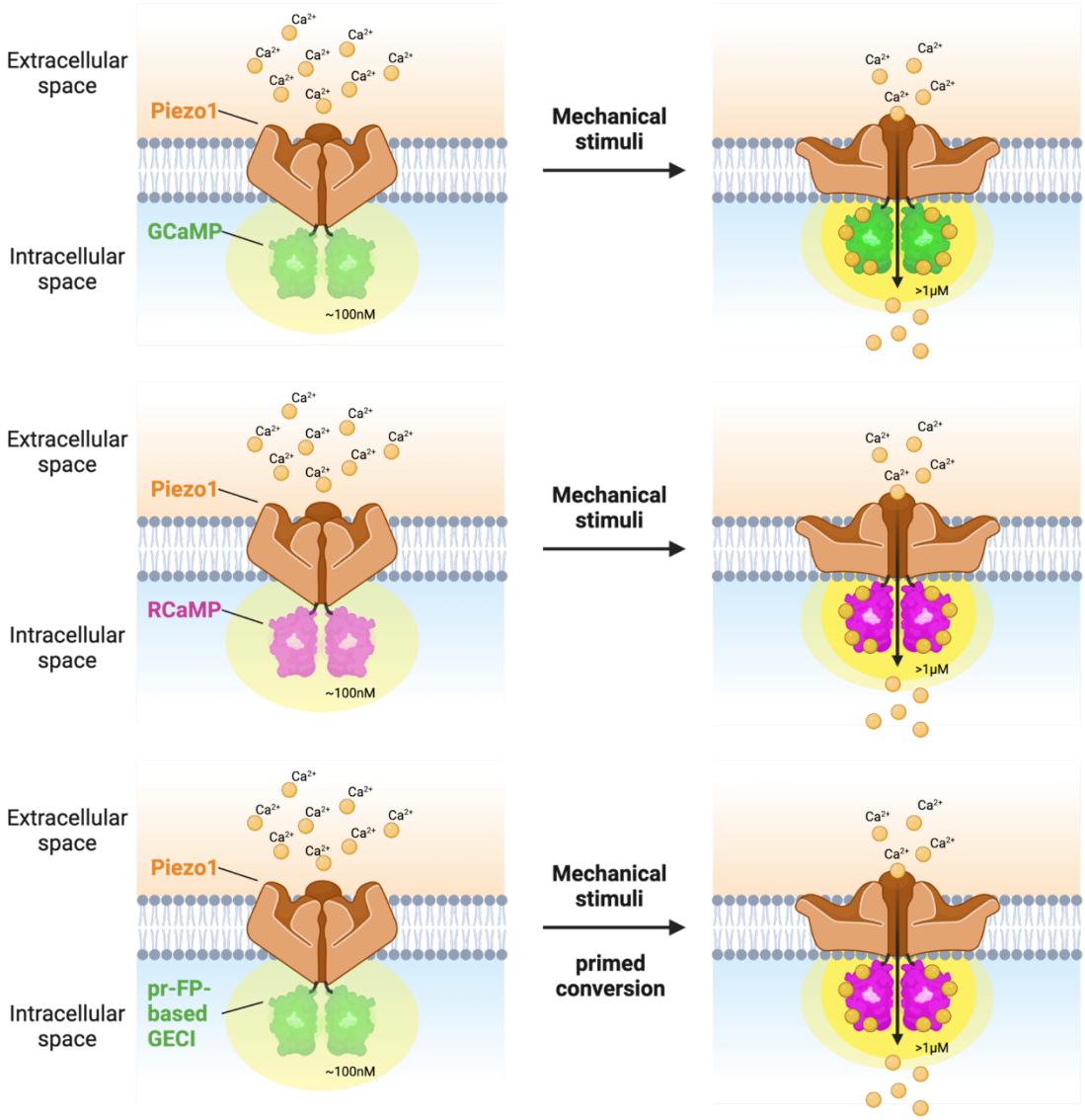


Fig. 47. Future engineering of GenEPi could produce other biosensors for Piezo1-dependent activity. Our current efforts are focused on engineering different colour (red and primed convertible) variants of GenEPi that could be multiplexed with other biosensors and fluorescent reporters. Future engineering to incorporate concentration dependent FLIM calcium biosensors could be used to measure single GenEPi cluster calcium dynamics, especially in combination with super-resolution techniques, such as TIRF-SIM and traction force microscopy (Barbieri et al., 2021). *(Created with Biorender.com).*

Chapter 3. Primed conversion advanced imaging toolkit

«Ποταμῷ γὰρ οὐκ ἔστιν ἐμβῆναι δὶς τῷ αὐτῷ»

"It is not possible to step in the same river twice"

Heraclitus

3.1 Develop of an in-house high-throughput protein screening methodology

Previous efforts to perform *in vitro* assessment of primed conversion efficiency of FPs of interest were based on purified protein embedded in polyacrylamide gel (Mohr et al., 2016, Mohr et al., 2017). Bacterial expression of a recombinant pr-FP was followed by protein purification using commercially available affinity chromatography systems. Then, the purified protein was embedded in a polyacrylamide gel into an eight-well-chambered cover glass for further fluorescence evaluation and photoconversion.

Although this setup provided reliable and accurate results, it is too laborious to serve as main screening methodology for protein engineering approaches. To increase parallelisation and screening speed, we set out to scale up from previously eight proteins to maximum 96 per screening round. To this end, we developed an

improved screening methodology in which bacterial cells expressing the FP of interest are used instead of purified protein (**Fig. 48**).

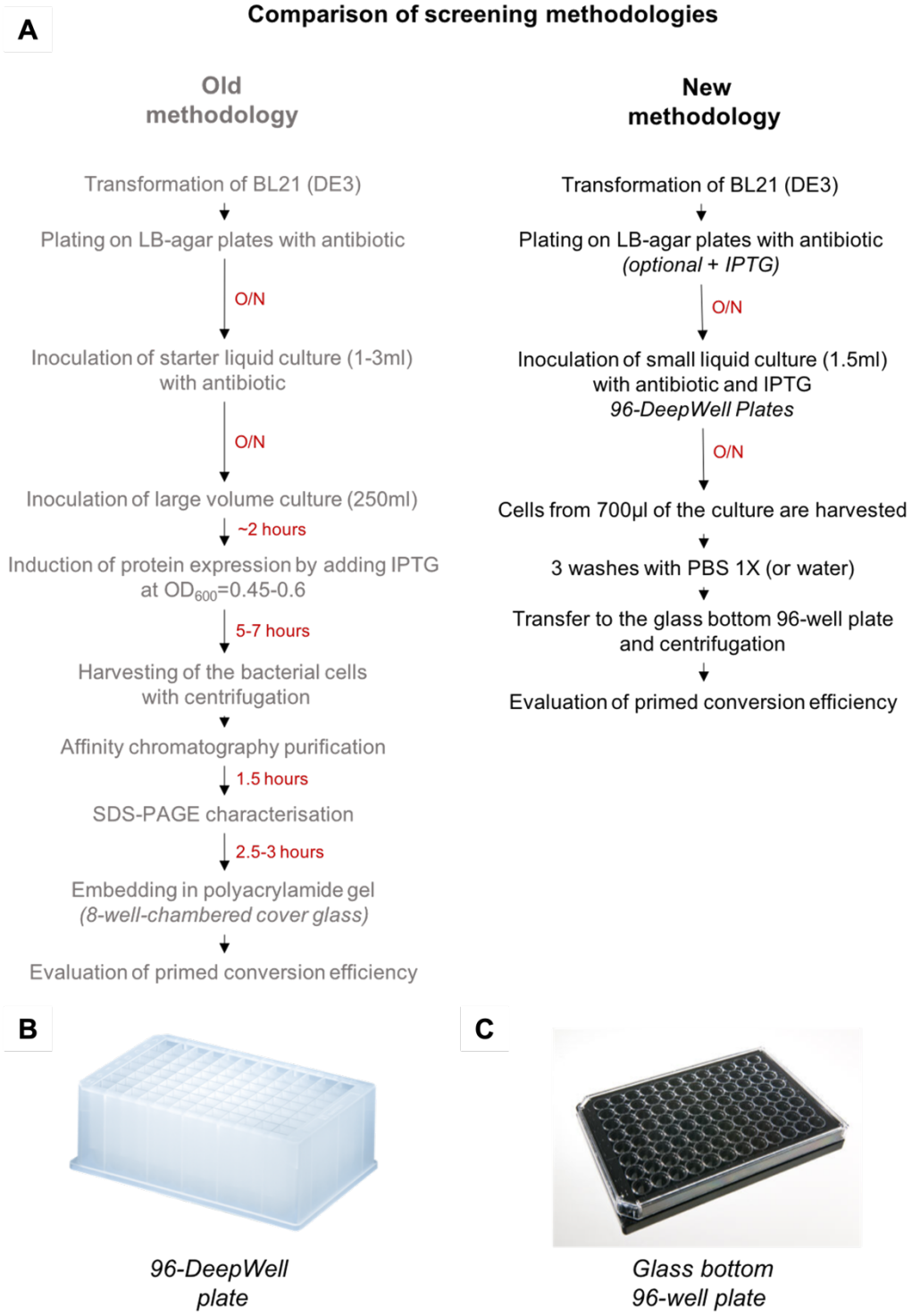


Fig. 48. A new screening methodology for faster and less laborious screening of protein engineered FP variants. (A) The steps of the two methodologies used for the screening of pr-FP variants. (B) 96-DeepWell plate used in the new screening methodology. (C) A glass bottom 96-well plate used in the new screening methodology.

Briefly, BL21 (DE3) competent cells were chemically transformed with the DNA construct carrying the pr-FP gene and they were plated on LB-agar plates with the adequate antibiotic/selective marker. The next day, a small volume liquid media with the right expression inducer and antibiotic/selective marker were inoculated with single colonies in sterile 2ml 96-DeepWell™ Plates. The plates were then carefully sealed with sterile and air-permeable Nunc™ Sealing Tapes to reduce evaporation/contamination and are incubated overnight (O/N) at 37°C in an orbital shaker incubator. The use of 96-DeepWell™ plates enables the scaling-up of the procedure and multiple colonies of different mutants can be grown in parallel. The following day, 700μl of each liquid culture were added in a 1.5ml tube and they were centrifuged at 11,000rcf for 1 minute at 4°C to harvest the bacterial cells. After the centrifugation, the supernatant was discarded and the bacterial pellet was resuspended in 700μl of sterile 1X PBS and centrifuged at 11,000rcf for 1 minute at 4°C. This washing step was repeated three times to remove remaining media and excreted flavins, which mainly cause green autofluorescence (Mihalcescu et al., 2015) that can complicate the fluorescence-based photoconversion analysis. Finally, the bacterial pellet was resuspended in 100μl of 1X PBS (or water) and the bacteria were transferred to 96-well Corning® High Content Imaging Microplates and were pelleted via centrifugation at 2.000rcf at 4°C for 15 minutes. After this final centrifugation step, the bacterial pellets were available for further fluorescence analysis.

To evaluate the reliability of the new screening methodology for photoconversion, a series of trial experiments were conducted using the well characterised pr-FP Dendra2. Bacteria chemically transformed with Dendra2 were prepared following the new screening methodology and their green-to-red photoconversion was optically assessed pre- and post- 405nm illumination for 1min using a standard DAPI filter cube (BP 390-420, FT 425, LP 450) and a mercury lamp. As shown in

Fig. 49A, bacteria expressing Dendra2 were successfully photoconverted in the circular region illuminated by the 405nm light, resulting in both significant decrease and increase in the green and red signal, respectively (**Fig. 49B**). Consequently, bacterial cells expressing Dendra2 prepared using the methodology described above could be successfully imaged using standard excitation/emission filters and photoconverted using 405nm illumination.

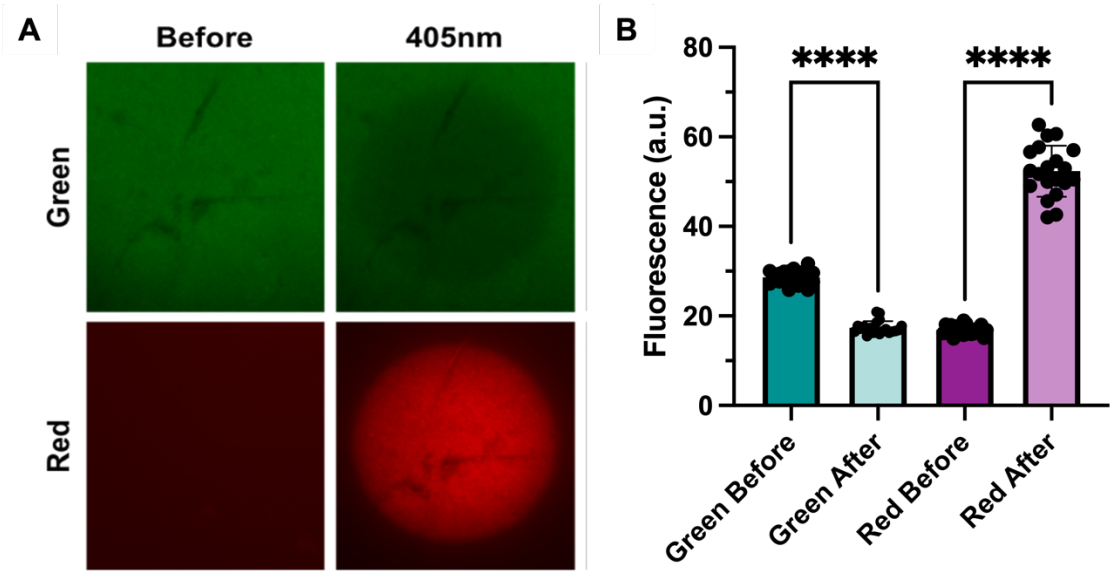


Fig. 49. Successful fluorescence imaging and 405nm photoconversion of pelleted bacterial cells expressing Dendra2 prepared following the new screening methodology. (A) Pre- and post-405nm photoconversion images of pelleted bacterial cells expressing Dendra2. (B) Raw intensity values of green and red fluorescence pre- and post-405nm photoconversion of pelleted bacterial cells expressing Dendra2. (n=20 ROIs for each condition, error bars: Standard deviation (SD)). Ordinary one-way ANOVA test.

3.2 Optimisation of primed conversion conditions

At ETH Zurich, the Pantazis lab previously utilised a confocal system equipped with a multiphoton laser that can be used as a continuous-wave 730nm illumination source required for primed conversion (Mohr et al., 2016). However, as such a system was not available at Imperial College London, we evaluated two alternative primed conversion methodologies. First, we tested primed conversion using a 460LP excitation filter and then primed conversion using 488nm and 633nm light illumination.

The Pantazis lab has previously employed a xenon lamp and a 460LP excitation filter placed before the sample as an alternative primed conversion methodology **(Fig. 50)**.

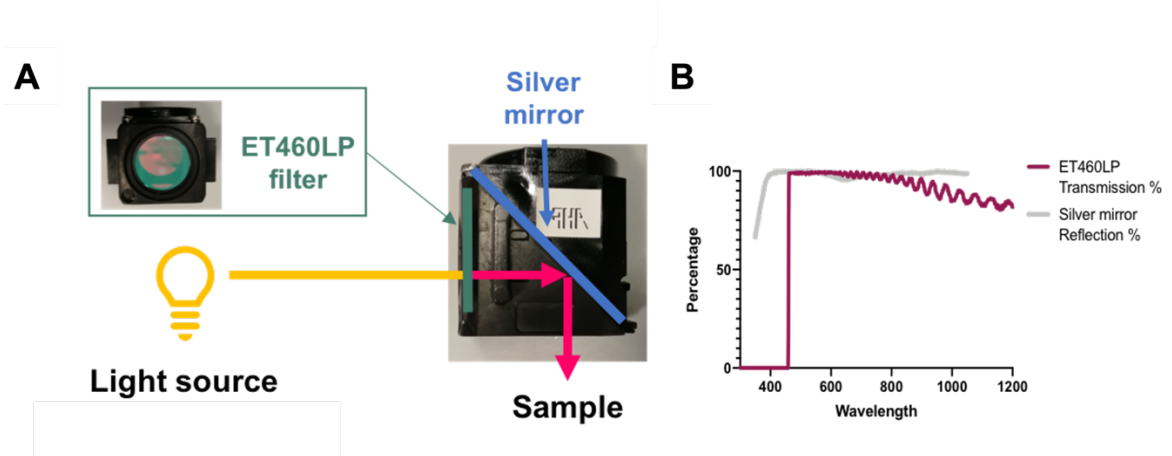


Fig. 50. Primed conversion using a ET460LP filter. (A) The light path and the design of the filter cube with the excitation filter and the silver mirror. An excitation 460LP filter fitted in a common push and click Zeiss filter cube with a silver mirror without an emission filter was placed in the filter turret of an inverted Zeiss LSM780 confocal microscope and a xenon lamp (Carl Zeiss XBO 75) was used as a light source. When the light source is switched-on and the right light path is selected in the system, the incoming light passes through the excitation filter which only transmits light with wavelengths greater than 460nm. Then, the transmitted light is reflected by the silver mirror to the sample. (B) The optical characteristics of ET460LP (transmission percentage per wavelength) and silver mirror (reflection percentage per wavelength).

As xenon lamps were not available both at the Facility for Imaging by Light Microscopy (FILM) and at the Department of Bioengineering, we evaluated available light sources based on mercury lamps, such as the Leica EL6000 and the

Carl Zeiss HXP 120 C. To determine whether a xenon lamp light source can be replaced by a mercury lamp, we placed the ET460LP filter cube into an inverted Zeiss widefield microscope equipped with a Carl Zeiss HXP 120C light source. Purified Dendra2 embedded in polyacrylamide gel and pelleted bacterial cells expressing Dendra2 were used to assess primed conversion efficiency using the 460LP excitation filter. A DAPI filter cube (BP 390-420, FT 425, LP 450) was used to achieve 405nm control photoconversion. As shown in **Fig. 51**, a decrease of the green and an increase of the red signal could be detected for both purified protein and bacterial pelleted cells after 1 min exposure using the DAPI filter. However, when the 460LP excitation filter was used under the same light-source conditions, green-to-red photoconversion could not be detected.

To assess the effect of illumination time for primed conversion using the 460LP excitation filter, we used different illumination times ranging from 1 to 20min. As shown in **Fig. 52**, no increase of red signal was detected for primed conversion even after 20 minutes of illumination with maximum power intensity of the mercury lamp, whereas 405nm illumination led to pronounced increase of the red signal after 1 minute of illumination.

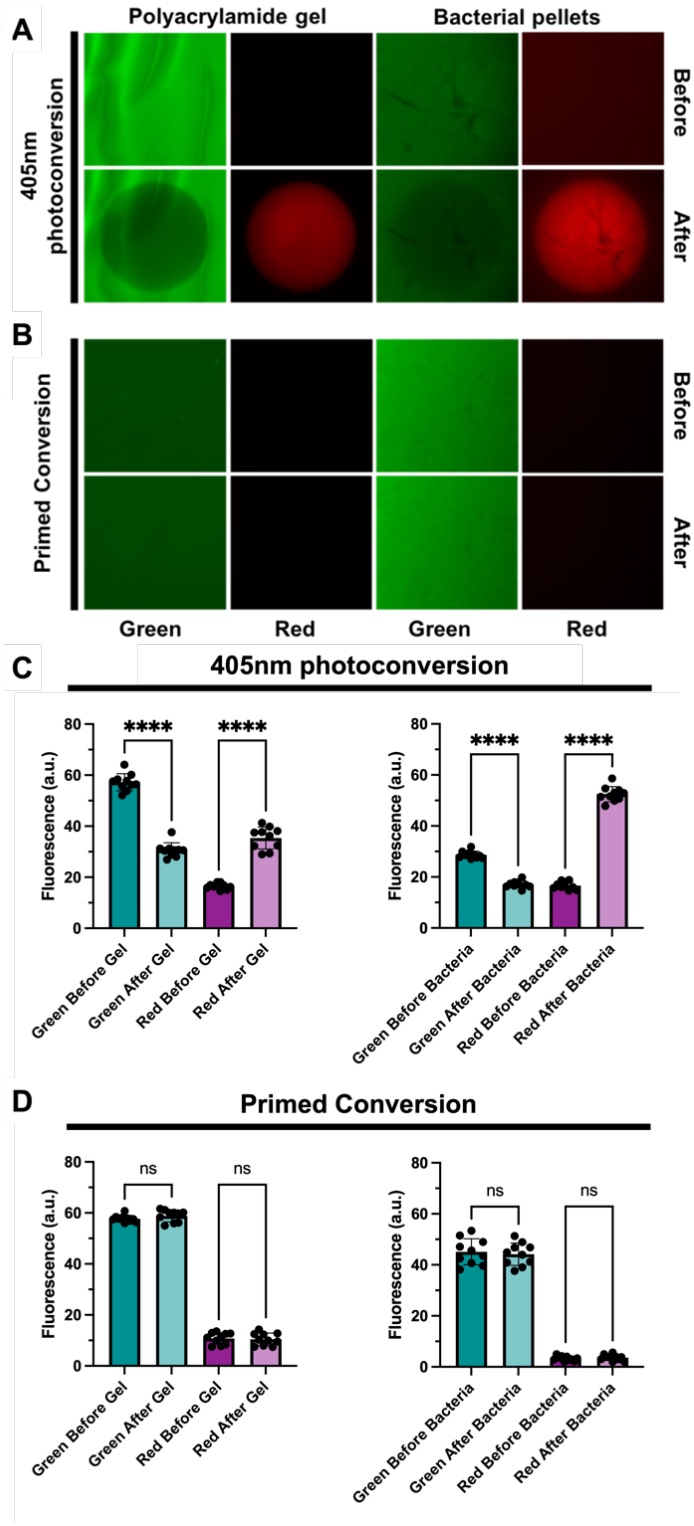


Fig. 51. Primed conversion of Dendra2 using the 460LP excitation filter is not successful. (A) Successful 405nm photoconversion of purified Dendra2 embedded in polyacrylamide gel and pelleted bacterial cells expressing the same pr-FP. (B) Primed conversion using the ET460LP filter and a mercury lamp shows no detected photoconversion. (C, D) Raw intensity values of green and red fluorescence pre- and post- (C) 405nm photoconversion and (D) primed conversion of purified Dendra2 embedded in polyacrylamide gel and pelleted bacterial cells expressing the same pr-FP. (n=10 ROIs for each condition, error bars: SD). Ordinary one-way ANOVA test.

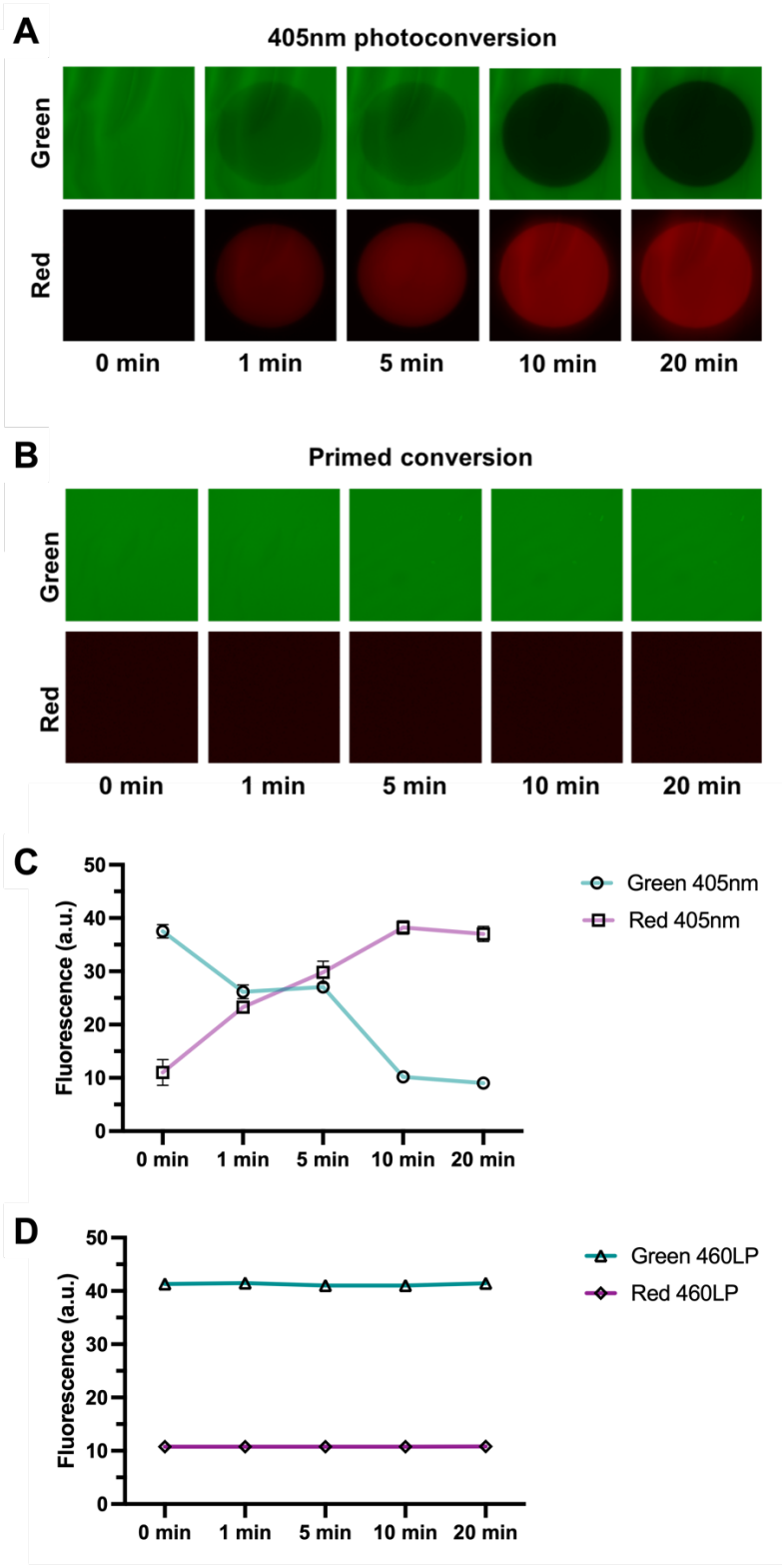


Fig. 52. Increasing illumination time using 460LP excitation filter does not lead to primed conversion of purified Dendra2. (A) 405nm photoconversion of Dendra2 embedded in polyacrylamide gel at different illumination times. (B) Primed conversion of Dendra2 embedded in polyacrylamide gel at different illumination times using the 460LP excitation filter. (C, D) Green and red intensity changes at different illumination times for (C) 405nm photoconversion and (D) primed conversion using the 460LP excitation filter.

3.3 Evaluation of primed conversion using 488nm and 633nm simultaneous illumination in a CLSM

Given that the combination of the 460LP excitation filter with the mercury lamp as illumination source for the screening setup proved futile, we focussed on performing primed conversion using a confocal laser scanning microscope. Instead of using 730nm, we assessed whether primed conversion can be accomplished using simultaneous 488nm and 633nm illumination.

In order to assess primed conversion in a commercial system, Dendra2 protein was expressed, purified and embedded in polyacrylamide gel. The gel was imaged using a confocal system and several combinations of 488nm and 633nm relative powers were evaluated for their ability to convert Dendra2. For the priming beam, the relative power of 488nm light was set between 5% and 25%. For the converting beam, the relative power of the 633nm laser was initially set at 100% to ensure maximum conversion efficiency. As shown in **Fig. 53A-B**, Dendra2 could be photoconverted using 488nm and 633nm simultaneous illumination while maximum photoconversion was observed when 15% blue laser and 100% red relative laser powers were used. Extensive photobleaching was noticed for high power levels of 488nm, whereas lower power levels of 633nm reduced photoconversion efficiency. Consequently, the optimal combination of relative powers was around 15% for 488nm light and 100% for 633nm light. To confirm that the laser powers used for primed conversion where in the range of previously reported optimal powers for primed conversion (Mohr et al., 2016), we assessed the effective laser powers at the focal plane for both the priming and converting beams. As shown in **Fig. 53C**, 15% of relative 488nm laser power was about 10µW at the focal plane which is in the range of previously used laser powers for primed conversion. Interestingly, 100% of relative 633nm laser power was about 750µW, which is at least one order of magnitude less than previously used 730nm laser

powers, suggesting that 633nm primed conversion can be a preferable equivalent for minimising illumination powers when primed converting sensitive biological samples.

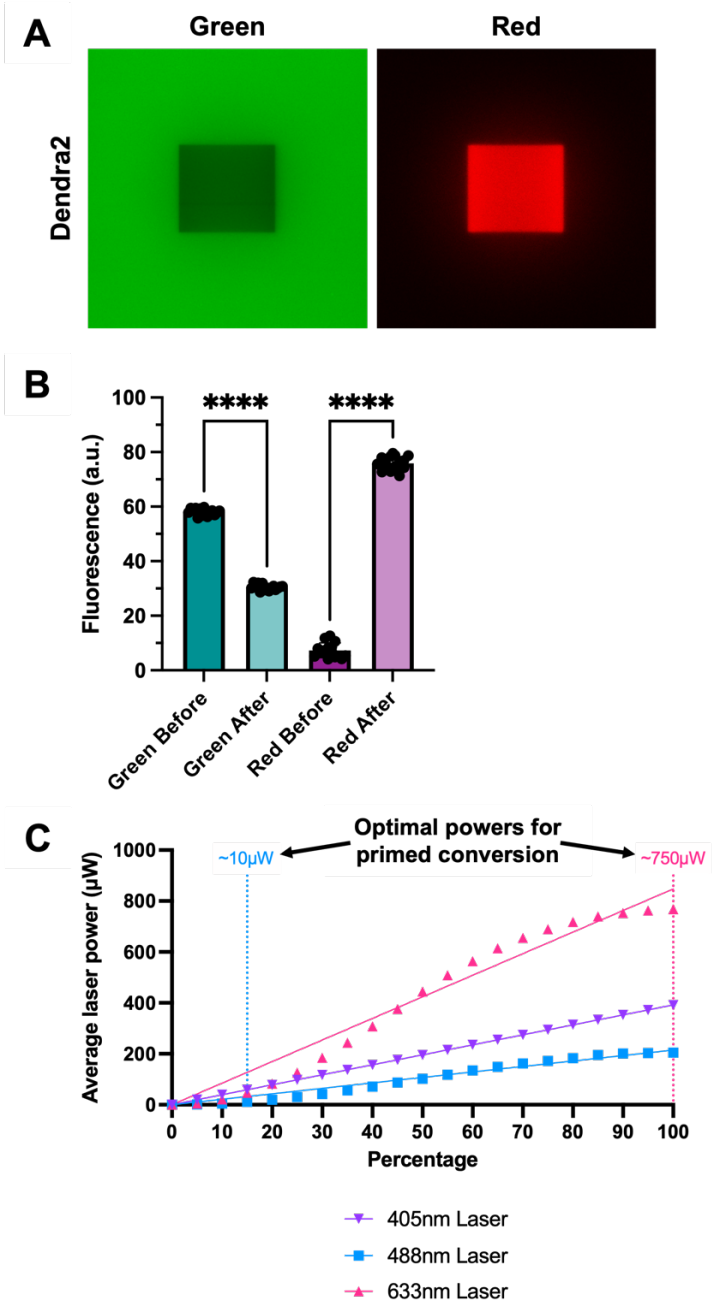


Fig. 53. Primed conversion using 488nm and 633nm simultaneous illumination. (A) Purified Dendra2 embedded in polyacrylamide gel was primed converted using 15% relative 488nm and 100% 633nm laser powers. (B) Raw intensity values of green and red fluorescence pre- and post- primed conversion of purified Dendra2 embedded in polyacrylamide gel. (n=15 ROIs for each condition, error bars: SD). Ordinary one-way ANOVA test. (C) Average illumination powers of the lasers used for primed conversion in A, and of a 405nm diode laser for comparison. Optimal laser powers used for primed conversion (10 μW for 488nm and 750 μW) depicted with dashed lines. A simple linear regression model was used to fit the measured values and is depicted with solid lines for each laser.

To confirm that primed conversion with 488nm and 633nm can be used with pr-FP variants other than Dendra2, several pr-FP variants were also expressed, purified and then embedded in polyacrylamide gels for further characterisation. Using the identified optimal power ratios for 488nm and 633nm light, primed conversion of pr-mEosFP, pr-mEos2, pr-mEos3.1 and pr-mEos4b could also be achieved **(Fig. 54A)**. Notably, the different pr-FPs showed differences in their primed conversion efficiency ranging from ~25% to ~130% relatively to Dendra2 (**Fig. 54B**).

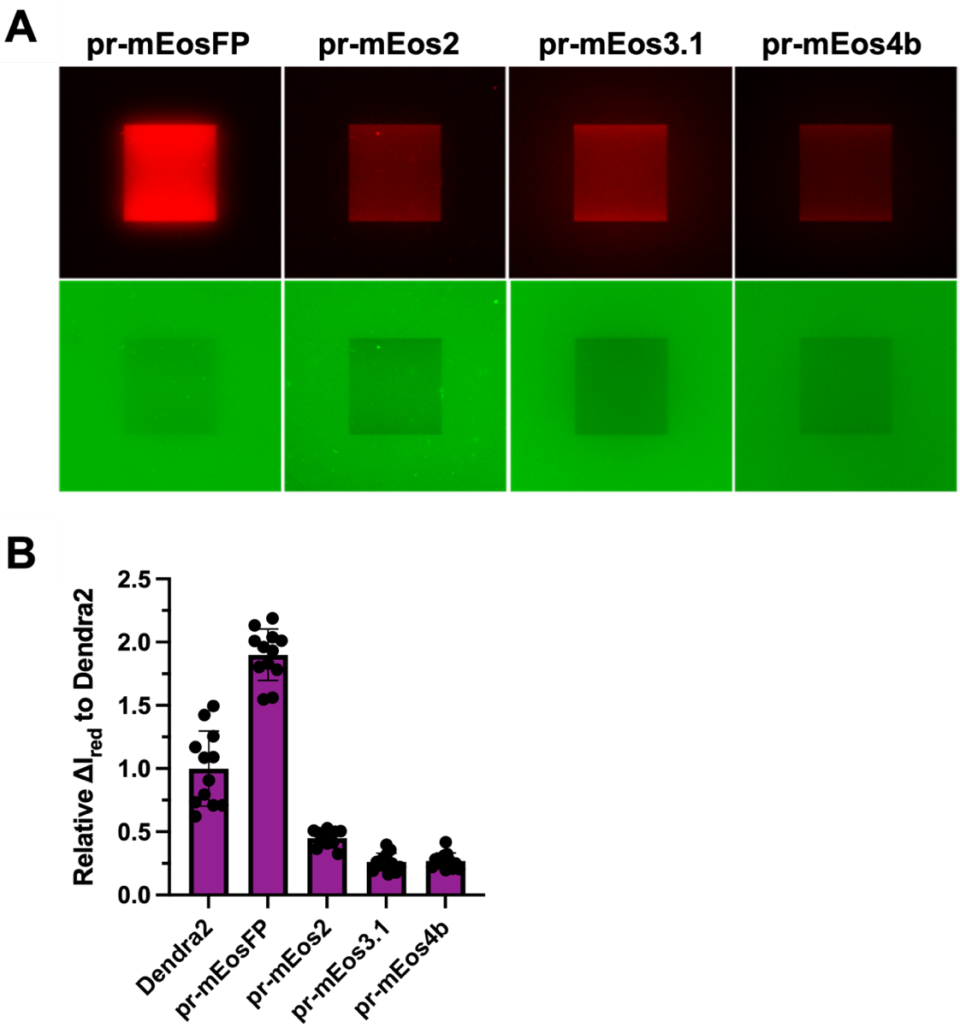


Fig. 54. Other pr-FPs can be also primed converted with 488nm and 633nm simultaneous illumination. (A) The FPs pr-mEosFP, pr-mEos2, pr-mEos3.1 and pr-mEos4b were expressed, purified, embedded in polyacrylamide gels and photoconverted using 488nm and 633nm simultaneous illumination in a confocal microscope. (B) Relative red intensity changes upon primed conversion using 488nm and 633nm simultaneous illumination normalised to average Dendra2 red intensity change. (n=15 ROIs for each condition, error bars: SD).

3.4 Rational engineering of primed conversion using the mEos protein family

Recently, the Pantazis lab (Mohr et al., 2017) showed that primed convertibility can be rationally engineered by introducing a single amino acid substitution. Among the FPs which were engineered, photoconvertible members of the mEos family were rendered primed convertible. The mEos FP family is a group of photochromic FPs consisting of both photoconvertible and photoswitchable proteins. All the members of the family were developed following rational and random protein engineering approaches mutating the parental tetrameric green-to-red photoconvertible protein mEos (Wiedenmann et al., 2004, McKinney et al., 2009, Zhang et al., 2012, Paez-Segala et al., 2015) **(Fig. 55)**. Thus, members of this protein family show a high percentage of sequence similarity and about 95% of their sequences is identical.

Primed conversion results showed that different pr- variants of mEos family exhibit different primed conversion efficiencies (**Fig. 54**). Interestingly, pr-mEosFP showed superior primed convertibility compared to other members of the same protein family and Dendra2 (**Fig. 54B**). Taking advantage of the differences in primed conversion efficiency, the high similarity between the mEos family FPs and the available knowledge of previous engineering efforts in this family, we decided to investigate which positions are responsible for the efficiency difference observed. To this end, the protein sequences of pr-mEosFP, pr-mEos2, pr-mEos3.1 and pr-mEos4b were aligned using the M-Coffee sequence aligner (Notredame et al., 2000). As shown in **Fig. 56**, the four pr-FP variants differ only in 12 positions, while the rest of the sequence is identical. To identify positions that may affect the primed convertibility of these variants, we followed two strategies.

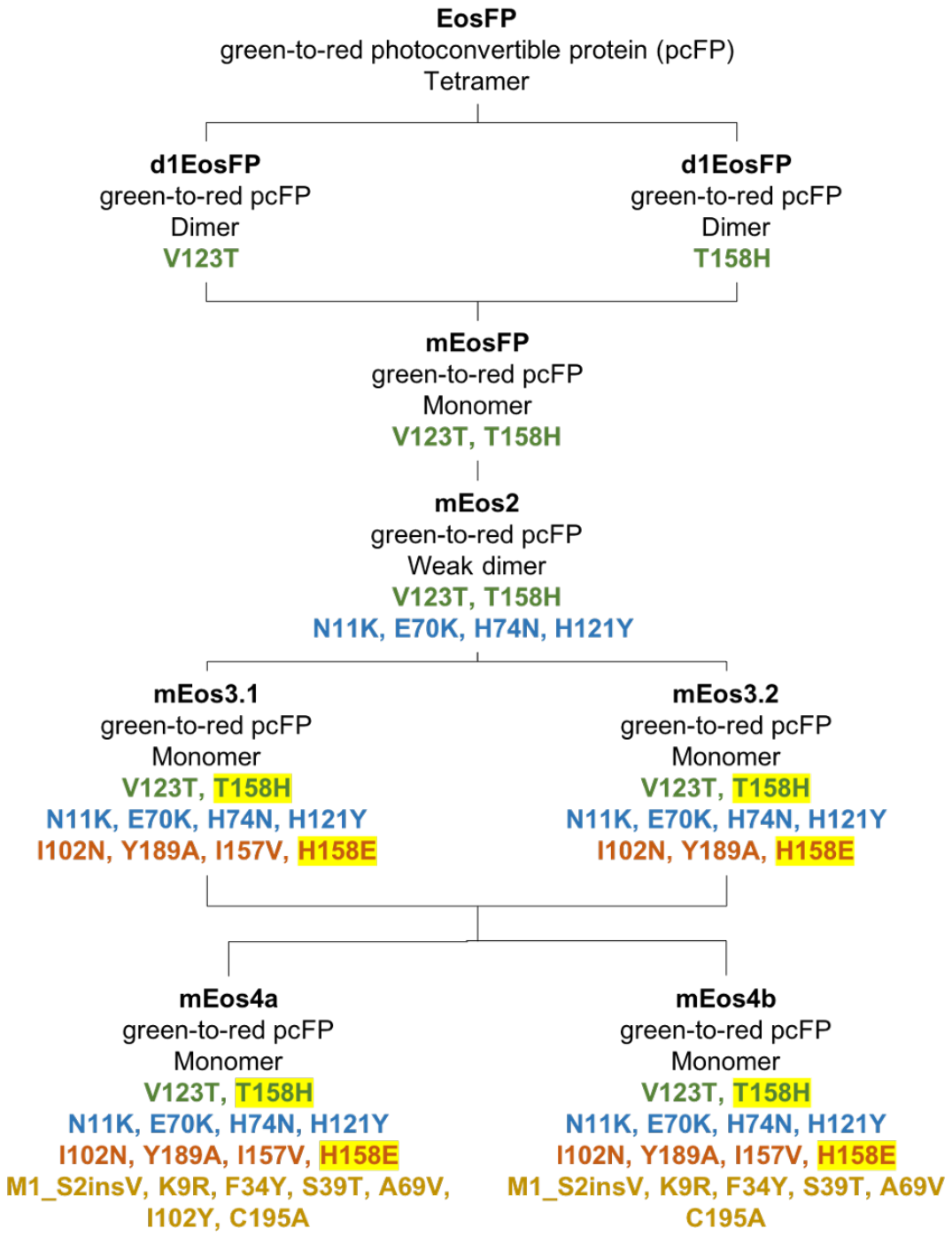


Fig. 55. mEos fluorescent protein family and mutations introduced to generate protein variants with different characteristics. All the members of the family were developed using rational or random protein engineering approaches. Position H158 (highlighted in yellow) has been mutated more than once and the variants mEos3.1, mEos3.2, mEos4a and mEos4b carry the mutated position H158E and not the T158H.

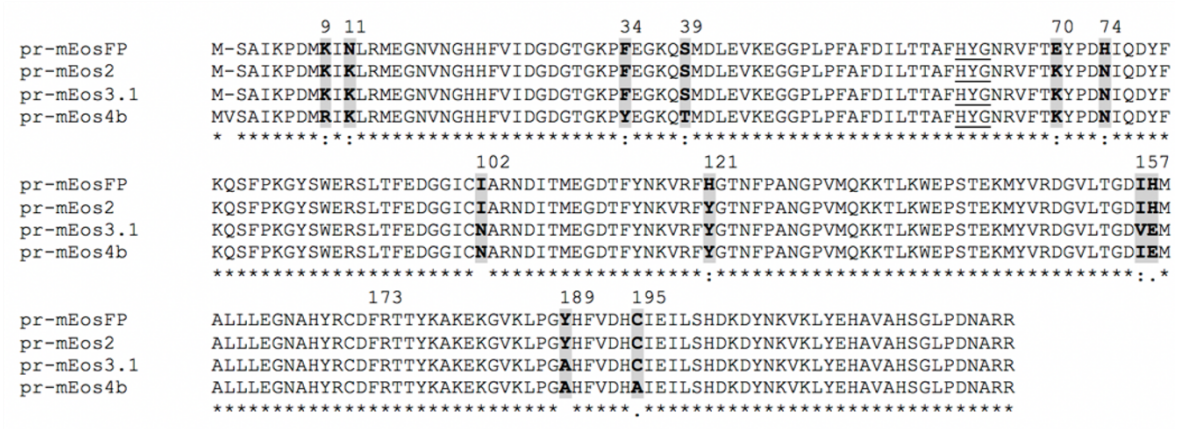


Fig. 56. Rational engineering of primed conversion using the mEos FP family. Sequence alignment of pr-mEosFP, pr-mEos2, pr-mEos3.1 and pr-mEos4b highlighting the 12 differences between the protein sequences.

First, to isolate positions positively affecting primed conversion, we annotated the positions in which pr-mEosFP uniquely differs from the other variants. Only four positions met this criterium (**Fig. 57A**): the positions N11, E70, H74 and H121 (position annotation of pr-mEosFP). These positions were introduced to the sequence of mEosFP to generate mEos2. After the introduction of these mutations to mEosFP, brightness increased but also weak dimeric interactions were noticed. To identify which position are more likely to affect these weak dimeric interactions, the structures of mEosFP and mEos2 were structurally imposed (**Fig. 57B**). The side chains of N11K and H121Y (orange and cyan, respectively) protrude to the external part of the barrel and the nature of substitutions (here: positively charged H to hydrophobic Y and polar uncharged N to positive charged K) indicate that these positions could affect protein-protein interactions. The positions 70 and 74 are relatively close to the chromophore and could potentially influence its conformation. In the 3D structure of pr-mEosFP these two residues form a turn between the third and fourth β-strand. As shown by the structural imposition, the introduction of E70K and H74N distort the positioning of the side chains inside the chromophore pocket and thus the secondary structures do not overlap.

Interestingly, A60 changes its secondary structure between the two mutants, demonstrating that also the chromophore conformation can be affected.

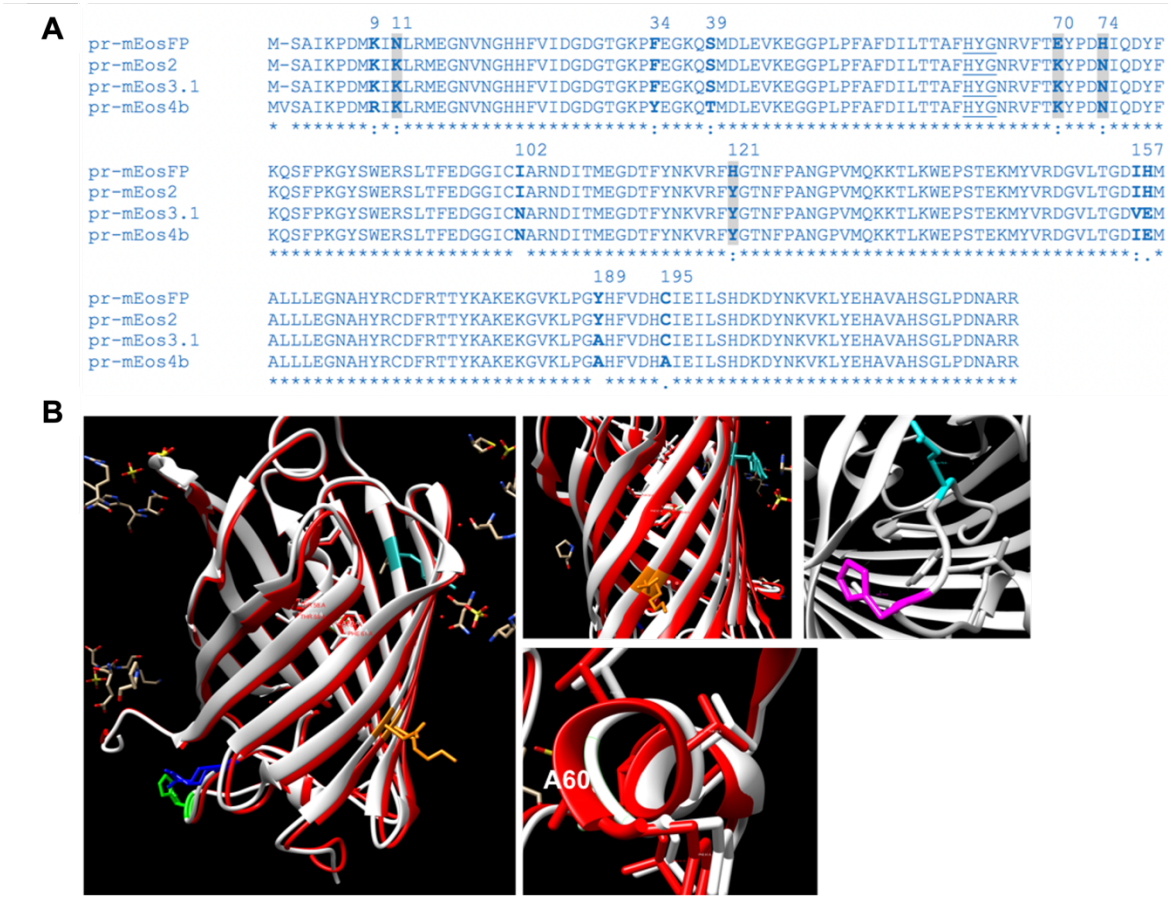


Fig. 57. Positions that could affect positively primed conversion. (A) Sequence alignment of the FPs pr-mEosFP, pr-mEos2, pr-mEos3.1 and pr-mEos4b. The positions that could positively affect primed conversion are highlighted with grey. (B) 3D structures of proteins mEosFP (PDB: 3P8U) and mEos2 (PBD:3S05) imposed and visualised using Chimera (Pettersen et al., 2004). The positions that could affect primed conversion positively are labelled with different colours.

To identify positions that negatively affect primed conversion, we annotated the positions in which pr-mEos4b, the variant that shows the lowest primed convertibility, uniquely differs from the pr-mEosFP. As shown in the alignment (**Fig. 58A**) pr-mEos4b differs uniquely from the other pr-FP variants in four positions (R9, Y34, T39 and A195; position annotation of pr-mEosFP). The 3D structure of mEos4b illustrates that all the amino acids in these positions protrude their side chains to the external region of the barrel. However, localisation of Y34 exactly on a turn between

two β-strands could possibly affect the conformation of the two strands and indirectly the chromophore environment. Interestingly, the secondary structure of A60 again is changed that could affect the chromophore.

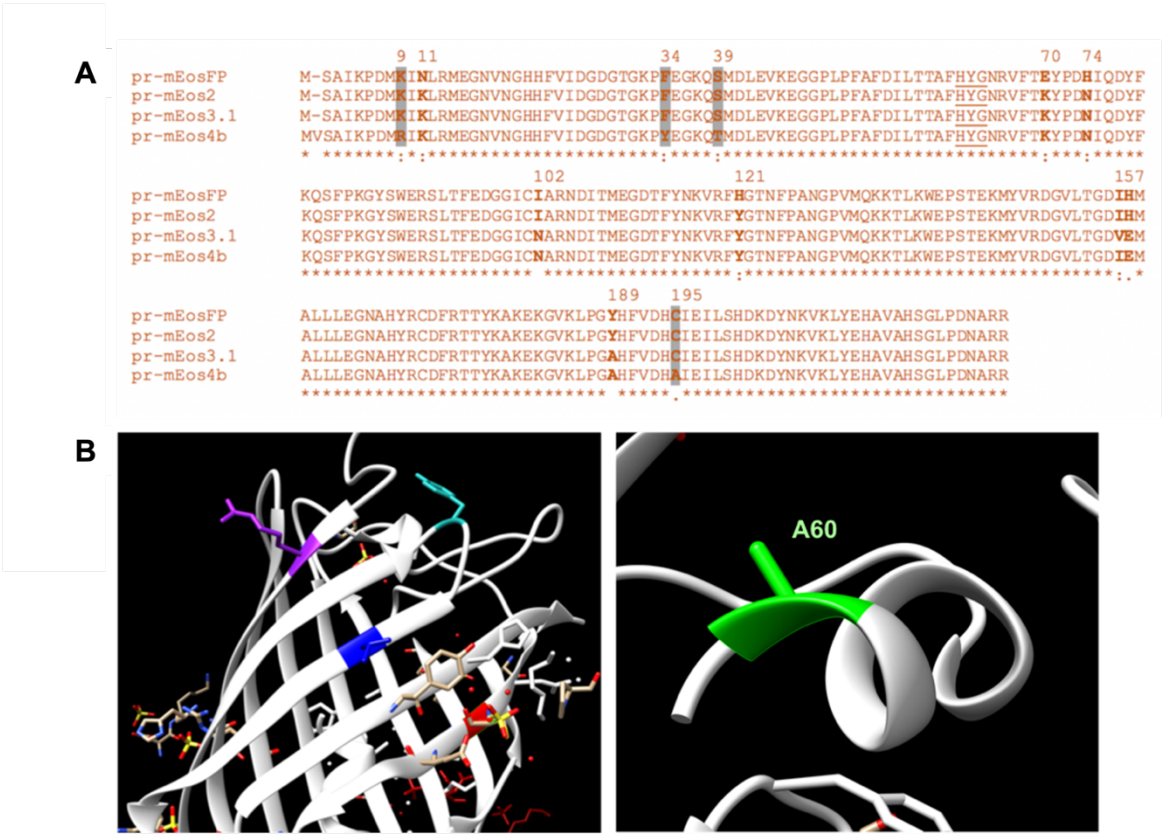


Fig. 58. Positions that could affect negatively primed conversion. (A) Sequence alignment of the FPs pr-mEosFP, pr-mEos2, pr-mEos3.1 and pr-mEos4b. The positions that could negatively affect primed conversion are highlighted with grey. (B) 3D structure of protein mEos4b (PDB: 6YLS) visualised using Chimera (Pettersen et al., 2004). The positions that could affect primed conversion negatively are labelled with different colours.

To investigate whether the annotated positions affect primed conversion efficiency, site-directed mutagenesis was used and two strategies were followed (**Fig. 59**). First, mutations at positions which we identified to potentially improve primed conversion (N11, E70, H74 and H121; position annotation of pr-mEosFP)) were introduced to the sequence of pr-mEos4b to assess whether primed convertibility could be improved. Secondly, mutations identified at positions that could negatively affect primed conversion were introduced to the sequence of pr-mEosFP

to evaluate whether primed convertibility could be reduced. The brightness of the variants was also compared to the brightness of Dendra2 to monitor any other changes to the variant's fluorescence. As shown in **Fig. 60**, the introduction of E70K and H74N to pr-mEosFP led to fluorescence loss, whereas the introduction of N11K and H121Y affected negatively both primed conversion efficiency and brightness. The introduction of R10K and A196C to pr-mEos4b led to fluorescence loss, while the introduction of Y35F and T40S increased both primed conversion efficiency and the brightness of the variants. Notably, the introduction of T40S led to an impressive 23-fold increase of primed conversion efficiency of the pr-mEos4b variant. These results confirmed our mutagenesis hypothesis and the majority of the positions showed either negative or positive effect to primed convertibility as expected.

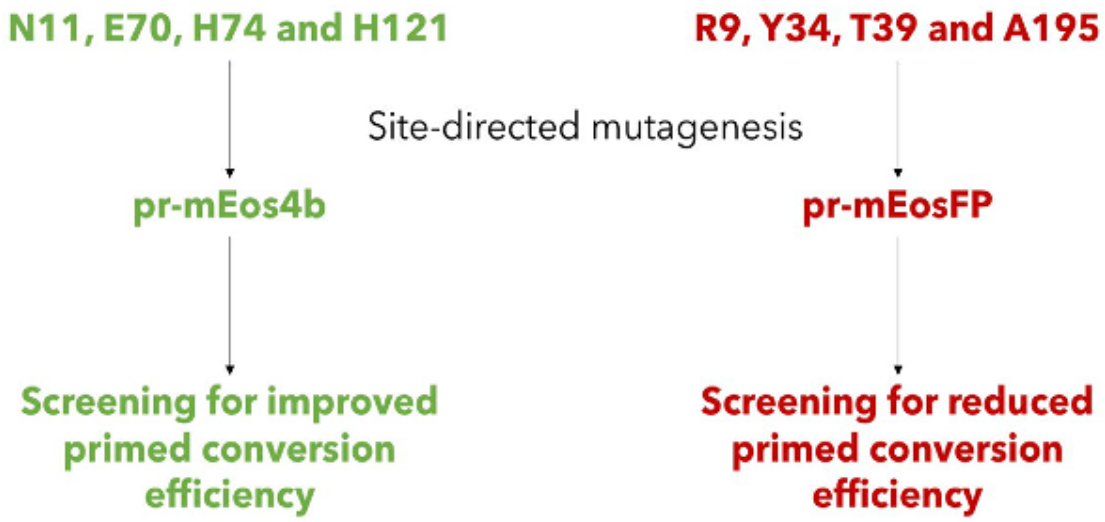


Fig. 59. Site directed mutagenesis plan to identify positions that affect primed conversion. Following the sequence analysis, we decided to follow two mutagenesis approaches. Mutations that can affect positively primed conversion were introduced to pr-mEos4b and mutations that can affect negatively primed conversion were introduced to pr-mEosFP.

As the pr-mEos4b-T40S mutant showed pronounced primed convertibility, we set out to test whether the introduction of this single mutation can render mEos4b primed convertible. To do this, the positive mutagenesis mutations were introduced

to the sequence of mEos4b by site-directed mutagenesis. As shown in **Fig. 61**, all mutations led to decrease in primed conversion efficiency and brightness, suggesting that the introduction of T40S is not sufficient to engineer primed convertibility and highlighted the fundamental role of position 69 for primed conversion. Interestingly, the introduction of R10K and A196C to mEos4b does not lead to fluorescence loss.

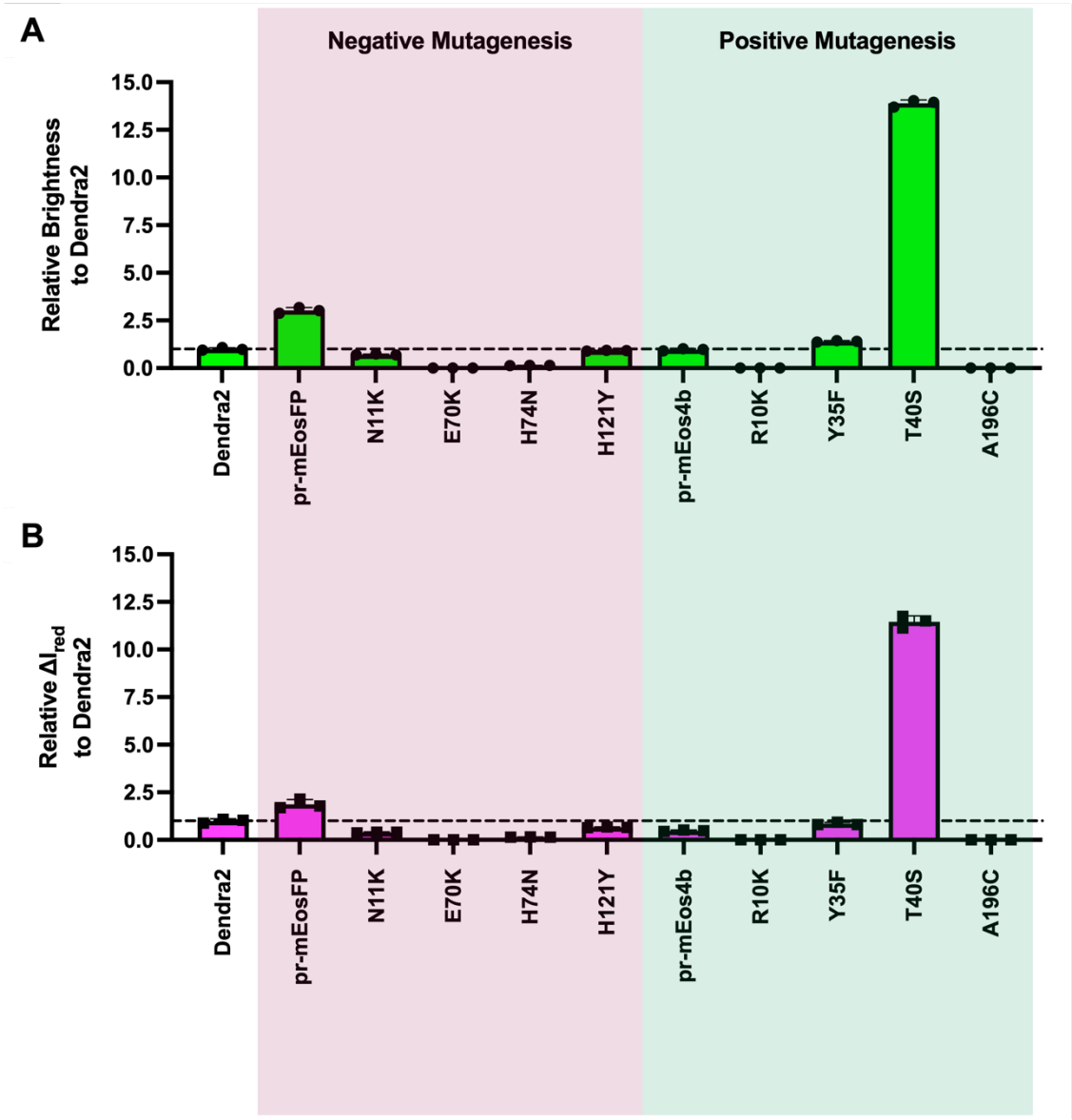


Fig. 60. Site-directed mutagenesis of pr-mEosFP and pr-mEos4b suggests that position 40 is important for improving primed conversion efficiency. (A) Relative brightness of mutated variants normalised to the average brightness of Dendra2. (n=3 ROIs for each condition, error bars: SD). (B) Relative red intensity changes upon primed conversion using 488nm and 633nm simultaneous illumination normalised to average Dendra2 red intensity change. (n=3 ROIs for each condition, error bars: SD). The results confirmed our hypothesis that specific positions would affect primed conversion either negatively or positively.

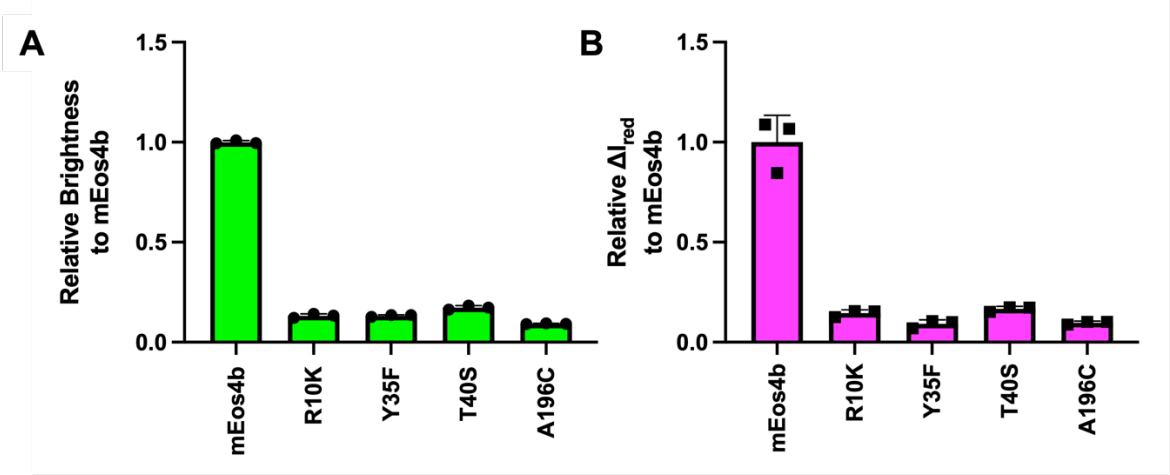


Fig. 61. Site-directed mutagenesis of mEos4b shows that T40S is not sufficient to engineer primed convertibility. (A) Relative brightness of mutated variants normalised to the average brightness of mEos4b. (n=3 ROIs for each condition, error bars: SD). (B) Relative red intensity changes upon primed conversion using 488nm and 633nm simultaneous illumination normalised to average mEos4b red intensity change. (n=3 ROIs for each condition, error bars: SD). The results demonstrate the fundamental role of position 69 from primed conversion.

3.5 X-ray crystallography of pr-mEosFP

To understand the primed conversion mechanism at the atomic level and guide a more structure-based FP engineering approach as previously described (Nasu et al., 2021), we conducted a series of protein crystallisation experiments of pr-mEosFP followed by X-ray crystallography. To this end, pr-mEosFP was expressed in bacteria on large scale and subsequently purified using affinity chromatography to produce highly concentrated protein solutions needed for the initial crystallisation experiments (see **Materials and Methods, Protein purification**) (**Fig. 62**).

Although the structure of the mEosFP green state has been previously solved, our attempts to replicate the crystallisation conditions did not yield any protein crystals for pr-mEosFP. To this end, we initially screened 50 crystallisation conditions using the commercially available Crystal Screen kit from Hampton Research, which contains solutions with different salts, buffers and precipitants that have been

previously used to crystallise a variety of proteins (Jancarik and Kim, 1991). An in-house hanging drop method (1:1 protein:solution ratio for each drop) was used to setup the initial crystallisation screen consisting of simple 24-well cell culture plates, 19mm round coverslips and silicone grease bought from Amazon for sealing each well (**Fig. 63A-B**). After each plate preparation each drop was examined under a stereoscope and then subsequently monitored every day for crystal formation (**Fig. 63C**).

After five days of incubation, crystals were present in solution 21 (0.2M Magnesium acetate tetrahydrate, 0.1M Sodium cacodylate trihydrate pH 6.5 and 30% v/v (+/-)-2-Methyl-2,4-pentanediol) of the Crystal Screen kit, with an average size of around 90-150μm (**Fig. 64A-B**). Green fluorescence was detected, while individual crystals were successfully primed converted using 488nm and 633nm simultaneous illumination in the confocal microscope (**Fig. 64C-F**). After direct cryopreservation, X-ray crystallography was conducted at the Diamond Light Source (UK's national synchrotron light source) at the beam I24 in collaboration with Dr Sam Horrell. Unfortunately, the crystallographic data showed big dark diffraction spots (**Fig. 64G**) which indicates that the content of the individual crystals was salt instead of protein.

Considering that the initial screen proved futile, we decided to start a new more extensive screening of different conditions with the support of Dr Marc Morgan at the Centre for Structural Biology at Imperial College London. To this end, a robot-automated sitting drop method (1:1 protein:solution ratio for each drop) was used in which 200nl of each screening solution was mixed with 200nl of concentrated pr-mEosFP protein. In total, 192 conditions (PEG Ion 1, PEG Ion 2 and Index crystallisation screening kits from Hampton Research) were tested. After two weeks of incubation, yellow crystals were present in solution #77 of the Index screening kit

(0.2 M Lithium sulfate monohydrate, 0.1 M Tris pH 8.5, 25% w/v Polyethylene glycol (PEG) 3,350) (**Fig. 65A-B**) which were cryopreserved and sent to I24 at the Diamond Light source for X-ray crystallography. The crystallographic data confirmed the protein nature of the crystals, yet no high resolution diffraction spots were detected (**Fig. 65C**), rendering further processing of the data impossible.

To improve the quality of the acquired protein crystals, we set out to run two optimisation screens in which several concentrations of the precipitant (PEG 3,350 from 20% to 31% with 1% increments), salt (Lithium sulfate from 0.05M to 0.4M with 0.05M increments) and pH (ranging from 7.5 to 9.0 with 0.22 increments) were tested. Again, a robot-automated sitting drop method (1:1 protein:solution ratio for each drop) was used. After one day of incubation, yellow crystals were formed in the PEG/pH screening plate (PEG 22% and pH 8.35) (**Fig. 66A-B**), whereas no crystals were formed in the PEG/Lithium sulfate screening plate. Individual crystals were cryopreserved and sent for X-ray crystallographic analysis. As shown in **Fig. 66C**, diffraction spots confirmed again the protein nature of the crystals, yet high resolution spots were not detected. This time the resolution improved to around 4-4.5Å which permitted molecular replacement using the already solved structure of mEosFP. However, manual improvement of the structure proved not possible, as the electron density map could not resolve the positions of individual atoms. Altogether, these data suggest that further optimisation of the crystallisation conditions and/or the cryopreservation method is needed.

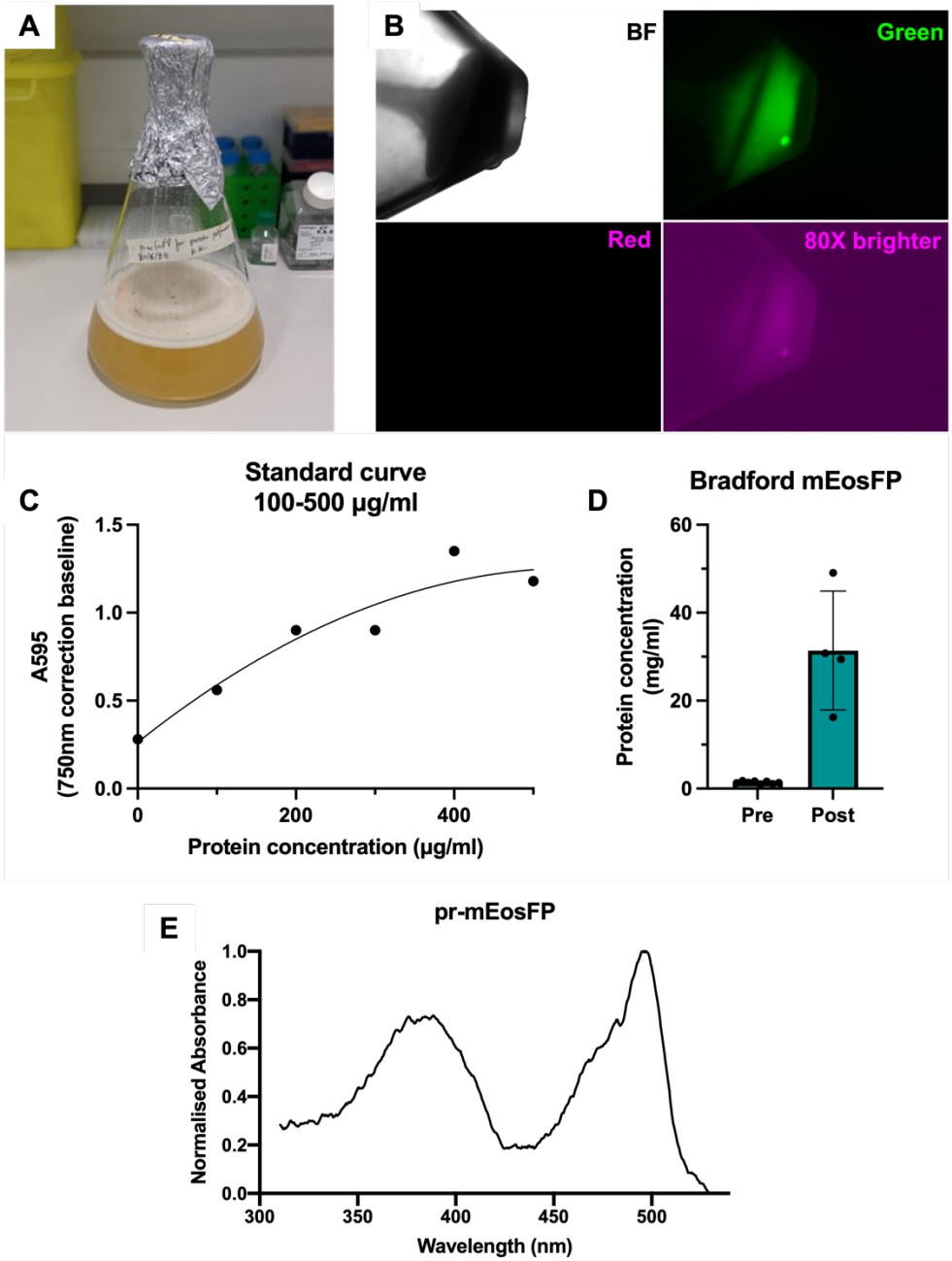


Fig. 62. Successful large-scale pr-mEosFP protein expression and characterisation. (A) A 2L bacterial culture for pr-mEosFP purification. (B) pr-mEosFP fluorescent bacterial pellets on the bottom of a 50ml falcon tube confirmed the induction of the FP expression. (C) Protein concentration after affinity chromatography was calculated using the Bradford method and interpolation from a standard curve. (Polynomial fitting according to manufacturer's instructions). (D) Protein solutions where further concentrated using desalting columns with a 10K molecular weight cut-off. Here, the concentration of pr-mEosFP increased from around 3mg/ml to around 30mg/ml, in the range of preferable protein concentrations for crystallographic experiments. (D) The identity of the purified protein was confirmed by absorbance measurements which showed the typical peaks of the green neutral and anionic form of the pr-mEosFP chromophore.

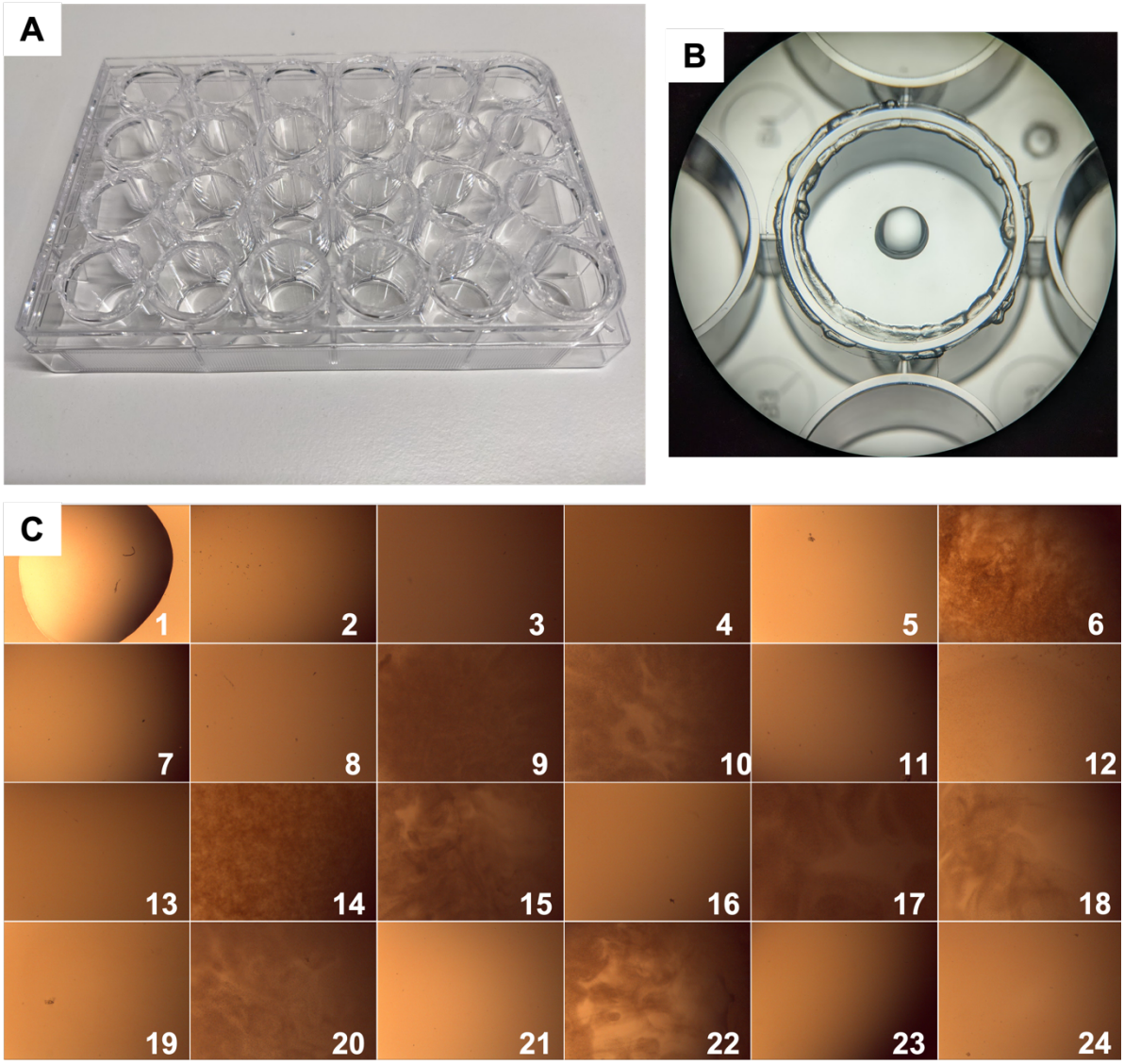


Fig. 63. Setup of the in-house hanging drop crystallisation setup. (A) A typical 24-well cell culture plate that was used for the in-house crystallisation screen. (B) Representative image of a single well showing the hanging drop setup. The liquid drop is in the middle of a 19mm glass coverslip which sits onto the walls of an individual well in the 24-well plate. Each well is sealed with silicone grease bought by Amazon. The total cost of 1 plate is less than £0.20. (C) Representative image of drops directly after setting up a crystallisation screen. In (1) a clear whole drop can be seen, while several conditions (2-24) form an amorphous precipitate.

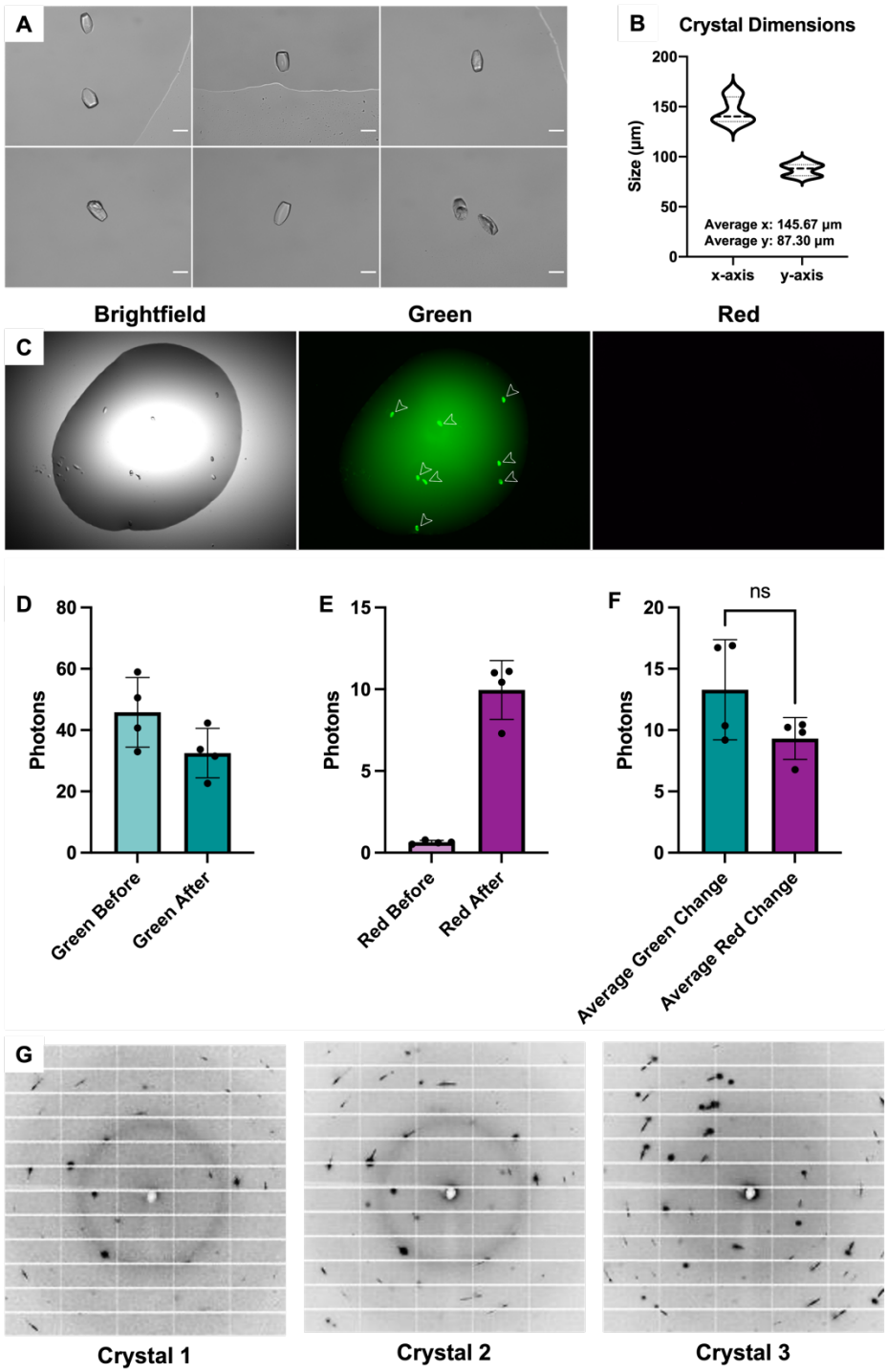


Fig. 64. Initial crystallisation screen resulted in salt crystals instead of protein crystals. (A) Representative crystals formed in solution 21 of the Crystal Screen kit from Hampton Research. (B) Average dimensions of crystals formed in solution 21. (n=8 crystals). (C) Representative fluorescence images of crystals formed in solution 21 sowing bright green fluorescence. (D-F) Single crystals formed in solution 21 can be primed converted in a confocal microscope. (n=4 crystals and values are presented as counted photons). (G) Diffraction pattern of single crystals formed in solution 21. The big dark spots indicate that the crystals are made of salt. The fluorescence of the crystals in C can be attributed to pr-mEosFP molecules trapped on the surface of the crystals which did not detach during the extensive washing.

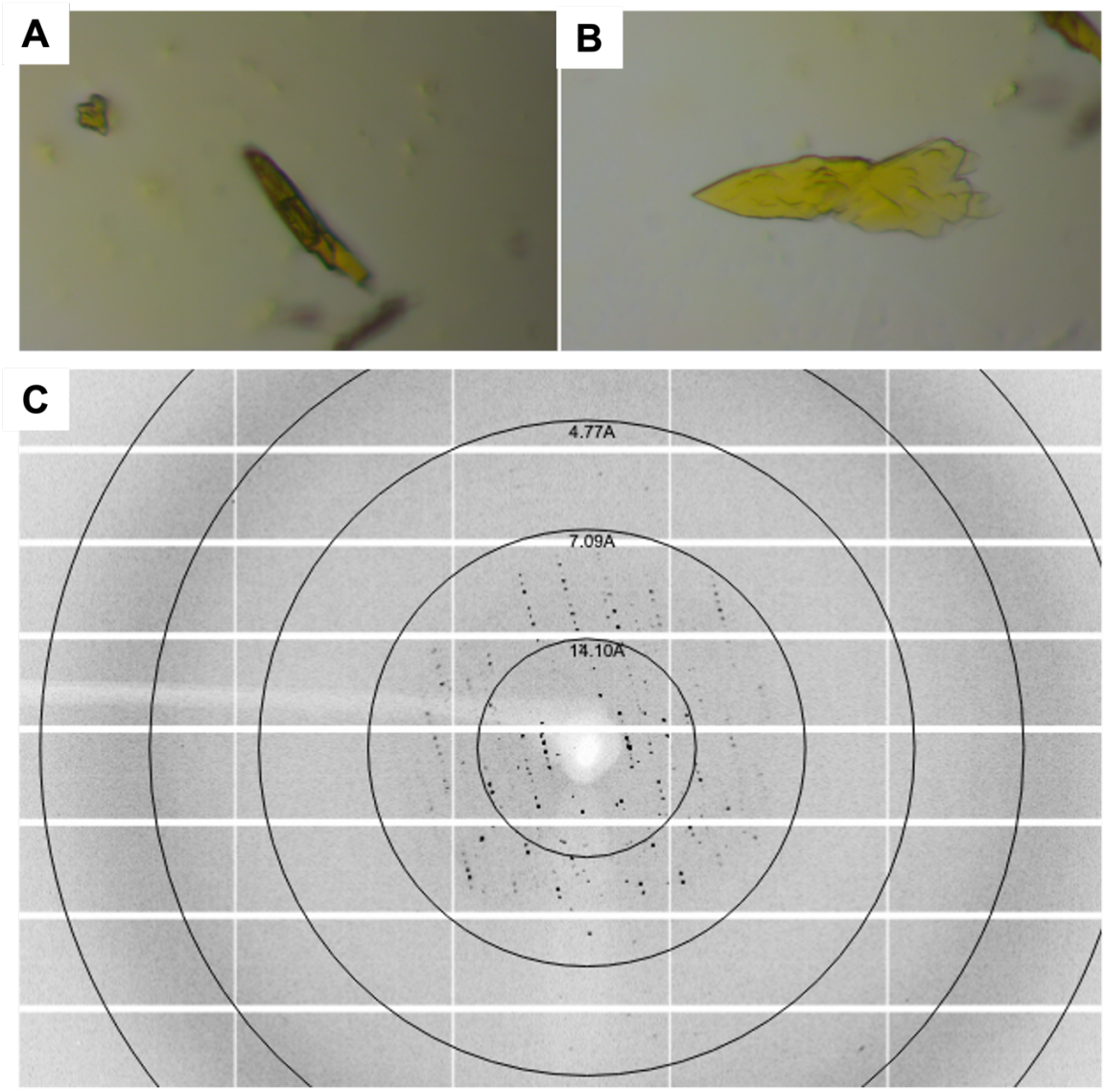


Fig. 65. pr-mEosFP protein crystals and representative diffraction pattern upon X-ray irradiation. (A-B) The second more extensive screening yielded single yellow crystals which were then sent for X-ray crystallography analysis. (C) Representative diffraction pattern of a single yellow crystal, like the ones in A and B. Please note the individual small black spots in the low resolution regions confirming that the crystals are made of protein.

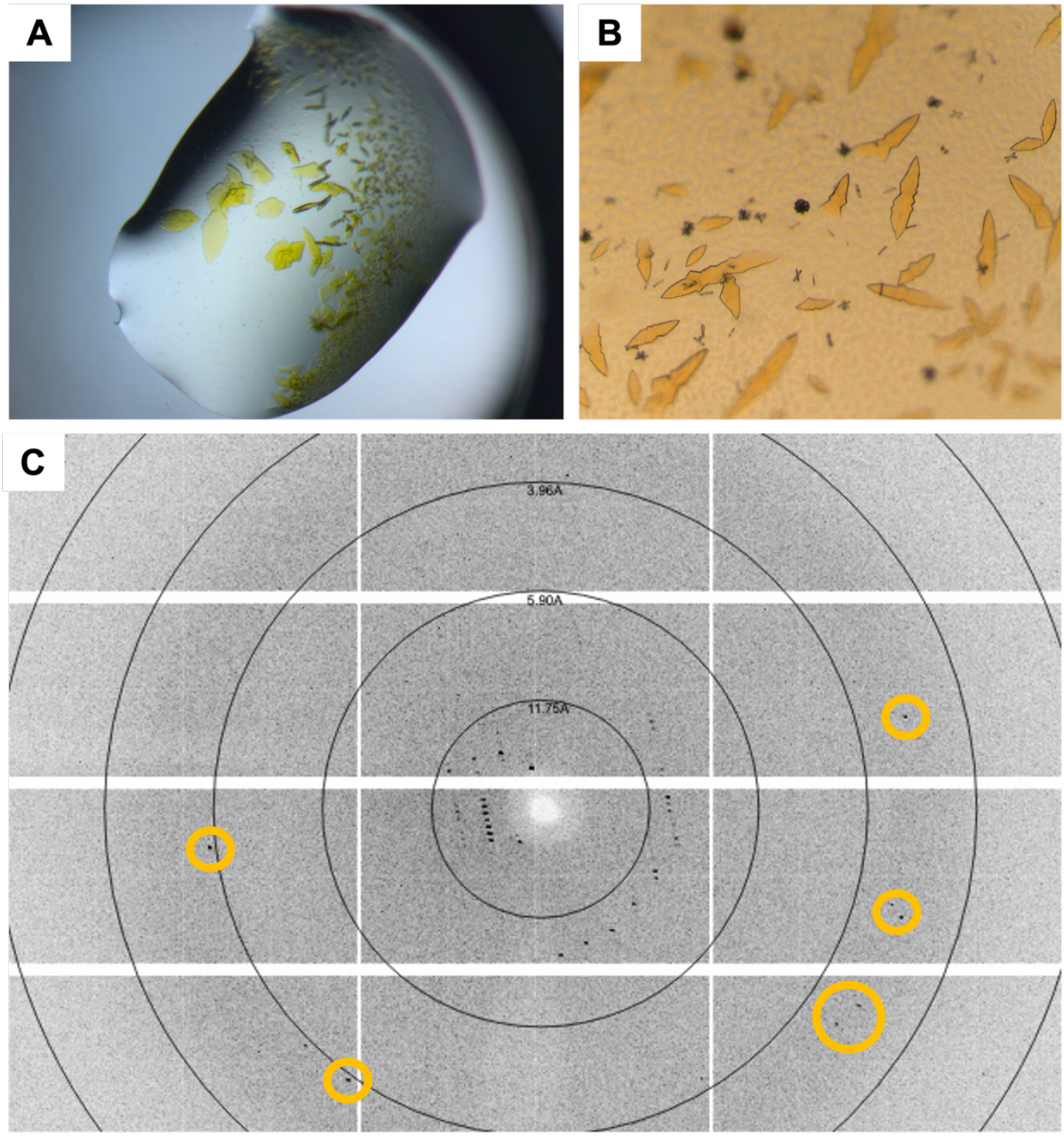


Fig. 66. pr-mEosFP protein crystals of the optimisation screening and representative diffraction pattern upon X-ray irradiation. (A-B) The optimisation screening yielded nicely formed single yellow crystals which were then sent for X-ray crystallography analysis. (C) Representative diffraction pattern of a single yellow crystal, like the ones in A and B. Please note that there are individual small black spots in higher resolution regions (circled with yellow line).

3.6 Evaluation of primed conversion implementation in a single-objective light-sheet microscope

Despite the advantages of primed conversion for precise cell labelling and tracking, the implementation of the technique into a volumetric imaging system is lacking. To this end, in collaboration with Dr Chris Rowlands, we developed a single-objective light-sheet microscope with primed conversion capabilities (pcOPM) (**Fig. 67**) based on previously introduced Oblique Plane Microscopy (OPM) designs (Dunsby, 2008, Bouchard et al., 2015, Yang et al., 2019). The main advantage of OPM designs is that they can perform light-sheet imaging with a single objective overcoming the geometry constraints of sample placement between two orthogonal objectives in other light-sheet setups (Wu et al., 2011). To perform primed conversion using the pcOPM, light from the priming 488nm and the converting 685nm diode lasers is expanded onto a set of galvo mirrors which are used for scanning in x- and y- axis. Then, the two lasers overlap at the focus by the scan lens and are subsequently merged onto the sample for primed conversion. When conventional OPM imaging is to be performed, a narrow 488nm beam strikes the edge of the back focal plane of Objective 1. The resulting tilted light sheet is imaged onto a tilted plane, which is reimaged onto two cameras by Objective 3.

In order to assess primed conversion efficiency in the pcOPM system, Dendra2 protein was expressed, purified and embedded in polyacrylamide gel. Then, the gel was imaged at the pcOPM primed conversion mode using the priming 488nm and converting 685nm lasers. The overlapping focus of the two lasers was scanned through the sample at different focal points generating a smiley pattern. As shown in **Fig. 68A**, primed conversion of Dednra2 was successful, producing a sharp-edged smiley across the protein gel. One second simultaneous dual laser illumination led to a significant decrease of green Dendra2 fluorescence and

significant increase of the red fluorescence of photoconverted Dendra2 across the smiley pattern (**Fig. 68B**).

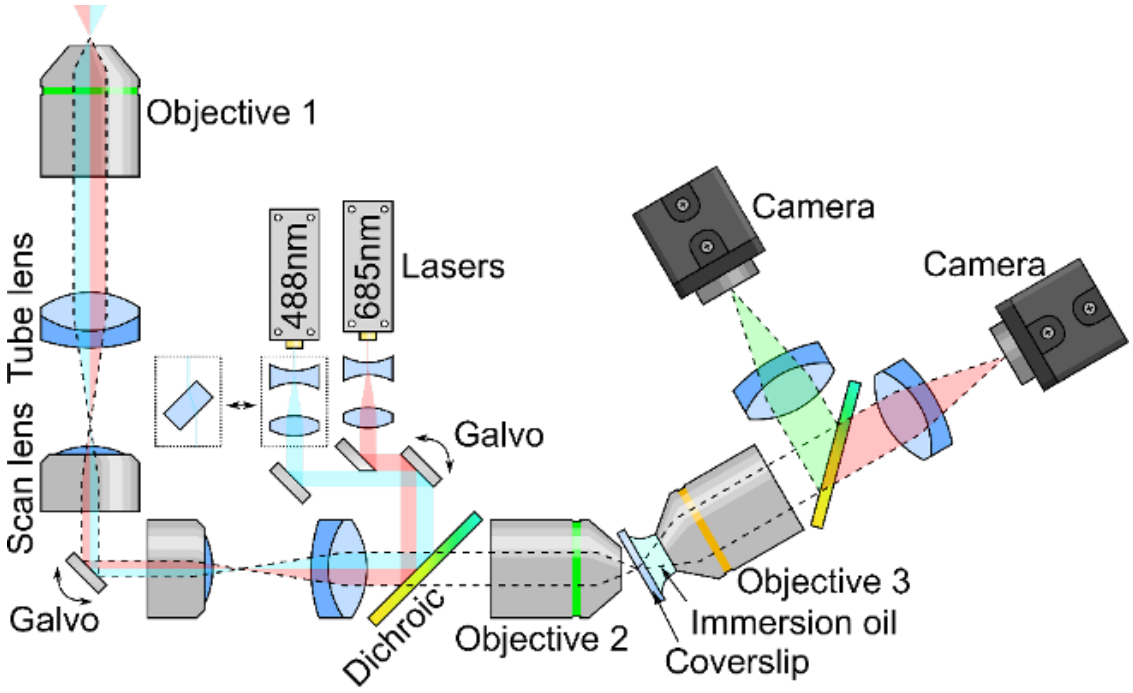


Fig 67. Schematic diagram of the single-objective primed conversion light-sheet microscope (pcOPM). The microscope can operate as a conventional eSPIM system or as a primed conversion excitation system. Briefly, for primed conversion setup, which is shown here, light from the 488nm and 685nm diode lasers is expanded onto a set of galvo mirrors (x- and y-axis scanning). Then, the two lasers overlap at the focus by the scan lens and are subsequently merged onto the sample. In the conventional OPM imaging configuration, no 685nm beam is used and a narrow 488nm beam strikes the edge of the back focal plane of Objective 1. The resulting tilted light sheet is imaged onto a tilted plane, which is reimaged onto two cameras (observing different colour channels) by Objective 3. *(credit: Dr Chris Rowlands).*

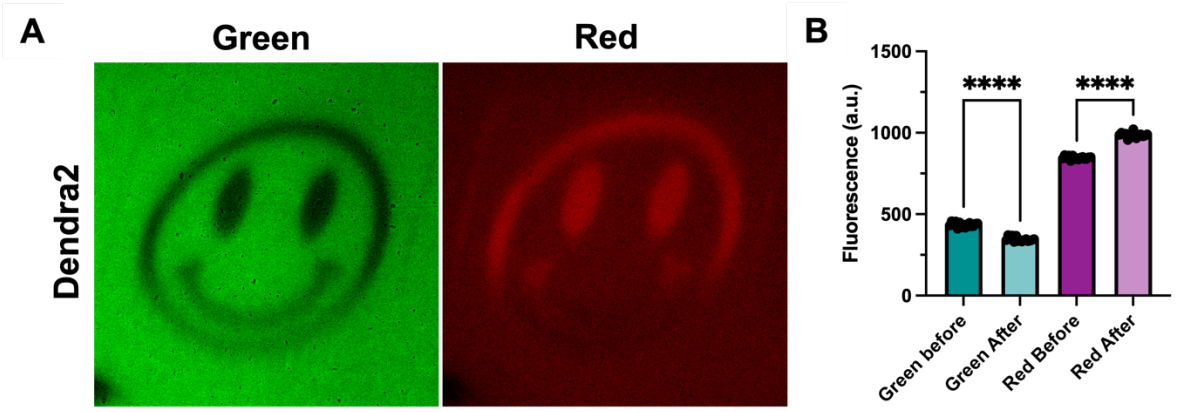


Fig. 68. Successful primed conversion of Dendra2 using the pcOPM. (A) Purified Dendra2 embedded in polyacrylamide gel was primed converted using 488nm and 685nm lasers to produce a smiley pattern. (B) Raw intensity values of green and red fluorescence pre- and post- primed conversion of purified Dendra2 embedded in polyacrylamide gel. (n=15 ROIs for each condition, error bars: SD). Ordinary one-way ANOVA test.

To assess whether primed conversion can be also achieved *in vivo*, we imaged at the pcOPM primed conversion mode PhOTO-N transgenic zebrafish which ubiquitously express nuclear Dendra2 (Dempsey et al., 2012a). Primed conversion of around 10% relative red signal increase was observed in individual cells after 1 min illumination (**Fig. 69**). However, the heterogeneous photoconversion observed across the imaging path, suggests that further optimisation is needed (**Fig. 69**).

3.7 Discussion on primed conversion

The rapid development of molecular biology techniques revealed in more detail the complex biochemical nature of cells which govern the processes of life. Since the discovery and the subsequent protein engineering of the GFP, several new microscopy techniques and imaging probes have developed, pushing the boundaries of what can be labelled and how it can be imaged.

Primed conversion was discovered as a novel and fundamentally different method for axially confined and less phototoxic photoconversion. The main difference of primed conversion in comparison with traditional 405nm photoconversion is that primed conversion is a dual illumination process. In primed conversion, the simultaneous illumination of a photoconvertible FP, such as Dendra2, with 488nm and near-infrared (730nm) light leads to spectral changes similar to traditional 405nm photoconversion. The same red species are produced by using either primed conversion or traditional photoconversion, yet with the added benefit of axial confinement for primed conversion. Recently, the initially uncharacterised "primed" state was identified as a "dark" T_1 triplet state which can absorb a wide range of red to near-infrared light, spanning from ~600-850nm. This discovery opened the way for primed conversion to overcome its niche existence, as commercially available lasers, such as HeNe 633nm laser, could be now used for successful primed conversion in confocal laser scanning microscopes (**Fig. 53-54**).

Furthermore, the simple rational engineering of primed conversion extended the platform of available pr-FPs which possess different characteristics, such as brightness and oligomerisation states.

Despite the recent advances in terms of understanding the nature of the process, primed conversion efficiency is still inferior to traditional 405nm photoconversion. To this end, we set out to develop a new screening methodology (**Fig. 48**) that would be used for semi-rational engineering of pr-FPs to improve primed conversion efficiency. After successfully optimising primed conversion conditions using 488nm and 633nm simultaneous illumination (**Fig. 53-54**), we observed that different pr-FPs, members of the mEos protein family (**Fig. 55**), exhibit differential primed conversion efficiencies (**Fig. 54**). We took advantage of this knowledge to identify positions that could affect primed conversion (**Fig. 56-59**) and we used site-directed mutagenesis to test our hypothesis. We demonstrated that the substitution of position 40 (pr-mEosFP sequence annotation) to a Serine in pr-mEos4b led to dramatic increase of primed conversion efficiency (**Fig. 60**). However, the introduction of this mutation to the non-primed convertible parental protein mEos4b did not render it primed convertible (**Fig. 61**), suggesting that Serine in position 40 probably stabilises the changes established on the chromophore niche by the substitution to Threonine at position 69.

Furthermore, in order to understand primed conversion at the atomic level, we focused our efforts to crystallise pr-mEosFP which was the pr-FP variant with the highest primed conversion efficiency at that time. After extensive screening, we identified and optimised the crystallisation conditions for pr-mEosFP (**Fig. 63-66**). Despite our crystallisation efforts increased progressively the quality of the crystals and their diffraction, we did not manage to produce data of sufficient resolution to produce a final and accurate structural model of pr-mEosFP. Currently, we are

evaluating methodologies to further improve the quality of the crystals, such as microseeding (Oswald et al., 2008). In the future, we aspire to use the produced crystals for time-resolved serial X-ray crystallography (Baxter et al., 2022). In such experiments, single microcrystals will be primed converted *in situ*, cryopreserved and subsequently analysed to produce a "time-lapse" of the chromophore during primed conversion. In addition, as we would like to solve both the 405nm photoconverted and primed converted state of pr-mEosFP, we aim to use the solved structures for molecular dynamics-based protein engineering (Lu et al., 2021), to identify more positions that could affect primed conversion.

As primed conversion has been mainly restricted to confocal laser scanning microscopes, we developed a single-objective light-sheet microscope in collaboration with the Rowland's lab at the Department of Bioengineering at Imperial College London. The Rowland's lab built the system with our support and we set out to characterise primed conversion implementation both *in vitro* and *in vivo* (**Fig. 68-69**). Although primed conversion of purified Dendra2 was impressively successful, *in vivo* primed conversion efficiency of nuclear Dendra2 in a zebrafish transgenic model was very weak. Considering the heterogeneous primed conversion of Dendra2 across the x-axis in the transgenic zebrafish, we reasoned that light scattering affects the overlapping of the two laser beams and their power density at the focus, a critical outcome that could lead to poor photoconversion efficiency. In the future, we aim to optimise primed conversion efficiency using 2D cell cultures and simpler 3D models, such as tumour organoids in collaboration with Dr Pascal Meier at Institute of Cancer Research.

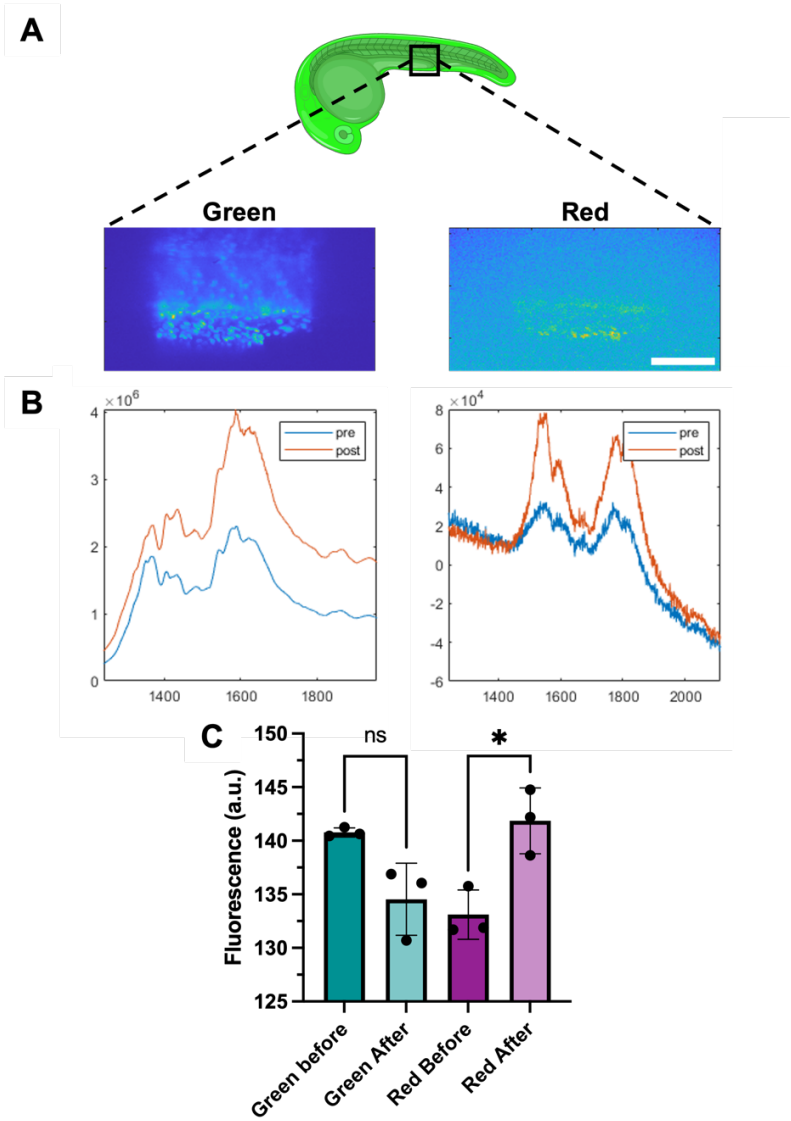


Fig. 69. Successful *in vivo* primed conversion using the pcOPM system. (A) Representative images of a PhOTO-N transgenic zebrafish showing a weakly primed converted region of the trunk depicted with rectangular in the schematic. Scale bar, 500 μm. (B) Raw intensity profile lines showing the decrease in the green fluorescence and the weak increase of red fluorescence across an x- section of the primed converted region. (C) Raw intensity values of green and red fluorescence pre- and post- primed conversion in a PhOTO-N zebrafish. (n=3 ROIs for each condition, error bars: SD). Ordinary one-way ANOVA test. *(Schematic in A was created with Biorender.com)*

Chapter 4. Characterisation of bioharmonophores degradation

«Καὶ εἶπεν ὁ Θεός· γενηθήτω φῶς·...
καὶ διεχώρισεν ὁ Θεὸς ἀνὰ μέσον τοῦ φωτὸς καὶ ἀνὰ μέσον τοῦ σκότους»

"And God said, "Let there be light"...
and he separated the light from the darkness"

Genesis

4.1 Bioharmonophores degradation characterisation in vitro using TEM

As mentioned in Chapter 1, bioharmonophores are a new class of polymer encapsulated biodegradable SHG nanoprobes. Triphenylalanine, pentalanine and trileucine peptides have been shown to produce strong SHG signal upon miniaturisation and encapsulation. To investigate the nano structure of the different peptide bioharmonophores, we synthesised bioharmonophores from these three peptides and characterised their morphology using TEM. As shown in **Fig. 70**, bioharmonophores made from triphenylalanine, trileucine and pentalanine have similar nanostructures with a diameter of around 100 nm.

Previous work in the Pantazis lab demonstrated that bioharmonophores can be degraded by proteases, such as proteinase K, by monitoring the decreasing SHG signal. However, how the degradation of the probes affects the nanostructure of the probes has not been investigated. To characterise bioharmonophores

nanostructure upon degradation, we treated freshly synthesised triphenylalanine bioharmonophores with Proteinase K for different incubation times and took representative images using TEM. Our results show progressive degradation of bioharmonophores within around 4 hours of Proteinase K treatment (**Fig. 71**). Notably, after this point we could not reliably identify bioharmonophores in the samples analysed. While imaging early stages of degradation was informative and showed the degradation process, TEM after 4 hours of Proteinase K treatment became challenging, as surfactants and impurities in the sample could be falsely interpreted as remnants of bioharmonophore structures.

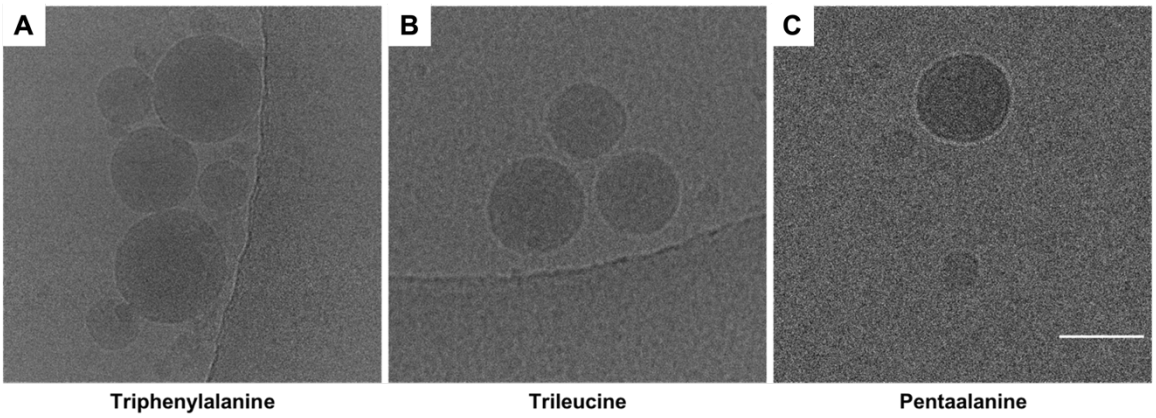


Fig. 70. Synthesised bioharmonophores have similar structures when characterised using Transmission Electron Microscopy. Representative images of bioharmomophores with different peptide cores: (A) Triphenylalanine, (B) Trileucine and (C) Pentaalanine. Scale bar, 100nm. *(Adapted from (Sonay et al., 2021))*.

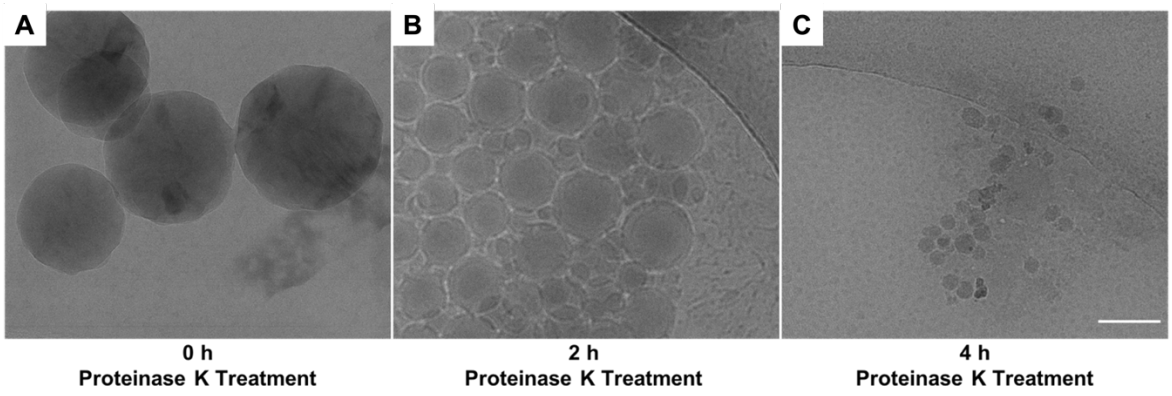


Fig. 71. Proteinase K induced bioharmonophores degradation characterised by Transmission Electron Microscopy at different time points. Representative images of bioharmonophores treated with Proteinase K and imaged at different time points. (A) 0 hour, (B) 2 hours, and (C) 4 hours of Proteinase K treatment. The magnification is the same for the different timepoints, illustrating the degradation of bioharmonophore structures into smaller fragments within 4 hours. Scalebar, 100 nm. *(Adapted from (Sonay et al., 2021)).*

4.2 Bioharmonophores degradation upon cellular uptake

Following the *in vitro* structural characterisation of bioharmonophores degradation, we decided to investigate the subcellular localisation of bioharmonophores upon cellular uptake. HeLa cells were incubated with thiol-PEG functionalised bioharmonophores to promote cellular uptake (Loretz et al., 2007, Gasparini et al., 2015) or 1X PBS (control) for 24 hours and subsequently stained for the lysosomal associated membrane 2 (LAMP2) to label late endosomes/lysosomes. **Fig. 72** demonstrates that endocytosed bioharmonophores mainly localise in late endosomes/lysosomes after 24 hours of cell incubation, visible as large and bright SHG signal spots positive for LAMP2 (white arrows). Only a minor fraction of smaller SHG signal spots can be detected without co-labelling with LAMP2 (**Fig. 72A-F**, white arrowheads), whereas no SHG signal spots are detected in the control cells (**Fig. 72G-I**). Our data show that internalised bioharmonophores accumulate in lysosomes, where they can produce a bright, pH resistant SHG signal prior to biodegradation.

4.3 Discussion on bioharmonophores

As we detailed previously, SHG nanoprobes have been used for successful cell labelling and targeting both *in vitro* and *in vivo*. The main advantage of SHG nanoprobes lies in their superiority compared to fluorescent probes; SHG nanoprobes do not exhibit the inherent limitations of fluorescence, such as blinking, bleaching and saturation. Despite their advantages over fluorescent probes, such as fluorescent proteins, their inorganic nature is a cause of concern. Especially for clinical and therapeutic imaging where biocompatibility is preferred and nanoprobes accumulation sparks health-related apprehension for long-term toxicity risks (Xuan et al., 2023).

In the Pantazis lab, to overcome this limitation of inorganic SHG nanoprobes, we developed bioharmonophores which are both biocompatible and biodegradable SHG nanoprobes made of self-assembling peptides (**Fig. 15**). Bioharmonophores possess the same qualities of their inorganic predecessors in terms of light conversion efficiency while simultaneously being biodegradable due to their peptide-core nature. Although previous work in the Pantazis lab showed that bioharmonophores can be degraded by proteinases, such as Proteinase K, by monitoring the decrease of SHG signal, structural analysis of the process and the cellular degradation pathway they follow upon cellular uptake remained unknown.

To provide a structural view of bioharmonophores degradation via proteinases and visualise the effect of their degradation to their structural integrity, we performed TEM on freshly produced triphenylalanine bioharmonophores incubated with proteinase K at different time points (**Fig 71**). Our results showed that bioharmonophores are effectively degraded by proteinase K in around 4 hours whereas almost 50% of their structural integrity is lost at around 2 hours. Considering these results, future applications of bioharmonophores especially for

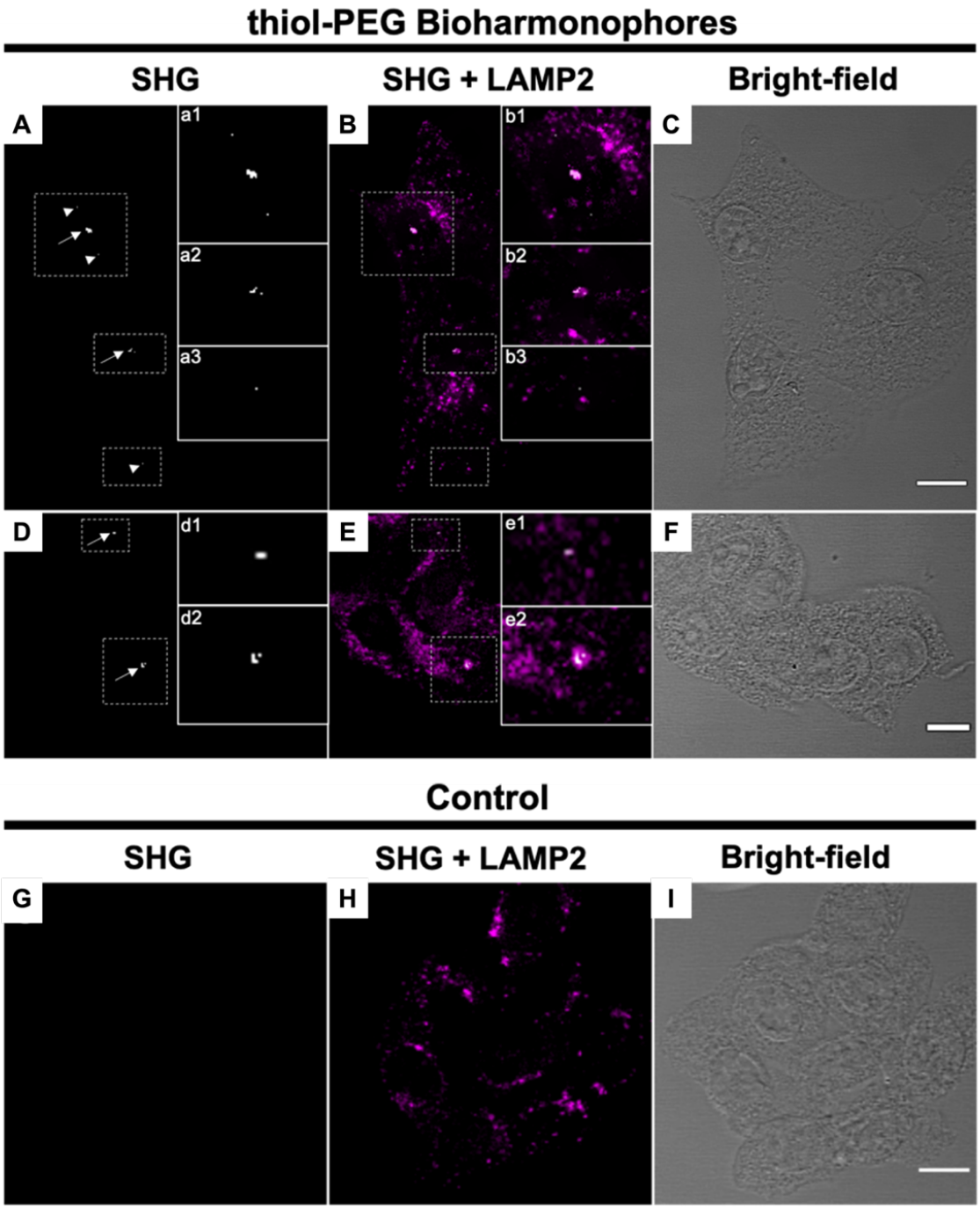


Fig. 72. Bioharmonophores accumulate in lysosomes after cellular uptake and produce a bright SHG signal prior to biodegradation. Representative images of bioharmonophores and lysosomes localisation in HeLa cells incubated with thiol-PEG functionalised bioharmonophores (A-F) or 1X PBS (G-I) for 24 hours followed by immunofluorescence staining for LAMP2. (A, D) SHG signal by internalised bioharmonophores. (B, E) Overlay images of SHG signal and fluorescent LAMP2 immunostaining of late endosomes/lysosomes that demonstrate bioharmonophores accumulation in LAMP2 positive vesicles. (C, F) Brightfield images of cells in A-B and D-E. (G, H) No SHG signal is detected in the 1X PBS control. (I) Brightfield image of the cells in G-H. Scale bars, 10μm.

diagnostic or therapeutic purposes should carefully evaluate the bioavailability of bioharmonophores and minimise their time on blood stream as they will potentially show reduced clearance time due to degradation.

When we evaluated the fate of bioharmonophores upon cellular uptake, we observed noticeable accumulation in lysosomes (**Fig. 72**). This accumulation in lysosomes indicates that bioharmonophores follow the endosome-lysosomal pathway; yet, further investigations into the the cellular degradation pathway are essential to ensure a thorough understanding of bioharmonophore behaviour post-internalisation. Unravelling these mechanisms will enable us to fine-tune the properties of bioharmonophores for enhanced efficacy in diagnostic and therapeutic applications.

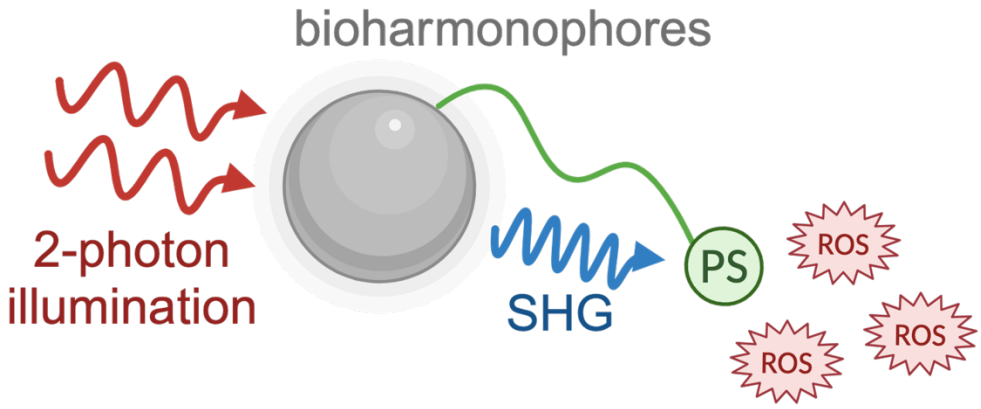


Fig. 73. The concept of bioharmonophores mediated photodynamic therapy. Cancer-targeting bioharmonophores are chemically conjugated with photosensitising agents (PS). The SHG signal produced by bioharmonophores is used to effectively excite the photosensitising agents which subsequently produce reactive oxygen species (ROS) resulting in localised cell death. *(Created with Biorender.com).*

The most potent future application for bioharmonophores lies in their use for Photodynamic Therapy (PDT) (**Fig. 73**), an emerging and highly promising therapeutic modality (Correia et al., 2021) that has already gained approval for treating several types of cancer, including skin cancer (Ou-Yang et al., 2023), oesophageal cancer (Inoue and Ishihara, 2021), and lung cancer (Crous and

Abrahamse, 2022). PDT involves employing photosensitising agents to generate reactive oxygen species upon exposure to light, leading to targeted cell damage or death. Bioharmonophores, with their intrinsic characteristic of highly localised light conversion (SHG signal), offer a unique advantage for PDT treatment. The conjugation of cancer-targeting bioharmonophores with an appropriate photosensitiser provides both cancer cell specificity and efficient excitation of the photosensitiser, coupled with greater tissue penetration due to the use of near-infrared (nIR) light. This combination maximises the treatment's effectiveness. Additionally, the self-assembling peptides forming the core of bioharmonophores introduce a novel dimension of safety and versatility for therapeutic use in PDT, without posing the long-term health risks associated with bioharmonophores' inorganic counterparts.

Altogether, bioharmonophores represent a significant leap forward in addressing the limitations associated with traditional inorganic SHG nanoprobes. Their biocompatibility and biodegradable nature, coupled with sustained imaging capabilities even within lysosomal compartments, where conventional fluorescence imaging becomes challenging, position bioharmonophores as a promising tool for future biomedical applications, diagnostic imaging and therapy in combination with other contrast and therapeutic agents.

Chapter 5. Conclusions and Outlook

«Τὰ ἀφανῆ τοῖς φανεροῖς τεκμαίρου»

"What is not seen you infer based on what is seen"

Solon

In the various biological kingdoms and magnitudes of life on the planet, multicellular living organisms, and thus humans, showcase organisational structures with highly dynamic behaviours. Shared among all these structures is a dual nature: the imperative to safeguard information for robust and reproducible organismal development and the fundamental requirement to perceive and adjust to environmental shifts, whether chemical or mechanical. Therefore, for a comprehensive understanding of a biological system, an all-encompassing approach would prove most suitable, necessitating scrutiny of both its biochemical and biomechanical constituents. This is what we can call as "systems biology," a field that was first introduced a bit more than 20 years ago (Chuang et al., 2010) and lies in the realm of the modern "4D cellular physiology."

During my PhD, I aimed to unravel the intricate interplay between biochemical and mechanical signals across biological scales by developing new tools to holistically study development, disease, and homeostasis across animal kingdoms and organisational levels; from the single cell to the whole organism. In my pursuit, I led the development of an advanced toolkit of versatile bioimaging tools that have broad applicability in biomedical sciences and establish new classes of novel

imaging probes and biosensors. This toolkit encompasses the first genetically-encoded biosensor for the mechanosensitive ion channel Piezo1 (GenEPi), new improved green-to-red photoconvertible fluorescent proteins (primed conversion), a cutting-edge volumetric imaging microscope (primed conversion), and the first biodegradable SHG nanoprobes (bioharmonophores) that could potentially transform biomedical diagnostic and therapeutic imaging. All these new tools are interrelated and interconnected under the umbrella of bioimaging, a field of research that has changed the way we approach biological research since the discovery of the first fluorescent protein in the early 60s, ushering in a new era of understanding the fundamental processes of life.

GenEPi as a versatile tool to image mechanosensation

The recent advances in the study of cellular biomechanics underscore the role of mechanical forces in guiding cell responses in development, disease, and homeostasis. However, there is an increasing need to develop new tools and methods to study mechanics in a non-invasive, non-destructive, and quantitative way. As I have always been fascinated by the idea of making invisible things, such as mechanical forces, visible, I continued previous efforts in the Pantazis lab to develop and meticulously characterise GenEPi, the first biosensor that enables the visualisation and study of Piezo1 in a non-invasive and highly specific way.

Using a variety of experimental approaches in a highly collaborative manner, I proved that GenEPi provides a truthful functional readout of Piezo1-dependent activity, showcasing effectiveness from the microscopic to organismal levels. Using TIRF imaging and GenEPi, I revealed previously described (Pathak et al., 2014, Ellefsen et al., 2019) transient, local Piezo1 activities in the plasma membrane of individual cells, simultaneously demonstrating GenEPi's ability to unify the study of localisation and function dynamics of Piezo1. Moving to the tissue level, I resolved

contraction-triggered Piezo1 stimulation within mESC-derived cardiac microtissues, showcasing for the first time a qualitative correlation of GenEPi responses to the amplitude of the applied force shown in the norepinephrine experiments. The qualitative nature of GenEPi responses were also be observed in the case of chemical agonism using Yoda1, enabling relative comparisons.

Eventually, moving to the organismal level, I generated, in collaboration with the Holley lab, a zebrafish GenEPi transgenic line, which enables the robust and reliable monitoring of Piezo1-dependent activity *in vivo*. Interestingly, GenEPi fluorescence across the body of GenEPi zebrafish embryos seemed to vary among different tissues and organs, indicating different levels of Piezo1 baseline activity. These differences could be attributed to the differential mechanical status of the various cells and organs, either in the form of membrane tension or intrinsic cellular forces, which subsequently activate Piezo1, leading to the fluorescence increase. Future experiments and combinatorial calibration measurements of GenEPi and tension sensors such as Flipper-TR (Pandzic et al., 2022) could answer the question of why GenEPi activity levels vary in different organs and cells, considering that the expression levels of GenEPi are similar among the tissues.

Upon answering this question, imaging of the zebrafish and the currently being developed mouse GenEPi transgenic lines will enable the extraction of "force maps" during embryo development, disease progression, and general homeostasis, answering key questions on how cell mechanics and specifically Piezo1 activity regulate biological processes. In the future, the design principle of GenEPi will lay a solid foundation for developing similar optical biosensors for various ion channels, such as Piezo2 (Coste et al., 2010), to study their role in development and disease progression. While GenEPi excels in reporting Ca^{2+} influx upon Piezo1 activation with high resolution, challenges persist in correlating different forces with its on-off

fluorescence response. Overcoming these challenges will necessitate meticulous *in vitro* calibrations and the potential integration of improved fluorescent probes with advanced capabilities and dynamic ranges. For instance, the introduction of chemigenetic- (Farrants et al., 2023, Claire et al., 2020), FLIM- (van der Linden et al., 2021b) and bioluminescence- (Gerard et al., 2023) based ion indicators presents a promising avenue for obtaining a quantitative readout of calcium dynamics during Piezo1 activation. Altogether, I believe that GenEPi's novel capabilities open new avenues for studying cellular biomechanics and promise to unravel the intricate dynamics of Piezo1 and other ion channels across biological scales.

The next generation of primed conversion bioimaging toolkit

As I mentioned above, the study of cellular mechanics is increasingly revealing novel ways in which cell behaviours are regulated. Nonetheless, the importance of genetic factors cannot be overlooked if we aim to fully understand systems biology, given the critical role of biochemical components in interacting with mechanics and shaping the adaptive nature of cells, tissues, and organisms. Traditionally, bioimaging approaches have played a vital role in cell labelling, tracking, and lineage tracing, resulting in remarkable accomplishments in fate mapping and understanding the complex dynamics within cell populations during development or disease progression. Among various lineage tracing methods, dual labelling techniques utilising green-to-red photoconvertible fluorescent proteins stand out for their effectiveness in capturing the dynamics of both the sparsely labelled, photoconverted cells or structures, and the remaining, green-labelled global population. However, concerns arise with the use of traditional 405nm photoconversion, as its high energy can cause phototoxicity and cytotoxicity (Ramakrishnan et al., 2016, Waldchen et al., 2015). Additionally, the single-photon nature of 405nm photoconversion leads to non-axially confined photoconversion,

limiting its application when fine structures need to be photoconverted in dense 3D environments.

In 2015, the Pantazis lab discovered primed conversion as a novel method to convert green-to-red photoconvertible fluorescent proteins for dual labelling precision imaging. Primed conversion was introduced as an innovative approach for axially confined and non-toxic photoconversion and has since represented a significant leap forward from conventional methods for lineage tracing using 405nm photoconversion. Primed conversion is a dual illumination process utilising 488nm and red to nIR light, resulting in axially confined photoconversion.

Intrigued by the nature of this novel photochemical process, I worked on developing the next generation of primed conversion imaging toolkit, which comprises improved fluorescent proteins and a novel single-objective light sheet microscope.

To enhance primed conversion efficiency of currently available pr-FPs, I employed a semi-rational protein engineering approach and conducted X-ray crystallography experiments. My approach has yielded promising results, and the screening methodology I pursued identified amino acid positions that influence primed conversion efficiency either negatively or positively. My initial hypothesis that some positions would affect primed conversion efficiency was confirmed, yet the role of these positions seems to be secondary in further stabilising the chromophore and cannot render a non-pr-FP primed convertible. In the future, saturated mutagenesis of these positions could yield combinations of amino acids that could challenge this notion and provide insight into the primed conversion mechanism. Continuation of the crystallography experiments, now that the crystallisation conditions have been established and optimised, and more advanced time-resolved serial X-ray

crystallography experiments will unravel the exact chromophore dynamics as primed conversion occurs. These results could then be used for molecular dynamics simulations to further guide protein engineering of pr-FPs, as previously described by the Campbell lab for the photoconvertible optogenetic tool PhOCl2 (Lu et al., 2021). A fascinating future avenue for exploration would be to investigate whether primed conversion can be generalised as a feature of all fluorescent proteins. More intriguing would be to develop fluorescent proteins that require double excitation, providing confinement and sectioning similar to traditional 2P imaging without the need for a pulsed laser.

As primed conversion has only been implemented in confocal laser scanning microscopes, which possess inherent limitations, in the pursuit of developing the next generation of the primed conversion imaging toolkit, I worked on the evaluation of primed conversion in a single-objective volumetric imaging platform based on an OPM design in collaboration with the Rowlands lab. *In vitro* tests proved impressive, as primed conversion of purified protein embedded in gels was pronounced and well-confined, permitting even the drawing of a smiley face by primed converting the protein. In contrast, *in vivo* primed conversion using the OPM microscope proved challenging as light scattering affected the overlap of the laser beams. Yet, future experiments using phantom media to mimic tissue scattering and further adaptations using improved pr-FPs will permit primed conversion *in vivo* using this system. Moreover, technical adaptations of the microscope itself to perform dual-side illumination (such as in (Yang et al., 2022a)) will contribute to better imaging quality and overcome concerns related to tissue light scattering for both imaging and primed conversion. Such a system will be an ideal platform for primed conversion lineage tracing experiments using zebrafish, mouse embryos and organoids. The most fascinating avenue would be to adapt such a system to be a smart microscope in which an initially primed converted population of cells of

interest performed by the experimenter will be infinitely monitored and the red fluorescence of the progenies of the first cells will be continuously primed converted when their fluorescence goes below a specific limit. A smart microscope like that would permit the monitoring of cells in a non-supervised way while maintaining the fidelity of the lineage tracing (Welling et al., 2019, Welling et al., 2020).

Overall, the evolution and use of primed conversion, coupled with improvements in fluorescent proteins and the novel volumetric imaging platform, mark a substantial advancement in deciphering cellular dynamics, promising improved precision imaging of biological systems.

Bioharmonophores as the next generation of SHG nanoprobes

In fluorescence-based bioimaging experiments, such as the dual labelling lineage tracing I described above, the inherent limitations of blinking, saturation, and bleaching associated with the fluorescent probes can impede accurate observations, especially in prolong imaging sessions. To overcome these challenges, SHG nanoprobes have been proven effective for both *in vitro* and *in vivo* cell imaging.

SHG nanoprobes produce light in a second-order nonlinear optical process, where two photons interact with the non-symmetric material of the nanoprobe. This interaction results in the generation of a single photon with double the frequency of the incident photons and half the wavelength. Unlike their fluorescent counterparts, SHG nanoprobes exhibit no blinking or bleaching, and their signal remains unaffected by increasing illumination intensity, a feature that can be extremely useful in long-term imaging experiments. As the application of SHG nanoprobes in conventional microscopy setups involves the use of nIR light, SHG

nanoprobes are well-suited for deep tissue imaging, a scenario where fluorescence imaging often faces significant challenges. Hence, the use of SHG nanoprobes represents a promising strategy to enhance the reliability and depth of bioimaging experiments, addressing critical limitations associated with traditional fluorescent probes.

While inorganic SHG nanoprobes, such as $BaTiO_3$, offer distinct advantages over fluorescent proteins, their extended stability within cells and *in vivo* for prolonged periods raises concerns regarding potential long-term health effects (Staedler et al., 2012). These concerns become particularly significant when considering the application of such nanoprobes for diagnostic or therapeutic purposes, including cancer treatment.

Efforts to enhance the biocompatibility of nanoprobes, as demonstrated by eliminating cellular uptake (Luo et al., 2018), are essential. However, a challenge arises in balancing biocompatibility with the diagnostic and therapeutic requirements. Specifically, for effective diagnosis and therapy, nanoprobes need to exhibit specific uptake to enhance diagnostic precision and eliminate "sick" cells while sparing the surrounding healthy tissue. This delicate balance underscores the complex requirements in deploying inorganic SHG nanoprobes for applications with potential health implications.

Recently, research in the Pantazis lab was focused on overcoming the limitation of inorganic SHG nanoprobes by introducing the first biodegradable SHG nanoprobes, known as bioharmonophores. As a novel class of biocompatible and biodegradable SHG nanoprobes, bioharmonophores address concerns linked to the inorganic nature of their traditional counterparts. During my PhD, I focused on bioharmonophores and conducted a detailed structural analysis of their

degradation via proteinases, a crucial aspect of their advantages over inorganic nanoprobes. Collaborating with the Landfester lab and employing TEM imaging, I revealed the temporal degradation profile of bioharmonophores *in vitro* while demonstrating that different peptide-core bioharmonophores produce nanoprobes with very similar structures. Transitioning to a cell-based *in vitro* system, I investigated the cellular uptake of bioharmonophores and showed that they accumulate in lysosomes, suggesting movement through the endosome-lysosomal pathway upon endocytosis. Unravelling the exact endocytosis mechanism and post-internalisation cellular degradation pathway is vital for refining bioharmonophores for enhanced efficacy in diagnostic and therapeutic applications. Moreover, the utilisation of alternative canonical and non-canonical peptides as cores for bioharmonophores could yield improved and brighter SHG nanoprobes with better light conversion efficiency. An exciting avenue for future experimentation involves designing genetically-encoded bioharmonophores, representing a natural progression in the evolution of these probes. Such improved and genetically-encoded SHG nanoprobes will find applications in both basic research and biomedical imaging. In future applications of bioharmonophores in PDT, their highly localised light conversion properties offer a unique advantage for targeted cell damage or death. Coupled with their self-assembling peptide core, bioharmonophores introduce a novel dimension of safety and versatility for therapeutic use in PDT, mitigating long-term health risks associated with traditional inorganic nanoprobes.

Hence, the ongoing advancements in bioharmonophores, from refining their structural properties to exploring genetically-encoded variations, hold great promise for ushering in a new era of biocompatible and highly efficient SHG nanoprobes. As these innovative probes continue to demonstrate their potential in diagnostic and therapeutic applications, particularly in PDT, they not only enhance

precision in cellular imaging but also mitigate long-term health risks, marking a significant stride towards safer and more effective biomedical tools.

Future of Advanced Optical Precision Imaging in systems biology

In essence, this integrated advanced imaging toolkit, comprising GenEPi, primed conversion, and bioharmonophores, signifies a key step in expanding our ability to understand the complex interplay between biochemical and mechanical signals in systems biology. GenEPi's versatility and novel way to image mechanosensation across scales, ongoing efforts to enhance primed conversion efficiency, and its emergence as a novel player for precise and non-toxic photoconversion, alongside the promising potential of bioharmonophores in therapeutic applications, collectively will advance the field of systems biology in ways that were not possible before. The envisioned improvements of the technologies presented in my thesis and the future breakthroughs that will accompany the use of this advanced imaging toolkit underscore the dynamic nature of advanced optical precision imaging, laying the groundwork for a more profound understanding of the fundamental processes governing life.

Looking ahead, the convergence of such advanced bioimaging technologies is a natural step to provide a holistic view of biological systems, from their genetic components and the dynamics of transcription factors to the biomechanical feedback loops. The integration of novel genetically-encoded mechanosensation biosensors, primed conversion imaging, and biocompatible SHG nanoprobes will offer a multi-dimensional view. In addition, the merging of primed conversion abilities with mechanosensation biosensors will unlock new dimensions for studying mechanotransduction and ion channels. This convergence will not only enhance our ability to decipher cellular dynamics but will also contribute to the development of safer and more effective tools for diagnostic and therapeutic applications.

In summary, as we stand on the cusp of a new era in imaging systems biology, the fusion of advanced optical precision imaging techniques with innovative genetic tools and probes will reveal the intricacies of life processes with unprecedented resolution and clarity. The journey through systems biology, propelled by these advancements, promises a future where the invisible becomes visible, and the complexities of biological systems are deciphered with precision that was once unimaginable.

Chapter 6. Materials and Methods

«[...] λίθοι τε καὶ πλίνθοι καὶ ξύλα καὶ κέραμος
ἀτάκτως μὲν ἐρριμμένα οὐδὲν χρήσιμά ἐστιν...»

"[...] stones and bricks, woodwork and tiles,
tumbled together in a heap are of no use at all..."

Xenophon

Molecular cloning

The human Piezo1 cDNA was previously obtained from Kazusa Inc, Japan and the generation of the first four types of GCaMPs; mGCaMP6s-EF4 (GCaMP-G1), mGCaMP6f-EF4 (GCaMP-G2), mGCaMP6s RS1-EF3 (GCaMP-G3) and mGCaMP6s RS1-EF4 (GCaMP-G4) were described by (Helassa et al., 2016). Fast-GCaMP-EF20 (here denoted as GCaMP-G5) was a gift from Samuel Wang (Addgene plasmid #52645) (Sun et al., 2013). pGP-CMV-NES-jRCaMP1a was a gift from Douglas Kim (Addgene plasmid #61462) (Dana et al., 2016).

The XLone-GenEPi (XLGenEPi) plasmid was prepared by subcloning GenEPi from the original pCMV-GenEPi (Addgene plasmid #140236) to the XLone-EGFP backbone with traditional restriction enzyme cloning. XLone-GFP (Randolph et al., 2017) was a gift from Xiaojun Lian (Addgene plasmid #96930; http://n2t.net/addgene:96930; RRID: Addgene_96930). The original pCMV-GenEPi (Addgene #140236) and XLone-EGFP plasmids were digested with HindIII and KpnI, respectively. Both sticky ends were blunted (HindIII filled-in, KpnI overhangs removed) using the Quick Blunting Kit (NEB, E201), digested with SphI

and ligated using T4 Ligase (M0202, NEB). Clones were screened using restriction digest and sequenced by Eurofins Genomics (https://eurofinsgenomics.eu/) using our custom-made sequencing primers (see **Appendix A.1**). Plasmid DNA isolation was carried out using Qiagen Plasmid Midi Kit (Qiagen, 12143).

The hsp70:GenEPi plasmid was prepared using Gibson Assembly (NEB, E2611L) following manufacturer's instructions. The backbone vector containing the 1517 bp hsp70-I promoter sequence was amplified with PCR using the Gibson Assembly primers (see **Appendix A.1**). The original pCMV-GenEPi plasmid (Addgene plasmid #140236) was linearized using NotI/HindIII. Clones were screened using restriction digest and sequenced by Eurofins Genomics (https://eurofinsgenomics.eu/) using our custom-made sequencing primers (see **Appendix A.1**). Plasmid DNA isolation was carried out using Qiagen Plasmid Midi Kit (Qiagen, 12143).

For site-directed mutagenesis, the Q5 Site-Directed Mutagenesis Kit (NEB, E0554S) was used following manufacturer's instructions. The site-directed mutagenesis primers were designed using NEBaseChanger (https://nebasechanger.neb.com/) and they are listed in **Appendix A.1**. Clones were sequenced by Eurofins Genomics (https://eurofinsgenomics.eu/). Plasmid DNA isolation was carried out using Qiagen Plasmid Midi Kit (Qiagen, 12143).

Cell culture and transfection

HEK293T, HFF and HeLa cells were cultured at 37°C, 5% CO_2, in high glucose DMEM with GlutaMAX (10569010, Thermo Fisher), supplemented with 10% FBS (P40-37500, Pan Biotech) and 1X Penicillin-Streptomycin solution (15140122, Thermo Fisher). Cells were routinely tested and were negative for mycoplasma infection using Mycoplasma detection kit (B39032, LuBioScience GmBH). Plasmid

DNA for transfections was isolated from 50 ml LB culture (244610, BD Bioscience) containing appropriate antibiotics using the Zymopure Plasmid Midiprep kit (D4200, Zymo Research) or the Qiagen Plasmid Midi Kit (Qiagen, 12143). The amount of DNA was measured using the Nanodrop 2000c or NanoDrop One_c Spectrophotometer (Thermo Fisher).

For the Yoda1 and EGTA experiments, HeLa cells were transfected with the XLGenEPi plasmid (Tet-on, dox-inducible expression) using lipofection (L3000001, Lipofectamine 3000, Thermo Fisher) following manufacturer's instructions. At 24 hours post transfection, the cells were dissociated and seeded onto 0.1% gelatine-coated 20 mm-wide cover-glass bottom confocal dishes (734-2906, VWR), with a density of 200,000 cells per well. 200 ng/ml doxycycline (D9891, Merck) was added to induce GenEPi 's expression 24 hours prior to imaging. 200 ng/ml doxycycline was used to induce GenEPi's expression and generate sufficient contrast which is in the lower range of previously used concentrations(Randolph et al., 2017). We used several concentrations of Yoda1 (5586, Tocris Bioscience) diluted in DMSO (D8418, Sigma-Aldrich) ranging from 5μM to 50μM and 2mM EGTA (OmniPur EGTA, 4100) diluted in water.

For the loss-of-function GenEPi experiments, HeLa cells were transfected with the XLGenEPi-S217L plasmid (Tet-on, dox-inducible expression) using lipofection (L3000001, Lipofectamine 3000, Thermo Fisher) following manufacturer's instructions. At 24 hours post transfection, the cells were dissociated and seeded onto 0.1% gelatine-coated 20 mm-wide cover-glass bottom confocal dishes (734-2906, VWR), with a density of 200,000 cells per well. 200 ng/ml doxycycline (D9891, Merck) was added to induce GenEPi 's expression 24 hours prior to imaging. We used 10μM Yoda1 (5586, Tocris Bioscience) diluted in DMSO (D8418, Sigma-Aldrich).

For TIRFM imaging experiments, HEK293T, HFF and HeLa cells were transfected with the XLGenEPi plasmid (Tet-on, dox-inducible expression) using lipofection (L3000001, Lipofectamine 3000, Thermo Fisher) following manufacturer's instructions. At 24 hours post transfection, the cells were dissociated and seeded onto 0.1% gelatine-coated 20 mm-wide cover-glass bottom confocal dishes (734-2906, VWR), with a density of 200,000 cells per well. 200 ng/ml doxycycline (D9891, Merck) was added to induce GenEPi 's expression 24 hours prior to imaging.

Generation of inducible GenEPi-mESC cell lines

Doxycycline-inducible GenEPi-mESCs were generated using ZX1 mESCs carrying rtTA in the Rosa26 locus and dox-inducible cre flanked by self-incompatible LoxP sites in the HPRT locus (Iacovino et al., 2011), kindly provided by Dr. Michael Kyba. ZX1 mESCs were cultured in DMEM (Life Technologies), 15% FBS (PAN Biotech), 2 mM L-Glutamine (Invitrogen), 1X non-essential amino acids, 0.1 mM β-mercaptoethanol, 100 U/ml leukemia inhibitory factor (Peprotech), 1 µM PD0325901 (Selleckchem) and 3 µM CHIR99201 (R&D Systems) on 0.1% gelatine coated plates. Prior to electroporation, ZX1 mESCs were exposed to 500 ng/ml doxycycline (D9891, Merck) for 24 hours. 1 x 10^6 ZX1 mESCs were electroporated with 3 µg p2lox-GenEPi plasmid in a 0.4 cm electroporation cuvette at 230 mV, 500 µF and maximum resistance in a Biorad electroporator (Biorad Genepulser Xcell). 24 hours after electroporation, antibiotic selection was started with 300 µg/ml G418 (Sigma). Colonies that incorporated GenEPi were verified by FACS analysis and expanded. Dox-inducible GenEPi mESCs were differentiated to cardiomyocytes as previously described (Wang et al., 2011). GenEPi mESCs were seeded as 500 cell / 20 µl in hanging drops on non-adherent plates to generate embryoid bodies (EBs) in EB medium, IMDM (Life Technologies), 20% FBS (PAN Biotech), 2 mM L-Glutamine (Invitrogen), 1X non-essential amino acids and 0.1 mM β-mercaptoethanol. After 2 days, EBs were transferred to uncoated petri dishes.

From day 3-5, 1 µM XAV939 was added to the culture conditions and EBs were plated on 0.1% gelatine coated dishes from day 4. Beating EBs appeared at day 10 of differentiation. Beating EBs were either directly imaged within the multi-patch beating microtissue environment or manually dissected and dissociated using 2 mg/ml Collagenase/Dispase (Sigma) to generate smaller beating patches and single-cells. For blebbistatin experiments, 40-120 µM Blebbistatin (B0560, Sigma-Aldrich) diluted in DMSO (D8418, Sigma-Aldrich) was applied to the cells until contractions were stopped. For norepinephrine experiments, 10 nM-10 µM of Norepinephrine (1468501, Merck) diluted in PBS was applied to the cells. Under these experimental conditions we did not observe cardiomyocyte beating irregularities, such as arrhythmia. For nifedipine experiments, 100nM of Nifedipine (Merck, N7634) diluted in PBS was applied to the cells.

Confocal and Total Internal Reflection Microscopy (TIRFM) imaging

Images were acquired either on a Zeiss 780 confocal laser scanning microscope equipped with an argon laser, a 561 nm diode pumped solid-state laser and a 633 nm HeNe laser using a C-Apochromat 40x/1.1 DICIII water immersion objective or on a Leica SP8 confocal laser scanning microscope equipped with a white light laser (WLL, Leica) using either an HC PL APO CS2 40x/1.3 oil immersion objective or an HC PL APO CS2 63x/1.2 water immersion objective or on a STELLARIS 8 confocal laser scanning microscope equipped with a white light laser (WLL, Leica) using either an HC PL APO CS2 40x/1.3 oil immersion objective or an HC PL APO CS2 63x/1.2 water immersion objective. Images of single-cells were acquired at 8- or 16-bit depth, excited with 488 nm. To ensure fast image acquisition, we imaged small regions of interest within the field of view, recording a single z-plane over several minutes (pinhole size ranged from 3 Airy units to maximum pinhole size) using the maximum acquisition speed. When imaging was performed on the Leica SP8 confocal, bidirectional scanning with off-set correction was used to increase

acquisition speed even more. Live imaging of cells was carried out either in Live Cell Imaging Solution (A14291DJ, ThermoFisher) or culture medium without phenol red.

TIRFM images were obtained on an inverted widefield microscope (Ti Eclipse, Ti-TIRF-E Motorized TIRFM Illuminator, Nikon) operating in TIRFM mode, equipped with a 488 nm diode laser for excitation coupled with a 525/50 nm emission filter under ambient temperature conditions of 37°C, 5 % CO_2 using a 60x CFI Plan Apo TIRF NA 1.49 oil immersion objective (Nikon). Time lapse images were recorded at 10 frames per second using a sCMOS camera (Neo sCMOS camera, Andor) combined with the Nikon NIS-Elements (Nikon) software to facilitate imaging. To minimize drift in the focus across time and multiple regions, the perfect focus system (Nikon) was used to maintain axial focus.

The concentration of calcium is 1.8 mM in Live Cell Imaging Solution, 1.8 mM in DMEM culture medium, 1.5 mM in IMDM culture medium and 33 nM in E3 zebrafish medium.

Primed conversion was performed on a Leica SP5 confocal laser scanning microscope equipped with an argon laser and a 633 nm HeNe laser. Effective laser powers were measured using a laser power meter (Coherent) and were about ~10 μW for 488nm and ~750 μW for 633nm lasers at the focus.

X-ray crystallography

Generated crystals were cryopreserved and then subsequently sent to Diamond Light Source for X-ray diffraction characterisation. Briefly, individual crystals stored in liquid nitrogen were mounted in front of the X-ray optics at the synchrotron while a cooling N_2 stream was securing that the temperature of the crystals was

maintained. Data were acquired at a 2.50 Å resolution, exposure time of 0.1 seconds, beam size of 7x7 µm and transmission 50%. Auto processing software was used to calculate several parameters of the acquired data, such as resolution and space group. When possible, molecular replacement was performed using Phenix (Liebschner et al., 2019) and the previously solved mEosFP structure (PDB: 3P8U). Electron density maps were visualised with Coot (Emsley et al., 2010).

Patch-clamp electrophysiology

HEK293T cells were transfected with the plasmids using lipofectamine 2000 (Invitrogen) following manufacturer's instructions. 48 hours after transfection, whole-cell and cell-attached patch-clamp recordings were made on the cells at room temperature with the Axopatch-200B (Axon Instruments, Inc.) equipped with the Digidata 1550B and the pCLAMP 10.6 software (Molecular Devices, Sunnyvale, CA, USA). The tip resistance of recording glass pipettes was between 3 and 5 MΩ. The currents were sampled at 20 kHz and filtered at 2 kHz. The mechanical force was applied through a recording pipette using a Patchmaster-controlled pressure-clamp HSPC-1 device (ALA Scientific Instruments).

For whole-cell recordings, the external solution consisted of 133 mM NaCl, 3 mM KCl, 2.5 mM $CaCl_2$, 1 mM $MgCl_2$, 10 mM HEPES and 10 mM glucose (pH 7.3 with NaOH). The pipette solution was composed of 133 mM CsCl, 1 mM $CaCl_2$, 1 mM $MgCl_2$, 5 mM EGTA, 10 mM HEPES, 4 mM MgATP and 0.4 mM Na_2GTP (pH 7.3 with CsOH).

For cell-attached recordings, the extracellular solutions were composed of 140 mM KCl, 1 mM $MgCl_2$, 10 mM glucose and 10 mM HEPES (pH 7.3 with KOH). The pipette solutions consisted of 130 mM NaCl, 5 mM KCl, 1 mM $CaCl_2$, 1 mM $MgCl_2$, 10 mM TEA-Cl and 10 mM HEPES (pH 7.3 with NaOH).

Live staining and immunostaining

Live cell staining of cells was achieved using the ER tracker red (E34250, Thermo-Fisher) or BODIPY TR Ceramide (Thermo Fisher, D7540) according to product specifications. For antibody staining, the cells were washed with 1X PBS, fixed with 4% PFA for 15 min, permeabilized with 1X PBST (1X PBS containing 0.01% Tween20) for 15 min, blocked with 10% goat serum in 1X PBST for at least 1 h, and incubated overnight with mouse anti-LAMP2 (ab25631, Abcam, 1:200), Alexa fluor647 anti-GFP (ThermoFisher Scientific, A31852, 1:200 dilution) in 5% goat serum at 4 °C. The next day, cells were rinsed with 1X PBST and ,if needed, incubated for 1 hour with the goat anti-mouse Alexa488 conjugated secondary antibody (A28175, Thermo Scientific, 1:1000), washed thoroughly with 1X PBST and mounted in mowiol mounting medium containing 2.5% v/v DABCO (290734, Merck).

Zebrafish transgenesis and in vivo experiments

Experiments involving zebrafish were conducted in accordance with UK Home Office requirements (Animals Scientific Procedures Act 1986, project license P219D3ABD). All experiments were conducted up to 5 days post-fertilization.

To generate a GenEPi zebrafish transgenic line, Tol2-mediated transgenesis was used. 30 pg of the hsp70:GenEPi plasmid and 120 pg of Tol2 transposase mRNA were injected into the blastomere of single WT/TL zebrafish embryos at the one-cell stage. The injected zebrafish embryos were heat-shocked at 16 hpf (hours post fertilization) and those showing fluorescence were raised to adulthood. F1 founders were subsequently screened and stable transgenic strains were established by selecting fish at F3 generation. Before imaging, *Tg(hsp70:GenEPi)* embryos were heat-shocked at 37.5°C for 1 hour to induce the expression of the GenEPi and optically screened ~4-5 hours post-heat-shock. All the zebrafish images were

acquired at least 5 hours post-heat-shock when a steady state of fluorescence is reached.

For the *in vivo* pharmacological intervention experiments, dechorionated zebrafish embryos were anesthetized in 0.2 mg/ml tricaine. Then, single embryos were sequentially transferred in aqueous solutions of (i) 10 μM Yoda1, (ii) 10 μM Yoda1 and 10 μM Ruthenium Red, (iii) 10 μM Ruthenium Red and washed out in the original egg medium (E3 medium). After 5 min in each condition, each embryo was imaged in a MVX10 stereo microscope (Olympus), equipped with a X-Cite® 120Q excitation light source (Lumen Dynamics), using a 2x MV PLAPO objective (Olympus). ZEISS Efficient Navigation (ZEN) blue software was used to facilitate imaging.

For the longitudinal analysis of GenEPi expression post-heat-shock, individual embryos were placed in a glass-bottom 96-well plate (Greiner) and imaged every 30 minutes using the Imaging Machine (Acquifer) with a 4X objective at 28°C.

For membrane colocalisation analysis, zebrafish embryos were either injected with mRFP RNA or live stained with 100μM BODIPY TR Ceramide (Thermo Fisher, D7540) for 1 hour or overnight before imaging.

Zebrafish heart beating measurements were manually measured over a MVX10 stereo microscope (Olympus) at specific timepoints and data were further analysed and plotted using GraphPad Prism 9.

Protein purification

For the 405nm photoconversion, primed conversion and X-ray crystallography experiments Dendra2 and pr-mEosFP were expressed in BL21 (DE3) cells by IPTG

induction. After 5-7 hours of incubation, bacteria were pelleted by centrifugation at 13000 rcf for 5-10 min at 4 °C and protein purification using affinity chromatography columns (Protino, Macherey-Nagel) was performed following manufacturer's instructions. Desalting of the elutes was performed in 1X PBS using Pierce protein concentrators with a 10K molecular weight cut-off (Thermo Fisher) following manufacturer's instruction. Protein concentration was measured using the Bradford method (Abcam) following manufacturer's instructions. The absorption spectrum of protein solutions was measured using NanoDrop One_c Spectrophotometer (Thermo Fisher) and was further analysed and plotted using GraphPad Prism 9.

Bioharmonophores synthesis and functionalisation

30 mg of PLLA was dissolved in 3 ml of chloroform (Sigma) along with 15 mg of triphenylalanine, 30 mg of pentalalanine (Bachem), and 30 mg of trileucine (Sigma) peptides in separate glass vials. The resulting suspension was mixed with aqueous SDS (Sigma) solution with a final 0.3% SDS concentration. A macroemulsion was obtained by stirring the samples at 1000 rpm for 1 h. Then, the samples were sonicated (Branson Sonifier) with a 1.5 in. tip at 70% power in a pulsed mode (30 s ON and 10 s OFF) for 2 min under ice cooling. The chloroform was evaporated from the obtained emulsions by stirring the samples at 500 rpm at 40 °C overnight.

For bioharmonophores functionalisation, the bioharmonophores suspension was centrifuged at 13500 rpm for 3 min and resuspended in 1% Tween 80 in 1X PBS and mixed with 10 mg of N-(3-(dimethylamino)propyl)-N′-ethylcarbodiimide hydrochloride (EDC) (Sigma), 10 mg of N-hydroxysuccinimide (NHS) (Sigma), and 10 mg of thiol-PEG-NH_2 (Sigma) for 2 h. The suspension was centrifuged and resuspended in 1% Tween 80 in 1X PBS and stored at 4 °C prior to use.

Transmission Electron Microscopy

Bioharmonophore samples were spun down to remove aggregated nanoparticles at 3000 rpm for 3 min. Five microliters of the sample (i.e., the supernatant of the centrifuged solution) was placed on a carbon coated grid (Quantifoil, D) previously glow-discharged for 30 s (Emitech K100X, GB). The drop was allowed to remain for 60 s; after this interval, excess fluid was drained along the periphery using a piece of filter paper followed by staining with 2% uranyl acetate for 1 and 15 s, respectively. Excess moisture was drained after each step, and when dry, the grid was examined in an FEI Morgagni 268 TEM operated at 100 kV.

For the *in vitro* degradation experiments, 1 ml of bioharmonophores suspension was incubated with 100 µg/ml final proteinase K concentration at 37 °C. TEM analysis was performed as described above every 2 hours.

Subcellular localisation of bioharmonophores upon cellular uptake

HeLa cells were cultured at 37 °C, 5% CO2, in high glucose DMEM with GlutaMAX (10569010, Thermo Fisher), supplemented with 10% FBS (P40-37500, Pan Biotech) and 1× penicillin–streptomycin solution (15140122, Thermo Fisher). A 13 mm round coverslip was coated with 0.1% gelatine (G1393, Merck) for 1 h, and cells were seeded to reach around 70% confluency. The following day, 400 µL of freshly prepared thiol-PEG functionalised bioharmonophores (2 mg/ml) or an equal volume of 1X PBS (control) was added to the cells and incubated for 24 h. Immunostainings were performed as described above.

Image processing and analysis

Image analysis of the local and systemic responses of GenEPi in the differentiated cardiomyocytes experiments was performed using FiJi/ImageJ (Schindelin et al., 2012) (release 1.53f51). F/F_0 images were calculated using the built-in image

calculator function (F_0 was the average of the first 5 frames of the time-lapse). The resulting F/F_0 images were pseudo-colored with the mpi-Inferno LUT to better demonstrate the fold increase differences. Quantitative data of the F/F_0 changes over time were collected from regions of interest or whole images using the plot z-axis profile (where z dimension was time, usually in milliseconds or seconds). Data were further analysed and plotted using GraphPad Prism 9.

Image analysis of TIRFM imaging was performed with FiJi/ImageJ(Schindelin et al., 2012) (release 1.53f51). To segment GenEPi (Piezo1) clusters 8- or 16- bit single channel TIRFM images were masked by (i) subtracting background (rolling ball radius of 2 pixels), (ii) applying a median filter (radius of 2 pixels) and (iii) thresholding (Otsu). The mask image was then subsequently watersheded, dilated and watersheded again before the built-in analyze particles function of FiJi/ImageJ was used to obtain quantitative data, such as mean gray value, area and perimeter in the original image. Single-pixel measurements due to masking artifacts were excluded from the subsequent analysis. Average camera noise was subtracted from images that are displayed. When further filtering was used for illustration purposes it is stated in the Fig. legends. To track individual GenEPi (Piezo1) membrane clusters Trackmate (Tinevez et al., 2017) was used with LoG detector (Laplacian of Gaussian filter), estimated object diameter of 1 µm, quality threshold of 1.0 and sub-pixel localisation. The tracker used was the simple LAP tracker with linking max distance of 1 µm, gap closing distance and frames of 1 µm and 20 frames, respectively. Data were saved as xml files and subsequently analysed with MATLAB (R2021b) and @msdanalyser(Tarantino et al., 2014). Data were further analysed and plotted using GraphPad Prism 9.

To quantify fluorescence intensity changes in the zebrafish experiments, images were opened on FiJi/ImageJ (Schindelin et al., 2012) (release 1.53f51) and a

rectangular region of interest was manually selected. Then, mean intensity values were exported and analysed/plotted using GraphPad Prism 9.

To quantify fluorescence intensity changes in the zebrafish longitudinal analysis experiments, images were opened on FiJi/ImageJ (Schindelin et al., 2012) (release 1.53f51) and a circular region of interest covering the whole embryo was manually selected. Then, mean intensity values for individual embryos were exported and analysed/plotted using PlotTwist (Goedhart, 2020) (Shiny apps).

Colocalisation analyses were performed on FiJi/ImageJ (Schindelin et al., 2012) (release 1.53f51). Images were opened and a rectangular region covering one or more individual cells was manually selected. Then, the colocalisation analysis Coloc2 plugin was used to implement and perform the pixel intensity correlation over space Pearson method. Individual Pearson's correlation coefficients were exported and analysed/plotted using GraphPad Prism 9.

To quantify fluorescence intensity changes pre- and post- primed conversion in purified protein gels, bacterial pellets or zebrafish, images were opened on FiJi/ImageJ (Schindelin et al., 2012) (release 1.53f51) and a rectangular region of interest was manually selected. Then, mean intensity values were exported and analysed/plotted using GraphPad Prism 9.

TEM images were also analysed on FiJi/ImageJ (Schindelin et al., 2012) (release 1.53f51) and had to be rescaled for illustration purposes.

Statistical analysis

All data are expressed means ± SEM or SD. Sample sizes (n) are provided in the text or Fig. legend of each experiment. Each data set was subjected to the Shapiro-Wilk

normality test to determine whether the data set has a Gaussian distribution; $p>0.05$ indicated it has a Gaussian distribution and $p<0.05$ indicated it did not. When all the compared data sets had Gaussian distribution, two-tailed Student's t-test was applied to compare two independent datasets; with an F-test to compare variances. When F-test resulted in $p<0.05$, Welch's correction was applied to the t-test. When more than 2 datasets were present with Gaussian distribution, one-way ANOVA was used to compare datasets, followed by Holm-Sidak's post hoc multiple comparisons test. When at least one of the compared data sets did not have a Gaussian distribution, Mann-Whitney test was applied to compare two independent datasets; and Wilcoxon rank-sum test was applied when the data sets were paired. When more than 2 datasets were present without Gaussian distribution, Kruskal-Wallis test was applied, followed by Dunn's post hoc multiple comparisons test. For all statistics, either p-value number was reported or with n.s.=$p>0.05$, *=$p<0.05$, **=$p<0.01$, ***=$p<0.001$ and ****=$p<0.0001$. Mean Squared Displacement analysis and linear fitting of the GenEPi (Piezo1) membrane clusters tracking dynamics were performed using MATLAB (R2021b) and @msdanalyser (Tarantino et al., 2014).

References

ABREMSKI, K. & HOESS, R. 1984. Bacteriophage P1 site-specific recombination. Purification and properties of the Cre recombinase protein. *Journal of Biological Chemistry,* 259**,** 1509-1514.

ABREMSKI, K., HOESS, R. & STERNBERG, N. 1983. Studies on the properties of P1 site-specific recombination: evidence for topologically unlinked products following recombination. *Cell,* 32**,** 1301-1311.

AGLIALORO, F., HOFSINK, N., HOFMAN, M., BRANDHORST, N. & VAN DEN AKKER, E. 2020. Inside Out Integrin Activation Mediated by PIEZO1 Signaling in Erythroblasts. *Frontiers in Physiology,* 11.

ALBUISSON, J., MURTHY, S. E., BANDELL, M., COSTE, B., LOUIS-DIT-PICARD, H., MATHUR, J., FENEANT-THIBAULT, M., TERTIAN, G., DE JAUREGUIBERRY, J. P., SYFUSS, P. Y., CAHALAN, S., GARCON, L., TOUTAIN, F., SIMON ROHRLICH, P., DELAUNAY, J., PICARD, V., JEUNEMAITRE, X. & PATAPOUTIAN, A. 2013. Dehydrated hereditary stomatocytosis linked to gain-of-function mutations in mechanically activated PIEZO1 ion channels. *Nat Commun,* 4**,** 1884.

ANDO, R., MIZUNO, H. & MIYAWAKI, A. 2004. Regulated fast nucleocytoplasmic shuttling observed by reversible protein highlighting. *Science,* 306**,** 1370-3.

ANDOLFO, I., ALPER, S. L., DE FRANCESCHI, L., AURIEMMA, C., RUSSO, R., DE FALCO, L., VALLEFUOCO, F., ESPOSITO, M. R., VANDORPE, D. H., SHMUKLER, B. E., NARAYAN, R., MONTANARO, D., D'ARMIENTO, M., VETRO, A., LIMONGELLI, I., ZUFFARDI, O., GLADER, B. E., SCHRIER, S. L., BRUGNARA, C., STEWART, G. W., DELAUNAY, J. & IOLASCON, A. 2013. Multiple clinical forms of dehydrated hereditary stomatocytosis arise from mutations in PIEZO1. *Blood,* 121**,** 3925-35, s1-12.

ANDRESEN, M., WAHL, M. C., STIEL, A. C., GRATER, F., SCHAFER, L. V., TROWITZSCH, S., WEBER, G., EGGELING, C., GRUBMULLER, H., HELL, S. W. & JAKOBS, S. 2005. Structure and mechanism of the reversible photoswitch of a fluorescent protein. *Proc Natl Acad Sci U S A,* 102**,** 13070-4.

ARISTOTLE & PECK, A. L. 1943. *Generation of animals, with an English translation by A.L. Peck,* Cambridge, Harvard University Press.

AUSTEN, K., RINGER, P., MEHLICH, A., CHROSTEK-GRASHOFF, A., KLUGER, C., KLINGNER, C., SABASS, B., ZENT, R., RIEF, M. & GRASHOFF, C. 2015. Extracellular rigidity sensing by talin isoform-specific mechanical linkages. *Nat Cell Biol,* 17**,** 1597-606.

BAE, C., GNANASAMBANDAM, R., NICOLAI, C., SACHS, F. & GOTTLIEB, P. A. 2013. Xerocytosis is caused by mutations that alter the kinetics of the mechanosensitive channel PIEZO1. *Proc Natl Acad Sci U S A,* 110**,** E1162-8.

BAE, C., SACHS, F. & GOTTLIEB, P. A. 2011. The mechanosensitive ion channel Piezo1 is inhibited by the peptide GsMTx4. *Biochemistry,* 50**,** 6295-300.

BAI, X., BOUFFARD, J., LORD, A., BRUGMAN, K., STERNBERG, P. W., CRAM, E. J. & GOLDEN, A. 2020. Caenorhabditis elegans PIEZO channel coordinates multiple reproductive tissues to govern ovulation. *eLife,* 9**,** e53603.

BAIER, H., KLOSTERMANN, S., TROWE, T., KARLSTROM, R. O., NUSSLEIN-VOLHARD, C. & BONHOEFFER, F. 1996. Genetic dissection of the retinotectal projection. *Development,* 123**,** 415-25.

BAMBARDEKAR, K., CLÉMENT, R., BLANC, O., CHARDÈS, C. & LENNE, P.-F. 2015. Direct laser manipulation reveals the mechanics of cell contacts in vivo. *Proceedings of the National Academy of Sciences,* 112**,** 1416-1421.

BARBIERI, L., COLIN-YORK, H., KOROBCHEVSKAYA, K., LI, D., WOLFSON, D. L., KAREDLA, N., SCHNEIDER, F., AHLUWALIA, B. S., SETERNES, T., DALMO, R. A., DUSTIN, M. L., LI, D. & FRITZSCHE, M. 2021. Two-dimensional TIRF-SIM–traction force microscopy (2D TIRF-SIM-TFM). *Nature Communications,* 12**,** 2169.

BAXTER, J. M., HUTCHISON, C. D. M., MAGHLAOUI, K., CORDON-PRECIADO, V., ALLER, P., BUTRYN, A., AXFORD, D., HORRELL, S., OWEN, R. L., STORM, S. L. S., DEVENISH, N. E. & VAN, T. J. J. 2022. Observation of Cation Chromophore Photoisomerization of a Fluorescent Protein Using Millisecond Synchrotron Serial Crystallography and Infrared Vibrational and Visible Spectroscopy. *JOURNAL OF PHYSICAL CHEMISTRY B*.

BLUMENTHAL, N. R., HERMANSON, O., HEIMRICH, B. & SHASTRI, V. P. 2014. Stochastic nanoroughness modulates neuron-astrocyte interactions and function via mechanosensing cation channels. *Proc Natl Acad Sci U S A,* 111**,** 16124-9.

BORGHI, N., SOROKINA, M., SHCHERBAKOVA, O. G., WEIS, W. I., PRUITT, B. L., NELSON, W. J. & DUNN, A. R. 2012. E-cadherin is under constitutive actomyosin-generated tension that is increased at cell-cell contacts upon externally applied stretch. *Proc Natl Acad Sci U S A,* 109**,** 12568-73.

BOUCHARD, M. B., VOLETI, V., MENDES, C. S., LACEFIELD, C., GRUEBER, W. B., MANN, R. S., BRUNO, R. M. & HILLMAN, E. M. 2015. Swept confocally-aligned planar excitation (SCAPE) microscopy for high speed volumetric imaging of behaving organisms. *Nat Photonics,* 9**,** 113-119.

BRIXIUS, K., GROSS, T., TOSSIOS, P., GEISSLER, H. J., MEHLHORN, U., SCHWINGER, R. H. & HEKMAT, K. 2005. Increased vascular selectivity and prolonged pharmacological efficacy of the L-type Ca2+ channel antagonist lercanidipine in human cardiovascular tissue. *Clin Exp Pharmacol Physiol,* 32**,** 708-13.

CAI, D., CHEN, S. C., PRASAD, M., HE, L., WANG, X., CHOESMEL-CADAMURO, V., SAWYER, J. K., DANUSER, G. & MONTELL, D. J. 2014. Mechanical feedback through E-cadherin promotes direction sensing during collective cell migration. *Cell,* 157**,** 1146-59.

CAMPAS, O. 2016. A toolbox to explore the mechanics of living embryonic tissues. *Semin Cell Dev Biol,* 55**,** 119-30.

CAMPAS, O., MAMMOTO, T., HASSO, S., SPERLING, R. A., O'CONNELL, D., BISCHOF, A. G., MAAS, R., WEITZ, D. A., MAHADEVAN, L. & INGBER, D. E. 2014. Quantifying cell-generated mechanical forces within living embryonic tissues. *Nat Methods,* 11**,** 183-9.

CANALES COUTIÑO, B. & MAYOR, R. 2021. The mechanosensitive channel Piezo1 cooperates with semaphorins to control neural crest migration. *Development,* 148**,** dev200001.

CARNEY, T. J., DUTTON, K. A., GREENHILL, E., DELFINO-MACHIN, M., DUFOURCQ, P., BLADER, P. & KELSH, R. N. 2006. A direct role for Sox10 in specification of neural crest-derived sensory neurons. *Development,* 133**,** 4619-30.

CASSAR, S., ADATTO, I., FREEMAN, J. L., GAMSE, J. T., ITURRIA, I., LAWRENCE, C., MURIANA, A., PETERSON, R. T., VAN CRUCHTEN, S. & ZON, L. I. 2020. Use of Zebrafish in Drug Discovery Toxicology. *Chemical Research in Toxicology,* 33**,** 95-118.

CHALFIE, M., TU, Y., EUSKIRCHEN, G., WARD, W. W. & PRASHER, D. C. 1994. Green fluorescent protein as a marker for gene expression. *Science,* 263**,** 802-5.

CHEN, X., ZARO, J. L. & SHEN, W. C. 2013. Fusion protein linkers: property, design and functionality. *Adv Drug Deliv Rev,* 65**,** 1357-69.

CHUANG, H.-Y., HOFREE, M. & IDEKER, T. 2010. A Decade of Systems Biology. *Annual Review of Cell and Developmental Biology,* 26**,** 721-744.

CLAIRE, D., AHMED, S. A., HERSH, K. B., ADAM, J. B., NATALIE, F., BENJAMIEN, M., MARIAM, C., LUKE, D. L. & ERIC, R. S. 2020. Bright and tunable far-red chemigenetic indicators. *bioRxiv***,** 2020.01.08.898783.

CLAPHAM, D. E. 2007. Calcium signaling. *Cell,* 131**,** 1047-58.

CODY, C. W., PRASHER, D. C., WESTLER, W. M., PRENDERGAST, F. G. & WARD, W. W. 1993. Chemical structure of the hexapeptide chromophore of the Aequorea green-fluorescent protein. *Biochemistry,* 32**,** 1212-8.

CORREIA, J. H., RODRIGUES, J. A., PIMENTA, S., DONG, T. & YANG, Z. 2021. Photodynamic Therapy Review: Principles, Photosensitizers, Applications, and Future Directions. *Pharmaceutics,* 13.

COSTE, B., MATHUR, J., SCHMIDT, M., EARLEY, T. J., RANADE, S., PETRUS, M. J., DUBIN, A. E. & PATAPOUTIAN, A. 2010. Piezo1 and Piezo2 are essential components of distinct mechanically activated cation channels. *Science,* 330**,** 55-60.

COSTE, B., MURTHY, S. E., MATHUR, J., SCHMIDT, M., MECHIOUKHI, Y., DELMAS, P. & PATAPOUTIAN, A. 2015. Piezo1 ion channel pore properties are dictated by C-terminal region. *Nat Commun,* 6**,** 7223.

COSTE, B., XIAO, B., SANTOS, J. S., SYEDA, R., GRANDL, J., SPENCER, K. S., KIM, S. E., SCHMIDT, M., MATHUR, J., DUBIN, A. E., MONTAL, M. & PATAPOUTIAN, A. 2012. Piezo proteins are pore-forming subunits of mechanically activated channels. *Nature,* 483**,** 176-81.

COX, C. D., BAE, C., ZIEGLER, L., HARTLEY, S., NIKOLOVA-KRSTEVSKI, V., ROHDE, P. R., NG, C.-A., SACHS, F., GOTTLIEB, P. A. & MARTINAC, B. 2016. Removal of the mechanoprotective influence of the cytoskeleton reveals PIEZO1 is gated by bilayer tension. *Nature Communications,* 7**,** 10366.

COX, C. D., BAVI, N. & MARTINAC, B. 2017. Origin of the Force: The Force-From-Lipids Principle Applied to Piezo Channels. *Curr Top Membr,* 79**,** 59-96.

CROUS, A. & ABRAHAMSE, H. 2022. Photodynamic therapy of lung cancer, where are we? *Front Pharmacol,* 13**,** 932098.

CULIC-VISKOTA, J., DEMPSEY, W. P., FRASER, S. E. & PANTAZIS, P. 2012. Surface functionalization of barium titanate SHG nanoprobes for in vivo imaging in zebrafish. *Nat Protoc,* 7**,** 1618-33.

DALGHI, M. G., RUIZ, W. G., CLAYTON, D. R., MONTALBETTI, N., DAUGHERTY, S. L., BECKEL, J. M., CARATTINO, M. D. & APODACA, G. 2021. Functional roles for PIEZO1 and PIEZO2 in urothelial mechanotransduction and lower urinary tract interoception. *JCI insight,* 6**,** e152984.

DANA, H., MOHAR, B., SUN, Y., NARAYAN, S., GORDUS, A., HASSEMAN, J. P., TSEGAYE, G., HOLT, G. T., HU, A., WALPITA, D., PATEL, R., MACKLIN, J. J.,

BARGMANN, C. I., AHRENS, M. B., SCHREITER, E. R., JAYARAMAN, V., LOOGER, L. L., SVOBODA, K. & KIM, D. S. 2016. Sensitive red protein calcium indicators for imaging neural activity. *Elife,* 5.

DELLA PIETRA, A., MIKHAILOV, N. & GINIATULLIN, R. 2020. The Emerging Role of Mechanosensitive Piezo Channels in Migraine Pain. *International Journal of Molecular Sciences,* 21**,** 696.

DEMPSEY, W. P., FRASER, S. E. & PANTAZIS, P. 2012a. PhOTO zebrafish: a transgenic resource for in vivo lineage tracing during development and regeneration. *PLoS One,* 7**,** e32888.

DEMPSEY, W. P., FRASER, S. E. & PANTAZIS, P. 2012b. SHG nanoprobes: advancing harmonic imaging in biology. *Bioessays,* 34**,** 351-60.

DEMPSEY, W. P., GEORGIEVA, L., HELBLING, P. M., SONAY, A. Y., TRUONG, T. V., HAFFNER, M. & PANTAZIS, P. 2015. In vivo single-cell labeling by confined primed conversion. *Nat Methods,* 12**,** 645-8.

DEMPSEY, W. P., QIN, H. & PANTAZIS, P. 2014. In vivo cell tracking using PhOTO zebrafish. *Methods Mol Biol,* 1148**,** 217-28.

DICKSON, R. M., CUBITT, A. B., TSIEN, R. Y. & MOERNER, W. E. 1997. On/off blinking and switching behaviour of single molecules of green fluorescent protein. *Nature,* 388**,** 355-8.

DUDA, M., KIRKLAND, N. J., KHALILGHARIBI, N., TOZLUOGLU, M., YUEN, A. C., CARPI, N., BOVE, A., PIEL, M., CHARRAS, G., BAUM, B. & MAO, Y. 2019. Polarization of Myosin II Refines Tissue Material Properties to Buffer Mechanical Stress. *Dev Cell,* 48**,** 245-260.e7.

DUNSBY, C. 2008. Optically sectioned imaging by oblique plane microscopy. *Optics Express,* 16**,** 20306-20316.

EHMKE, H. 2018. The mechanotransduction of blood pressure. *Science,* 362**,** 398-399.

EISENHOFFER, G. T., LOFTUS, P. D., YOSHIGI, M., OTSUNA, H., CHIEN, C. B., MORCOS, P. A. & ROSENBLATT, J. 2012. Crowding induces live cell extrusion to maintain homeostatic cell numbers in epithelia. *Nature,* 484**,** 546-9.

ELLEFSEN, K. L., HOLT, J. R., CHANG, A. C., NOURSE, J. L., ARULMOLI, J., MEKHDJIAN, A. H., ABUWARDA, H., TOMBOLA, F., FLANAGAN, L. A., DUNN, A. R., PARKER, I. & PATHAK, M. M. 2019. Myosin-II mediated traction forces evoke localized Piezo1-dependent Ca2+ flickers. *Communications Biology,* 2.

EMSLEY, P., LOHKAMP, B., SCOTT, W. G. & COWTAN, K. 2010. Features and development of Coot. *Acta Crystallogr D Biol Crystallogr,* 66**,** 486-501.

EVANS, E. L., CUTHBERTSON, K., ENDESH, N., RODE, B., BLYTHE, N. M., HYMAN, A. J., HALL, S. J., GAUNT, H. J., LUDLOW, M. J., FOSTER, R. & BEECH, D. J. 2018. Yoda1 analogue (Dooku1) which antagonizes Yoda1-evoked activation of Piezo1 and aortic relaxation. *Br J Pharmacol,* 175**,** 1744-1759.

EXTERMANN, J., BONACINA, L., CUÑA, E., KASPARIAN, C., MUGNIER, Y., FEURER, T. & WOLF, J. P. 2009. Nanodoublers as deep imaging markers for multi-photon microscopy. *Opt Express,* 17**,** 15342-9.

FARMAN, G. P., TACHAMPA, K., MATEJA, R., CAZORLA, O., LACAMPAGNE, A. & DE TOMBE, P. P. 2008. Blebbistatin: use as inhibitor of muscle contraction. *Pflugers Arch,* 455**,** 995-1005.

FARRANTS, H., SHUAI, Y., LEMON, W. C., HERNANDEZ, C. M., YANG, S., PATEL, R., QIAO, G., FREI, M. S., GRIMM, J. B., HANSON, T. L., TOMASKA, F., TURNER, G. C., STRINGER, C., KELLER, P. J., BEYENE, A. G., CHEN, Y., LIANG, Y., LAVIS, L. D. & SCHREITER, E. R. 2023. A modular chemigenetic calcium indicator enables in vivo functional imaging with near-infrared light. *bioRxiv*.

FAUCHERRE, A., KISSA, K., NARGEOT, J., MANGONI, M. E. & JOPLING, C. 2014. Piezo1 plays a role in erythrocyte volume homeostasis. *Haematologica,* 99**,** 70-5.

FAUCHERRE, A., MOHA OU MAATI, H., NASR, N., PINARD, A., THERON, A., ODELIN, G., DESVIGNES, J. P., SALGADO, D., COLLOD-BÉROUD, G., AVIERINOS, J. F., LEBON, G., ZAFFRAN, S. & JOPLING, C. 2020. Piezo1 is required for outflow tract and aortic valve development. *J Mol Cell Cardiol,* 143**,** 51-62.

FÖLLING, J., BOSSI, M., BOCK, H., MEDDA, R., WURM, C. A., HEIN, B., JAKOBS, S., EGGELING, C. & HELL, S. W. 2008. Fluorescence nanoscopy by ground-state depletion and single-molecule return. *Nat Methods,* 5**,** 943-5.

FOO, Y. Y., PANT, S., TAY, H. S., IMANGALI, N., CHEN, N., WINKLER, C. & YAP, C. H. 2020. 4D modelling of fluid mechanics in the zebrafish embryonic heart. *Biomechanics and Modeling in Mechanobiology,* 19**,** 221-232.

FOTIOU, E., MARTIN-ALMEDINA, S., SIMPSON, M. A., LIN, S., GORDON, K., BRICE, G., ATTON, G., JEFFERY, I., REES, D. C., MIGNOT, C., VOGT, J., HOMFRAY, T., SNYDER, M. P., ROCKSON, S. G., JEFFERY, S., MORTIMER, P. S., MANSOUR, S. & OSTERGAARD, P. 2015. Novel mutations in PIEZO1 cause an autosomal recessive generalized lymphatic dysplasia with non-immune hydrops fetalis. *Nat Commun,* 6**,** 8085.

FREIKAMP, A., COST, A. L. & GRASHOFF, C. 2016. The Piconewton Force Awakens: Quantifying Mechanics in Cells. *Trends Cell Biol,* 26**,** 838-847.

FUKUI, H., CHOW, R. W., XIE, J., FOO, Y. Y., YAP, C. H., MINC, N., MOCHIZUKI, N. & VERMOT, J. 2021. Bioelectric signaling and the control of cardiac cell identity in response to mechanical forces. *Science,* 374**,** 351-354.

GARCIA-PARAJO, M. F., SEGERS-NOLTEN, G. M. J., VEERMAN, J. A., GREVE, J. & VAN HULST, N. F. 2000. Real-time light-driven dynamics of the fluorescence emission in single green fluorescent protein molecules. *Proceedings of the National Academy of Sciences,* 97**,** 7237-7242.

GASPARINI, G., SARGSYAN, G., BANG, E. K., SAKAI, N. & MATILE, S. 2015. Ring Tension Applied to Thiol-Mediated Cellular Uptake. *Angew Chem Int Ed Engl,* 54**,** 7328-31.

GAUB, B. M. & MULLER, D. J. 2017. Mechanical Stimulation of Piezo1 Receptors Depends on Extracellular Matrix Proteins and Directionality of Force. *Nano Lett,* 17**,** 2064-2072.

GAUTIER, H. O., THOMPSON, A. J., ACHOURI, S., KOSER, D. E., HOLTZMANN, K., MOEENDARBARY, E. & FRANZE, K. 2015. Atomic force microscopy-based force measurements on animal cells and tissues. *Methods Cell Biol,* 125**,** 211-35.

GENG, J., LIU, W., ZHOU, H., ZHANG, T., WANG, L., ZHANG, M., LI, Y., SHEN, B., LI, X. & XIAO, B. 2020. A Plug-and-Latch Mechanism for Gating the Mechanosensitive Piezo Channel. *Neuron,* 106**,** 438-451.e6.

GERARD, G. L., EMMANUEL, L. C., JEREMY, M., DANIELA, B., SELENA, L., DMITRIJS, C., STEPHANIE, V., JUNRU, H., BRITTANY, S., MAYA, O. T., RICHARD, O., DANIEL, H., AIDAN, B. B., ALBERTINA, T.-Z., ALI, H., DIANE, L., CHRISTOPHER, I. M., UTE, H. & NATHAN, C. S. 2023. CaBLAM! A high-contrast bioluminescent Ca²⁺ indicator derived from an engineered Oplophorus gracilirostris luciferase. *bioRxiv***,** 2023.06.25.546478.

GOEDHART, J. 2020. PlotTwist: A web app for plotting and annotating continuous data. *PLoS Biol,* 18**,** e3000581.

GÓMEZ-MÁRQUEZ, J. 2021. What is life? *Mol Biol Rep,* 48**,** 6223-6230.

GOTTLIEB, P. A., BAE, C. & SACHS, F. 2012. Gating the mechanical channel Piezo1: a comparison between whole-cell and patch recording. *Channels (Austin),* 6**,** 282-9.
GOULT, B. T., BROWN, N. H. & SCHWARTZ, M. A. 2021. Talin in mechanotransduction and mechanomemory at a glance. *Journal of Cell Science,* 134.
GRASHOFF, C., HOFFMAN, B. D., BRENNER, M. D., ZHOU, R., PARSONS, M., YANG, M. T., MCLEAN, M. A., SLIGAR, S. G., CHEN, C. S., HA, T. & SCHWARTZ, M. A. 2010. Measuring mechanical tension across vinculin reveals regulation of focal adhesion dynamics. *Nature,* 466**,** 263-6.
GU, Y. & GU, C. 2014. Physiological and pathological functions of mechanosensitive ion channels. *Mol Neurobiol,* 50**,** 339-47.
GUDIPATY, S. A., LINDBLOM, J., LOFTUS, P. D., REDD, M. J., EDES, K., DAVEY, C. F., KRISHNEGOWDA, V. & ROSENBLATT, J. 2017. Mechanical stretch triggers rapid epithelial cell division through Piezo1. *Nature,* 543**,** 118-121.
GUILLUY, C., OSBORNE, L. D., VAN LANDEGHEM, L., SHAREK, L., SUPERFINE, R., GARCIA-MATA, R. & BURRIDGE, K. 2014. Isolated nuclei adapt to force and reveal a mechanotransduction pathway in the nucleus. *Nat Cell Biol,* 16**,** 376-81.
GURSKAYA, N. G., VERKHUSHA, V. V., SHCHEGLOV, A. S., STAROVEROV, D. B., CHEPURNYKH, T. V., FRADKOV, A. F., LUKYANOV, S. & LUKYANOV, K. A. 2006. Engineering of a monomeric green-to-red photoactivatable fluorescent protein induced by blue light. *Nat Biotechnol,* 24**,** 461-5.
HA, T., ENDERLE, T., CHEMLA, D. S., SELVIN, P. R. & WEISS, S. 1997. Quantum jumps of single molecules at room temperature. *Chemical Physics Letters,* 271**,** 1-5.
HABUCHI, S., COTLET, M., GENSCH, T., BEDNARZ, T., HABER-POHLMEIER, S., ROZENSKI, J., DIRIX, G., MICHIELS, J., VANDERLEYDEN, J., HEBERLE, J., DE SCHRYVER, F. C. & HOFKENS, J. 2005. Evidence for the isomerization and decarboxylation in the photoconversion of the red fluorescent protein DsRed. *J Am Chem Soc,* 127**,** 8977-84.
HALLORAN, M. C., SATO-MAEDA, M., WARREN, J. T., SU, F., LELE, Z., KRONE, P. H., KUWADA, J. Y. & SHOJI, W. 2000. Laser-induced gene expression in specific cells of transgenic zebrafish. *Development,* 127**,** 1953-60.
HAMILL, O. P. & MCBRIDE, D. W. 1996. The pharmacology of mechanogated membrane ion channels. *Pharmacological reviews,* 48**,** 231-252.
HANDELMAN, A., KURITZ, N., NATAN, A. & ROSENMAN, G. 2016. Reconstructive Phase Transition in Ultrashort Peptide Nanostructures and Induced Visible Photoluminescence. *Langmuir,* 32**,** 2847-2862.
HANDELMAN, A., LAVROV, S., KUDRYAVTSEV, A., KHATCHATOURIANTS, A., ROSENBERG, Y., MISHINA, E. & ROSENMAN, G. 2013. Nonlinear Optical Bioinspired Peptide Nanostructures. *Advanced Optical Materials,* 1**,** 875-884.
HANNEZO, E. & HEISENBERG, C.-P. 2019. Mechanochemical Feedback Loops in Development and Disease. *Cell,* 178**,** 12-25.
HAUPTS, U., MAITI, S., SCHWILLE, P. & WEBB, W. W. 1998. Dynamics of fluorescence fluctuations in green fluorescent protein observed by fluorescence correlation spectroscopy. *Proc Natl Acad Sci U S A,* 95**,** 13573-8.
HEISENBERG, C. P. & BELLAICHE, Y. 2013. Forces in tissue morphogenesis and patterning. *Cell,* 153**,** 948-62.
HELASSA, N., PODOR, B., FINE, A. & TOROK, K. 2016. Design and mechanistic insight into ultrafast calcium indicators for monitoring intracellular calcium dynamics. *Sci Rep,* 6**,** 38276.

HERRMANN, C., WRAY, J., TRAVERS, F. & BARMAN, T. 1992. Effect of 2, 3-butanedione monoxime on myosin and myofibrillar ATPases. An example of an uncompetitive inhibitor. *Biochemistry,* 31**,** 12227-12232.

HOLT, J. R., ZENG, W.-Z., EVANS, E. L., WOO, S.-H., MA, S., ABUWARDA, H., LOUD, M., PATAPOUTIAN, A. & PATHAK, M. M. 2021. Spatiotemporal dynamics of PIEZO1 localization controls keratinocyte migration during wound healing. *eLife,* 10**,** e65415.

HONIG, M. G. & HUME, R. I. 1986. Fluorescent carbocyanine dyes allow living neurons of identified origin to be studied in long-term cultures. *J Cell Biol,* 103**,** 171-87.

HONIG, M. G. & HUME, R. I. 1989. Dil and diO: versatile fluorescent dyes for neuronal labelling and pathway tracing. *Trends Neurosci,* 12**,** 333-5, 340-1.

HOPKIN, M. 2006. Troublesome gene names get the boot. *Nature*.

HSIEH, C.-L., GRANGE, R., PU, Y. & PSALTIS, D. 2009. Three-dimensional harmonic holographic microcopy using nanoparticles as probes for cell imaging. *Optics Express,* 17**,** 2880-2891.

HUANG, L., LI, L., CHEN, X., ZHANG, H. & SHI, Z. 2016. MiR-103a targeting Piezo1 is involved in acute myocardial infarction through regulating endothelium function. *Cardiol J,* 23**,** 556-562.

HUISKEN, J., SWOGER, J., DEL BENE, F., WITTBRODT, J. & STELZER, E. H. K. 2004. Optical Sectioning Deep Inside Live Embryos by Selective Plane Illumination Microscopy. *Science,* 305**,** 1007.

HUNG, W. C., YANG, J. R., YANKASKAS, C. L., WONG, B. S., WU, P. H., PARDO-PASTOR, C., SERRA, S. A., CHIANG, M. J., GU, Z., WIRTZ, D., VALVERDE, M. A., YANG, J. T., ZHANG, J. & KONSTANTOPOULOS, K. 2016. Confinement Sensing and Signal Optimization via Piezo1/PKA and Myosin II Pathways. *Cell Rep,* 15**,** 1430-1441.

IACOVINO, M., BOSNAKOVSKI, D., FEY, H., RUX, D., BAJWA, G., MAHEN, E., MITANOSKA, A., XU, Z. & KYBA, M. 2011. Inducible cassette exchange: a rapid and efficient system enabling conditional gene expression in embryonic stem and primary cells. *Stem Cells,* 29**,** 1580-8.

ICHIKAWA, T., NAKAZATO, K., KELLER, P. J., KAJIURA-KOBAYASHI, H., STELZER, E. H. K., MOCHIZUKI, A. & NONAKA, S. 2013. Live imaging of whole mouse embryos during gastrulation: migration analyses of epiblast and mesodermal cells. *PloS one,* 8**,** e64506-e64506.

INGHAM, P. W. 2018. From Drosophila segmentation to human cancer therapy. *Development,* 145.

INOUE, T. & ISHIHARA, R. 2021. Photodynamic Therapy for Esophageal Cancer. *Clin Endosc,* 54**,** 494-498.

JANCARIK, J. & KIM, S.-H. 1991. Sparse matrix sampling: a screening method for crystallization of proteins. *Journal of applied crystallography,* 24**,** 409-411.

JEMIELITA, M., TAORMINA, M. J., DELAURIER, A., KIMMEL, C. B. & PARTHASARATHY, R. 2013. Comparing phototoxicity during the development of a zebrafish craniofacial bone using confocal and light sheet fluorescence microscopy techniques. *Journal of biophotonics,* 6**,** 920-928.

JIANG, F., YIN, K., WU, K., ZHANG, M., WANG, S., CHENG, H., ZHOU, Z. & XIAO, B. 2021a. The mechanosensitive Piezo1 channel mediates heart mechano-chemo transduction. *Nature Communications,* 12.

JIANG, W., DEL ROSARIO, J. S., BOTELLO-SMITH, W., ZHAO, S., LIN, Y.-C., ZHANG, H., LACROIX, J., ROHACS, T. & LUO, Y. L. 2021b. Crowding-induced opening of the mechanosensitive Piezo1 channel in silico. *Communications Biology,* 4**,** 84.

JIN, P., JAN, L. Y. & JAN, Y.-N. 2020. Mechanosensitive Ion Channels: Structural Features Relevant to Mechanotransduction Mechanisms. *Annual Review of Neuroscience,* 43**,** 207-229.

KACHYNSKI, A. V., KUZMIN, A. N., NYK, M., ROY, I. & PRASAD, P. N. 2008. Zinc Oxide Nanocrystals for Non-resonant Nonlinear Optical Microscopy in Biology and Medicine. *J Phys Chem C Nanomater Interfaces,* 112**,** 10721-10724.

KAI, F., LAKLAI, H. & WEAVER, V. M. 2016. Force Matters: Biomechanical Regulation of Cell Invasion and Migration in Disease. *Trends Cell Biol,* 26**,** 486-497.

KALYVIOTIS, K., QIN, H. & PANTAZIS, P. 2020. Chapter 19 - PhOTO zebrafish and primed conversion: advancing the mechanistic view of development and disease. *In:* GERLAI, R. T. (ed.) *Behavioral and Neural Genetics of Zebrafish.* Academic Press.

KELLER, P. J., SCHMIDT, A. D., WITTBRODT, J. & STELZER, E. H. 2008. Reconstruction of zebrafish early embryonic development by scanned light sheet microscopy. *Science,* 322**,** 1065-9.

KENT, I. A. & LELE, T. P. 2017. Microtubule-based force generation. *Wiley Interdiscip Rev Nanomed Nanobiotechnol,* 9.

KLEMENTIEVA, N. V., LUKYANOV, K. A., MARKINA, N. M., LUKYANOV, S. A., ZAGAYNOVA, E. V. & MISHIN, A. S. 2016. Green-to-red primed conversion of Dendra2 using blue and red lasers. *Chem Commun (Camb),* 52**,** 13144-13146.

KONOLD, P., REGMI, C. K., CHAPAGAIN, P. P., GERSTMAN, B. S. & JIMENEZ, R. 2014. Hydrogen bond flexibility correlates with Stokes shift in mPlum variants. *J Phys Chem B,* 118**,** 2940-8.

KULKARNI, S., MARQUEZ, J., DATE, P., VENTRELLA, R., MITCHELL, B. J. & KHOKHA, M. K. 2021. Mechanical stretch scales centriole number to apical area via Piezo1 in multiciliated cells. *eLife,* 10**,** e66076.

LE DOUARIN, N. M. 2008. Developmental patterning deciphered in avian chimeras. *Development, Growth & Differentiation,* 50**,** S11-S28.

LE DOUARIN, N. M. & TEILLET, M. A. 1974. Experimental analysis of the migration and differentiation of neuroblasts of the autonomic nervous system and of neurectodermal mesenchymal derivatives, using a biological cell marking technique. *Dev Biol,* 41**,** 162-84.

LECUIT, T., LENNE, P.-F. & MUNRO, E. 2011. Force generation, transmission, and integration during cell and tissue morphogenesis. *Annual review of cell and developmental biology,* 27**,** 157-184.

LEE, J., MOGHADAM, M. E., KUNG, E., CAO, H., BEEBE, T., MILLER, Y., ROMAN, B. L., LIEN, C. L., CHI, N. C., MARSDEN, A. L. & HSIAI, T. K. 2013. Moving domain computational fluid dynamics to interface with an embryonic model of cardiac morphogenesis. *PLoS One,* 8**,** e72924.

LEE, W., LEDDY, H. A., CHEN, Y., LEE, S. H., ZELENSKI, N. A., MCNULTY, A. L., WU, J., BEICKER, K. N., COLES, J., ZAUSCHER, S., GRANDL, J., SACHS, F., GUILAK, F. & LIEDTKE, W. B. 2014. Synergy between Piezo1 and Piezo2 channels confers high-strain mechanosensitivity to articular cartilage. *Proc Natl Acad Sci U S A,* 111**,** E5114-22.

LEE, W., NIMS, R. J., SAVADIPOUR, A., ZHANG, Q., LEDDY, H. A., LIU, F., MCNULTY, A. L., CHEN, Y., GUILAK, F. & LIEDTKE, W. B. 2021. Inflammatory signaling sensitizes Piezo1 mechanotransduction in articular chondrocytes as a pathogenic feed-forward mechanism in osteoarthritis. *Proceedings of the National Academy of Sciences,* 118**,** e2001611118.

LEWIS, P. J. & ERRINGTON, J. 1996. Use of green fluorescent protein for detection of cell-specific gene expression and subcellular protein localization during sporulation in Bacillus subtilis. *Microbiology,* 142 (Pt 4)**,** 733-40.

LI, C., REZANIA, S., KAMMERER, S., SOKOLOWSKI, A., DEVANEY, T., GORISCHEK, A., JAHN, S., HACKL, H., GROSCHNER, K., WINDPASSINGER, C., MALLE, E., BAUERNHOFER, T. & SCHREIBMAYER, W. 2015. Piezo1 forms mechanosensitive ion channels in the human MCF-7 breast cancer cell line. *Sci Rep,* 5**,** 8364.

LI, J., HOU, B., TUMOVA, S., MURAKI, K., BRUNS, A., LUDLOW, M. J., SEDO, A., HYMAN, A. J., MCKEOWN, L., YOUNG, R. S., YULDASHEVA, N. Y., MAJEED, Y., WILSON, L. A., RODE, B., BAILEY, M. A., KIM, H. R., FU, Z., CARTER, D. A., BILTON, J., IMRIE, H., AJUH, P., DEAR, T. N., CUBBON, R. M., KEARNEY, M. T., PRASAD, R. K., EVANS, P. C., AINSCOUGH, J. F. & BEECH, D. J. 2014. Piezo1 integration of vascular architecture with physiological force. *Nature,* 515**,** 279-282.

LIANG, J., HUANG, B., YUAN, G., CHEN, Y., LIANG, F., ZENG, H., ZHENG, S., CAO, L., GENG, D. & ZHOU, S. 2017. Stretch-activated channel Piezo1 is up-regulated in failure heart and cardiomyocyte stimulated by AngII. *Am J Transl Res,* 9**,** 2945-2955.

LICHTMAN, J. W. & CONCHELLO, J. A. 2005. Fluorescence microscopy. *Nat Methods,* 2**,** 910-9.

LIEBSCHNER, D., AFONINE, P. V., BAKER, M. L., BUNKÓCZI, G., CHEN, V. B., CROLL, T. I., HINTZE, B., HUNG, L. W., JAIN, S., MCCOY, A. J., MORIARTY, N. W., OEFFNER, R. D., POON, B. K., PRISANT, M. G., READ, R. J., RICHARDSON, J. S., RICHARDSON, D. C., SAMMITO, M. D., SOBOLEV, O. V., STOCKWELL, D. H., TERWILLIGER, T. C., URZHUMTSEV, A. G., VIDEAU, L. L., WILLIAMS, C. J. & ADAMS, P. D. 2019. Macromolecular structure determination using X-rays, neutrons and electrons: recent developments in Phenix. *Acta Crystallogr D Struct Biol,* 75**,** 861-877.

LIVET, J., WEISSMAN, T. A., KANG, H., DRAFT, R. W., LU, J., BENNIS, R. A., SANES, J. R. & LICHTMAN, J. W. 2007. Transgenic strategies for combinatorial expression of fluorescent proteins in the nervous system. *Nature,* 450**,** 56-62.

LONG, Q., MENG, A., WANG, H., JESSEN, J. R., FARRELL, M. J. & LIN, S. 1997. GATA-1 expression pattern can be recapitulated in living transgenic zebrafish using GFP reporter gene. *Development,* 124**,** 4105-4111.

LORETZ, B., THALER, M. & BERNKOP-SCHNÜRCH, A. 2007. Role of sulfhydryl groups in transfection? A case study with chitosan-NAC nanoparticles. *Bioconjug Chem,* 18**,** 1028-35.

LU, X., WEN, Y., ZHANG, S., ZHANG, W., CHEN, Y., SHEN, Y., LEMIEUX, M. J. & CAMPBELL, R. E. 2021. Photocleavable proteins that undergo fast and efficient dissociation. *Chem Sci,* 12**,** 9658-9672.

LUKACS, V., MATHUR, J., MAO, R., BAYRAK-TOYDEMIR, P., PROCTER, M., CAHALAN, S. M., KIM, H. J., BANDELL, M., LONGO, N., DAY, R. W., STEVENSON, D. A., PATAPOUTIAN, A. & KROCK, B. L. 2015. Impaired PIEZO1 function in patients with a novel autosomal recessive congenital lymphatic dysplasia. *Nat Commun,* 6**,** 8329.

LUO, D., CUI, S., LIU, Y., SHI, C., SONG, Q., QIN, X., ZHANG, T., XUE, Z. & WANG, T. 2018. Biocompatibility of Magnetic Resonance Imaging Nanoprobes Improved by Transformable Gadolinium Oxide Nanocoils. *Journal of the American Chemical Society,* 140**,** 14211-14216.

MA, X., LYNCH, H. E., SCULLY, P. C. & HUTSON, M. S. 2009. Probing embryonic tissue mechanics with laser hole drilling. *Physical Biology,* 6**,** 036004.

MACRAE, C. A. & PETERSON, R. T. 2015. Zebrafish as tools for drug discovery. *Nature Reviews Drug Discovery,* 14**,** 721-731.
MAGOUROUX, T., EXTERMANN, J., HOFFMANN, P., MUGNIER, Y., LE DANTEC, R., JACONI, M. E., KASPARIAN, C., CIEPIELEWSKI, D., BONACINA, L. & WOLF, J.-P. 2012. High-Speed Tracking of Murine Cardiac Stem Cells by Harmonic Nanodoublers. *Small,* 8**,** 2752-2756.
MAÎTRE, J. L., BERTHOUMIEUX, H., KRENS, S. F., SALBREUX, G., JÜLICHER, F., PALUCH, E. & HEISENBERG, C. P. 2012. Adhesion functions in cell sorting by mechanically coupling the cortices of adhering cells. *Science,* 338**,** 253-6.
MALEK, A. M., ALPER, S. L. & IZUMO, S. 1999. Hemodynamic shear stress and its role in atherosclerosis. *Jama,* 282**,** 2035-42.
MALKINSON, G., MAHOU, P., CHAUDAN, É., GACOIN, T., SONAY, A. Y., PANTAZIS, P., BEAUREPAIRE, E. & SUPATTO, W. 2020. Fast In Vivo Imaging of SHG Nanoprobes with Multiphoton Light-Sheet Microscopy. *ACS Photonics,* 7**,** 1036-1049.
MAMMOTO, T., MAMMOTO, A. & INGBER, D. E. 2013. Mechanobiology and developmental control. *Annu Rev Cell Dev Biol,* 29**,** 27-61.
MANNHARDT, I., EDER, A., DUMOTIER, B., PRONDZYNSKI, M., KRÄMER, E., TRAEBERT, M., SÖHREN, K. D., FLENNER, F., STATHOPOULOU, K., LEMOINE, M. D., CARRIER, L., CHRIST, T., ESCHENHAGEN, T. & HANSEN, A. 2017. Blinded Contractility Analysis in hiPSC-Cardiomyocytes in Engineered Heart Tissue Format: Comparison With Human Atrial Trabeculae. *Toxicol Sci,* 158**,** 164-175.
MARSHALL, A. R., MANIOU, E., MOULDING, D., GREENE, N. D. E., COPP, A. J. & GALEA, G. L. 2022. Two-Photon Cell and Tissue Level Laser AblationLaser ablations Methods to Study Morphogenetic BiomechanicsBiomechanics. *In:* CHANG, C. & WANG, J. (eds.) *Cell Polarity Signaling: Methods and Protocols.* New York, NY: Springer US.
MARTINS, J. R., PENTON, D., PEYRONNET, R., ARHATTE, M., MORO, C., PICARD, N., KURT, B., PATEL, A., HONORÉ, E. & DEMOLOMBE, S. 2016. Piezo1-dependent regulation of urinary osmolarity. *Pflugers Arch,* 468**,** 1197-1206.
MATZ, M. V., FRADKOV, A. F., LABAS, Y. A., SAVITSKY, A. P., ZARAISKY, A. G., MARKELOV, M. L. & LUKYANOV, S. A. 1999. Fluorescent proteins from nonbioluminescent Anthozoa species. *Nat Biotechnol,* 17**,** 969-73.
MCHUGH, B. J., BUTTERY, R., LAD, Y., BANKS, S., HASLETT, C. & SETHI, T. 2010. Integrin activation by Fam38A uses a novel mechanism of R-Ras targeting to the endoplasmic reticulum. *J Cell Sci,* 123**,** 51-61.
MCHUGH, B. J., MURDOCH, A., HASLETT, C. & SETHI, T. 2012. Loss of the integrin-activating transmembrane protein Fam38A (Piezo1) promotes a switch to a reduced integrin-dependent mode of cell migration. *PLoS One,* 7**,** e40346.
MCKINNEY, S. A., MURPHY, C. S., HAZELWOOD, K. L., DAVIDSON, M. W. & LOOGER, L. L. 2009. A bright and photostable photoconvertible fluorescent protein. *Nature Methods,* 6**,** 131.
MENG, F., SUCHYNA, T. M., LAZAKOVITCH, E., GRONOSTAJSKI, R. M. & SACHS, F. 2011. Real Time FRET Based Detection of Mechanical Stress in Cytoskeletal and Extracellular Matrix Proteins. *Cell Mol Bioeng,* 4**,** 148-159.
MIHALCESCU, I., VAN-MELLE GATEAU, M., CHELLI, B., PINEL, C. & RAVANAT, J.-L. 2015. Green autofluorescence, a double edged monitoring tool for bacterial growth and activity in micro-plates. *Physical Biology,* 12**,** 066016.
MIYAMOTO, T., MOCHIZUKI, T., NAKAGOMI, H., KIRA, S., WATANABE, M., TAKAYAMA, Y., SUZUKI, Y., KOIZUMI, S., TAKEDA, M. & TOMINAGA, M.

2014. Functional role for Piezo1 in stretch-evoked Ca^{2+} influx and ATP release in urothelial cell cultures. *J Biol Chem,* 289**,** 16565-75.
MIZUNO, H., MAL, T. K., TONG, K. I., ANDO, R., FURUTA, T., IKURA, M. & MIYAWAKI, A. 2003. Photo-induced peptide cleavage in the green-to-red conversion of a fluorescent protein. *Mol Cell,* 12**,** 1051-8.
MOHR, M. A., ARGAST, P. & PANTAZIS, P. 2016. Labeling cellular structures in vivo using confined primed conversion of photoconvertible fluorescent proteins. *Nat Protoc,* 11**,** 2419-2431.
MOHR, M. A., KOBITSKI, A. Y., SABATER, L. R., NIENHAUS, K., OBARA, C. J., LIPPINCOTT-SCHWARTZ, J., NIENHAUS, G. U. & PANTAZIS, P. 2017. Rational Engineering of Photoconvertible Fluorescent Proteins for Dual-Color Fluorescence Nanoscopy Enabled by a Triplet-State Mechanism of Primed Conversion. *Angew Chem Int Ed Engl,* 56**,** 11628-11633.
MOHR, M. A. & PANTAZIS, P. 2016. Single neuron morphology in vivo with confined primed conversion. *Methods Cell Biol,* 133**,** 125-38.
MORONI, M., SERVIN-VENCES, M. R., FLEISCHER, R., SÁNCHEZ-CARRANZA, O. & LEWIN, G. R. 2018. Voltage gating of mechanosensitive PIEZO channels. *Nature Communications,* 9**,** 1096.
MOSIMANN, C., KAUFMAN, C. K., LI, P., PUGACH, E. K., TAMPLIN, O. J. & ZON, L. I. 2011. Ubiquitous transgene expression and Cre-based recombination driven by the ubiquitin promoter in zebrafish. *Development,* 138**,** 169-77.
MOUSAVI, S. A. R., DUBIN, A. E., ZENG, W.-Z., COOMBS, A. M., DO, K., GHADIRI, D. A., KEENAN, W. T., GE, C., ZHAO, Y. & PATAPOUTIAN, A. 2021. PIEZO ion channel is required for root mechanotransduction in Arabidopsis thaliana. *Proceedings of the National Academy of Sciences,* 118**,** e2102188118.
NASU, Y., SHEN, Y., KRAMER, L. & CAMPBELL, R. E. 2021. Structure- and mechanism-guided design of single fluorescent protein-based biosensors. *Nature Chemical Biology,* 17**,** 509-518.
NGUETSE, C. N., PURINGTON, N., EBEL, E. R., SHAKYA, B., TETARD, M., KREMSNER, P. G., VELAVAN, T. P. & EGAN, E. S. 2020. A common polymorphism in the mechanosensitive ion channel PIEZO1 is associated with protection from severe malaria in humans. *Proceedings of the National Academy of Sciences,* 117**,** 9074-9081.
NIENHAUS, K., NIENHAUS, G. U., WIEDENMANN, J. & NAR, H. 2005. Structural basis for photo-induced protein cleavage and green-to-red conversion of fluorescent protein EosFP. *Proc Natl Acad Sci U S A,* 102**,** 9156-9.
NOMARSKI, G. 1952. lnterferornetre a potartsenon. *Bre-vet francais No. 1059123*.
NOTREDAME, C., HIGGINS, D. G. & HERINGA, J. 2000. T-Coffee: A novel method for fast and accurate multiple sequence alignment. *J Mol Biol,* 302**,** 205-17.
NÜSSLEIN-VOLHARD, C. & WIESCHAUS, E. 1980. Mutations affecting segment number and polarity in Drosophila. *Nature,* 287**,** 795-801.
OSWALD, C., SMITS, S. H. J., BREMER, E. & SCHMITT, L. 2008. Microseeding - a powerful tool for crystallizing proteins complexed with hydrolyzable substrates. *Int J Mol Sci,* 9**,** 1131-1141.
OU-YANG, Y., ZHENG, Y. & MILLS, K. E. 2023. Photodynamic therapy for skin carcinomas: A systematic review and meta-analysis. *Front Med (Lausanne),* 10**,** 1089361.
PACI, G. & MAO, Y. 2021. Forced into shape: Mechanical forces in Drosophila development and homeostasis. *Semin Cell Dev Biol,* 120**,** 160-170.

PAEZ-SEGALA, M. G., SUN, M. G., SHTENGEL, G., VISWANATHAN, S., BAIRD, M. A., MACKLIN, J. J., PATEL, R., ALLEN, J. R., HOWE, E. S., PISZCZEK, G., HESS, H. F., DAVIDSON, M. W., WANG, Y. & LOOGER, L. L. 2015. Fixation-resistant photoactivatable fluorescent proteins for CLEM. *Nature Methods,* 12**,** 215.

PAN, Y. A., FREUNDLICH, T., WEISSMAN, T. A., SCHOPPIK, D., WANG, X. C., ZIMMERMAN, S., CIRUNA, B., SANES, J. R., LICHTMAN, J. W. & SCHIER, A. F. 2013. Zebrabow: multispectral cell labeling for cell tracing and lineage analysis in zebrafish. *Development,* 140**,** 2835-46.

PANCIERA, T., AZZOLIN, L., CORDENONSI, M. & PICCOLO, S. 2017. Mechanobiology of YAP and TAZ in physiology and disease. *Nat Rev Mol Cell Biol,* 18**,** 758-770.

PANDZIC, E., WHAN, R. & MACMILLAN, A. 2022. Rapid FLIM Measurement of Membrane Tension Probe Flipper-TR. *Methods Mol Biol,* 2402**,** 257-283.

PANTAZIS, P., MALONEY, J., WU, D. & FRASER, S. E. 2010. Second harmonic generating (SHG) nanoprobes for in vivo imaging. *Proc Natl Acad Sci U S A,* 107**,** 14535-40.

PATHAK, M. M., NOURSE, J. L., TRAN, T., HWE, J., ARULMOLI, J., LE, D. T. T., BERNARDIS, E., FLANAGAN, L. A. & TOMBOLA, F. 2014. Stretch-activated ion channel Piezo1 directs lineage choice in human neural stem cells. *Proceedings of the National Academy of Sciences,* 111**,** 16148-16153.

PATTERSON, G. H. & LIPPINCOTT-SCHWARTZ, J. 2002. A photoactivatable GFP for selective photolabeling of proteins and cells. *Science,* 297**,** 1873-7.

PETTERSEN, E. F., GODDARD, T. D., HUANG, C. C., COUCH, G. S., GREENBLATT, D. M., MENG, E. C. & FERRIN, T. E. 2004. UCSF Chimera--a visualization system for exploratory research and analysis. *J Comput Chem,* 25**,** 1605-12.

PEYRONNET, R., MARTINS, J. R., DUPRAT, F., DEMOLOMBE, S., ARHATTE, M., JODAR, M., TAUC, M., DURANTON, C., PAULAIS, M., TEULON, J., HONORÉ, E. & PATEL, A. 2013. Piezo1-dependent stretch-activated channels are inhibited by Polycystin-2 in renal tubular epithelial cells. *EMBO Rep,* 14**,** 1143-8.

PINZON-OLEJUA, A., WELTE, C., CHEKURU, A., BOSAK, V., BRAND, M., HANS, S. & STUERMER, C. A. 2017. Cre-inducible site-specific recombination in zebrafish oligodendrocytes. *Dev Dyn,* 246**,** 41-49.

PISTON, D. W. & KREMERS, G. J. 2007. Fluorescent protein FRET: the good, the bad and the ugly. *Trends Biochem Sci,* 32**,** 407-14.

PLACHTA, N., BOLLENBACH, T., PEASE, S., FRASER, S. E. & PANTAZIS, P. 2011. Oct4 kinetics predict cell lineage patterning in the early mammalian embryo. *Nat Cell Biol,* 13**,** 117-23.

PLOEG, M. C., MUNTS, C., PRINZEN, F. W., TURNER, N. A., VAN BILSEN, M. & VAN NIEUWENHOVEN, F. A. 2021. Piezo1 Mechanosensitive Ion Channel Mediates Stretch-Induced Nppb Expression in Adult Rat Cardiac Fibroblasts. *Cells,* 10.

PRASHER, D. C., ECKENRODE, V. K., WARD, W. W., PRENDERGAST, F. G. & CORMIER, M. J. 1992. Primary structure of the Aequorea victoria green-fluorescent protein. *Gene,* 111**,** 229-33.

RABOTYAGOVA, O. S., CEBE, P. & KAPLAN, D. L. 2010. Role of Polyalanine Domains in β-Sheet Formation in Spider Silk Block Copolymers. *Macromolecular Bioscience,* 10**,** 49-59.

RADIN, I., RICHARDSON, R. A., COOMEY, J. H., WEINER, E. R., BASCOM, C. S., LI, T., BEZANILLA, M. & HASWELL, E. S. 2021. Plant PIEZO homologs modulate vacuole morphology during tip growth. *Science,* 373**,** 586-590.

RAMAKRISHNAN, P., MACLEAN, M., MACGREGOR, S. J., ANDERSON, J. G. & GRANT, M. H. 2016. Cytotoxic responses to 405nm light exposure in mammalian and bacterial cells: Involvement of reactive oxygen species. *Toxicology in Vitro,* 33**,** 54-62.

RANADE, S. S., QIU, Z., WOO, S. H., HUR, S. S., MURTHY, S. E., CAHALAN, S. M., XU, J., MATHUR, J., BANDELL, M., COSTE, B., LI, Y. S., CHIEN, S. & PATAPOUTIAN, A. 2014. Piezo1, a mechanically activated ion channel, is required for vascular development in mice. *Proc Natl Acad Sci U S A,* 111**,** 10347-52.

RANDOLPH, L. N., BAO, X., ZHOU, C. & LIAN, X. 2017. An all-in-one, Tet-On 3G inducible PiggyBac system for human pluripotent stem cells and derivatives. *Sci Rep,* 7**,** 1549.

RETAILLEAU, K., DUPRAT, F., ARHATTE, M., RANADE, S. S., PEYRONNET, R., MARTINS, J. R., JODAR, M., MORO, C., OFFERMANNS, S., FENG, Y., DEMOLOMBE, S., PATEL, A. & HONORÉ, E. 2015. Piezo1 in Smooth Muscle Cells Is Involved in Hypertension-Dependent Arterial Remodeling. *Cell Rep,* 13**,** 1161-1171.

RIDONE, P., PANDZIC, E., VASSALLI, M., COX, C. D., MACMILLAN, A., GOTTLIEB, P. A. & MARTINAC, B. 2020. Disruption of membrane cholesterol organization impairs the activity of PIEZO1 channel clusters. *Journal of General Physiology,* 152.

RIDONE, P., VASSALLI, M. & MARTINAC, B. 2019. Piezo1 mechanosensitive channels: what are they and why are they important. *Biophysical Reviews,* 11**,** 795-805.

RIVELINE, D., ZAMIR, E., BALABAN, N. Q., SCHWARZ, U. S., ISHIZAKI, T., NARUMIYA, S., KAM, Z., GEIGER, B. & BERSHADSKY, A. D. 2001. Focal contacts as mechanosensors: externally applied local mechanical force induces growth of focal contacts by an mDia1-dependent and ROCK-independent mechanism. *J Cell Biol,* 153**,** 1175-86.

RIZZO, M. A., SPRINGER, G. H., GRANADA, B. & PISTON, D. W. 2004. An improved cyan fluorescent protein variant useful for FRET. *Nat Biotechnol,* 22**,** 445-9.

RODRIGUEZ, E. A., CAMPBELL, R. E., LIN, J. Y., LIN, M. Z., MIYAWAKI, A., PALMER, A. E., SHU, X., ZHANG, J. & TSIEN, R. Y. 2017. The Growing and Glowing Toolbox of Fluorescent and Photoactive Proteins. *Trends Biochem Sci,* 42**,** 111-129.

ROESSLER, E., BELLONI, E., GAUDENZ, K., JAY, P., BERTA, P., SCHERER, S. W., TSUI, L.-C. & MUENKE, M. 1996. Mutations in the human Sonic Hedgehog gene cause holoprosencephaly. *Nature Genetics,* 14**,** 357-360.

ROSIŃCZUK, J., TARADAJ, J., DYMAREK, R. & SOPEL, M. 2016. Mechanoregulation of Wound Healing and Skin Homeostasis. *Biomed Res Int,* 2016**,** 3943481.

SANTORO, S. W. & SCHULTZ, P. G. 2002. Directed evolution of the site specificity of Cre recombinase. *Proceedings of the National Academy of Sciences,* 99**,** 4185-4190.

SATOH, K., HATA, M., TAKAHARA, S., TSUZAKI, H., YOKOTA, H., AKATSU, H., YAMAMOTO, T., KOSAKA, K. & YAMADA, T. 2006. A novel membrane protein, encoded by the gene covering KIAA0233, is transcriptionally induced in senile plaque-associated astrocytes. *Brain Res,* 1108**,** 19-27.

SAVIN, T., KURPIOS, N. A., SHYER, A. E., FLORESCU, P., LIANG, H., MAHADEVAN, L. & TABIN, C. J. 2011. On the growth and form of the gut. *Nature,* 476**,** 57-62.

SCHINDELIN, J., ARGANDA-CARRERAS, I., FRISE, E., KAYNIG, V., LONGAIR, M., PIETZSCH, T., PREIBISCH, S., RUEDEN, C., SAALFELD, S., SCHMID, B., TINEVEZ, J.-Y., WHITE, D. J., HARTENSTEIN, V., ELICEIRI, K., TOMANCAK, P. & CARDONA, A. 2012. Fiji: an open-source platform for biological-image analysis. *Nature Methods,* 9**,** 676-682.

SHANER, N. C., CAMPBELL, R. E., STEINBACH, P. A., GIEPMANS, B. N., PALMER, A. E. & TSIEN, R. Y. 2004. Improved monomeric red, orange and yellow fluorescent proteins derived from Discosoma sp. red fluorescent protein. *Nat Biotechnol,* 22**,** 1567-72.

SHANER, N. C., LIN, M. Z., MCKEOWN, M. R., STEINBACH, P. A., HAZELWOOD, K. L., DAVIDSON, M. W. & TSIEN, R. Y. 2008. Improving the photostability of bright monomeric orange and red fluorescent proteins. *Nat Methods,* 5**,** 545-51.

SHELLARD, A. & MAYOR, R. 2021. Collective durotaxis along a self-generated stiffness gradient in vivo. *Nature,* 600**,** 690-694.

SHI, X., ABBYAD, P., SHU, X., KALLIO, K., KANCHANAWONG, P., CHILDS, W., REMINGTON, S. J. & BOXER, S. G. 2007. Ultrafast excited-state dynamics in the green fluorescent protein variant S65T/H148D. 2. Unusual photophysical properties. *Biochemistry,* 46**,** 12014-25.

SHIMOMURA, O., JOHNSON, F. H. & SAIGA, Y. 1962. Extraction, purification and properties of aequorin, a bioluminescent protein from the luminous hydromedusan, Aequorea. *J Cell Comp Physiol,* 59**,** 223-39.

SIKKEL, M. B., KUMAR, S., MAIOLI, V., ROWLANDS, C., GORDON, F., HARDING, S. E., LYON, A. R., MACLEOD, K. T. & DUNSBY, C. 2016. High speed sCMOS-based oblique plane microscopy applied to the study of calcium dynamics in cardiac myocytes. *J Biophotonics,* 9**,** 311-23.

SOLOMON, B. D., MERCIER, S., VÉLEZ, J. I., PINEDA-ALVAREZ, D. E., WYLLIE, A., ZHOU, N., DUBOURG, C., DAVID, V., ODENT, S., ROESSLER, E. & MUENKE, M. 2010. Analysis of genotype-phenotype correlations in human holoprosencephaly. *Am J Med Genet C Semin Med Genet,* 154c**,** 133-41.

SONAY, A. Y., KALYVIOTIS, K., YAGANOGLU, S., UNSAL, A., KONANTZ, M., TEULON, C., LIEBERWIRTH, I., SIEBER, S., JIANG, S., BEHZADI, S., CRESPY, D., LANDFESTER, K., ROKE, S., LENGERKE, C. & PANTAZIS, P. 2021. Biodegradable Harmonophores for Targeted High-Resolution In Vivo Tumor Imaging. *ACS Nano*.

SPEMANN, H. & MANGOLD, H. 1924. Induction of Embryonic Primordia by Implantation of Organizers from a Different Species. *Archiv für Mikroskopische Anatomie und Entwicklungsmechanik,* 100**,** 599–63.

STAEDLER, D., MAGOUROUX, T., HADJI, R., JOULAUD, C., EXTERMANN, J., SCHWUNG, S., PASSEMARD, S., KASPARIAN, C., CLARKE, G., GERRMANN, M., LE DANTEC, R., MUGNIER, Y., RYTZ, D., CIEPIELEWSKI, D., GALEZ, C., GERBER-LEMAIRE, S., JUILLERAT-JEANNERET, L., BONACINA, L. & WOLF, J.-P. 2012. Harmonic Nanocrystals for Biolabeling: A Survey of Optical Properties and Biocompatibility. *ACS Nano,* 6**,** 2542-2549.

STAFF, R. H., SCHAEFFEL, D., TURSHATOV, A., DONADIO, D., BUTT, H.-J., LANDFESTER, K., KOYNOV, K. & CRESPY, D. 2013. Particle Formation in the Emulsion-Solvent Evaporation Process. *Small,* 9**,** 3514-3522.

STEINHAUER, C., FORTHMANN, C., VOGELSANG, J. & TINNEFELD, P. 2008. Superresolution microscopy on the basis of engineered dark states. *J Am Chem Soc,* 130**,** 16840-1.

STUART, G. W., MCMURRAY, J. V. & WESTERFIELD, M. 1988. Replication, integration and stable germ-line transmission of foreign sequences injected into early zebrafish embryos. *Development,* 103**,** 403-412.

SUGIMURA, K., LENNE, P.-F. & GRANER, F. 2016. Measuring forces and stresses in situ in living tissues. *Development,* 143**,** 186-196.

SUGIYAMA, N., SONAY, A. Y., TUSSIWAND, R., COHEN, B. E. & PANTAZIS, P. 2018. Effective Labeling of Primary Somatic Stem Cells with BaTiO3 Nanocrystals for Second Harmonic Generation Imaging. *Small,* 14.

SULSTON, J. E., SCHIERENBERG, E., WHITE, J. G. & THOMSON, J. N. 1983. The embryonic cell lineage of the nematode Caenorhabditis elegans. *Dev Biol,* 100**,** 64-119.

SUN, X. R., BADURA, A., PACHECO, D. A., LYNCH, L. A., SCHNEIDER, E. R., TAYLOR, M. P., HOGUE, I. B., ENQUIST, L. W., MURTHY, M. & WANG, S. S. 2013. Fast GCaMPs for improved tracking of neuronal activity. *Nat Commun,* 4**,** 2170.

SYEDA, R., FLORENDO, M. N., COX, C. D., KEFAUVER, J. M., SANTOS, J. S., MARTINAC, B. & PATAPOUTIAN, A. 2016. Piezo1 channels are inherently mechanosensitive. *Cell reports,* 17**,** 1739-1746.

SYEDA, R., XU, J., DUBIN, A. E., COSTE, B., MATHUR, J., HUYNH, T., MATZEN, J., LAO, J., TULLY, D. C., ENGELS, I. H., PETRASSI, H. M., SCHUMACHER, A. M., MONTAL, M., BANDELL, M. & PATAPOUTIAN, A. 2015. Chemical activation of the mechanotransduction channel Piezo1. *Elife,* 4.

TARANTINO, N., TINEVEZ, J.-Y., CROWELL, E. F., BOISSON, B., HENRIQUES, R., MHLANGA, M., AGOU, F., ISRAËL, A. & LAPLANTINE, E. 2014. TNF and IL-1 exhibit distinct ubiquitin requirements for inducing NEMO–IKK supramolecular structures. *Journal of Cell Biology,* 204**,** 231-245.

TINEVEZ, J. Y., PERRY, N., SCHINDELIN, J., HOOPES, G. M., REYNOLDS, G. D., LAPLANTINE, E., BEDNAREK, S. Y., SHORTE, S. L. & ELICEIRI, K. W. 2017. TrackMate: An open and extensible platform for single-particle tracking. *Methods,* 115**,** 80-90.

TSIEN, R. Y. 1998. The green fluorescent protein. *Annu Rev Biochem,* 67**,** 509-44.

TURKOWYD, B., BALINOVIC, A., VIRANT, D., CARNERO, H. G. G., CALDANA, F., ENDESFELDER, M., BOURGEOIS, D. & ENDESFELDER, U. 2017. A General Mechanism of Photoconversion of Green-to-Red Fluorescent Proteins Based on Blue and Infrared Light Reduces Phototoxicity in Live-Cell Single-Molecule Imaging. *Angew Chem Int Ed Engl,* 56**,** 11634-11639.

UHLÉN, M., FAGERBERG, L., HALLSTRÖM, B. M., LINDSKOG, C., OKSVOLD, P., MARDINOGLU, A., SIVERTSSON, Å., KAMPF, C., SJÖSTEDT, E., ASPLUND, A., OLSSON, I., EDLUND, K., LUNDBERG, E., NAVANI, S., SZIGYARTO, C. A.-K., ODEBERG, J., DJUREINOVIC, D., TAKANEN, J. O., HOBER, S., ALM, T., EDQVIST, P.-H., BERLING, H., TEGEL, H., MULDER, J., ROCKBERG, J., NILSSON, P., SCHWENK, J. M., HAMSTEN, M., VON FEILITZEN, K., FORSBERG, M., PERSSON, L., JOHANSSON, F., ZWAHLEN, M., VON HEIJNE, G., NIELSEN, J. & PONTÉN, F. 2015. Tissue-based map of the human proteome. *Science,* 347**,** 1260419.

VAN DER LINDEN, F. H., MAHLANDT, E. K., ARTS, J. J. G., BEUMER, J., PUSCHHOF, J., DE MAN, S. M. A., CHERTKOVA, A. O., PONSIOEN, B., CLEVERS, H., VAN BUUL, J. D., POSTMA, M., GADELLA, T. W. J. & GOEDHART, J. 2021a. A turquoise fluorescence lifetime-based biosensor for quantitative imaging of intracellular calcium. *Nature Communications,* 12**,** 7159.

VAN DER LINDEN, F. H., MAHLANDT, E. K., ARTS, J. J. G., BEUMER, J., PUSCHHOF, J., DE MAN, S. M. A., CHERTKOVA, A. O., PONSIOEN, B., CLEVERS, H., VAN BUUL, J. D., POSTMA, M., GADELLA, T. W. J., JR. & GOEDHART, J. 2021b. A turquoise fluorescence lifetime-based biosensor for quantitative imaging of intracellular calcium. *Nat Commun,* 12**,** 7159.

VELASCO-ESTEVEZ, M., GADALLA, K. K. E., LIÑAN-BARBA, N., COBB, S., DEV, K. K. & SHERIDAN, G. K. 2020. Inhibition of Piezo1 attenuates demyelination in the central nervous system. *Glia,* 68**,** 356-375.

VIAN, A., POCHITALOFF, M., YEN, S.-T., KIM, S., POLLOCK, J., LIU, Y., SLETTEN, E. & CAMPÀS, O. 2022. In situ quantification of osmotic pressure within living embryonic tissues. *bioRxiv***,** 2022.12.04.519060.

VIGNES, H., VAGENA-PANTOULA, C. & VERMOT, J. 2022. Mechanical control of tissue shape: Cell-extrinsic and -intrinsic mechanisms join forces to regulate morphogenesis. *Seminars in Cell & Developmental Biology,* 130**,** 45-55.

VINING, K. H. & MOONEY, D. J. 2017. Mechanical forces direct stem cell behaviour in development and regeneration. *Nat Rev Mol Cell Biol,* 18**,** 728-742.

VISSER, A. J. W. G. & HINK, M. A. 1999. New Perspectives of Fluorescence Correlation Spectroscopy. *Journal of Fluorescence,* 9**,** 81-87.

VOGT, W. 1925. *Gestaltungsanalyse am Amphibienkeim mit ortlicher Vitalfarbung. Vorwarts uber Wege und Ziele. I. Methodik und Wirkungsweise der Vitalfarbung mit Agar als Farbtrager*.

WADDINGTON, C. H. 1932. Experiments on the Development of Chick and Duck Embryos, Cultivated in vitro. *Philosophical Transactions of the Royal Society of London. Series B, Containing Papers of a Biological Character* 221**,** 179–230.

WALDCHEN, S., LEHMANN, J., KLEIN, T., VAN DE LINDE, S. & SAUER, M. 2015. Light-induced cell damage in live-cell super-resolution microscopy. *Sci Rep,* 5**,** 15348.

WALLINGFORD, J. B. 2019. We Are All Developmental Biologists. *Developmental Cell,* 50**,** 132-137.

WANG, H., HAO, J. & HONG, C. C. 2011. Cardiac induction of embryonic stem cells by a small molecule inhibitor of Wnt/beta-catenin signaling. *ACS Chem Biol,* 6**,** 192-7.

WANG, S., CHENNUPATI, R., KAUR, H., IRING, A., WETTSCHURECK, N. & OFFERMANNS, S. 2016. Endothelial cation channel PIEZO1 controls blood pressure by mediating flow-induced ATP release. *J Clin Invest,* 126**,** 4527-4536.

WANG, Y., CHI, S., GUO, H., LI, G., WANG, L., ZHAO, Q., RAO, Y., ZU, L., HE, W. & XIAO, B. 2018. A lever-like transduction pathway for long-distance chemical- and mechano-gating of the mechanosensitive Piezo1 channel. *Nature Communications,* 9**,** 1300.

WANG, Y., DE ARCANGELIS, V., GAO, X., RAMANI, B., JUNG, Y.-S. & XIANG, Y. 2008. Norepinephrine- and Epinephrine-induced Distinct β2-Adrenoceptor Signaling Is Dictated by GRK2 Phosphorylation in Cardiomyocytes. *Journal of Biological Chemistry,* 283**,** 1799-1807.

WELLING, M., KALYVIOTIS, K. & PANTAZIS, P. 2020. Primed Track: Reliable Volumetric Single-cell Tracking and Lineage Tracing of Living Specimen with Dual-labeling Approaches. *Bio-protocol,* 10**,** e3645.

WELLING, M., MOHR, M. A., PONTI, A., RULLAN SABATER, L., BONI, A., KAWAMURA, Y. K., LIBERALI, P., PETERS, A. H., PELCZAR, P. & PANTAZIS, P. 2019. Primed Track, high-fidelity lineage tracing in mouse pre-implantation embryos using primed conversion of photoconvertible proteins. *Elife,* 8.

WHITMAN, C. O. 1878. *The embryology of Clepsine,* London, J.E. Adlard.

WIEDENMANN, J., IVANCHENKO, S., OSWALD, F., SCHMITT, F., ROCKER, C., SALIH, A., SPINDLER, K. D. & NIENHAUS, G. U. 2004. EosFP, a fluorescent marker protein with UV-inducible green-to-red fluorescence conversion. *Proc Natl Acad Sci U S A,* 101**,** 15905-10.

WITZANY, G. 2020. What is Life? *Frontiers in Astronomy and Space Sciences,* 7.

WU, J., LEWIS, A. H. & GRANDL, J. 2017. Touch, Tension, and Transduction - The Function and Regulation of Piezo Ion Channels. *Trends Biochem Sci,* 42**,** 57-71.

WU, Y., GHITANI, A., CHRISTENSEN, R., SANTELLA, A., DU, Z., RONDEAU, G., BAO, Z., COLÓN-RAMOS, D. & SHROFF, H. 2011. Inverted selective plane illumination microscopy (iSPIM) enables coupled cell identity lineaging and neurodevelopmental imaging in Caenorhabditis elegans. *Proceedings of the National Academy of Sciences,* 108**,** 17708-17713.

XI, J., KHALIL, M., SHISHECHIAN, N., HANNES, T., PFANNKUCHE, K., LIANG, H., FATIMA, A., HAUSTEIN, M., SUHR, F., BLOCH, W., REPPEL, M., SARIĆ, T., WERNIG, M., JÄNISCH, R., BROCKMEIER, K., HESCHELER, J. & PILLEKAMP, F. 2010. Comparison of contractile behavior of native murine ventricular tissue and cardiomyocytes derived from embryonic or induced pluripotent stem cells. *Faseb j,* 24**,** 2739-51.

XIE, J., MURONE, M., LUOH, S.-M., RYAN, A., GU, Q., ZHANG, C., BONIFAS, J. M., LAM, C.-W., HYNES, M., GODDARD, A., ROSENTHAL, A., EPSTEIN, E. H. & DE SAUVAGE, F. J. 1998. Activating Smoothened mutations in sporadic basal-cell carcinoma. *Nature,* 391**,** 90-92.

XUAN, L., JU, Z., SKONIECZNA, M., ZHOU, P. K. & HUANG, R. 2023. Nanoparticles-induced potential toxicity on human health: Applications, toxicity mechanisms, and evaluation models. *MedComm (2020),* 4**,** e327.

YANG, B., CHEN, X., WANG, Y., FENG, S., PESSINO, V., STUURMAN, N., CHO, N. H., CHENG, K. W., LORD, S. J., XU, L., XIE, D., MULLINS, R. D., LEONETTI, M. D. & HUANG, B. 2019. Epi-illumination SPIM for volumetric imaging with high spatial-temporal resolution. *Nat Methods,* 16**,** 501-504.

YANG, B., LANGE, M., MILLETT-SIKKING, A., ZHAO, X., BRAGANTINI, J., VIJAYKUMAR, S., KAMB, M., GÓMEZ-SJÖBERG, R., SOLAK, A. C., WANG, W., KOBAYASHI, H., MCCARROLL, M. N., WHITEHEAD, L. W., FIOLKA, R. P., KORNBERG, T. B., YORK, A. G. & ROYER, L. A. 2022a. DaXi-high-resolution, large imaging volume and multi-view single-objective light-sheet microscopy. *Nat Methods,* 19**,** 461-469.

YANG, X., LIN, C., CHEN, X., LI, S., LI, X. & XIAO, B. 2022b. Structure deformation and curvature sensing of PIEZO1 in lipid membranes. *Nature,* 604**,** 377-383.

YANG, X. N., LU, Y. P., LIU, J. J., HUANG, J. K., LIU, Y. P., XIAO, C. X., JAZAG, A., REN, J. L. & GULENG, B. 2014. Piezo1 is as a novel trefoil factor family 1 binding protein that promotes gastric cancer cell mobility in vitro. *Dig Dis Sci,* 59**,** 1428-35.

ZARYCHANSKI, R., SCHULZ, V. P., HOUSTON, B. L., MAKSIMOVA, Y., HOUSTON, D. S., SMITH, B., RINEHART, J. & GALLAGHER, P. G. 2012. Mutations in the mechanotransduction protein PIEZO1 are associated with hereditary xerocytosis. *Blood,* 120**,** 1908-15.

ZHANG, M., CHANG, H., ZHANG, Y., YU, J., WU, L., JI, W., CHEN, J., LIU, B., LU, J., LIU, Y., ZHANG, J., XU, P. & XU, T. 2012. Rational design of true monomeric and bright photoactivatable fluorescent proteins. *Nature Methods,* 9**,** 727.

ZHANG, Y., SU, S.-A., LI, W., MA, Y., SHEN, J., WANG, Y., SHEN, Y., CHEN, J., JI, Y., XIE, Y., MA, H. & XIANG, M. 2021. Piezo1-Mediated Mechanotransduction Promotes Cardiac Hypertrophy by Impairing Calcium Homeostasis to Activate Calpain/Calcineurin Signaling. *Hypertension,* 78**,** 647-660.

ZHAO, Q., WU, K., GENG, J., CHI, S., WANG, Y., ZHI, P., ZHANG, M. & XIAO, B. 2016. Ion Permeation and Mechanotransduction Mechanisms of Mechanosensitive Piezo Channels. *Neuron,* 89**,** 1248-1263.

ZHAO, Q., ZHOU, H., CHI, S., WANG, Y., WANG, J., GENG, J., WU, K., LIU, W., ZHANG, T., DONG, M. Q., WANG, J., LI, X. & XIAO, B. 2018. Structure and mechanogating mechanism of the Piezo1 channel. *Nature,* 554**,** 487-492.

ZHIVOTOVSKY, B. & ORRENIUS, S. 2011. Calcium and cell death mechanisms: a perspective from the cell death community. *Cell Calcium,* 50**,** 211-21.

ZHOU, Z., LI, J. V., MARTINAC, B. & COX, C. D. 2021. Loss-of-Function Piezo1 Mutations Display Altered Stability Driven by Ubiquitination and Proteasomal Degradation. *Front Pharmacol,* 12**,** 766416.

ZHU, J., LUO, B.-H., XIAO, T. S., ZHANG, C., NISHIDA, N. & SPRINGER, T. A. 2008. Structure of a complete integrin ectodomain in a physiologic resting state and activation and deactivation by applied forces. *Molecular cell,* 32 6**,** 849-61.

Appendix

A.1 List of primers

Oligo name	Oligo sequence (5'>3')
Gibson Assembly F	GAAGTAAGGAAGGAAAAAAGCGGCCGCGTCTAGAGATCCAGACATGATAAGATACATTG
Gibson Assembly R	CATCATTTTGGCAAAGAAATCAAGCTTATCGCATGGAGCCGCACGT
GenEPiSeqFW1	GAGGTCTATATAAGCAGAGCTGG
GenEPiSeqFW2	CTACCTGCTGCTCTTCCTGG
GenEPiSeqFW3	CTGTATGGGATGACGCTGTG
GenEPiSeqFW4	CTCACAGGCAGGATGCAGTG
GenEPiSeqFW5	CAGCTGGACCAGGATCTGC
GenEPiSeqFW6	CGTCACCGTCATCATCTCCAA
GenEPiSeqFW7	GAACAGGCAGGACAGCTACC
GenEPiSeqFW8	ATCCCGAGGCCCAGCAA
GenEPiSeqFW9	ATCATCATTTTTGGCTTCTGGGC
GenEPiSeqFW10	CTGTTCACCATGAGCGCC
GenEPiSeqFW11	GACCGCATCCTCAAGCTCT
GenEPiSeqFW12	GGCAAGCTGACCCTGAAGTT
XLGenEPi_S217L_FW	TGGCCCTCTCCAGTGTCTACCTGCTGCTC
XLGenEPi_S217L_R	GGGGGTGGGCGATGCCTGCCAGTGCAAG
R10K_Q5SD_F	CCAGACATGAAGATCAAACTC
R10K_Q5SD_R	CTTAATCGCACTCACCATG
Y35F_Q5SD_F	GGCAAGCCTTTTGAGGGAAAAC
Y35F_Q5SD_R	TGTACCATCTCCGTCGATC
T40S_Q5SD_F	GGAAAACAGAGCATGGATCTTG
T40S_Q5SD_R	CTCATAAGGCTTGCCTGTAC
A196C_Q5SD_F	TGTGGACCACTGCATTGAGATTTTAAGCCATGAC
A196C_Q5SD_R	AAGTGGGCGCCTGGTAAC
N11K_Q5SD_F	TGAAGATCAAACTCCGTATGG
N11K_Q5SD_R	TGTCTGGCTTAATCGCAC
E70K_Q5SD_F	GGTATTCACCAAATATCCAGACC
E70K_Q5SD_R	CTGTTGCCGTAATGGAATG
H121Y_Q5SD_F	AGTTCGATTTTACGGTACAAAC
H121Y_Q5SD_R	TTATTATAGAAAGTGTCCCC
H74N_Q5SD_F	ATATCCAGACAACATACAAGACTATTTTAAG
H74N_Q5SD_R	TCGGTGAATACCCTGTTG

A.2 List of plasmids

Plasmid name	Used for
pCMV-GenEPi	Overexpression of GenEPi in different cell lines, electrophysiology analyses
XLGenEPi	Temporally controlled inducible expression of GenEPi in different cell lines, TIRFM
XLGenEPi-S217L	Temporally controlled inducible expression of GenEPi-S217L mutant in different cell lines
p2lox-GenEPi	Generation of inducible GenEPi-mESCs
hsp70-GenEPi	Generation of the *Tg(hsp70:GenEPi)* zebrafish transgenic line
pRSET-Dendra2	Bacterial expression of pr-FP Dendra2
pQE32-pr-mEosFP	Bacterial expression of pr-FP pr-mEosFP
pRSET-pr-mEos2	Bacterial expression of pr-FP pr-mEos2
pRSET-pr-mEos3.1	Bacterial expression of pr-FP pr-mEos3.1
pRSET-pr-mEos3.2	Bacterial expression of pr-FP pr-mEos3.2
pRSET-pr-mEos4a	Bacterial expression of pr-FP pr-mEos4a
pRSET-pr-mEos4b	Bacterial expression of pr-FP pr-mEos4b
pRSET-mEos4b	Bacterial expression of the non-primed convertible FP mEos4b

A.3 Different fluorescent proteins and their respective maximum excitation and emission wavelengths used to generate Fig. 6C

Fluorescent Protein	Excitation Wavelength (nm)	Emission Wavelength (nm)
Sirius	355	424
Sandercyanin	375	630
shBFP-N158S/L173I	375	458
Azurite	383	450
EBFP2	383	448
mKalama1	385	456
mTagBFP2	399	454
Sapphire	399	511
T-Sapphire	399	511
shBFP	401	458
TagBFP	402	457
mAmetrine	406	526
Aquamarine	430	474
ECFP	433	475
Cerulean	433	475
mCerulean3	433	475
SCFP3A	433	474
mTurquoise	434	474
mTurquoise2	434	474
CyPet	435	477
LSSmOrange	437	572
mKeima	440	620
mBeRFP	446	611
TagCFP	458	480
LSS-mKate2	460	605
mTFP1	462	492
LSS-mKate1	463	624
monomeric Midoriishi-Cyan	470	496
TurboGFP	482	502
TagGFP2	483	506
mUKG	483	499
Superfolder GFP	485	510
Emerald	487	509
EGFP	488	507
Monomeric Azami Green	492	505
mWasabi	493	509
NowGFP	494	502
CyOFP1	497	589
Clover	505	515
mNeonGreen	506	517

mClover3	506	518
TagYFP	508	524
EYFP	513	527
Topaz	514	527
Venus	515	528
SYFP2	515	527
Citrine	516	529
Ypet	517	530
IanRFP-ΔS83	521	592
mCyRFP1	528	594
mPapaya1	530	541
Monomeric Kusabira-Orange	548	559
mOrange	548	562
mOrange2	549	565
mKOκ	551	563
mKO2	551	565
tdTomato	554	581
TagRFP	555	584
TagRFP-T	555	584
RRvT	556	583
mRuby	558	605
mNectarine	558	578
mRuby3	558	592
mRuby2	559	600
mTangerine	568	585
mApple	568	592
mScarlet	569	594
mScarlet-I	569	593
mStrawberry	574	596
FusionRed	580	608
mCherry	587	610
mKate2	588	633
HcRed-Tandem	590	637
mPlum	590	649
mStable	597	633
mRaspberry	598	625
TagRFP675	598	675
mGarnet2	598	671
mNeptune	600	650
mCardinal	604	659
NirFP	605	670
mMaroon1	609	657
TagRFP657	611	657
TDsmURFP	642	670
miRFP670	642	670
iRFP670	643	670

iRFP682	663	682
iRFP702	673	702
mIFP	683	704
iFP1.4	684	708
iRFP713 (iRFP)	690	713
iFP2.0	690	711
iRFP720	702	720

A.4 Piezo1 and Piezo2 protein sequences used for the similarity analyses

>Human_Piezo1

MEPHVLGAVLYWLLLPCALLAACLLRFSGLSLVYLLFLLLLPWFPGPTRCGLQGHTGRLL
RALLGLSLLFLVAHLALQICLHIVPRLDQLLGPSCSRWETLSRHIGVTRLDLKDIPNAIRLVA
PDLGILVVSSVCLGICGRLARNTRQSPHPRELDDDERDVDASPTAGLQEAATLAPTRRS
RLAARFRVTAHWLLVAAGRVLAVTLLALAGIAHPSALSSVYLLLFLALCTWWACHFPIST
RGFSRLCVAVGCFGAGHLICLYCYQMPLAQALLPPAGIWARVLGLKDFVGPTNCSSPH
ALVLNTGLDWPVYASPGVLLLLCYATASLRKLRAYRPSGQRKEAAKGYEARELELAELD
QWPQERESDQHVVPTAPDTEADNCIVHELTGQSSVLRRPVRPKRAEPREASPLHSLGH
LIMDQSYVCALIAMMVWSITYHSWLTFVLLLWACLIWTVRSRHQLAMLCSPCILLYGMT
LCCLRYVWAMDLRPELPTTLGPVSLRQLGLEHTRYPCLDLGAMLLYTLTFWLLLRQFVK
EKLLKWAESPAALTEVTVADTEPTRTQTLLQSLGELVKGVYAKYWIYVCAGMFIVVSFA
GRLVVYKIVYMFLFLLCLTLFQVYYSLWRKLLKAFWWLVVAYTMLVLIAVYTFQFQDFPA
YWRNLTGFTDEQLGDLGLEQFSVSELFSSILVPGFFLLACILQLHYFHRPFMQLTDMEH
VSLPGTRLPRWAHRQDAVSGTPLLREEQQEHQQQQQEEEEEEEDSRDEGLGVATPH
QATQVPEGAAKWGLVAERLLELAAGFSDVLSRVQVFLRRLLELHVFKLVALYTVWVALK
EVSVMNLLLVVLWAFALPYPRFRPMASCLSTVWTCVIIVCKMLYQLKVVNPQEYSSNCT
EPFPNSTNLLPTEISQSLLYRGPVDPANWFGVRKGFPNLGYIQNHLQVLLLLVFEAIVYRR
QEHYRRQHQLAPLPAQAVFASGTRQQLDQDLLGCLKYFINFFFYKFGLEICFLMAVNVI
GQRMNFLVTLHGCWLVAILTRRHRQAIARLWPNYCLFLALFLLYQYLLCLGMPPALCID
YPWRWSRAVPMNSALIKWLYLPDFFRAPNSTNLISDFLLLLCASQQWQVFSAERTEEW
QRMAGVNTDRLEPLRGEPNPVPNFIHCRSYLDMLKVAVFRYLFWLVLVVVFVTGATRISI
FGLGYLLACFYLLLFGTALLQRDTRARLVLWDCLILYNVTVIISKNMLSLLACVFVEQMQ
TGFCWVIQLFSLVCTVKGYYDPKEMMDRDQDCLLPVEEAGIIWDSVCFFFLLLQRRVFL
SHYYLHVRADLQATALLASRGFALYNAANLKSIDFHRRIEEKSLAQLKRQMERIRAKQEK
HRQGRVDRSRPQDTLGPKDPGLEPGPDSPGGSSPPRRQWWRPWLDHATVIHSGDYFL
FESDSEEEEEAVPEDPRPSAQSAFQLAYQAWVTNAQAVLRRRQQEQEQARQEQAG

QLPTGGGPSQEVEPAEGPEEAAAGRSHVVQRVLSTAQFLWMLGQALVDELTRWLQE
FTRHHGTMSDVLRAERYLLTQELLQGGEVHRGVLDQLYTSQAEATLPGPTEAPNAPST
VSSGLGAEEPLSSMTDDMGSPLSTGYHTRSGSEEAVTDPGEREAGASLYQGLMRTASE
LLLDRRLRIPELEEAELFAEGQGRALRLLRAVYQCVAAHSELLCYFIIILNHMVTASAGSLV
LPVLVFLWAMLSIPRPSKRFWMTAIVFTEIAVVVKYLFQFGFFPWNSHVVLRRYENKPYFP
PRILGLEKTDGYIKYDLVQLMALFFHRSQLLCYGLWDHEEDSPSKEHDKSGEEEQGAEE
GPGVPAATTEDHIQVEARVGPTDGTPEPQVELRPRDTRRISLRFRRRKKEGPARKGAAAI
EAEDREEEEGEEEKEAPTGREKRPSRSGGRVRAAGRRLQGFCLSLAQGTYRPLRRFFHD
ILHTKYRAATDVYALMFLADVVDFIIIIFGFWAFGKHSAATDITSSLSDDQVPEAFLVMLLI
QFSTMVVDRALYLRKTVLGKLAFQVALVLAIHLWMFFILPAVTERMFNQNVVAQLWYF
VKCIYFALSAYQIRCGYPTRILGNFLTKKYNHLNLFLFQGFRLVPFLVELRAVMDWVWTD
TTLSLSSWMCVEDIYANIFIIKCSRETEKKYPQPKGQKKKKIVKYGMGGLIILFLIAIIWFPLL
FMSLVRSVVGVVNQPIDVTVTLKLGGYEPLFTMSAQQPSIIPFTAQAYEELSRQFDPQPL
AMQFISQYSPEDIVTAQIEGSSGALWRISPPSRAQMKRELYNGTADITLRFTWNFQRDL
AKGGTVEYANEKHMLALAPNSTARRQLASLLEGTSDQSVVIPNLFPKYIRAPNGPEANP
VKQLQPNEEADYLGVRIQLRREQGAGATGFLEWWVIELQECRTDCNLLPMVIFSDKVS
PPSLGFLAGYGIMGLYVSIVLVIGKFVRGFFSEISHSIMFEELPCVDRILKLCQDIFLVRETR
ELELEEELYAKLIFLYRSPETMIKWTREKE

>Mouse_Piezo1

MEPHVLGAGLYWLLLPCTLLAASLLRFNALSLVYLLFLLLLPWLPGPSRHSIPGHTGRLLR
ALLCLSLLFLVAHLAFQICLHTVPHLDQFLGQNGSLWVKVSQHIGVTRLDLKDIFNTTRL
VAPDLGVLLASSLCLGLCGRLTRKAGQSRRTQELQDDDDDDDDDDEDIDAAPAVGLK
GAPALATKRRLWLASRFRVTAHWLLMTSGRTLVIVLLALAGIAHPSAFSSIYLVVFLAICT
WWSCHFPLSPLGFNTLCVMVSCFGAGHLICLYCYQTPFIQDMLPPGNIWARLFGLKNF
VDLPNYSSPNALVLNTKHAWPIYVSPGILLLLYYTATSLLKLHKSCPSELRKETPREDEEHE
LELDHLEPEPQARDATQGEMPMTTEPDLDNCTVHVLTSQSPVRQRPVRPRLAELKEMS
PLHGLGHLIMDQSYVCALIAMMVWSIMYHSWLTFVLLLWACLIWTVRSRHQLAMLCSP

CILLYGLTLCCLRYVWAMELPELPTTLGPVSLHQLGLEHTRYPCLDLGAMLLYLLTFWLLL
RQFVKEKLLKKQKVPAALLEVTVADTEPTQTQTLLRSLGELVTGIYVKYWIYVCAGMFIV
VSFAGRLVVYKIVYMFLFLLCLTLFQVYYTLWRKLLRVFWWLVVAYTMLVLIAVYTFQFQ
DFPTYWRNLTGFTDEQLGDLGLEQFSVSELFSSILIPGFFLLACILQLHYFHRPFMQLTDL
EHVPPPGTRHPRWAHRQDAVSEAPLLEHQEEEEVFREDGQSMDGPHQATQVPEGTA
SKWGLVADRLLDLAASFSAVLTRIQVFVRRLLELHVFKLVALYTVWVALKEVSVMNLLLV
VLWAFALPYPRFRPMASCLSTVWTCIIIVCKMLYQLKIVNPHEYSSNCTEPFPNNTNLQP
LEINQSLLYRGPVDPANWFGVRKGYPNLGYIQNHLQILLLLVFEAVVYRRQEHYRRQHQ
QAPLPAQAVCADGTRQRLDQDLLSCLKYFINFFFYKFGLEICFLMAVNVIGQRMNFMV
ILHGCWLVAILTRRRREAIARLWPNYCLFLTLFLLYQYLLCLGMPPALCIDYPWRWSKAIP
MNSALIKWLYLPDFFRAPNSTNLISDFLLLLCASQQWQVFSAERTEEWQRMAGINTDH
LEPLRGEPNPIPNFIHCRSYLDMLKVAVFRYLFWLVLVVVFVAGATRISIFGLGYLLACFYL
LLFGTTLLQKDTRAQLVLWDCLILYNVTVIISKNMLSLLSCVFVEQMQSNFCWVIQLFSL
VCTVKGYYDPKEMMTRDRDCLLPVEEAGIIWDSICFFFLLLQRRIFLSHYFLHVSADLKAT
ALQASRGFALYNAANLKSINFHRQIEEKSLAQLKRQMKRIRAKQEKYRQSQASRGQLQ
SKDPQDPSQEPGPDSPGGSSPPRRQWWRPWLDHATVIHSGDYFLFESDSEEEEEALPE
DPRPAAQSAFQMAYQAWVTNAQTVLRQRRERARQERAEQLASGGDLNPDVEPVDV
PEDEMAGRSHMMQRVLSTMQFLWVLGQATVDGLTRWLRAFTKHHRTMSDVLCAERY
LLTQELLRVGEVRRGVLDQLYVGEDEATLSGPVETRDGPSTASSGLGAEEPLSSMTDDT
SSPLSTGYNTRSGSEEIVTDAGDLQAGTSLHGSQELLANARTRMRTASELLLDRRLHIPE
LEEAERFEAQQGRTLRLLRAGYQCVAAHSELLCYFIIILNHMVTASAASLVLPVLVFLWA
MLTIPRPSKRFWMTAIVFTEVMVVTKYLFQFGFFPWNSYVVLRRYENKPYFPPRILGLEKT
DSYIKYDLVQLMALFFHRSQLLCYGLWDHEEDRYPKDHCRSSVKDREAKEEPEAKLES
QSETGTGHPKEPVLAGTPRDHIQGKGSIRSKDVIQDPPEDLKPRHTRHISIRFRRRKETPG
PKGTAVMETEHEEGEGKETTERKRPRHTQEKSKFRERMKAAGRRLQSFCVSLAQSFYQ
PLQRFFHDILHTKYRAATDVYALMFLADIVDIIIIIFGFWAFGKHSAATDIASSLSDDQVP
QAFLFMLLVQFGTMVIDRALYLRKTVLGKLAFQVVLVVAIHIWMFFILPAVTERMFSQNA
VAQLWYFVKCIYFALSAYQIRCGYPTRILGNFLTKKYNHLNLFLFQGFRLVPFLVELRAV

MDWVWTDTTLSLSNWMCVEDIYANIFIIKCSRETEKKYPQPKGQKKKKIVKYGMGGLIIL
FLIAIIWFPLLFMSLIRSVVGVVNQPIDVTVTLKLGGYEPLFTMSAQQPSIVPFTPQAYEEL
SQQFDPYPLAMQFISQYSPEDIVTAQIEGSSGALWRISPPSRAQMKQELYNGTADITLR
FTWNFQRDLAKGGTVEYTNEKHTLELAPNSTARRQLAQLLEGRPDQSVVIPHLFPKYIR
APNGPEANPVKQLQPDEEEDYLGVRIQLRREQVGTGASGEQAGTKASDFLEWWVIEL
QDCKADCNLLPMVIFSDKVSPPSLGFLAGYGIVGLYVSIVLVVGKFVRGFFSEISHSIMFE
ELPCVDRILKLCQDIFLVRETRELELEEELYAKLIFLYRSPETMIKWTRERE

>Rat_Piezo1

MEPHVLGAGLYWLLLPCTLLAASLLRFNALSLVYLLFLLLLPWLPGPSRHSIPGHTGRLLR
ALLCLSLLFLVAHVAFQICLHTMPRLNQLLGQNCNLWANVSQHIGVTRLDLKDIFNTTR
LVAPDLGVLVASSLCLGLCGRLTRKARQSQRTQELEEDDIDAAPAAGLQGAPTLATKRR
LWLAPRFRITAHWLLVTSGRMLVIVLLALAGIAHPSAFSSVYLMVFLAICTWWSCHFPLSS
LGFNTLCVMVSCFGAGHLVCLYCYQTPFVQSVLLPGSLWARLFGLKNFVDIPNCSSPN
VLVLNTKHAWPIYVSPGILLLLYYTATSLLKLRKGRFSELRKEIPREDEEHELELDQLEPEPQ
ARGTTQGATPTTTGPDIDNCTVHVLTSQSPVRQRPVRPRLAELKEMSPLHGLGHLILDQ
SYVCALIAMMVWSIMYHSWLTFVLLLWACLIWTVRSRHQLAMLCSPCILLYGLTLCCLR
YVWAMELPELPTTLGPVSLHQLGLEHTRYPCLDLGAMLLYLLTFWLLLRQFVKEKLLKKR
KAPSTLLEVTVSDTEPTQTQTLLRSLGELVTGIYVKYWIYVCAGMFIVVSFAGRLVVYKIVY
MFLFLLCLTLFQVYYTLWRKLLRVFWWLVVAYTMLVLIAVYTFQFQDFPTYWRNLTGFT
DEQLGDLGLEQFSVSELFSSILIPGFFLLACILQLHYFHRPFMQLTDLEHVPPPGTRRLRW
AHRQDTVSEAPLLQHQEEEEVFRDDGQSMDGPHQTTQVPEGTASKWGLVADRLLDL
ASSFSAVLTRIQVFVRCLLELHVFKLVALYTVWVALKEVSVMNLLLVVLWAFALPYPRFRP
MASCLSTVWTCIIIVCKMLYQLKIVNPHEYSSNCTEPFPNNTNLQPLEISQSLLYRGPVDP
ANWFGVRKGYPNLGYIQNHLQILLLLVFEAVVYRRQEHYRRQHQQAPLPAQALCADG
TRQRLDQDLLSCLKYFINFFFYKFGLEICFLMAVNVIGQRMNFMVILHGCWLVAILTRRR
REAIARLWPNYCLFLTLFLLYQYLLCLGMPPALCIDYPWRWSQAIPMNSALIKWLYLPDF
FRAPNSTNLISDFLLLLCASQQWQVFSAEQTEEWQRMAGVNTDHLEPLRGEPNPIPNF

IHCRSYLDMLKVAVFRYLFWLVLVVVFVTGATRISIFGLGYLLACFYLLLFGTTLLQKDTRA
QLVLWDCLILYNVTVIISKNMLSLLSCVFVEQMQSNFCWVIQLFSLVCTVKGYYDPKEM
KTRDRDCLLPVEEAGIIWDSICFFFLLLQRRVFLSHYFLHVSADLKATALQASRGFALYNA
ANIKNINFHRQTEERSLAQLKRQMKRIRAKQEKYRQSQASRGQLQSTDPQEPGPDSPG
GSSPPRTQWWRPWQDHATVIHSGDYFLFESDSEEEEEALPEDPRPAAQSAFQMAYQ
AWVTNAQTVLRQRREQARRDRAEQLASGGDLSPEVELVDVPENEMAGHSHVMQRVL
STMQFLWVLGQATVDGLTRWLRTFTKDHRTMSDVLCAERYLLTQELLRGGEVHRGVL
DQLYVSEDEIALSGPVENRDGPSTASSGLGAEEPLSSMTDDTGSPLSTGYNTRSGSEEII
TDTGGLQAGTSLHGSQELLANARTRMRTASELLLDRRLRIPELEEAEQFEAQQGRTLRL
LRAMYQCVAAHSELLCYFIIILNHMVTASAASLVLPVLVFLWAMLTIPRPSKRFWMTAIVF
TEVMVVTKYLFQFGFFPWNSYIVLRRYENKPYFPPRILGLEKTDSYIKYDLVQLMALFFHR
SQLLCYGLWDHEEDGVPKDHCRSSEKDQEAEEESEAKLESQPETGTGHPEEPVLTGTP
KDHIQGKGSVRSKDEIQDPPEDLKPQHRRHISIRFRRRKETQGPKGAAVVEAEHEEGEE
GREAAGRKRLRRPREGLKIREKMKAAGRRLQSFCLSLAQSFYQPLRRFFHDILHTKYRAA
TDVYALMFLADIVDIVVIIFGFWAFGKHSAATDIASSLSDDQVPQAFLFMLLVQFGTMVI
DRALYLRKTVLGNLAFQVVLVVAIHLWMFFILPAVTERMFRQNAVAQLWYFVKCIYFAL
SAYQIRCGYPTRILGNFLTKKYNHLNLFLFQGFRLVPFLVELRAVMDWVWTDTTLSLSN
WMCVEDIYANIFIIKCSRETEKKYPQPKGQKKKKIVKYGMGGLIILFLIAIIWFPLLFMSLIR
SVVGVVNQPIDVTVTLKLGGYEPLFTMSAQQPSIVPFTPEDYEELSQQFDPYPLAMQFIS
QYSPEDIVTAQIEGSSGALWRISPPSRAQMKHELYNGTADITLRFTWNFQRDLAKGGSV
EYTNEKHTLELAPNSTARRQLAQLLEGRPDQSVVIPHLFPKYIRAPNGPEANPVKQLQP
DEEEDYLGVRIQLRREQVGTGTSGEQAGTKASDFLEWWVIELQDCQAECNLLPMVIFS
DKVSPPSLGFLAGYGIVGLYVSIVLVVGKFVRGFFSDISHSIMFEELPCVDRILKLCQDIFLV
RETRELELEEELYAKLIFLYRSPETMIKWTREKE

>Zebrafish_Piezo1

DSYLALCTLLLPSAVTCIFRYNALSLVYLLYLLLLPWFQWPNKHTLRGHTGCYIKALFSTSL
IFILGHVTFQICLYTIPSLDDALGHNCSSWETLSRHVGVSRLPLEDPQGVLWLLTPDLGVF

IMSLITLILCSRLLKKRDEGSVPHMSADETEDDDEDVEGEDEGMLSCSETEDEESPSSSS
AAQLAARLRATAQRFLRNMGRILAVTLLALAGITLPSAFSAFYFLLFIGVCTWWACHFPI
SHLGFNALCVMVAFFTGGHLVCLYLYQSSFAQAMFSPAGLWARLFGLKDLVTPGNCT
TFEVTLNTQYDWPVYVNPGILLLLYISVTIVLKINSNTGEEVELRLWEARRQSSEDDTKQT
LLTTVDSTLSESHITKEPVINGSSQHDIGPSGEATVDNPLRLVGRMVLQQSYICALIAMM
VWSITYHSWLTFVLLLWSCVIWMLRTRQRFAAYCSPFILLYGLALCCLQYVWAMDLETE
LPQHIGSMSLHQLGLDRAQYPCLRLGALLLFTLTFWLLLRQSVKDTFSRKKSLTVPLQEV
TTGESTGRNESILKVFGGLVMSLYAKYWIYVCGGMFIMVSFAGKLVAYKIVYMLLFLLCM
CLYQVYYSLWRRLLKAFWWMVVAYTMVVLIAIYTFQFEDFPGYWGNFTGFTEQQLAD
MGLETFKLSELFTSIVIPGFFLLACILQLHYFHKPFMKITDLENVSPIHRHEPEEEELIVDQD
DYPSEADEVIPSKWGLVMDRLMVLSRKFSDTLTHVQSFIWRVLELHIVKIVAFFVVWVAL
LEPSAMNLVLVVLWSFAMPYGRFRAMASCLSTIWVCVIIVCKMLYQLSVVNPAEYSNNC
TAPMVNETSLEPDEVLNSTLYRASVDPASWFGVRKDDTVLGYVKDHLLVLMLLVFEATV
YRHQIHHYRQQQRSPPPIPVIFPQATRDTLDQGLLHCIKYMLNYSFYKFGLEICFLMTVN
VIGQRMNFLVIIHGCWLVAIMVRRRRANIATIWSKYCLFLVVFMIYQYVLCVGIPPALCID
YPWRWRSTVTIHSALVKWMYLPDFYTVPNSKNLISDFLLLMCASQQWTVFDNEKKEE
WMVMGGENRDNPDPMENMLFNPAPNFINCRSYLDMAKILVFRYMFWFVLSVVFVTG
ATRISVFGLGYLMACFFFLLFGTKLLTKPSRTRLVMWDCLIIYNVAVIISKNILSILACVFVM
EMQKNFCWVIQLFSLVCTVKGYYDPESVCNKDCSLPVEEAGIIWDSICFFFLLLQRRVFL
SFYFLHVSADLQASARQASRGFELFRASIIKNMHFHQQAERKSIQQLKESMKRIRGKQQ
KYKDGRITSDIEEQPSEQKKETKLSKSKSWQYPWVDHATVLHSGEYYMFESDSGEEDE
TFQEEQKPRRQTAFQLAYQAWVTSAKDALKERQQRQRKQRAEAEKQQNAQATDD
AEEGETVFDGENSQHAEEMQEEGEDAGGDMVQRILDILKFLWVLFLAMVDGFTMWL
NLLTKQYVDTSMVLSEERYLFIHNVSQRASRENMDDQISHDSEDLTLETCLDETDTDNI
CDTNVVESETLGGFAKSRDFSSTTLSSELTLELDCEPFYSQTASELLSERPFRVDELIQSRE
FYSSQNRLLKLLFALYNVLAAHSELVCYFIIVLNNLVTASVISLVLPVLVFLWAMLSVPRPSK
RFWMTAIIYTEVMVVVKYLFQFGFFPWNTEYELKLNEDKPFFPPRILGLEKTDNYIRYDLL
QLLVLFFHRSLLQRYGLWDQEGPLEEKSDLSPAENKPNTETDPEPNSHTNNTKTSDTVK

NDGMKKSHFLRFRKKKKAEPDAVQKEPKKKKKKCKTKHSKETSKKLLNAIEGKFKSLFLS
VVKNVYRPTWDFFQNILHAEYRASTDVYALMFLTDVVDFIIIIFGFWAFGKHSAAADIAS
SLSEDQVPEAFLVMLLIQFSTMIIDRALYLRKSILGKLIFQVILVFGIHLWMFFILPAVTERM
FNHNSVAQLWYFFKCIYFTLSAYQIRCGYPTRILGNFLTKKFNHLNLFLFQGFRLVPFLVE
LRAVMDWVWTDTTLSLSNWMCVEDIYANIFIIKCSRETEKKYPQPKGQKKKRIVKYGM
GGLIILFLICIIWFPLLFISLVKSVVGVVNHPVDVTVTVKLGGYEPLFTMSVQQQSIQPFTES
RYNQLNNQFSKNAVAMQFITMYSYEDIVTANIEGSSGSVWRISPPSRQELIKELLSSTGD
MTLRLDWNFQRDLGKGGTVENTFDKHSISLAPKNPVRADLASLLLGTRKDPVHVPHMF
PNYIRAPSGAEAKPVMQLFDGDEEGFQDVTVSLMREASVNTTGAQEWWDISIADCKE
SCNVLPMIIFNDKVSPPSLGFLAGYGIMGLYVSVVLVIGKFVRGFFSEISHSIMFEELPCAD
RILKLCMDIFLVRETGELELEEELYSKLIFLYRSPETMIKWTREKNHN

>Chimpanzee_Piezo1

MEPHVLGAVLYWLLLPCALLAACLLRFSGLSLVYLLFLLLLPWFPGPTRCGLQGHTGRLL
RALLGLSLLFLVAHLALQICLHTVPHLDQLLGPSCSRWETLSRHIGVTRLDLKDIPNAIRLV
APDLGILVVSSVCLGICGRLARNTRQSPHPRELDDDERDVDASPTAGLQEAATLAPTRR
SRLAARFRVTAHWLLVAAGRVLAVTLLALAGIAHPSALSSVYLLLFLATCTWWACHFPIS
TRGFSRLCVAVGCFGAGHLICLYCYQMPLAQALLPPAGIWARVLGLKDFVGPTNCSSP
HALVLNTSLDWPVYASPGVLLLLCYATASLRKLRAYRSSGQRKEAAKGYEARELELAELD
QWPQERESDQHVVPTAPDTEADNCIVHELTGQSSLRQRPVRPKRAEPREASPLHSLGH
LIMDQSYVCALIAMMVWSITYHSWLTFVLLLWACLIWTVRSRHQLAMLCSPCILLYGMT
LCCLRYVWAMDLRPELPTTLGPVSLRQLGLEHTRYPCLDLGAMLLYTLTFWLLLRQFVK
EKLLKWAESPAALTEVTVADTEPTRTQTLLQSLGELVKGVYAKYWIYVCAGMFIVVSFA
GRLVVYKIVYMFLFLLCLTLFQVYYSLWRKLLKAFWWLVVAYTMLVLIAVYTFQFQDFPA
YWRNLTGFTDEQLGDLGLEQFSVSELFSSILVPGFFLLACILQLHYFHRPFMQLTDMEH
VSLPGTRLPRWAHRQDAVSGTPLLQEEQEEQQQEEEEDSRNEGLGVATPHQATQVPE
GAAKWGLVAERLLELAAGFSDVLSRVQVFLRRLLELHVFKLVALYTVWVALKEVSVMNL
LLVVLWAFALPYPRFRPMASCLSTVWTCVIIVCKMLYQLKVVNPQEYSSNCTEPSPNSTN

LLPTEISQSLLYRGPVDPANWFGVRKGFPNLGYIQNHLQVLLLLVFEAIVYRRQEHYRRQ
HQLAPLPAQAVFASGTRQQLDQDLLGCLKYFINFFFYKFGLEICFLMAVNVIGQRMNF
LVILHGCWLVAILTRRHRQAIARLWPNYCLFLALFLLYQYLLCLGMPPALCIDYPWRWSR
AVPMNSALIKWLYLPDFFRAPNSTNLISDFLLLLCASQQWQVFSAERTEEWQRMAGVN
SDRLEPLRGEPNPVPNFIHCRSYLDMLKVAVFRYLFWLVLVVVFVTGATRISIFGLGYLLA
CFYLLLFGTALLQRDTRARLMLWDCLILYNVTVVISKNMLSLLACVFVEQMQTGFCWVI
QLFSLVCTVKGYYDPKEMMDRDQDCLLPVEEAGIIWDSVCFFFLLLQRRVFLSHYYLHV
RADLQATALLASRGFALYNAANLKSIDFHRRIEEKSLAQLKRQMERIRAKQEKHRQGRV
DRSRPQDTLGPKDPGLEPGPDSPGGSSPPRRQWWRPWLDHATVIHSGDYFLFESDSE
EEEEAVPEDLRPSAQSAFQLAYQAWVINAQTVLRRRQQEQEQARQEQAGQLPTGGG
PSQEVEPAEGPEEAAAGRSHVVQRVLSTAQFLWMLGQALVDGLTRWLQEFTRHHGT
MSDVLRAERYLLTQELLQGGEVHRGVLDQLYTSQAEATLPGPTEAPNAPSTVSSGLGA
EEPLSSMTDDTGSPLSTGYHTRSGSEEAVTDPGEREAGASLYQGRMRTASELLLDRRLRI
PELEEAELFAEGQGRALRLLRAVYQCVAAHSELFCYFIIILNHMVTASAGSLVLPVLVFLW
AMLSIPRPSKRFWMTAIVFTEIAVVVKYLFQFGFFPWNSHVVLRRYENKPYFPPRILGLEK
TDGYIKYDLVQLMALFFHRSQLLCYGLWDHEEESPSKEHDKSGEEEQGAEEGPGVPA
ATTKDHVQVEARVGPTDGTPEPQVELRPRDTRRISLRFRRRKKEEGPARKGAAAIEAEDR
EEEEGEEEKEAPTGREKRPSRSGGRVRAAGRRLQGFCLSLAQGTYRPLRRFFHDILHTKY
RAATDVYALMFLADVVDFIIIIFGFWAFGKHSAATDITSSLSDDQVPEAFLVMLLIQFSTM
VVDRALYLRKTVLGKLAFQVVLVLAIHLWMFFILPAVTERMFNQNVVAQLWYFVKCIYF
ALSAYQIRCGYPTRILGNFLTKKYNHLNLFLFQGFRLVPFLVELRAVMDWVWTDTTLSLS
SWMCVEDIYANIFIIKCSRETEKRYPQPKGQKKKKIVKYGMGGLIILFLIAIIWFPLLFMSLV
RSVVGVVNQPIDVTVTLKLGGYEPLFTMSAQQPSIIPFTAQAYEELSRQFDPQPLAMQFI
SQYSPEDIVTAQIEGSSGALWRISPPSRAQMKRELYNGTADITLRFTWNFQRDLAKGGT
VEYANEKHMLALAPNSTARQQLASLLEGTSDQSVVIPNLFPKYIRAPNGPEANPVKQLQ
PNEEADYLGVRIQLRREQGAGATGFLEWWVIELQECRTDCNLLPMVIFSDKVSPPSLGF
LAGYGIMGLYVSIVLVIGKFVRGFFSEISHSIMFEELPCVDRILKLCQDIFLVRETRELELEEE
LYAKLIFLYRSPETMIKWTREKE

>Bovine_Piezo1

MEPHVLGAVLYWLLLPFALLAACLFRVNALSLVYLLFLLLLPWFPGPSRHSIRGHTGRLLR
ALLGFSLLFLAAHITFQICLHTVPRLDQLLEPNCSTGDAITWDAISQLIGVTRLDLKDIPNA
IRLVAPDLGILVVSSLCLGVCRRLTRTARRSQHVQEPDDDSEELDTGSLGELREAPELSPT
RRSRLAARFRITAHWLLVAAGRTLAIMLLALAGIAHPSAFSSVYFLLFLAIGTWWACHFPI
SLLGFNTLCVMVSCIGTGHLICLYCYQTPLAQATLPPAGIWARVFGLKDFLAPTNCSSP
NVLVINANHDWPVYVSPGILLLLCYTVTSLLKLHAHQPVDQRKEAAGDDDTREVELTEV
DQWPQGQARVVAIKEEGAAQHTMPTPTTPDPEDNCIIHDLTGHSAVQQRTSCPRLAE
PKETSPLHGLGHLIMDQSYVCALIAMMVWSITYHSWLTFVLLLWACLIWTVRSRHQLA
MLCSPFILLYGLALCCLRYVWAMDLRPELPTALGPVSLRQLGLEHTRYPCLDLGAMLLCT
LTFWLLLRQFVKEKLLRRARAPVALTEVTVAATEPTRTQMLLRSLGELVRGIYAKYWIYVC
AGMFIVVSFAGRLVVYKIVYMLLFLLCLILFQVYYSLWRKLLKAFWWLVVAYTMLVLVAV
YTFQFQDFPAYWRNLTGLTDEQLGDLGLEQFSVSELFSSILVPGFFLLACILQLHYFHRP
FMQLTDPEHRPLPGACTPRWVPGRDAVSRTPLLQQEEEEEVPRDEGLGTASPHQVTQ
VPEASKWGLVAERLLDLATGFSDVITRVQVLVRRLLELHVFKLVALYTVWVALKEVSVLN
FLLVVLWAFALPYPRFRPMASCLATVWTCIIIVCKMLYQLKVVNPHEYASNCTEPFPNST
NLQKTEIRQSLLYRGPVDPANWFGVRKGFPNLGYIQNHLQILLLLVFEAMVYRSQDYHH
RRHQLAPLPAQAVCAEGTRQRLDRDLPSCLKYYVNFFFYKFGLEVCFLAAVNVIGQRM
NFMVILHGCWLVAILTRRRREAIARLWPNYCLFLALFLLYQYLLCLGVPPALCIDYPWRW
SRAVPMNSALIKWLYLPDFFSTPNATNLISDFLLLLCASQQWQVFSAERMEEWRHMAG
VNTDRLEPLRGEPNPVPNFIHCRSYLDMLKVAVFRYFFWLVLVVVFITGATRISVFGLGYL
LACFYLLLFGTSLQQKDTRARLVLWDCLILYNVTVIVSKNMLSLLSCVFVEQMQSSFCW
VIQLFSLVCTVKGYYDPKEMLGRDQDCLLPVEEAGVLWDSVCFLFLLLQRRVFLSYYFLH
VQAELRATALQASRGFALYNAANLKTIELHRRAEEKSLAQLKRQMERIRAKQEKHRQG
RANRGCLQGSPDPGQEPGPSSPGGSSPPQQQWWRPWLDHATVIHSGDYFLFESDSE
EEEEAQPEDPRPSSQSAFQMAYQAWVTNAQTVLRQQRQQRAEQLRTGGDPSQEAG
PAEGLEDEVTGRSHVMQRVLSAVQFLWVLGQALVDGLTRWLHDFTRHHRAISDVLRA
ERYLLTQELLRGGEVRRDVLDQLYANEAEAARDALSTASSGLGVEEPLSSVTEDTSSPLS

TGYNTRSSSEEVVTEPGASLRSSGELPAGGRARMRTASELLVDRRVHIPELEEAEQFAAG
RGRALRLLEALYQCVAAHSELLCYFVIVLNHMVTASATSLVLPVLVFLWAMLSIPRPSKRF
WMTAIIFTEVTVVAKYLFQFGFFPWNSHAVLRRYENKPYFPPRILGLEKSDSYVKYDLLQL
MALFFHRAQLLCYGLWDHEDPPLSKEHDRGSAKEKGAEEEPALPAPQEEPGGAARPP
AEDNVQAEAKGGPLEPGGKRRISLRFRRRRKESTETRGQAIEGEEEEEEAAVAVVAAGA
ATLRREKRRSRPQERVRVLGVRLQSFCLSLARSMYWPVRRFFQDILHTKYRAATDVYAL
MFLADVIDFIIIIFGFWAFGKHSAATDITSSLSDDQVPEAFLVMLLIQFSTMVIDRALYLRK
TVLGKLAFQVVLVLAVHLWMFFILPAVTERMFSQNAVAQLWYFVKCIYFALSAYQIRCG
YPTRILGNFLTKKYNHLNLFLFQGFRLVPFLVELRAVMDWVWTDTTLSLSNWMCVEDIY
ANIFIIKCSRETEKKYPQPKGQKKKKIVKYGMGGLIILFLVAIIWFPLLFMSLVRSVVGVVN
QPIDVTVTLKLGGYEPLFTMSAQQPSIVPFTHHAYEELSKQFDPHPLAMQFISQYSPEDI
VTVHIEGSSGALWRISPPSRAQMKRELYNGTADITLRFTWNFQRDLAKGGSVEYTNEKH
TLDLAPNSTARRQLASLLEGTSDQSVVIPHLFPKYIRAPSGPEANPVKQLQPNEEADYLG
VRIQLRRERVGTGAAGFLEWWVIELQDCQANCNLLPMVIFSDKVSPPSLGFLAGYGIM
GLYVSIVLVIGKFVRGFFSEISHSIMFEELPCVDRILKLCQDIFLVRETRELELEEELYAKLIFL
YRSPETMIKWTRDKE

>Gorilla_Piezo1

MEPHVLGAVLYWLLLPCALLAACLLRFSGLSLVYLLFLLLLPWFPGPTRCGLQGHTGRLL
RALLGLSLLFLVAHLALQICLHTVPHLDQLLGPSCSRWETLSRHIGVTRLDLKDIPNAIRLV
GPDLGILMVSSVCLGICGRLARNTRQSPHPRELDDDERDVDASPTAGLREAATLAPTRR
SRLAARFRVTAHWLLVAAGRVLAVTLLALAGIAHPSALSSVYLLLFLATCTWWACHFPIS
TRSFSRLCVAVGCFGAGHLICLYCYQMPLAQALLPPAGIWARVLGLKDFVGPTNCSSP
HALVVNTSLDWPVYASPGVLLLLCYATASLHKLRAYRPSGQRKEAAKGYEARELELAEL
DQWPQERESDQHVVPTAPDTEADNCIVHELTGQSSLRQRPVRPKRAEPREASPLHSLG
HLIMDQSYVCALIAMMVWSITYHSWLTFVLLLWACLIWTVRSRHQLAMLCSPCILLYGM
TLCCLRYVWAMDLRPELPTTLGPVSLRQLGLEHTRYPCLDLGAMLLYTLTFWLLLRQFVK
EKLLNWAESPAALTEVTVADTEPTRTQTLLQSLGELVKGVYAKYWIYVCAGMFIVVSFA

GRLVVYKIVYMFLFLLCLTLFQVYYSLWRKLLKAFWWLVVAYTMLVLIAVYTFQFQDFPA
YWRNLTGFTDEQLGDLGLEQFSVSELFSSILVPGFFLLACILQLHYFHRPFMQLTDMEH
VSLPGTRLPRWAHRQDAVSGTPLLQEEQEEQQQEEESRDEVLGVATPHQATQVPEGA
AKWGLVAERLLELAAGFSDVLSRVQVFLRRLLELHVFKLVALYTVWVALKEVSVMNLLLV
VLWAFALPYPRFRPMASCLSTVWTCVIIVCKMLYQLKVVNPQEYSSNCTEPSPNSTNLLP
TEISQSLLYQGPVDPANWFGVRKGFPNLGYIQNHLQVLLLLVFEAIVYRRQEHYRRQHQ
LAPLPAQAVFSSGTRQQLDQDLLGCLKYFINFFFYKFGLEVRQGHCLPLGQGLAVGRE
GRLHRAQAIARLWPNYCLFLALFLLYQYLLCLGMPPALCIDYPWRWSRAVPMNSALIK
WLYLPDFFRAPNSTNLISDFLLLLCASQQWQVFSAERTEEWQRMAGVNTDRLEPLRGE
PNPVPNFIHCRSYLDMLKVAVFRYLFWLVLVVVFITGATRISIFGLGYLLACFYLLLFGTALL
QRDTRARLVLWDCLILYNVTVIISKNMLSLLACVFVEQMQTGFCWVIQLFSLVCTVKGY
YDPKEMMDRDQDCLLPVEEAGIIWDSVCFFFLLLQRRVFLSYYYLHVRADLQATALLAS
RGFALYNAANLKSIDFHRRIEEKSLAQLKRQMERIRAKQEKHRQGRVDRSHPQDTLGPK
DPGLEPRPDSPGGSSPPRRQWWRPWLDHATVIHSGDYFLFESDSEEEEEAVPEDPRPS
AQSAFQLAYQAWVTNAQTVLRRRQQEQEQARQEQAGQLPTGGGPSQEVEPAEGPE
EAAEGRSHVVQRVLSTAQFLWMLGQALVDGLTRWLQEFTRHHGTMSDVLRAERYLLT
QELLQGGEVHRGVLDQLYTSQAEAKLPGPAEAPNAPSTVSSGLGAEEPLSSMTDDTG
SPLSTGYHTRSGSEEAVTDPGEREAGASLYQGRMRTASELLLDRRLHIPELEEAELFAEG
HGRALRLLRAMYQCVAAHSELLCYFIIILNHMVTASAGSLVLPVLVFLWAMLSIPRPSKRF
WMTAIVFTEIAVVVKYLFQFGFFPWNSHVVLRRYENKPYFPPRILGLERTEGYIKYDLVQL
MALFFHRSQLLCYGLWDHEEDSPSKEHDKSGEEEQGAKEGPGVPAATTKDHVQVEA
RVGPTDGTPEPQVELRPRDTRRISLRFRRRKKEGPAQKGEAAIEAEDREEEEGEEEKEAP
MGREKRPSRSGGRVRAAGRRLQGFCLSLAQGTYRPLRRFFHDILHTKYRAATDVYALM
FLADVVDFIIIIFGFWAFGKHSAATDITSSLSDDQVPEAFLVMLLIQFSTMVVDRALYLRKT
VLGKLAFQVVLVLAIHLWMFFILPAVTERWAHTAVSDGVLDLDVQPECGGPAVVLREV
HLLRPVPHLTGTLAVGRFRLVPFLVELRAVMDWVWTDTTLSLSSWMCVEDIYANIFIIKCS
RETEKKYPQPKGQKKKKIVKYGMGGLIILFLIAIIWFPLLFMSLVRSVVGVVNQPIDVTVTL
KLGGYEPLFTMSAQQPSIIPFTAQAYEELSQQFDPQPLAMQFISQYSPEDIITAQIEGSS

GALWRISPPSRAQMKRELYNGTADITLRFTWNFQRDLAKGGTVEYANEKHMLALAPNS
TARQQLASLLEGTSDQSVVIPNLFPKYIRAPNGPEANPVKQLQPNEEADYLGVRIQLRRE
QGAGATGFLEWWVIELQECQTNCNLLPMVIFSDKVSPPSLGFLAGYGIMGLYVSIVLVI
GKFVRGFFSEISHSIMFEELPCVDRILKLCQDIFLVRETRELELEEELYAKLIFLYRSPETMIK
WTREKE

>Killifish_Piezo1

SRFNLLSLVYLIFLLLLPWFSSPNKYSLRGHTGCFLRAVLCTSLLFVLAHVCFQTVLYTFPPL
SEALGDNCSQWDTISRHIGLSRYVCTDLSVSSTLDQLIFLNLCIRRWHIHDGCHRTEEET
SGDEDQEEDSLNADPEEVFTATRAKHLAEHLKATAWKVLQDLGRILAVGLLGLAGITLP
SGFSAFYFLFFLGVCTWWACHLPISQLGFSALCVMVGFFAAGHIVCLYLYQSLLAQALF
PPHSLWARLFGLKDFIVPGNCSLPDELILNTNHDWPVYVNPGILLLLYVTVVAVLRSGSHT
RVQGSHPRDPSPLKQQGGPEAPVLEPCPQSRGCRTLERPSPPMTRFLAEHETPLSLLYS
YSNAFLFLRPSGESPFFLLGKVVMQQSYVSALIAMMVWSITYHSWLTFVLLLWACLIWIL
RARRHAATLCSPFILLYGLVLCCLQYIWAMELHPELPTSVGTMSLRQLGLDKAQYPCLRL
GAMLLFVLTFWLLLRQAVMENFRRKSSSQTPLQEVATKGQNQSMLKVVGGMVMSCY
AKYWIYVCGGMFIMVSFAGKLVAYKIVYMLLFLLCLCFYQVYYSLWRHLLKLFWWLVVA
YTMLVLITIYTYQFEDFPVYWKNLTGFTDEQLAAIGLETFDLSELFTSILIPGFFLLACILQL
HYFHKPFMRITDLENVTPTHKRRNSDAVGSADAVELNTEEDPSNTEESADEGRTQKTTK
ELMPSKWGLVMDRLLVLSRKFSEILSKVQVFLWRLLELHILKMVAFFTVWVALQEASVM
NLVLVVLWSLATPFCRFRPMASCLSTVWVCVIIICKMLYQLSVVNPEEYSRNCSTPLTNH
TKLLLNSSLYKEPVDPAKWFGIRKDATALGYSKNHLIVLMLLVFEATVYRHQAHHYRQL
QRSPPPIPAVFPSATRDSLDQGLVACLKYLVNYTFYKFGLEICFLMTVNVIGQRMNFLVLI
HGCWMVAILVRRRRAAIARIWPKYCLFLSIFMIYQYLLCVGIPPVLCMDYPWRWSNPVL
QDWGTLDALIKWLYLPDFFTVPNSGNLMADFVLLMCASQQWKVFDCERTEEWMVLA
GENSDEPEPMEGRLFNPAPNFINCRSYLDMLKVLVFRYFFWFVLSVVFITGASRISVFGL
GYLLGCFFFLLFGTKLMVKRSRTRLILWDCLIIYNVAVIISKSVLSILACVFVFKMQERFCW
VIQLFSLVCTVKGYYDRDDTCTLPIEEAGILWDGFCFICLLLQRRVFLSFYFLHVSAELQA

SAKQASRGFELFRASMMKNMDFHKQAEDKSLSQLKRSQTLMSCCAAVIHSGEYYLFE
SDSEDEEDLSSEEKRPRRLTASQMQALHEHVFPSWRTRLHGEMLQKILDVLRLLWAIILA
LVDGLTDWLNLLTKQYRETSTVLCNERYLITHKIQQVRAVRDSLLSSSSSGVCSDIMKMS
SSSFGSSSHLLNEETRPSGSSGLQPNMFTAHRRPELFLREFFESQNRLLKLLLALYSLLSA
HSELLCYLIIVLNNVVSASVISVVLPILVFLWAMLALPRPSKRFWMTAIVYTEVMVVLKYIFQ
FGFFSWNSAHEMTVNKDRPFFPPRILGLEKTDNYLRYDLLQLLALFFHRALLMVCTLNLK
SFRPDQEALLAKAAALRKKEALVPEEIHLRAKEEEEEMRLRAKKEQLELETDLTVASARLK
VYESLKDVQSSPAQNFFKNLMHNKHQASTDVYALMFLTDMVDFVIIIFGFWAFGKHSA
AADIASTLSEDQVPEAFLVMLLIHFSTMIIDRALYLRKAVLGKLIFQGILVLGIHVWMFFILP
SVTERKFNQNFVAQLWYFVKCIYFGLSAYQIRCGYPTRILGNFLTKNFGHLNLFLFQGFR
LVPFLVELRAVMDWVWTDTTLSLSNWMCVEDIYANIFIIKCSRETEKKYPQPKGQKKKKI
VKYGMGGLIVFFLICIIWFPLLFISLVRSVVGVVNHPIDVTVTVKLGGYEPLFTMSVQQQSI
QPFNNSQYEELTKMFKDNTAMQFITLYSYEDIVTAQIEGSSGSVWRISPPSRQEVIKELL
GSQVDLTLRLAWNFQRDLGKGGTVEHTFDKYSIDLEPGNLVRAELASLLIGNRTEPVLV
PNFFPNYIRAPNGAEAKPVSQLYKGGEDGYLGITLSLKSDRSSNSSGTREWWDIAVEGC
VPPSCGVLRMVIFNDKVSPPSLGFLAGYGIMGLYVSVVLVIGKFVRGFFSEISHSIMFEELP
CVDRILKLCTDIFLVRETGELELEEELYSKLIFLYRSPETMIKWTRENRAANRD

>Human_Piezo2

MASEVVCGLIFRLLLPICLAVACAFRYNGLSFVYLIYLLLIPLFSEPTKTTMQGHTGRLLKSL
CFISLSFLLLHIIFHITLVSLEAQHRIAPGYNCSTWEKTFRQIGFESLKGADAGNGIRVFVP
DIGMFIASLTIWLLCRNIVQKPVTDEAAQSNPEFENEELAEGEKIDSEEALIYEEDFNGG
DGVEGELEESTKLKMFRRLASVASKLKEFIGNMITTAGKVVVTILLGSSGMMLPSLTSSVY
FFVFLGLCTWWSWCRTFDPLLFSCLCVLLAIFTAGHLIGLYLYQFQFFQEAVPPNDYYA
RLFGIKSVIQTDCSSTWKIIVNPDLSWYHHANPILLLVMYYTLATLIRIWLQEPLVQDEGT
KEEDKALACSPIQITAGRRRSLWYATHYPTDERKLLSMTQDDYKPSDGLLVTVNGNPVD
YHTIHPSLPMENGPGKADLYSTPQYRWEPSDESSEKREEEEEEKEEFEEERSREEKRSIKV
HAMVSVFQFIMKQSYICALIAMMAWSITYHSWLTFVLLIWSCTLWMIRNRRKYAMISSP

FMVVYGNLLLILQYIWSFELPEIKKVPGFLEKKEPGELASKILFTITFWLLLRQHLTEQKAL
QEKEALLSEVKIGSQENEEKDEELQDIQVEGEPKEEEEEEAKEEKQERKKVEQEEAEEE
DEQDIMKVLGNLVVAMFIKYWIYVCGGMFFFVSFEGKIVMYKIIYMVLFLFCVALYQVHY
EWWRKILKYFWMSVVIYTMLVLIFIYTYQFENFPGLWQNMTGLKKEKLEDLGLKQFTVA
ELFTRIFIPTSFLLVCILHLHYFHDRFLELTDLKSIPSKEDNTIYRLAHPEGSLPDLTMMHLTA
SLEKPEVRKLAEPGEEKLEGYSEKAQKGDLGKDSEESEEDGEEEEESEEEEETSDLRNK
WHLVIDRLTVLFLKFLEYFHKLQVFMWWILELHIIKIVSSYIIWVSVKEVSLFNYVFLISWAF
ALPYAKLRRLASSVCTVWTCVIIVCKMLYQLQTIKPENFSVNCSLPNENQTNIPFNELNK
SLLYSAPIDPTEWVGLRKSSPLLVYLRNNLLMLAILAFEVTIYRHQEYYRGRNNLTAPVSRT
IFHDITRLHLDDGLINCAKYFINYFFYKFGLETCFLMSVNVIGQRMDFYAMIHACWLIAVL
YRRRRKAIAEIWPKYCCFLACIITFQYFICIGIPPAPCRDYPWRFKGASFNDNIIKWLYFPD
FIVRPNPVFLVYDFMLLLCASLQRQIFEDENKAAVRIMAGDNVEICMNLDAASFSQHNP
VPDFIHCRSYLDMSKVIIFSYLFWFVLTIIFITGTTRISIFCMGYLVACFYFLLFGGDLLLKPIK
SILRYWDWLIAYNVFVITMKNILSIGACGYIGTLVHNSCWLIQAFSLACTVKGYQMPAA
NSPCTLPSGEAGIIWDSICFAFLLLQRRVFMSYYFLHVVADIKASQILASRGAELFQATIV
KAVKARIEEEKKSMDQLKRQMDRIKARQQKYKKGKERMLSLTQEPGEGQDMQKLSEE
DDEREADKQKAKGKKKQWWRPWVDHASMVRSGDYYLFETDSEEEEEEELKKEDEEP
PRRSAFQFVYQAWITDPKTALRQRHKEKKRSAREERKRRRKGSKEGPVEWEDREDEPIK
KKSDGPDNIIKRIFNILKFTWVLFLATVDSFTTWLNSISREHIDISTVLRIERCMLTREIKKGN
VPTRESIHMYYQNHIMNLSRESGLDTIDEHPGAASGAQTAHRMDSLDSHDSISSEPTQC
TMLYSRQGTTETIEEVEAEQEEEAGSTAPEPREAKEYEATGYDVGAMGAEEASLTPEEE
LTQFSTLDGDVEAPPSYSKAVSFEHLSFGSQDDSAGKNRMAVSPDDSRTDKLGSSILPP
LTHELTASELLLKKMFHDDELEESEKFYVGQPRFLLLFYAMYNTLVARSEMVCYFVIILNH
MVSASMITLLLPILIFLWAMLSVPRPSRRFWMMAIVYTEVAIVVKYFFQFGFFPWNKNVE
VNKDKPYHPPNIIGVEKKEGYVLYDLIQLLALFFHRSILKCHGLWDEDDMTESGMAREES
DDELSLGHGRRDSSDSLKSINLAASVESVHVTFPEQQTAVRRKRSGSSSEPSQRSSFSSN
RSQRGSTSTRNSSQKGSSVLSIKQKGKRELYMEKLQEHLIKAKAFTIKKTLEIYVPIKQFFY
NLIHPEYSAVTDVYVLMFLADTVDFIIIVFGFWAFGKHSAAADITSSLSEDQVPGPFLVMV

LIQFGTMVVDRALYLRKTVLGKVIFQVILVFGIHFWMFFILPGVTERKFSQNLVAQLWYF
VKCVYFGLSAYQIRCGYPTRVLGNFLTKSYNYVNLFLFQGFRLVPFLTELRAVMDWVWT
DTTLSLSSWICVEDIYAHIFILKCWRESEKRYPQPRGQKKKKVVKYGMGGMIIVLLICIVW
FPLLFMSLIKSVAGVINQPLDVSVTITLGGYQPIFTMSAQQSQLKVMDQQSFNKFIQAF
SRDTGAMQFLENYEKEDITVAELEGNSNSLWTISPPSKQKMIHELLDPNSSFSVVFSWSI
QRNLSLGAKSEIATDKLSFPLKNITRKNIAKMIAGNSTESSKTPVTIEKIYPYYVKAPSDSNS
KPIKQLLSENNFMDITIILSRDNTTKYNSEWWVLNLTGNRIYNPNSQALELVVFNDKVSP
PSLGFLAGYGIMGLYASVVLVIGKFVREFFSGISHSIMFEELPNVDRILKLCTDIFLVRETGE
LELEEDLYAKLIFLYRSPETMIKWTREKTN

>Mouse_Piezo2

MASEVVCGLIFRLLLPICLAVACAFRYNGLSFVYLIYLLLIPLFSEPTKATMQGHTGRLLQS
LCITSLSFLLLHIIFHITLASLEAQHRITPAYNCSTWEKTFRQIGFESLKGADAGNGIRVFVP
DIGMFIASLTIWLVCRTIVKKPDTEEIAQLNSECENEELAGGEKMDSEEALIYEEDLDGEE
GMEGELEESTKLKILRRFASVASKLKEFIGNMITTAGKVVVTILLGSSGMMLPSLTSAVYFF
VFLGLCTWWSWCRTFDPLLFGCLCVLLAIFTAGHLIGLYLYQFQFFQEAVPPNDYYARL
FGIKSVIQTDCASTWKIIVNPDLSWYHHANPILLLVMYYTLATLIRIWLQEPLVQEEMAKE
DEGALDCSSNQNTAERRRSLWYATQYPTDERKLLSMTQDDYKPSDGLLVTVNGNPVD
YHTIHPSLPIENGPAKTDLYTTPQYRWEPSEESSEKKEEEEDKREDSEGEGSQEEKRSVR
MHAMVAVFQFIMKQSYICALIAMMAWSITYHSWLTFVLLIWSCTLWMIRNRRKYAMISS
PFMVVYANLLLVLQYIWSFELPEIKKVPGFLEKKEPGELASKILFTITFWLLLRQHLTEQKA
LREKEALLSEVKIGSQELEEKEDEELQDVQVEGEPTEKEEEEEEEIKEERHEVKKEEEEEV
EEDDDQDIMKVLGNLVVALFIKYWIYVCGGMFFFVSFEGKIVMYKIIYMVLFLFCVALYQ
VHYEWWRKILKYFWMSVVIYTMLVLIFIYTYQFENFPGLWQNMTGLKKEKLEDLGLKQF
TVAELFTRIFIPTSFLLVCILHLHYFHDRFLELTDLKSIPSKEDNTIYSHAKVNGRVYLIINRLA
HPEGSLPDLAIMNMTASLDKPEVQKLAESGEERPEECVKKTEKGEAGKDSDESEEEEDE
EEESEEEESSDLRNKWHLVIDRLTVLFLKFLEYFHKLQVFMWWILELHIIKIVSSYIIWVTVK
EVSLFNYVFLISWAFALPYAKLRRAASSVCTVWTCVIIVCKMLYQLQTIKPENFSVNCSLP

NENQTNIPLHELNKSLLYSAPVDPTEWVGLRKSSPLLVYLRNNLLMLAILAFEVTVYRHQ
EYYRGRNNLTAPVSKTIFHDITRLHLDDGLINCAKYFVNYFFYKFGLETCFLMSVNVIGQ
RMDFYAMIHACWLIGVLYRRRRKAIAEVWPKYCCFLACIITFQYFVCIGIPPAPCRDYPW
RFKGAYFNDNIIKWLYFPDFIVRPNPVFLVYDFMLLLCASLQRQIFEDENKAAVRIMAGD
NVEICMNLDAASFSQHNPVPDFIHCRSYLDMSKVIIFSYLFWFVLTIIFITGTTRISIFCMGY
LVACFYFLLFGGDLLLKPIKSILRYWDWLIAYNVFVITMKNILSIGACGYIGALVRNSCWLI
QAFSLACTVKGYQMPEDDSRCKLPSGEAGIIWDSICFAFLLLQRRVFMSYYFLHVVADI
KASQILASRGAELFQATIVKAVKARIEEEKKSMDQLKRQMDRIKARQQKYKKGKERMLS
LTQESGEGQDIQKVSEEDDEREADKQKAKGKKKQWWRPWVDHASMVRSGDYYLFE
TDSEEEEEEELKKEDEEPPRKSAFQFVYQAWITDPKTALRQRRKEKKKLAREEQKERRK
GSGDGPVEWEDREDEPVKKKSDGPDNIIKRIFNILKFTWVLFLATVDSFTTWLNSISREHI
DISTVLRIERCMLTREIKKGNVPTRESIHMYYQNHIMNLSRESGLDTIDEHSGAGSRAQA
AHRMDSLDSRDSISSCYTEATLLISRQSTLDDLDGQDPVPKTSERARPRLRKMFSLDMSS
SSADSGSVASSEPTQCTMLYSRQGTTETIEEVEAEAEEEVVEGLEPELHDAEEKEYAAEY
EAGVEEISLTPDEELPQFSTDDCEAPPSYSKAVSFEHLSFASQDDSGAKNHMVVSPDDS
RTDKLESSILPPLTHELTASDLLMSKMFHDDELEESEKFYVDQPRFLLLFYAMYNTLVARS
EMVCYFVIILNHMTSASIITLLLPILIFLWAMLSVPRPSRRFWMMAIVYTEVAIVVKYFFQFG
FFPWNKDLEIYKERPYFPPNIIGVEKKEGYVLYDLIQLLALFFHRSILKCHGLWDEDDIVDS
NTDKEGSDDELSLDQGRRGSSDSLKSINLAASVESVHVTFPEQPAAIRRKRSCSSSQISP
RSSFSSNRSKRGSTSTRNSSQKGSSVLSLKQKSKRELYMEKLQEHLIKAKAFTIKKTLQIYV
PIRQFFYDLIHPDYSAVTDVYVLMFLADTVDFIIIVFGFWAFGKHSAAADITSSLSEDQVP
GPFLVMVLIQFGTMVVDRALYLRKTVLGKVIFQVILVFGIHFWMFFILPGVTERKFSQNLV
AQLWYFVKCVYFGLSAYQIRCGYPTRVLGNFLTKSYNYVNLFLFQGFRLVPFLTELRAV
MDWVWTDTTLSLSSWICVEDIYAHIFILKCWRESEKRYPQPRGQKKKKAVKYGMGGMII
VLLICIVWFPLLFMSLIKSVAGVINQPLDVSVTITLGGYQPIFTMSAQQSQLKVMDNSKY
NEFLKSFGPNSGAMQFLENYEREDVTVAELEGNSNSLWTISPPSKQKMIQELTDPNSCF
SVVFSWSIQRNMTLGAKAEIATDKLSFPLAVATRNSIAKMIAGNDTESSNTPVTIEKIYPY
YVKAPSDSNSKPIKQLLSENNFMNITIILFRDNVTKSNSEWWVLNLTGSRIFNQGSQALE

LVVFNDKVSPPSLGFLAGYGIMGLYASVVLVIGKFVREFFSGISHSIMFEELPNVDRILKLC
TDIFLVRETGELELEEDLYAKLIFLYRSPETMIKWTREKTN

>Rat_Piezo2

MASEVVCGLIFRLLLPICLAVACAFRYNGLSFVYLIYLLLIPLFSEPTKATMQGHTGRLLQS
LCITSLSFLLLHIIFHITLASLEAQHRIAPAYNCSTWEKTFRQIGFESLKGADAGNGIRVFVP
DIGMFIASLTIWLVCRTIVKKPDTEEVAQFNSECENEELAGGEKMDSEEALIYEEDLDGE
EGMEGELEESTKLKMFRRLASVASKLKEFIGNMITTAGKVVVTILLGSSGMMLPSLTSAV
YFFVFLGLCTWWSWCRTFDPLLFGCLCVLLAIFTAGHLIGLYLYQFQFFQEAVPPNDYY
ARLFGIKSVIQTDCSSTWKIIVNPDLSWYHHANPILLLVMYYTLATLIRIWLQEPLVQEEM
SKEEEGALDGCSNQNTAERRRSLWYATQYPTDERKLLSMTQDDYKPSDGLLVTVNGN
PVDYHTIHPSLPIENGPAKTDLYTTPQYRWEPSEESSEKKEEEEDKREDSEGEGSQEEKR
SVRIHAMVAVFQFIMKQSYICALIAMMAWSITYHSWLTFVLLIWSCTLWMIRNRRKYAMI
SSPFMVVYANLLLVLQYIWSFELPEIKKVPGFLEKKEPGELASKILFTITFWLLLRQHLTEQ
KALQEKEALLSEVKIGSQELDEKDEELQDIQVEGEPIEKEEEEEEIKEDRHEVKKEEEEEE
EDDDDQDIMKVLGNLVVALFIKYWIYVCGGMFFFVSFEGKIVMYKIIYMVLFLFCVALYQ
VHYEWWRKILKYFWMSVVIYTMLVLIFIYTYQFENFPGLWQNMTGLKKEKLEDLGLKQF
TVAELFTRIFIPTSFLLVCILHLHYFHDRFLELTDLKSIPSKEDNTIYRLAHPEGSLPDLAIMN
MTASLDKPERQKLAEPGEERTEECAKKAEKGEAGKDSDESEEEEGEEEESEEEESSDLR
NKWHLVIDRLTVLFLKFLEYFHKLQVFMWWILELHIIKIVSSYIIWVTVKEVSLFNYVFLISW
AFALPYAKLRRVASSVCTVWTCVIIVCKMLYQLQTIKPENFSVNCSLPNENQTNIPLNEL
NKSLLYSAPVDPTEWVGLRKSSPLLVYLRNNLLMLAILAFEVTVYRHQEYYRGRNNLTAP
VSKTIFHDITRLHLDDGLINCAKYFVNYFFYKFGLETCFLMSVNVIGQRMDFYAMIHAC
WLIGVLYRRRRKAIAEVWPKYCCFLACIITFQYFVCIGIPPAPCRDYPWRFKGANFNDNII
KWLYFPDFIVRPNPVFLVYDFMLLLCASLQRQIFEDENKAAVRIMAGDNVEICMNLDAA
SFSQHNPVPDFIHCRSYLDMSKVIIFSYLFWFVLTIIFITGTTRISIFCMGYLVACFYFLLFGG
DLLLKPIKSILRYWDWLIAYNVFVITMKNILSIGACGYIGALVRNSCWLIQAFSLACTVKGY
KMPEDDSRCKLPSGEAGIIWDSICFAFLLLQRRVFMSYYFLHVVADIKASQILASRGAELF

QATIVKAVKARIEEEKKSMDQLKRQMDRIKARQQKYKKGKERMLSLTQESGEGQDIQK
VSEEDDEREADKQKAKGKKKQWWRPWVDHASMVRSGDYYLFETDSEEEEEEELKKE
DEEPPRKSAFQFVYQAWITDPKTALRQRRKEKKKMAREEQKGRRKGSGEGPVEWEDR
EDEPIKKKSDGPDNIIKRIFNILKFTWVLFLATVDSFTTWLNSISREHIDISTVLRIERCMLTR
EIKKGNVPTRESIHMYYQNHMMNLSRESGLDTIDEHSGAGSRAQAAHRMDSLDSHDSI
SSEPTQCTMLYSRQGTTETIEEVEAEAEEEVVESLEPELHDAEEKEYAADYEAGVEEVSL
TPDEELPQFSTDDGDVEAPPSYSKAVSFEHLSFASQDDSGGKNHMVVSPDDSRTDKLE
SSILPPLTHELTASDLLMSKMFRDDELEESEKFYVDQPRFLLLFYAMYNTLVARSEMVCYF
VIILNHMISASIITLLLPILIFLWAMLSVPRPSRRFWMMAIVYTEVAIVVKYFFQFGFFPWNK
DLEIYKDRPYFPPNIIGVEKKEGYVLYDLIQLLALFFHRSILKCHGLWDEDDIVDSNTDKE
GSDDELSLGQGRRGSSESLKSINLAASVESVHVTFPEQPAAIRRKRSCSSSQISPRSSFSS
NRSKRGSTSTRNSSQKGSSVLSIKQKSKRELYMEKLQEHLIKAKAFTIKKTLQIYVPIRQFF
YDLIHPDYSAVTDVYVLMFLADTVDFIIIVFGFWAFGKHSAAADITSSLSEDQVPGPFLV
MVLIQFGTMVVDRALYLRKTVLGKVIFQVILVFGIHFWMFFILPSVTERKFSQNLVAQLW
YFVKCVYFGLSAYQIRCGYPTRVLGNFLTKSYNYVNLFLFQGFRLVPFLTELRAVMDWV
WTDTTLSLSSWICVEDIYAHIFILKCWRESEKPIFTMSAQQSQLKVMDGTKYNEFIKSFG
PNSGAMQFLENYERQDITVAELEGNSNSLWTISPPSKQKMIQELTDPNSCFSVVFSWSI
QRNMTLGAKAEIATDKLSFPLTDATRSSIAKMIAGNDTESSNTPVTIEKIYPYYVKAPSDS
NSKPIKQLLSENNFMNITIILFRDNVTKSNSEWWVLNLTGSRIFNQGSQALELVVFNDKV
SPPSLGFLAGYGIMGLYASVVLVIGKFVREFFSGISHSIMFEELPNVDRILKLCTDIFLVRET
GELELEEDLYAKLIFLYRSPETMIKWTREKTN

>Bovine_Piezo2

MASEVVCGLVFRLLLPICLAVACAFRYNGLSFVYLIYLLLIPLFSEPTKATMQGHTGRLLKS
LCFTSLSFLLLHIIFHITLASLEAQHRIAPGYNCSTWEKTFRQIGFESLKGADAGNGIRVFV
PDVGMFIASLTIWLVCRNIVQKPVAEEAAQCNPEFENEESAGGEKIDSEEALIYEEDLDE
GDGAEGDLEESAKLKLFRRLASVASKLKEFIGNMITTAGKVVVTILLGSSGMMLPSLTSSV
YFFVFLGLCTWWSWCRTFDPLLFSCLCVLLAIFTAGHLIGLYLYQFQFFQEAVPPNDYY

ARLFGIKSVIQTDCSSTWKIIANPDLSWYHHANPIVLLVMYYTLATLIRIWLQEPVVQEER
TKEEDRALACSPAPITAERRRSLWYATHYPTDERKLLSMTQDDYKPSDGLLVTVNGNPV
DYHTIHPSLPLENGPAKADLYSTPQYRWEPAAASPEKKEEDDDEKEEFEEERSREEKRSV
KVHAMVSVFQFIMKQSYICALIAMMAWSITYHSWLTFVLLIWSCTLWMIRNRRKYAMIS
SPFMVVYGNLLLILQYIWSFELPEIKKVPGFLEKKEPGELASKILFTITFWLLLRQHLTEQKA
LQEKEALLSEVKIGSQEREEKDDEQDLQVDSEAQEKEEEEEPKEEQQERREEEEEEEAD
EQDVMKVLGNLVVALFIKYWIYVCGGMFFFVSFEGKIVMYKIIYMVLFLFCVALYQVHYE
WWRRILKYFWMSVVIYTMLVLIFIYTYQFENFPGLWQNMTGLKKEKLEDLGLKQFTVAE
LFTRIFIPTSFLLVCILHLHYFHDRFLELTDLKSIPTHASSARPSRPLTENLTYTCHDSQLAHP
EGSLPDLAMMKLTASLEVAEVKQLAGPGEEMPGGCPAKAKKGEPGRDSEDEDEDED
EEEEETSDLRNKWHLVIDRLTVLLLRFLEGFHQLQTFLWWILELHIVKIVSSYIIWVSVKEVS
LFNYVFLISWAFALPYARLRRLASSVCTVWTCVIIVCKMLYQLQTIKPENFSVNCSLPNEN
QTNIPLHQLNKSLLYSAPIDPTEWVGLRKSSPLLVYLRNNLLMLAILAFEVTVYRHQEYYR
GRNNLSTPVSKTIFHNITRLQLDDGLVNCAKYFINYFFYKFGLETCFLMSVNVIGQRMDF
YAMIHACWLIAVLYRRRRKAIAEIWPKYCCFLACIITFQYFICIGIPPAPCRDYPWRFKGAS
FNDNIVKWLYFPDFIVRPNPVFLVYDFMLLLCASLQRQIFEDENKAAVRIVAGDNVEICM
NLDAASFSQHNPVPDFIHCRSYLDMSKVVIFSYLFWFVLTIIFITGTTRISIFCMGYLVACF
YFLLFGGDLLLKPIKSILRYWDWLIAYNVFVITMKNILSIGACGYIEKLVQNSCWLIQAFSL
ACTVKGYKMPDDDSSCKLPSGEAGIIWDSICFAFLLLQRRVFMSYYFLHVVADIKASQIL
ASRWGLSFSRPPL

>Chimpanzee_Piezo2

MASEVVCGLIFRLLLPICLAVACAFRYNGLSFVYLIYLLLIPLFSEPTKTTMQGHTGRLLKSL
CFISLSFLLLHIIFHITLVSLEAQHRIAPGYNCSTWEKTFRQIGFESLKGADAGNGIRVFVP
DIGMFIASLTIWLLCRNIVQKPVTDEAAQSNPEFENEELAGGEKIDSEEALIYEEDFNGG
DGVEGELEESTKLKMFRRLASVASKLKEFIGNMITTAGKVVVTILLGSSGMMLPSLTSSVY
FFVFLGLCTWWSWCRTFDPLLFSCLCVLLAIFTAGHLIGLYLYQFQFFQEAVPPNDYYA
RLFGIKSVIQTDCSSTWKIIVNPDLSWYHHANPILLLVMYYTLATLIRIWLQEPLVQDEGT

KEEDKALACSPIQITAERRRSLWYATHYPTDERKLLSMTQDDYKPSDGLLVTVNGNPVD
YHTIHPSLPMENGPGKADLYSTPQYRWEPSDESSEKREEEEEEKEEFEEERSREEKRSIKV
HAMVSVFQFIMKQSYICALIAMMAWSITYHSWLTFVLLIWSCTLWMIRNRRKYAMISSP
FMVVYGNLLLILQYIWSFELPEIKKVPGFLEKKEPGELASKILFTITFWLLLRQHLTEQKAL
QEKEALLSEVKIGSQENEEKDEELQDIQVEGDPKEEEEEEAKEEKQERKKVEQEEAEEE
DEQDIMKVLGNLVVAMFIKYWIYVCGGMFFFVSFEGKIVMYKIIYMVLFLFCVALYQVHY
EWWRKILKYFWMSVVIYTMLVLIFIYTYQFENFPGLWQNMTGLKKEKLEDLGLKQFTVA
ELFTRIFIPTSFLLVCILHLHYFHDRFLELTDLKSIPSKEDNTIYRLAHPEGSLPDLTMMHLTA
SLEKPEVRKLAEPGEEKPEGYSEKAQKGDLGKDSEESEEDGEEEEESEEEEETSDLRNK
WHLVIDRLTVLFLKFLEYFHKLQVFVWWILELHIIKIVSSYIIWVSVKEVSLFNYVFLISWAFA
LPYAKLRRLASSVCTVWTCVIIVCKMLYQLQTIKPENFSVNCSLPNENQTNIPFNELNKSL
LYSAPIDPTEWVGLRKSSPLLVYLRNNLLMLAILAFEVTIYRHQEYYRGRNNLTAPVSRTIF
HDITRLHLDDGLINCAKYFINYFFYKFGLETCFLMSVNVIGQRMDFYAMIHACWLIAVLY
RRRRKAIAEIWPKYCCFLACIITFQYFICIGIPPAPCRDYPWRFKGASFNDNIIKWLYFPDFI
VRPNPVFLVYDFMLLLCASLQRQIFEDENKAAVRIMAGDNVEICMNLDAASFSQHNPV
PDFIHCRSYLDMSKVIVFSYLFWFVLTIIFITGTTRISIFCMGYLVACFYFLLFGGDLLLKPIK
SILRYWDWLIAYNVFVITMKNILSIGACGYIGTLVHNSCWLIQAFSLACTVKGYQMPAA
NSPCTLPSGEAGIIWDSICFAFLLLQRRVFMSYYFLHVVADIKASQILASRGAELFQATIV
KAVKARIEEEKKSMDQLKRQMDRIKARQQKYKKGKERMLSLTQEPGEGQDMQKLSEE
DDEREADKQKAKGKKKQWWRPWVDHASMVRSGDYYLFETDSEEEEEEELKKEDEEP
PRRSAFQFVYQAWITDPKTALRQRHKEKKRSAREERKRRRKGSKEGPVEWEEREDEPIK
KKSDGPDNIIKRIFNILKFTWVLFLATVDSFTTWLNSISREHIDISTVLRIERCMLTREIKKGN
VPTRESIHMYYQNHIMNLSRESGLDTIDEHPRAASGAQTAHRMDSLDSHDSISSEPTQC
TMLYSRQGTTETIEEVEAEQEEEAGSMAPEPREAKEYEATGYDVGAMGAEEASLTPEE
ELTQFSTLEGDVEAPPSYSKAVSFEHLSFGSQDDSAGKNHMAVSPDDSRTDKLGSSILP
PLTHELTASELLLKKMFHDNELEESEKFYVGQPRFLLLFYAMYNTLVARSEMVCYFVIILN
HMVSASMITLLLPILIFLWAMLSVPRPSRRFWMMAIVYTEVAIVVKYFFQFGFFPWNKNV
EVNKDKPYHPPNIIGVEKKEGYVLYDLIQLLALFFHRSILKCHGLWDEDDMTESGMDKE

ESDDELSLGHGRRDSSDSLKSINLAASVESVHVTFPEQQTAVRRKRSGSSSEPSQRSSFS
SNRSQRGSTSTRNSSQKGSSVLSTKQKSKRELYMEKLQEHLIKAKAFTIKKTLEIYVPIKQF
FYNLIHPEYSAVTDVYVLMFLADTVDFIIIVFGFWAFGKHSAAADITSSLSEDQVPGPFLV
MVLIQFGTMVVDRALYLRKTVLGKVIFQVILVFGIHFWMFFILPGVTERKFSQNLVAQLW
YFVKCVYFGLSAYQIRCGYPTRVLGNFLTKSYNYVNLFLFQGFRLVPFLTELRAVMDWV
WTDTTLSLSSWICVEDIYAHIFILKCWRESEKRYPQPRGQKKKKVVKYGMGGMIIVLLICI
VWFPLLFMSLIKSVAGVINQPLDVSVTITLGGYQPIFTMSAQQSQLKVMDQQSFNKFIQ
AFSRDTGAMQFLENYEKEDITVAELEGNSNSLWTISPPSKQKMIHELLDPNSSFSVVFS
WSIQRNLSLGAKSEIATDKLSFPLKNITRKNIAKMIAGNSTESSKTPVTIEKIYPYYVKAPSD
SNSKPIKQLLSENNFMDITIILSRDNTTKYNSEWWVLNLTGNRIYNPNSQALELVVFNDK
VSPPSLGFLAGYGIMGLYASVVLVIGKFVREFFSGISHSIMFEELPNVDRILKLCTDIFLVRE
TGELELEEDLYAKLIFLYRSPETMIKWTREKTN

>Killifish_Piezo2

MASEVACGLIFRFLLPLCLAAACLFRYNVLSFIYLIYLLLIPLFPEPTCTTMQGHTGCLLQSL
CFTSMSFLLLHIIYQITVNSLLAGNSISSNFSCSSWERSIRQIGFESVIGADAGNGIRVFIPDI
GMFVAGLAIWLVCRSLVQKRPPEDMALDNADFEAEEEDEEEKPSLDDDDILLEEDLEA
GYEAEEDEDNEELYGDEEEEYEEEEEEARESTKMKILRMVAEVASKVKEVIGNLITTAGK
VVVTVLLGMTGIMLPSLTSFVYFSIFLFLCTWWSLRRTFNTLIFSCMCVLMAIFSAGHLIVL
YLYQFQFFQDSIHPEDSYIRVFGISPIVQTNCSFTWKLIVRPERKWHHFVNPIMLLILYYTL
ATLIRLWLQEPIDQLMDKEDDVNEEEEHSGSRVNNSANRKRQMWWESRQGTDEKNA
IPTSNGTSFDFVATENGQVCLDLYSTPQYKPDKPTDGTEKKEECVYEVSLPPEDSGQKE
SEDEENDIKKKGVGAMVKIFHFIMKQSYICALIAMMTWSITYVSWQTFVFLMWSCILW
MVRDRRRYAMLSSPFMVAYGNLVIVLQYIGSFETMKPVPGFIVAKNNLFHSLSSKMMCL
VTFWLLLRQTLTEREEKTKEDNAGLSDVYVEDQKKKEEEQSEEGGEQDIMHVLGNLM
MSMLVKYWIYICGGMFFFVSFEGDIVMYKIIYMMMLLFCVALYQVHYEWWRRILKYFW
MTVVIYTMLVLTIVYTFQFERSEGFWVGMLNIKNESLKDLGLERFSLSTLFTRIFIPTSFLLV
CNLHLHYFHDRFLQLTDLQAVVAKEESTIYRLVDQDGSLADLTMLSGSSVDAALPKEKE

AQQEEQEGWDSEREKKQALVAVMDTDTHMTREKPRSFSDQRQSSTEESQHCSAATE
PEPSTEQSSGLKNKWHLVVDRLTVLFLKFLEYFHKLQLFIWWLLEIHIIKIVSCYIIMVTIYEV
SLLNYVFLATWAFALPYSKYRPLASIVCTVWTCVIIVCKMLYQLKSISPAPYNCTMDSRYE
PKQKEELAGSLLYSDKKGDPGNWVGLRKSTDLLGYLRYNLLMLALLAFEVTIYRHQEYF
RLRNKLLPPAARIIFHDITRQHLDIGIICFIKYFINYFFYKFGLETCLLLVVNVIGQRMDFYA
MLHAFALIAVMYRRRRKAIAEIWSKYCFFLASMLTLQYFICIGIPPAACKEYPWRLPGSYT
DSNVIKWLYIPDFLMRPNPNFLIYDFMLLLCASLQRQIFDDENKAAVRLMAGDNVEICR
DLDAASFSVHNPVPDFIHCRSYLDMLKVIMFSYLFWFVLTIIFFTGTTRISVFCMGYLVAC
FYFLLFGGNLLLKPIKKILHYWDFLIAYNIFVITMKNILSILACGYITSLVKNHCWLIQFFSLA
CTIKGYNTTLDIDSRKSCELPKDEAGIIWDSICFAFLLLQRRVFMSYYFLHVVADIRASQIL
ASRGAELFQATIVKAVKARLEEERKSVEQLKRQMDRIKVRQQKFKRGKEKMLSLAQESV
DGQTAAVQDEDDDDGAQRTKAKTKKKQWWRPWVDHASMVRSGDYYLFETDS

>Zebrafish_Piezo2

MFVVSLVTWLLCRSLEKPSIKEDSQHNSDFEVDNQEKEDEEEDENREKRELEDELLFED
FELRDGDCELPENEEEEEEAADADDGDLEEPDIEESTKTRILRQIADAASKLKEIVGNLIT
SAGKVVVTVLLGLTGMMLPSLTSSVYFFTFLGLCTWWSFCRSFDPLLFSCLCVLMAIFSA
GHLVFLYLYQFQFFQEAVPPGNTYASLFGISPVVQTDCSHTWMFKVNPALEWHHFVN
PIMLLVLYYTLATLIRLWLQESEDTVRDAEAEGKDDAASPENTDINVYTADQRRQLWRM
AHYHTDERNLLTAQEAYNSPEVLIVTSNGASLDFTSVSHEKRPKCVERNLYSTPHYKAD
QPESDTQSLDCGVYRIDSAYVELSELPVAVVRVNSVVKVFRFIMKQSYICALIAMMAWSI
TYVSWLTFVFLIWSCTLWMVRDRRKYSMVTSPFMVFYGNLLIILQYIWSFECLQPVPGLF
LKKEVPFRELGSKTLCLLSFWLLLRQFLTERREKHTDDPQLSDVTVDGHKLGLQDEAAG
HREMMEVLGSSLMAMLNKYWIYICGGMFFFVSFEGRIVMYKIIYMMMFLFCVALYQLH
YERWRWMLKYFWMSVVVYTMLVLILVYTFQFESSINVWSNMTGMSREKLEDLGLEKFS
VPALFTRIFIPTWFLLVCILHLHYFHERFLELTDIKTVADKQKSTISRLVHLDGSLVDISMIKP
TFNSTNEEEVEKQEDEEDNNYHNEDEDEDERVELEEEDVKQTEEQKMEDSLFTCPMT
ADPVLEQTSELKSKWHLVVERLTVLFLKFLDCIQKLQLFIWWILELHIIKIVSSYIIWVSVKE

VSLFNYVFVVSWAFALPFCQFRPLASSVCTVWTCIIIVCKMLYQLTSISPAAYARNCSMP
DNYTEAQRMDMAKSLLYIGPVDPANWIGLRKFSPLLEYLRNNLLMLALLAFEVTIYRHQ
DFYRMKNNITPPVTRTIFHNITRQHLDDGIVNCAKYFINYFFYKFGLETCFLLAVNVIGQR
MDFFAMLHAFGLIAVMYQRRRKAIAHVWSKYCCFLACLLSFQYLMCIGIPPAACTDYP
WRRSSSSMDSNVIKWLYFPDFHTKPNSLFLLYDFMLLLCASLQGRVFEEECVSPVQLLA
GDNVEICRDLDAATFSQHNPVPDFIHCRSYLDMLKVMVFSYLFWFVLTIIFITGTTRISIFC
MGYLVACFYFLIFGGELLLKPIKSILHYWDFLIAYNVFVITMKNILSIAACGYIKALVANHC
WLIQLFSLACTIKGYSKPEQQANKQCELPSDEAGIIWDSICFAFLLLQRRVFMSYYFLHV
VADIRSSQLLASRGAELFQATIVKAVKARIEEEKKSMDLLKRQMDRIKSRQQKFKRGKER
MLSLAQESGERHSVLKEEEEEEEEESSKEKKKGKRKQWWRPWVDHASMVRSGNYYLF
ETDSEEEEEDEDRKDEEPKRSAFQFVYHAWITDSKTAMKERRKEKRRFWQKYTESNTN
KREQKEANVTVEEGDQDGVTEDELSDSPDNMMKRVFNMVKFSWVLFLALLDSFTAW
LNSICQEHIDISSVLRIERCMLTHEAKKGNVPSRDSIRMYYQRQMCRPASTQSSLEPTEE
AYSDFSPLRTDPDLPPQEHTELQTSTENLASVYTESSIVEDSTLDEERVLKTSQRSRPKLC
RISGVDVPSSADSAASSEHTQGTELYSRQGTSDTVEECGADTLWSSASDLLQTPHRDV
PPSYSRATGLDCICDERKLKIQTPEDSSSGTPHTSSHRLTASELLQTRMFYDADLEQSER
FYRSQPQLLQLCYSLYNVLVSHSQMVCYLVIILNHMISASVATLVLPVLIFLWAMLSVPRP
SKRFWMTAIVYTEVTIVIKYFFQFGFFPFNQSIEVDKSKPFHPPNIIGVEKKEGYVHYDLV
QLLALFFHRSILKCYGLWDEEEPRSVSPHTHSGAEEKAECFSEKSPVEDTYTHALSHTHL
RLARKQQSSAGVRRQSSSISQRSARSKTGSSVSRSSVRRSLSAQQKSRKELLMEKLREQL
IRAKRFTVKTVLDVYIPIRQFFYSLIHPEYSAVTDVYVLMFLADTVDFIIIVFGFWAFGKHSA
AADITSSLSEDQVPEAFLVMVLIQFGTMVVDRALYLRKTVMGKVIFQVILVFGIHFWMFFI
LPGVTERRFSQNTVAQLWYFVKCIYFGLSAYQIRCGYPTRVLGNFLTKSYNYLNLFLFQG
FRLVPFLTELRAVMDWVWTDTTLSLSSWICVEDIYAHIFVLKCWRESEKRYPQPRGQKK
KKVVKYGMGGMIVMLLICIVWFPLLFMSLVKSVAGVVNKPLDVSVTITLGGFQPIFTMSA
QQNQLKELTESDFKNFINSYNYVPSAMQFLEAYRAEDVTVAELEGSSNSLWTISPPSRK
NLMDVLSKEDQFPVTMTWSIQRNLSLGAKSEFAMDKHVTYLDIKTRQELIALLNGTRNT
PVLIEQVFPCFIRAPSDSNAKPIEQLYEDGVYKSIQLDLERSANSSEDLQEWWIVDELRSA

QKQQREAGLQLYVFSDKVSPPSLGFLAGYGIMGLYASVVLVIGKFVREFFSGISHSIMFE

ELPCVDRILKLCTDIFLVRETGELELEEDLYAKLIFLYRSPETMIKWTREKNK

A.5 Statistical analysis results for Fig. 26

sample sizes (n)					
sample	cytosolic	no linker	1xGSGG	2xGSGG	stimuli
GCaMP G1	20	15	15	13	shear stress
	18	15	15	9	ionomycin
GCaMP G2	18	13	16	14	shear stress
	21	19	16	16	ionomycin
GCaMP-G3	17	9	15	14	shear stress
	15	17	16	15	ionomycin
GCaMP-G4	13	14	12	17	shear stress
	18	13	15	12	ionomycin
GCaMP-G5	18	14	11	14	shear stress
	19	11	14	17	ionomycin
eGFP			16		shear stress
			19		ionomycin

p value (Shapiro-Wilk normality test)					
sample	cytosolic	no linker	1xGSGG	2xGSGG	stimuli
GCaMP-G1	0.4059	0.8072	0.0014	0.0424	shear stress
	0.0507	0.0004	0.0106	0.4371	ionomycin
GCaMP-G2	0.2206	0.498	0.7152	0.681	shear stress
	0.0787	0.3892	0.0018	0.3099	ionomycin
GCaMP-G3	<0.0001	0.0139	0.0751	0.2232	shear stress
	0.2435	<0.0001	0.0171	0.4208	ionomycin
GCaMP-G4	0.796	0.6878	0.0384	0.1161	shear stress
	0.0415	0.2133	0.0002	0.0069	ionomycin
GCaMP-G5	0.0406	0.9933	0.223	0.2232	shear stress
	0.0183	0.0123	0.0879	0.001	ionomycin
eGFP			0.0263		shear stress
			0.1312		ionomycin

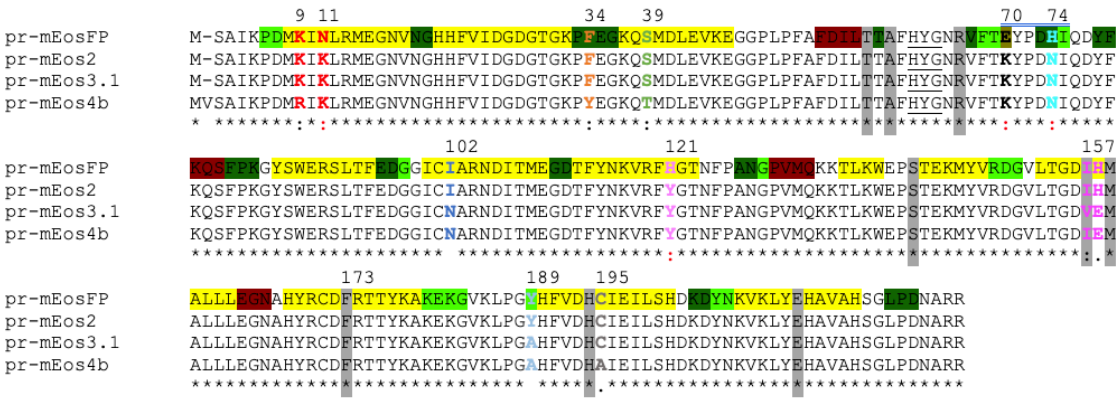
shear stress response (F/F0)				
p value	no linker	1xGSGG	2xGSGG	sample
cytosolic vs.	0.4232	0.0427	0.1694	GCaMP-G1
cytosolic vs.	0.3668	0.0035	0.0515	GCaMP-G2
cytosolic vs.	0.0388	0.0078	0.0209	GCaMP-G3
cytosolic vs.	0.7339	0.0188	0.0432	GCaMP-G4
cytosolic vs.	0.0001	0.0922	0.0143	GCaMP-G5

ionomycin response (F/F0)				
p value	no linker	1xGSGG	2xGSGG	sample
cytosolic vs.	<0.0001	<0.0001	0.0016	GCaMP-G1
cytosolic vs.	0.0002	0.0004	<0.0001	GCaMP-G2
cytosolic vs.	0.0003	<0.0001	0.0003	GCaMP-G3
cytosolic vs.	0.0036	<0.0001	0.3684	GCaMP-G4
cytosolic vs.	0.0183	0.0001	0.0231	GCaMP-G5

shear stress vs. ionomycin response (F/F0)				
sample	no linker	1xGSGG	2xGSGG	
GCaMP-G1	<0.0001	0.766	0.0004	p value
GCaMP-G2	0.5842	0.2811	0.53	
GCaMP-G3	0.7916	0.6189	0.0024	
GCaMP-G4	0.011	<0.0001	0.4187	
GCaMP-G5	0.2441	<0.0001	0.0586	

F/F0		
p value	PiezoG4	
Piezo1-eGFP vs.	<0.0001	shear stress (10 dyne/cm2)
	0.9454	ionomycin (1 μM)

A.6 Sequence alignment of pr-FPs of the mEos family and amino acid ratios per position



Position	pr-mEosFP	pr-mEos2	pr-mEos3.1	pr-mEos4b	Ratios
9	K	K	K	R	3K:1R
11	N	K	K	K	1N:3K
34	F	F	F	Y	3F:1Y
39	S	S	S	T	3S:1T
70	E	K	K	K	1E:3K
74	H	N	N	N	1H:3N
102	I	I	N	N	2I:2N
121	H	Y	Y	Y	1H:3Y
157	I	I	V	I	2I:1V:1I
158	H	H	E	E	2H:2E
189	Y	Y	A	A	2Y:2A
195	C	C	C	A	3C:1A

CLUSTAL W (1.83) multiple sequence alignment